

AD734752

A TURBULENT MODEL STUDY FOR THE MULTICOMPONENT NONSIMILAR TURBULENT BOUNDARY LAYER PROGRAM

Larry W. Anderson Howard L. Morse

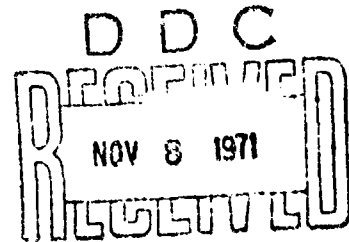
Aerotherm Corporation

TECHNICAL REPORT NO. AFWL-TR-71-57

October 1971

AIR FORCE WEAPONS LABORATORY
Air Force Systems Command
Kirtland Air Force Base
New Mexico

Reproduced by
NATIONAL TECHNICAL
INFORMATION SERVICE
Springfield, Va. 22151



Approved for public release; distribution unlimited.

UNCLASSIFIED

Security Classification

DOCUMENT CONTROL DATA - R & D

(Security classification of title, body of abstract and indexing annotation must be entered when the overall report is classified)

1. ORIGINATING ACTIVITY (Corporate author) Aerotherm Corporation 485 Clyde Avenue Mountain View, California 94040		2a. REPORT SECURITY CLASSIFICATION UNCLASSIFIED	
		2b. GROUP	
3. REPORT TITLE A TURBULENT MODEL STUDY FOR THE MULTICOMPONENT NONSIMILAR TURBULENT BOUNDARY LAYER PROGRAM			
4. DESCRIPTIVE NOTES (Type of report and inclusive dates) May 1970 through March 1971			
5. AUTHOR(S) (First name, middle initial, last name) Larry W. Anderson Howard L. Morse			
6. REPORT DATE October 1971	7a. TOTAL NO. OF PAGES 206	7b. NO. OF REFS 94	
8a. CONTRACT OR GRANT NO. F29601-70-C-0055	9a. ORIGINATOR'S REPORT NUMBER(S) AFWL-TR-71-57		
b. PROJECT NO. 5791	9b. OTHER REPORT NO(S) (Any other numbers that may be assigned this report)		
c. Task 27			
d.			
10. DISTRIBUTION STATEMENT Approved for public release; distribution unlimited.			
11. SUPPLEMENTARY NOTES		12. SPONSORING MILITARY ACTIVITY AFWL (SYT) Kirtland AFB, NM 87117	
13. ABSTRACT (Distribution Limitation Statement A) An investigation of the accuracy of the Air Force Weapons Laboratory Nonsimilar Turbulent Boundary Layer Computer Code through comparisons of predictions with experimental data is presented. Five complete data sets are selected from a literature survey which originally considered over one hundred separate turbulent boundary layer experimental investigations. The five data sets include flat plate supersonic flow, hypersonic flow with and without acceleration, supersonic flow with highly nonsimilar wall temperature distributions, subsonic flow with various wall blowing rates, and supersonic flow with wall blowing. Before the present study, the turbulent model in the AFWL code was relatively untested for compressible flows, but is left essentially unchanged after detailed comparisons with other popular turbulent models. Detailed predictions for each of the five data sets are carried out, and approximately 75 graphical comparisons are presented which include velocity, total temperature, and Mach number profiles at several axial stations, plus momentum thickness and drag coefficient variations along the flow direction. Overall agreement between the profile predictions and the experimental data is good for flow with and without blowing. Drag coefficient prediction for blown flows is typically below reported values for the data sets selected. However, these results are taken as inconclusive since there is disagreement among the turbulent boundary layer research community as to the validity of these data. Information on the correct use of the computer code for turbulent boundary layer predictions, and on a new entropy layer option, is also presented. The entropy layer model directly couples the inviscid flow entropy gradients caused by shock curvature with the boundary layer edge boundary conditions.			

DD FORM 1473
1 NOV 65

UNCLASSIFIED

Security Classification

ACCESSION #	
GPSTI	WHITE SECTION <input checked="" type="checkbox"/>
DDC	DIFF SECTION <input type="checkbox"/>
UNANNOUNCED	<input type="checkbox"/>
JUSTIFICATION	
BY	
DISTRIBUTION/AVAILABILITY CODES	
DIST.	AVAIL. CODE/IF SPECIAL
A	

AIR FORCE WEAPONS LABORATORY
Air Force Systems Command
Kirtland Air Force Base
New Mexico 87117

When US Government drawings, specifications, or other data are used for any purpose other than a definitely related Government procurement operation, the Government thereby incurs no responsibility nor any obligation whatsoever, and the fact that the Government may have formulated, furnished, or in any way supplied the said drawings, specifications, or other data, is not to be regarded by implication or otherwise, as in any manner licensing the holder or any other person or corporation, or conveying any rights or permission to manufacture, use, or sell any patented invention that may in any way be related thereto.

This report is made available for study with the understanding that proprietary interests in and relating thereto will not be impaired. In case of apparent conflict or any other questions between the Government's rights and those of others, notify the Judge Advocate, Air Force Systems Command, Andrews Air Force Base, Washington, DC 20331.

DO NOT RETURN THIS COPY. RETAIN OR DESTROY.

14 KEY WORDS	LINK A		LINK B		LINK C	
	ROLE	PT	ROLE	PT	ROLE	PT
Boundary layer Turbulent Turbulent model						

AFWL-TR-71-57

A TURBULENT MODEL STUDY FOR THE MULTICOMPONENT
NONSIMILAR TURBULENT BOUNDARY LAYER PROGRAM

Larry W. Anderson

Howard L. Morse

Aerotherm Corporation

TECHNICAL REPORT NO. AFWL-TR-71-57

Approved for public release; distribution unlimited.

ABSTRACT

(Distribution Limitation Statement A)

An investigation of the accuracy of the Air Force Weapons Laboratory Nonsimilar Turbulent Boundary Layer Computer Code through comparisons of predictions with experimental data is presented. Five complete data sets are selected from a literature survey which originally considered over one hundred separate turbulent boundary layer experimental investigations. The five data sets include flat plate supersonic flow, hypersonic flow with and without acceleration, supersonic flow with highly nonsimilar wall temperature distributions, subsonic flow with various wall blowing rates, and supersonic flow with wall blowing. Before the present study, the turbulent model in the AFWL code was relatively untested for compressible flows, but is left essentially unchanged after detailed comparisons with other popular turbulent models. Detailed predictions for each of the five data sets are carried out, and approximately 75 graphical comparisons are presented which include velocity, total temperature, and Mach number profiles at several axial stations, plus momentum thickness and drag coefficient variations along the flow direction. Overall agreement between the profile predictions and the experimental data is good for flow with and without blowing. Drag coefficient prediction for blown flows is typically below reported values for the data sets selected. However, these results are taken as inconclusive since there is disagreement among the turbulent boundary layer research community as to the validity of these data. Information on the correct use of the computer code for turbulent boundary layer predictions, and on a new entropy layer option, is also presented. The entropy layer model directly couples the inviscid flow entropy gradients caused by shock curvature with the boundary layer edge boundary conditions.

FOREWORD

This report was prepared by the Aerotherm Corporation, Mountain View, California, under Contract F29601-70-C-0055. The research was performed under Program Element 62301F, Project 5791, Task 27.

Inclusive dates of research were May 1970 through March 1971. The report was submitted 1 September 1971 by the Air Force Weapons Laboratory Project Officer, Sergeant Dennis W. Lankford (SYT).

This technical report has been reviewed and is approved.

Dennis W. Lankford
DENNIS W. LANKFORD
Sergeant USAF
Project Officer

Jay R. Roland
JAY R. ROLAND
Major USAF
Chief, Theoretical Branch

Carl B. Hilland
CARL B. HILLAND
Lt Colonel USAF
Chief, Technology Division

CONTENTS

<u>Section</u>	<u>Page</u>
I INTRODUCTION	1
II COLLECTION AND EVALUATION OF TURBULENT BOUNDARY LAYER DATA	3
1. Summary of Experimental Data Considered	3
2. Criteria Used for Data Selection	13
3. Selected Data Sets	14
a. Coles - Supersonic Flow With Zero Pressure Gradient	15
b. NOL - Hypersonic Flow With and Without Pressure Gradient	19
c. TRW - Hypersonic Flow With Step in Wall Temperature	19
d. Stanford - Zero Pressure Gradient Subsonic Flow With and Without Uniform Blowing, and With a Step in Blowing	20
e. Jeromin - Supersonic Flow With and Without Uniform Blowing	21
III TURBULENT MODEL SELECTION	23
1. Description of Leading Turbulent Models	24
a. Aerotherm Model	24
b. Cebeci - Smith Model	30
c. Bushnell - Beckwith Model	36
2. Turbulent Model Comparisons for the Law of the Wall Region	39
a. WALAW Program	39
b. Results for Three Near Wall Models	40
3. The Selected Turbulent Model	63
a. Wall Law	63
b. Wake Law	65
c. Turbulent Prandtl and Schmidt Number	65
IV PREDICTIONS AND COMPARISONS WITH DATA	68
1. Presentation of Comparisons	68
a. Coles Comparisons	68
b. NOL Comparisons	69
c. TRW Comparisons	105
d. Stanford Comparisons	120
e. Jeromin Comparisons	135
2. Rationalization of Results	150
a. Overview of Agreement Between Experiment and Theory	150
b. Changes in the Turbulent Model	152
c. Desirability of Turbulent Model Changes for Blown Flows	155
V CONCLUSIONS AND RECOMMENDATIONS	163
Appendix - General Discussion of Computer Code Setup and Options	167
References	183

ILLUSTRATIONS

<u>Figure</u>		<u>Page</u>
1	Velocity Ratio Profiles - Wieghardt, Subsonic Flow, Zero Pressure Gradient	26
2	Linear-Log Velocity Ratio Profile - Wieghardt, Subsonic Flow, Zero Pressure Gradient	27
3	Momentum Thickness Reynolds Number vs. Streamwise Location - Wieghardt, Subsonic Flow, Zero Pressure Gradient	28
4	Skin Friction Coefficient vs. Streamwise Location - Wieghardt, Subsonic Flow, Zero Pressure Gradient	29
5	Velocity Ratio Profiles - Kendall, Subsonic Flow, $F = 0.00325$	31
6	Linear-Log Velocity Ratio Profile - Kendall, Subsonic Flow, $F = 0.00325$	32
7	Momentum Thickness Reynolds Number vs. Streamwise Location - Kendall, Subsonic Flow, $F = 0.00325$	33
8	Skin Friction Coefficient vs. Streamwise Location - Kendall, Subsonic Flow, $F = 0.00325$	34
9	Variation of Damping Constant for Bushnell-Beckwith Wall Model	37
10	Variation of Mixing Length for Bushnell-Beckwith Wake Model	38
11	Mixing Length Variation with No Blowing	41
12	Mixing Length Variation with $F = 0.004$	42
13	Mixing Length Variation with $F = 0.010$	43
14	Linear-Log Velocity Ratio Profiles - Wieghardt, Subsonic Flow, Zero Pressure Gradient	44
15	Linear-Log Velocity Ratio Profile - Coles Run #20, Supersonic, Zero Pressure Gradient Flow	45
16	Linear-Log Mach Number Profile - NOL, Lee, et al., Run 12902, Hypersonic, Zero Pressure Gradient Flow	46
17	Linear-Log Static Temperature Profile - NOL, Lee, et al., Run 12902, Hypersonic, Zero Pressure Gradient Flow	47
18	Linear-Log Mach Number Profile - NOL, Lee et al., Run 2611, Hypersonic, Zero Pressure Gradient Flow	48
19	Linear-Log Static Temperature Profile - NOL, Lee, et al., Run 2611, Hypersonic Zero Pressure Gradient Flow	49
20	Linear-Log Velocity Ratio Profile - MIT, Kendall, Run C - 2×10^{-3} - 50, Low Speed Flow with Blowing	51
21	Linear-Log Velocity Ratio Profile - MIT, Kendall Run C - 3×10^{-3} - 50, Low Speed Flow with Blowing	52
22	Linear-Log Velocity Ratio Profile - MIT, Kendall Run C - 5×10^{-3} - 50, Low Speed Flow with Blowing	53
23	Linear-Log Velocity Ratio Profile - Stanford, Simpson Run 2367-3. Low Speed Flow without Blowing	55

ILLUSTRATIONS (continued)

<u>Figure</u>		<u>Page</u>
24	Linear-Log Velocity Ratio Profile - Stanford, Simpson Run 122366-2, Low Speed Flow with Blowing	56
25	Linear-Log Velocity Ratio Profile - Stanford, Simpson Run 122066-3, Low Speed Flow with Blowing	57
26	Linear-Log Velocity Ratio Profile - Stanford, Simpson Run 121966-4, Low Speed Flow with Blowing	58
27	Linear-Log Velocity Ratio Profile - Jeromin Run 2.5-0.0-1.40, Supersonic Flow without Blowing	59
28	Linear-Log Velocity Ratio Profile - Jeromin Run 2.5-1.2-1.40, Supersonic Flow with Blowing	60
29	Linear-Log Velocity Ratio Profile - Jeromin Run 3.5-0.0-1.40, Supersonic Flow without Blowing	61
30	Linear-Log Velocity Ratio Profile - Jeromin Run 3.5-2.1-1.40, Supersonic Flow with Blowing	62
31	Effect of Constant in Wake Region - Eddy Viscosity Expression	66
32	Effect of Turbulent Prandtl Number on Recovery Factor at $M = 3.7$	67
33	Mach Number Ratio Profile - Coles Run #27, Supersonic, Zero Pressure Gradient Flow	70
34	Velocity Ratio Profile - Coles Run #27, Supersonic, Zero Pressure Gradient Flow	71
35	Linear-Log Velocity Ratio Profile - Coles Run #27, Supersonic, Zero Pressure Gradient Flow	72
36	Mach Number Ratio Profile - Coles Run #20, Supersonic, Zero Pressure Gradient Flow	73
37	Velocity Ratio Profile - Coles Run #20, Supersonic, Zero Pressure Gradient Flow	74
38	Linear-Log Velocity Ratio Profile - Coles Run #20, Supersonic, Zero Pressure Gradient Flow	75
39	Momentum Thickness Reynolds Number vs Streamwise Location - Coles' Runs at Mach 2.6 and 3.7	76
40	Skin Friction Coefficient vs Streamwise Location - Coles' Run at Mach 2.6 and 3.7	77
41	Mach Number Ratio Profiles - NOL, Lee, et al., 5 Atm, Hypersonic, Zero Pressure Gradient Flow	79
42	Total Temperature Ratio Profiles - NOL, Lee, et al., 5 Atm, Hypersonic, Zero Pressure Gradient Flow	80
43	Velocity Ratio Profiles - NOL, Lee, et al., 5 Atm, Hypersonic, Zero Pressure Gradient Flow	81
44	Linear-Log Velocity Ratio Profiles - NOL, Lee, et al., 5 Atm, Hypersonic, Zero Pressure Gradient Flow	82

ILLUSTRATIONS (continued)

<u>Figure</u>		<u>Page</u>
45	Momentum Thickness Reynolds Number vs Streamwise Location - MQL, Lee, et al., 5 Atm, Hypersonic, Zero Pressure Gradient Flow	83
46	Skin Friction Coefficient vs Streamwise Location - MQL, Lee, et al., 5 Atm, Hypersonic, Zero Pressure Gradient Flow	84
47	Mach Number Ratio Profiles - MQL, Lee, et al., 10 Atm, Hypersonic, Zero Pressure Gradient Flow	85
48	Total Temperature Ratio Profiles - MQL, Lee, et al., 10 Atm, Hypersonic, Zero Pressure Gradient Flow	86
49	Velocity Ratio Profiles - MQL, Lee, et al., 10 Atm, Hypersonic, Zero Pressure Gradient Flow	87
50	Linear-log Velocity Ratio Profiles - MQL, Lee, et al., 10 Atm, Hypersonic, Zero Pressure Gradient Flow	88
51	Momentum Thickness Reynolds Number vs Streamwise Location - MQL, Lee, et al., 10 Atm, Hypersonic, Zero Pressure Gradient Flow	89
52	Skin Friction Coefficient vs Streamwise Location - MQL, Lee, et al., 10 Atm, Hypersonic, Zero Pressure Gradient Flow	90
53	Mach Number Ratio Profiles - MQL, Bratt, et al., 5 Atm, Hypersonic, Negative Pressure Gradient Flow	94
54	Total Temperature Ratio Profiles - MQL, Bratt, et al., 5 Atm, Hypersonic, Negative Pressure Gradient Flow	95
55	Velocity Ratio Profiles - MQL, Bratt, et al., 5 Atm, Hypersonic, Negative Pressure Gradient Flow	97
56	Linear-log Velocity Ratio Profiles - MQL, Bratt, et al., 5 Atm, Hypersonic, Negative Pressure Gradient Flow	97
57	Momentum Thickness Reynolds Number vs Streamwise Location - MQL, Bratt, et al., 5 Atm, Hypersonic, Negative Pressure Gradient Flow	98
58	Skin Friction Coefficient vs Streamwise Location - MQL, Bratt, et al., 5 Atm, Hypersonic, Negative Pressure Gradient Flow	99
59	Mach Number Ratio Profiles - MQL, Bratt, et al., 10 Atm, Hypersonic, Negative Pressure Gradient Flow	100
60	Total Temperature Ratio Profiles - MQL, Bratt, et al., 10 Atm, Hypersonic, Negative Pressure Gradient Flow	101
61	Velocity Ratio Profiles - MQL, Bratt, et al., 10 Atm, Hypersonic, Negative Pressure Gradient Flow	102
62	Linear-log Velocity Ratio Profiles - MQL, Bratt, et al., 10 Atm, Hypersonic, Negative Pressure Gradient Flow	103
63	Momentum Thickness Reynolds Number vs Streamwise Location - MQL, Bratt, et al., 10 Atm, Hypersonic, Negative Pressure Gradient Flow	104
64	Skin Friction Coefficient vs Streamwise Location - MQL, Bratt, et al., 10 Atm, Hypersonic, Negative Pressure Gradient Flow	105

ILLUSTRATIONS (continued)

<u>Figure</u>	<u>Page</u>
65 Wall Temperature vs X, Distance from Leading Edge of Cylinder TRW Step-Up in Wall Temperature	108
66 Mach Number Ratio Profiles - TRW, Step-Up in Wall Temperature, Supersonic	109
67 Total Temperature Ratio Profiles - TRW, Step-Up in Wall Temperature, Supersonic	110
68 Velocity Ratio Profiles - TRW, Step-Up in Wall Temperature, Supersonic	111
69 Linear-Log Velocity Ratio Profiles - TRW, Step-Up in Wall Temperature, Supersonic	112
70 Skin Friction Coefficient vs Streamwise Location - TRW, Step-Up in Wall Temperature, Supersonic	113
71 Wall Temperature vs X, Distance from Leading Edge of Cylinder, TRW, Step-Down in Wall Temperature	114
72 Mach Number Ratio Profiles - TRW, Step-Down in Wall Temperature, Supersonic	115
73 Total Temperature Ratio Profiles - TRW, Step-Down in Wall Temperature, Supersonic	116
74 Velocity Ratio Profiles - TRW, Step-Down in Wall Temperature, Supersonic	117
75 Linear-Log Velocity Ratio Profiles - TRW, Step-Down in Wall Temperature, Supersonic	118
76 Skin Friction Coefficient vs Streamwise Location - TRW, Step-Down in Wall Temperature, Supersonic	119
77 Velocity Ratio Profiles - Stanford, Simpson Run #2367, Subsonic, No Blowing	121
78 Linear-Log Velocity Ratio Profiles - Stanford, Simpson Run #2367, Subsonic, No Blowing	122
79 Velocity Ratio Profiles - Stanford, Simpson Run #122366, Subsonic, F = 0.002	123
80 Linear-Log Velocity Ratio Profiles - Stanford, Simpson Run #122366, Subsonic, F = 0.002	124
81 Velocity Ratio Profiles - Stanford, Simpson Run #122066, Subsonic, F = 0.004	125
82 Linear-Log Velocity Ratio Profiles - Stanford, Simpson Run #122066, Subsonic, F = 0.004	126
83 Velocity Ratio Profiles - Stanford, Simpson Run #121966, Subsonic, F = 0.008	127
84 Linear-Log Velocity Ratio Profiles - Stanford, Simpson Run #121966, Subsonic, F = 0.008	128

ILLUSTRATIONS (continued)

<u>Figure</u>		<u>Page</u>
85	Velocity Ratio Profiles - Stanford, Simpson Run #5867, Subsonic, Step-Up in Blowing	129
86	Linear-Log Velocity Ratio Profiles - Stanford, Simpson Run #5867, Step-Up in Blowing	130
87	Momentum Thickness Reynolds Number vs Streamwise Location - Stanford, Uniform Blowing Runs, Subsonic	131
88	Momentum Thickness Reynolds Number vs Streamwise Location - Stanford, Simpson Run #5867, Subsonic, Step-Up in Blowing	132
89	Skin Friction Coefficient vs Streamwise Location - Stanford, Uniform Blowing Runs, Subsonic	133
90	Skin Friction Coefficient vs Streamwise Location - Stanford, Simpson Run #5867, Subsonic, Step-Up in Blowing	134
91	Velocity Ratio Profiles - Jeromin Run 2.5-0.0, Supersonic, No Blowing	137
92	Linear-Log Velocity Ratio Profiles - Jeromin Run 2.5-0.0, Supersonic, No Blowing	138
93	Velocity Ratio Profiles - Jeromin Run 2.5-1.2, Supersonic, $F = 0.0012$	139
94	Linear-Log Velocity Ratio Profiles - Jeromin Run 2.5-1.2, Supersonic, $F = 0.0012$	140
95	Momentum Thickness Reynolds Number vs Streamwise Location - Jeromin Mach 2.5 Runs	141
96	Skin Friction Coefficient vs Streamwise Location - Jeromin Mach 2.5 Runs	142
97	Velocity Ratio Profiles - Jeromin Run 3.6-0.0, Supersonic, No Blowing	143
98	Linear-Log Velocity Ratio Profiles - Jeromin Run 3.6-0.0, Supersonic, No Blowing	144
99	Velocity Ratio Profiles - Jeromin Run 3.6-2.1, Supersonic, $F = 0.0021$	145
100	Linear-Log Velocity Ratio Profiles - Jeromin Run 3.6-2.1, Supersonic, $F = 0.0021$	146
101	Momentum Thickness Reynolds Number vs Streamwise Location - Jeromin Mach 3.6 Runs	147
102	Skin Friction Coefficients vs Streamwise Location - Jeromin Mach 3.6 Runs	148
103	Static Temperature Profiles, Jeromin, $M = 3.6$, $F = 0.000$	151
104	Diagram Showing Law of the Wall Nomenclature	153
105	Comparison of Predicted Skin Friction Coefficient for Zero Blowing Stanford Case to Data and Empirical Values	154

ILLUSTRATIONS (concluded)

<u>Figure</u>		<u>Page</u>
106	Effect of Wall Law Changes on Drag Coefficient in Unblown Flat Plate Flow	156
107	Effect of Wall Law Changes on Velocity Profile in Unblown Flat Plate Flow	157
108	Effect of Wall Law Changes on Velocity Profile in Flat Plate Flow With Blowing	158
109	Effect of Wall Law Changes on Drag Coefficient in Flat Plate Flow With Blowing	159
110	Comparison of Various Theories With Simpson Data, Taken From Reference 89	160
111	Comparison of Blowing Correction From Several Investigators, Taken From Reference 87	162
112	$\eta - \xi$ Coordinate System	168
113	Comparison of BLIMP Velocity Profile Predictions for Different Numbers of Nodes	170
114	Typical Velocity and Velocity Gradient Profiles in a Turbulent Boundary Layer	171
115	Overshoot of the Spline Fit Procedure	172
116	Definition of Near Wall Velocity Profile for Data Start Input	176
117	Response of Velocity Profile Following a Data Start; Example, Jeromin 2.5-1.2	177
118	α_H Constraint With Entropy Layer Flow	182

TABLES

<u>Table</u>		<u>Page</u>
I	Experimental Data With No Blowing	4
II	Experimental Data With Blowing	7
III	Types of Unblown Flow Data	10
IV	Types of Blown Flow Data	11
V	Test Conditions (Nominal) for BLIMP Comparison Data Sets	16
VI	Description of Instrumentation	17
VII	Determination of Key Parameters and Methods of Data Reduction	18
VIII	Magnitudes of Momentum Integral Equation Terms	22
IX	$C_f/2$ Comparisons for Stanford Runs	135
X	Variations in Momentum Integral Terms for Jeromin Comparisons	149
XI	Typical \bar{n} Distributions in the Outer Wake Region	173

SYMBOLS

A	parameter used in Cebeci mixing length formulation, defined by Equation (14); also, a similar parameter is used for the Bushnell and Beckwith formulation, defined by equation (25)
A [*]	parameter used in Bushnell and Beckwith mixing length formulation, found from graph in figure 9.
C _f	drag coefficient; $\tau_w \sqrt{2} / \rho_1 u_1^2$
C _{f_i}	drag coefficient in an incompressible flow
C _p	frozen specific heat of the gas mixture
F	dimensionless wall mass flux per unit area, $(\rho v)_w / (\rho_1 u_1)_e$
h	static enthalpy of the gas
h [*]	reference enthalpy, defined by equation (33)
M _i [*]	incompressible form factor, S_1^*/S_1
H _T	total enthalpy
k _m	momentum mixing length constant, 0.40-0.44
k _h	energy mixing length constant, 0.44
X _i	mass fraction of molecular species i
x	mixing length, defined by equation (4)
M	Mach number
N	number of nodal points across the boundary layer selected for the purpose of the numerical solution procedure; also parameter used in Cebeci mixing length formulation, defined by equation (15)
P	pressure
P ⁺	parameter used in Cebeci mixing length formulation, defined by equation (16)
Pr	frozen Prandtl number of the gas mixture
Pr _t	turbulent Prandtl number, defined by equation (11)
Pr _T	turbulent Prandtl number based on total enthalpy, defined by equation (27)
q	diffusion heat flux per unit area
r	recovery factor
r _c	local radius of body in a meridian plane for an axisymmetric shape

SYMBOLS
(continued)

Re	Reynolds number; subscripted with the length scale if other than s
Sc_t	turbulent Schmidt number, defined by equation (12)
T	temperature
u	velocity component parallel to body surface
v	velocity component normal to body surface
x	distance along the body surface
y	distance from surface into the boundary layer, measured normal to the surface
γ_a^*	constant in the mixing length differential equation (see equation 5)
γ	boundary layer outer edge intermittency, defined by equation (19)
δ	boundary layer thickness
δ^*	displacement thickness
δ_{i1}^*	incompressible or velocity displacement thickness, defined by equation (8)
ϵ_G	average turbulent eddy diffusivity for all species
ϵ_{G_i}	turbulent eddy diffusivity for species i , defined by equation (10)
ϵ_H	turbulent eddy conductivity, defined by equation (9)
ϵ_v	turbulent eddy viscosity, defined by equation (3)
η	transformed coordinate in a direction normal to the surface, defined by equation (41)
δ	momentum thickness
δ_{i1}	incompressible momentum thickness, defined by equation (26)
μ	shear viscosity
ν	kinematic viscosity
ξ	transformed streamwise coordinate, defined by equation (40)
ρ	density
$\rho_w v_w$	total mass flux per unit area into the boundary layer
τ	local shear stress

SYMBOLS
(concluded)

Subscripts

aw	pertains to adiabatic wall
e	pertains to boundary-layer edge
i	pertains to the i^{th} species or to the i^{th} nodal point in the boundary layer, starting with $i = 1$ at the surface
n	pertains to the n^{th} nodal point, corresponding to the outer edge of the boundary layer solution
r	pertains to recovery or adiabatic wall conditions
w	pertains to wall
0	pertains to stagnation condition
l	reference condition, usually taken as zero streamline from inviscid solution (synonymous with boundary-layer edge in the absence of an entropy layer)
∞	pertains to freestream

Superscripts

κ	equal to unity for axisymmetric bodies and zero for two-dimensional bodies
$()^*$	evaluated at the reference enthalpy condition
$()'$	signifies a turbulent fluctuation
$(\bar{ })$	signifies a time-averaged value

SECTION I
INTRODUCTION

The Air Force Weapons Laboratory recently sponsored the development of a boundary layer computer code (reference 1) for use in predicting multi-component, chemically-reacting, laminar or turbulent flows over ablating, reentry vehicle surfaces. This code has been designated BLIMP for Boundary Layer Integral Matrix Procedure. The turbulent model used in this code was recognized to be relatively untested for the high Mach number boundary layers of interest to the Air Force, although it had been shown to be satisfactory for low speed unblown and blown turbulent boundary layers (reference 2). This report presents the results of a study to validate and to improve that turbulent model for compressible and nonsimilar flow cases.

In this study, the available turbulent boundary layer literature was searched in detail for experimental data of sufficient accuracy for detailed boundary layer profile and integral parameter comparisons. Interviews with principal investigators were conducted to learn of new data or unreported data reduction techniques which are often missing from the usual final report. Five data sets were selected from approximately one hundred experiments originally considered.

The turbulent model in the BLIMP code was also re-evaluated in view of the numerous papers and reports on turbulence modeling currently becoming available in the literature. Limited changes in the existing BLIMP turbulent model (as described in reference 1) were made before the detailed data comparisons presented herein were finally generated. Extensive use of the BLIMP code on the selected test cases then resulted in approximately 75 graphical comparisons of the code predictions with the experimental data. Questions of code starting procedure, nodal spacing, etc. were also addressed in order to give a complete picture of the use of the BLIMP code and the kind of accuracy that can be expected from it.

This report discusses the turbulent model study in essentially the order in which it was carried out. Section II describes the literature survey phase including the criteria used for selecting the final five data sets. Section III describes the turbulent model used in BLIMP, and presents some limited comparisons with other turbulent models. Section IV presents the comparisons

AFWL-TR-71-57

between BLIMP predictions and the experimental data. Section V contains some conclusions and recommendations for further work. A general discussion on the use of the code for turbulent flow problems is included in an appendix.

SECTION II

COLLECTION AND EVALUATION OF TURBULENT BOUNDARY LAYER DATA

The number of experimental studies of turbulent boundary layer flows which have been conducted since the turn of the century is possibly in the tens of thousands. Of these numerous studies, possibly 1 to 10 percent were carried out with sufficient accuracy and detail to yield data of "acceptable" quality. Of these high quality experiments, perhaps 10 percent include the type of flow configurations and the necessary instrumentation to provide data of interest in a turbulent model study. This leaves possibly a few hundred papers and reports which should be reviewed for a study of the type being reported here. This survey was limited (by the constraints of both time and practicality) to reports or papers generally found or referenced in the recent open literature. Thus, approximately one hundred documents were surveyed briefly for pertinent data. Descriptions of test configurations, test conditions, instrumentation, and the type and quality of data taken for the most relevant experiments is presented later in this report.

In the remainder of this section of the report, the experiments referred to above are summarized and discussed in Section II.1. Criteria for selecting the best data sets are presented in Section II.2, and the final selected data sets are discussed in some detail in Section II.3.

1. SUMMARY OF EXPERIMENTAL DATA CONSIDERED

There are several ways in which the various experiments can be described; however, it is felt that a presentation in tabular form is the most efficient and will be most useful for future reference. Thus, two tables are presented here to summarize the experimental data which were considered. Table I includes flows without blowing, while Table II includes flows with blowing. Within each table, the experiments are placed in alphabetical order, according to the principal author's name in order to facilitate cross-referencing with Tables III or IV or the text of this report. A shorthand notation has been introduced for some columns (SFB for skin friction balance, etc.) and a "Remarks" column has been included to give additional details about the experiment. Often the remarks refer to the suitability of the data for turbulent model studies, since it is difficult to glean this information from the other tabular data.

TABLE 2
EXPERIMENTAL DATA WITH NO MACHINES

Author	Configuration	N	Re, 10^{-3}	P_0 atm	P_0 %	δ^*/δ	δ^*/δ	Profile instrumentation	Wall instrumentation	Remarks
Adcock, et al., ¹ 1945	20" Laminar layer- discharge hollow cylinder aligned with flow	6.0	10^7	25.7	875	no	no	Static probe, total temp probe, Schlieren photos	P_0 taps on inside wall of cylinder	Data near wall not consistent with wall shear TM in preparation
Allen, ⁶ 1970	Match-stem body of revolution in wind tunnel	2.5 2.04 2.02 2.06	1×10^6	1.0	630	no	varies along body	P_0 probe at $x = 2.5x$	P_0 taps	Technical note only. Mach TM in preparation
Witch & Moulton, ⁵ 1970	Measurements in throat region of half nozzle	subsonic no	---	1.0	540	no	varies through throat	P_0 probe	P_0 taps	
Scott, et al., 1967	Stem no flow	subsonic no	0.72-0.5 2×10^6	1.0-10.0	742	yes	yes	P_0 probe, P_0 probe static probe, film wire T/C probe	Same as top	A continuation of the low Re, all instrumentation is pressure, velocity lines
Cary, ⁷ 1945	Curved flat plate in laminar flow approximate to test	6.0	1.15×10^7 1.2×10^6 1.2×10^6	---	940	yes	no	None	T/C on backside of plate to measure heat transfer	Mach TM in preparation
Colin, ⁸ 1953	Flat plate in jet exhaustive tunnel	1.0-2.0 2.7-6.5	0.96-0.65 2×10^6	0.20- 1.35	530	no	no	P_0 probe	Static probe, film wire	Excellent set of experiment results
Escudier, ⁹ 1947	Low speed tunnel with low speed section	0-10	5×10^5	1.0	530	no	no	P_0 probe, P_0 probe	P_0 taps	Excellent low speed data survey included
Picquet et al., ¹⁰ 1970	Laminar 20" nozzle hollow cylinder vary on tunnel wall	20	0.43×10^6 2×10^6	60	540	no	no	P_0 probe, P_0 probe, static hot wire measurements	P_0 taps	Normal pressure gradient in boundary layer
Guder et al., ¹¹ 1967	20" half nozzle cone in jet exhaust shock tunnel (constant and cone nozzle)	10 low cone 10 low cone 5-15 low cone nozzle	3×10^5	100 270	2500 4150	yes	yes with con- tour waste	P_0 probe	P_0 taps, static probe	Data presented in insufficient detail for Mach studies
Hill, ¹² 1959	Tests on hypersonic tunnel wall in jet	0-10	2.5×10^6	27-40	1300- 1500	yes	moderate super- sonic turbulent	P_0 probe, P_0 probe	P_0 taps T/C on wall	Data are quite scattered
Hopkins & Moore, ¹³ 1949	Shock tube flow into a cylinder static probe aligned with flow	2.5-3.5	1.0×10^6	Max 4500	static temp 6000-11500	yes	no	None	Fluctuating static transducer at 2 stations	Character data questionable due to probe protrusion into flow
James & Piller, ¹⁴ 1970	Laminar 20" hypersonic tunnel, tests on nozzle wall	5.0-5.6	0.5-1.13 $\times 10^5$	Max 4500	static temp 6000-11500	small	small	P_0 probe, T/C	P_0 taps on wall temps	Cold tunnel h.t. may affect data
Julien et al., ¹⁵ 1945	Standard low speed jet and mass transfer for apparatus	0.02-0.10	2.5×10^5	1.0	530	small	const. velocity flow	P_0 probe	T/C in wall	Only velocity data in this report
McIntyre et al., ¹⁶ 1970	Standard low speed jet and mass transfer for apparatus	maximum of 0.08	4.7×10^5	1.0	530	yes	accelerating flow	P_0 probe, static probe	P_0 taps T/C in wall	This report concentrates on heat transfer effects
Lee et al., ¹⁷ 1945	Lower wall of half nozzle and transition, 12" static probe cooled	5.0	0.56×10^6	1.0-10.0	500-1210	yes	no	P_0 probe, static probe, equilibrium temp probe	Static probe T/C in laminar region for heat transfer, P_0 taps	Appears to be a good set of experiments. All data in laminar flow
Lewis, ¹⁸	20" nozzle, 6" diameter cylinder aligned with flow. Measurements along inside wall.	6.0	6.1×10^5	5.76	572	yes	no	P_0 probe, static probe, temp dist.	P_0 taps T/C's at surface heat flux calorimetry probe	Temperature profiles in h.t. take a long time to reach equilibrium after flow is started. Use for comparisons.

NOT REPRODUCIBLE

TABLE I (continued)

Author	Configuration	δ	ρ ft ⁻³	P_0	T_0 °K	d^2/dx	$\sqrt{V_0}$	Profile Instrumentation	Wall Instrumentation	Remarks
Wells 35 1947	Flat plate in shock tunnel plus measurements on nozzle wall	4.0-10.7	9-0.1110 ⁵	30.4-1260	1000-3000	yes	small	P_0 rake P_0 rake Electron beam for density probing T_0 probe T_0 probe	P_0 ports Thin film re- distance T_0 °C, T_0 °F SP, P_0 ports This film heat trans. gaps T_0 ports T_0 °C in plate P_0 tape	Data is scattered New instrumentation techniques for density measurements. Data fairly scattered This temperature data to be used in conjunction with Simpson velocity data This is considered to be a classic set of low speed data
Malace 36 1948	Tests on nozzle wall in shock tunnel	0.2-0.3	1.1-2.1x10 ⁵	15-50	2000-5015	yes	small	P_0 rake Electron beam for density probing T_0 probe T_0 probe	SP, P_0 ports Thin film heat trans. gaps T_0 ports T_0 °C in plate P_0 tape	See instrumentation techniques for density measurements. Data fairly scattered This temperature data to be used in conjunction with Simpson velocity data This is considered to be a classic set of low speed data
Whitten 37 1947	Standard low speed heat and mass transfer apparatus	0.04	2.6 x 10 ⁵	- 1.0	- 500	yes	no	P_0 probe T_0 probe T_0 probe	P_0 ports T_0 °C in plate P_0 tape	This temperature data to be used in conjunction with Simpson velocity data This is considered to be a classic set of low speed data
Stephens & Williams 38 1944	Wooden plate in low speed wind tunnel	0.050	6.6 x 10 ⁵	- 1.0	- 530	no	no	P_0 probe rake Mass	P_0 tape Wall T_0 's as thin skin calorimeters	This temperature data to be used in conjunction with Simpson velocity data This is considered to be a classic set of low speed data Cooled model heated up when injected into stream
Wilson 39	NOI hypersonic tunnel, 100 sharp cone model with natural transition	5.0	0.5-31.0 x 10 ⁵	10-80	760-1160	yes	no	Mass P_0 probe T_0 probe	Wall T_0 's as thin skin calorimeters P_0 tape T_0 probe	Unintentional variations in P_0 and T_0 between runs make data reduction difficult
Winkler & Cha 40 1959	NOI 12 x 12 cm hypersonic tunnel, tests in boundary layer	5.2	3.9 x 10 ⁵	6.6-7.5	610-855	yes	no	P_0 probe T_0 probe	P_0 tape T_0 probe	Unintentional variations in P_0 and T_0 between runs make data reduction difficult

Notes:
 δ = jet wire diameter
 ρ = stagnation density
 P_0 = stagnation pressure
 T_0 = stagnation temperature
 P_0 = static pressure
 T_0 = skin friction balance
 T_0 = static temperature
 T_0 = stator entries are T_0/T_0 ratios

NOT REPRODUCIBLE

TABLE II
EXPERIMENTAL DATA WITH BLOWING

Author	Configuration	M	Re ft ⁻¹	P_0 atm	T_0 °K	Injectant	q or wall	$\sqrt{C_f}$	Profile Instrumentation	Wall Instrumentation	Remarks
Lesjli, 41 1968	Low speed 7" x 7" x 36" U of U tunnel with blowing on one wall	0.023	1.54×10^5	-1.0	520	air	yes	1.87 max	P_0 probe Hot film probe, thermistor probe	T/C's, embedded and on surface	Good study of turbulent friction effects. Transficient dis- cussion of plate uniformity
Waber, 42 1967	Low speed jet impinging on a diamond wall	ϵ to 0.3 $\phi = 0$	2.03×10^6	-1.0	520	air	no	---	P_0 probe rate	none	
Waber & Leadow, 43 1963	3/4" x 4" section of turbulent flow in hypersonic tunnel; USC and CD Com- air. Test plate was 5/8" x 16"	2.0 3.2	$6.3-7.5 \times 10^6$	1.38 1.08 1.08	568	H ₂ N ₂ Ar CH ₄ CO ₂ C ₂ F ₆	yes	1.9 3.3	Some use of probes. Hot data not re- ported	T/C's at surface T/C's in depth P ₀ taps Guard heaters	Good study of effects of various injections on wall heat transfer
Wabers, 44 1959	MOL hypersonic tunnel No. 4. Blown plate mounted in tunnel	5.1	4.6×10^6	8.0	684	air	yes	4.2-6 5.0	P_0 probe T/C probe	T/C's in top surface of plate P ₀ taps	Peer injection mass flux dis- tribution
Wabers, 45 1964	Flat plate mounted at exit of 2-D nozzle	6.7	$2.4-5.8 \times 10^6$	15.2-38.0	930	air	yes	4.1 5.7 7.6	P_0 probe Equilibrium tem- perature probe	P ₀ taps T/C's attached in depth	Transition over significant portion of plate
Wahlin, et al., 46 1967	Porous wall in 3.5" x 6" wind tunnel	3.2	$6.9 \times 13.8 \times 10^6$	3.7 & 7.4	560-585	H ₂	no	---	Pilot measurements made but not pre- sented. Also some T ₀ reads.	Porous SPB	Strictly C _f data
Wernitzki & Wokel, 47 1969	Porous wall with side fences in 2" x 24" wind tunnel	2.6	2.6×10^6	-1.0	540	air Ar	no	---	P_0 probe	T/C's on backwall, P ₀ measured on diamonds	Concentrated on strong blowing where $C_f \sim 0.7/d$
Wernitzki, 48 1966	Small 2-D half cap- me; with porous test section in flat wall	2.5 & 3.5	$1.43-1.52 \times 10^7$	5.2 & 8.3	522	air	yes	0.3 0.3	P_0 probe, equilib- rium	T/C's near surface, T/C's in depth with T/C's to get P ₀ , P ₀ taps	Good discussion of plate uniformity, tabular data given by Aquino.
Wernitzki, 49 1970	Same as above, but for porous plate	0.03	2.1×10^5	-1.0	-530 Acc -530 Acc -530 Acc	H ₂ , H ₂	yes	1.10- 1.35	P_0 probe, P ₀ probe, tempera- ture probe	In depth and back- wall face T/C's	Comparison of H ₂ in boundary layer. Looked at negative pressure gradient No discussion on plate uniformity.

TABLE II (continued)

Author	Configuration	M	Re ft ⁻¹	P ₀ atm	T ₀ °C	Injectant	q & wall	γ, γ ₁	Profile Instrumentation	Wall Instrumentation	Remarks
Julien, et al., 15 1969	Stanford low speed heat and mass transfer apparatus. Rectangular cross-section duct - 20" wide, 40" long. Instrumented porous walls.	0.023-0.107	1.4-7.3 x 10 ⁵	-1.0	-530	air	no	---	P ₀ probe	T/C's in plate, P ₀ taps	This report concentrates on velocity data.
Kearney, et al., 16 1970	Stanford low speed heat and mass transfer apparatus.	0.021-0.084	1.4-4.3 x 10 ⁵	-1.0	-530	air	yes	0.95-1.09	P ₀ probe, T/C probe	T/C's in plate, P ₀ taps	This report concentrates on heat transfer effects.
Leont, et al., 30 1969	AEDC tunnel B, 50" dia. test section, porous wall flow nozzle, air-noise blower, etc.	0.0	0.55-3.6 x 10 ⁵	not given	1360	H ₂ , CO ₂	yes	---	Adjacent P ₀ , T/C probes	P ₀ taps, T/C's in wall	Primary purpose of these measurements was to obtain surface pressure data. Profile measurements are of poor quality.
Kuligin, 51 1972	Porous tube with rounded square tunnel in low speed flow in 15 ft.	0.008	5.5 x 10 ⁴	-1.0	-530	CH ₄	yes	2.4-2.8	P ₀ probe, T/C probe, concentration probe	T/C on wall, used P ₀ probe as Preston tube	Data in graphical form only. Reynolds number looks very low for completely turbulent flow.
Marcillucci, 52 1970	Sharp cone porous model in AEDC Tunnel B, 18" base x 48" long model	0.0	0.30-3.8 x 10 ⁶	44.2 51.4	1350	H ₂	yes	1.94-2.14 varied along body	P ₀ probe, T/C probe	P ₀ taps, T/C's (one in each porous wall section)	Similar to Kent, et al. but much better documentation. Still trouble with variations in blowing rate.
McQuaid, 53 1967	Low speed tunnel with 20" x 40" porous wall partition for transpiration system	0.045 0.136	1.0-9.2 x 10 ⁵	-1.0	530	air	no	---	P ₀ probe	P ₀ taps	One experiment with discontinuous injection, but poor data.
Moffatt & Kaya, 25 1967	Stanford low speed heat and mass transfer apparatus	0.04	2.6 x 10 ⁵	-1.0	-530	air	small	0.97-1.05	P ₀ probe	T/C's in plate, P ₀ taps	Excellent experimental facility.
Murray, 54 1967	Porous wall in 7" x 7" low speed tunnel	0.032 0.059	2.16 x 4.0 x 10 ⁵	-1.0	-530	H ₂	no	---	Pitot tube	None	Continuation of Moolstrap and Murray work.
Pappas & Okuno, 55 1960	Arms 2' x 2' transonic tunnel x 10" heat transfer for tunnel. Cone model of molded fiber mat.	0.3-0.7, 3.5-4.7 (free-stream)	1.03-6.75 x 10 ⁶	not given	not given	air He CCl ₄ , F ₂	no	---	None	P ₀ taps	Measured total drag only with velocity distribution. Poor injectant distribution.

NOT REPRODUCIBLE

TABLE II (continued)

Author	Configuration	M	Re (ft^{-1})	P_0 atm	T_0	Injectant	ξ (wall)	$\sqrt{r_0}$	Profile Instrumentation	Wall Instrumentation	Remarks
Page & Chao, ⁵⁴ 1961	Pyrex surface sharp nose	0.73-0.7, (see notes)	$3.0-4.0 \times 10^5$ (on cone)	not given	522, 750	air CO_2, F_2	---	not given	None	Surface T/C's	Pair amount of scatter from P_0 exp. Data in graph- of form only
Peterson, et al., ⁵⁷ 1966	20° Mach 5 tangley tem- pel. Sharp leading edge flat plate model with blowing slots. Plate was 34" long x 13" wide	3.0	10^7	0.42	570	air	no	---	P_0 probe	Surface T/C's $Pr_0 = 20^\circ$ P_0 taps	Looked at effects of slope in blowing, multiple slots, etc. Data in graphical form
Shanabha & S Shanabha, ⁵⁸ 1963	Low speed tunnel with poured wall section	0.075- 0.22	up to 3.5×10^5	-1.0	810-960	air, H_2 CO_2, CO, F_2	yes	1.0- 0.66	P_0 probe	T/C's on surface and backside	Journal article does not give profile data. Original report is Russian
Stinson, et al., ³³ 1967	Standard low speed heat and mass transfer appa- ratus	0.06	2.6×10^5	-1.0	-530	air	small	0.95- 1.09	P_0 probe	P_0 taps T/C's in plate	Took data with Moffat. Excellent experiments.
Smith, ⁵⁹ 1965	7" x 7" x 9" of quartz low speed tunnel	0.023	1.55×10^5	-1.0	-530	H_2, F_2 air	small	1.07	P_0 , T/C, mass- transfer probes, hot film probe	T/C's on surface and imbedded	This thesis concentrates on hot film development
Spire, ⁵⁹ 1966	Flow in jets, Mell- strand for tunnel. Str- down capability	1.0 2.5	0.9×10^7	1.02 3.04	555	air	small	1.02*	Pitot tube	Same as jetpots	This report also presents Jeremi's $M = 2.5$ data, and accurate study to other such numbers.
Thakkar, et al., ³⁴ 1965	Standard low speed heat and mass transfer appa- ratus	0.02- 0.112 (see notes)	$1.55-7.60 \times 10^5$	-1.0	-530	air	yes	0.97- 1.08	P_0 probe T/C probe	P_0 taps T/C's in plate	Accelerating flow, blowing and suction
Whitson, et al., ³⁷ 1967	Standard low speed heat and mass transfer appa- ratus	0.04	$1.3 \text{ to } 2.6 \times 10^5$	-1.0	-530	air	yes	0.97- 1.13	P_0 probe T/C probe	P_0 taps T/C's in plate	Uniform velocity, with slope in wall temp and blowing rates
Winstler, et al., ⁶¹ 1970	Approximately air heated tunnel. 7.25" porous cone with hole in cone, compartmented injection	12, 17	$1.0-4.0 \times 10^5$	not given	not given	Cl_2 through on air/acetylene (simultaneously)	yes?	not given	None	T/C's & calorim- eter in wall	Film injection at nose complicates results.
Winstler, et al., ⁶² 1969	Acetone in jet-tunnel duct configuration. Ablating deflam wall in tunnel.	2.3	not given	21. & 20.	4200- 4600	oxygen (oxidation)	yes	---	P_0 probe at duct exit	P_0 ports, surface T/C's in depth T/C's (near data), and Pr_0	Most of data from turbulent tests published in another report, AFWL TR 69-12
Woolridge & Murz, ⁶³ 1966	7" x 7" duct with porous wall	0.032	2.0×10^5	-1.0	-530	H_2 & F_2	yes (combination)	1.5- 2.0	Hot (some experi- mental), combination of hot film and Langmuir probe, P_0 probe	P_0 taps, T/C near airflow	Measurements at one station only

Notes:
 Starred (*) quantities are $\sqrt{r_0}$ ratios
 Re = hot wire Reynolds number
 P_0 = stagnation pressure
 T_0 = stagnation temperature
 Pr_0 = Prandtl number
 Pr_0 = static pressure
 Pr_0 = static pressure
 T/C = thermocouple

NOT REPRODUCIBLE

While the information provided in Tables I and II is useful for detailed review, it does not provide an overall impression of the availability of certain types of experimental data without a detailed review by the reader. Therefore, Tables III and IV were prepared. Table III applies to unblown flows while Table IV applies to blown flows. Referring to Table III, Unblown Flows, it is seen that very few subsonic cases are listed. This is entirely attributable to the fact that subsonic unblown data were not sought in the literature search. Matting, et al. (reference 22) plus several reports of the Stanford series present data on subsonic unblown layers; therefore this category was included for completeness. The other entry is from the 1968 AFOSR-Stanford-IFP Turbulent Boundary Layer Conference Proceeding (reference 64), and is regarded as top quality data useful for reference purposes.

There is a noticeable difference between the number of reports on supersonic flat plate flows ($1 < M < 4$); and hypersonic flows ($M > 4$); hypersonic flows seem to have received more attention from the experimentalist. This is attributable to the need over the last decade for data suitable for reentry calculations and comparisons. Thus, major test facilities around the country have been constructed and used primarily in the hypersonic flight range.

Data on accelerating boundary layers were also gathered during the literature survey phase. Pressure gradient investigations are often more unavoidable than intentional in many test facilities, thereby yielding rather uncertain flow data. However, there have been some research programs in which pressure gradient was varied systematically.

Turbulent boundary layers with a nonreactive transparent have been investigated for many years as a possible technique for heat transfer alleviation in turbine blades and reentry vehicle nose tips, among other applications. Air has been the most popular injectant for experiments, although possibly not the most practical in many actual cooling systems. The literature review for subsonic blown flows was intended to supplement that given in reference 2. Thus the Massachusetts Institute of Technology (MIT) work (i.e., references 65 and 66) was not included for re-evaluation. There is no shortage of new low speed data available. The Stanford investigations have resulted in at least 13 separate reports on blown turbulent boundary layers, with heat transfer and pressure gradient effects documented as well. Strangely enough, the great interest in low speed blowing investigations has not carried over to the supersonic and hypersonic flow regions. Particularly at Mach numbers greater than four, there is a real need for further basic flow data suitable for turbulent model investigation and development. The picture is equally

TABLE III
TYPES OF UNBLOWN FLOW DATA

Zero Pressure Gradient		Accelerating Flows			
Subsonic	Supersonic $1 < M < 4$	Hypersonic $M > 4$	Subsonic	Supersonic $1 < M < 4$	Hypersonic $M > 4$
Matting, et al ²²	Coles ⁸	Adcock et al ³	Brinich & Neumann ⁵	Allen ⁴	Allen ⁴
Moffat & Kays ²⁵	Hopkins & Nerem ¹³	Cary ⁷	Escudier ⁹	Michél et al ²⁴	Brott, et al ⁶
Simpson, et al ³³	Lewis ¹⁶	Coles ⁸	Julien, et al ¹⁵		Graber et al ¹¹
Wieghardt & Tillman ³⁸	Matting, et al ²²	Fischer, et al ¹⁰	Kearney, et al ¹⁶		Hill ¹²
	Meier & Rotta ²³	Graber, et al ¹⁴	Lloyd, et al ¹⁹		Matthews & Trimmer ²¹
	Moore & Arkness ²⁶	Jones & Teller ¹⁴	Noonan & Rand ²⁹		Nagamatsu, et al ²⁷
	Noonan & Rand ²⁹	Lee, et al ¹⁷	Thielbahr, et al ³⁴		Perry & East ³⁰
		Lobb, et al ²⁰			Scaggs ³²
		Matting, et al ²²			
		Meier & Rotta ²³			
		Neal ²⁸			
		Samuels, et al ³¹			
		Wallace ^{35,36}			
		Wilson ³⁹			
		Winkler & Cha ⁴⁰			

TABLE IV
TYPES OF BLOWN FLOW DATA

Nonreactive Blowing						Reactive Blowing		
Air or N ₂ Injection			Foreign Gas Injection			Subsonic	Supersonic	Hypersonic
Subsonic	Supersonic 1 < M < 4	Hypersonic M > 4	Subsonic	Supersonic 1 < M < 4	Hypersonic M > 4			
Aisaji ⁴¹	Bartle & Leadon ⁴³	Danberg ^{46,45}	Pappas & Okuno ^{55,56}	Bartle & Leadon ⁴³	Kent, et al ⁵⁰	Jones ⁴⁹	Winkler et al ⁶²	Wimberley et al ⁶¹
Baker ⁴²	Davshin et al ⁴⁶	Kent et al ⁵⁰	Romanenko & Kharchenko ⁵⁸	Fernandez & Zukoski ⁴⁷	Pappas & Okuno ^{55,56}	Kulgein ⁵¹		
Jones ⁴⁹	Fernandez & Zukoski ⁴⁷	Martellucci ⁵²		Pappas & Okuno ^{55,56}		Romanenko & Kharchenko ⁵⁸		
McQuaid ⁵³	Jeromin ⁴⁸	Pappas & Okuno ^{55,56}				Smith ⁵⁹		
Muzzy ⁵⁴	Pappas & Okuno ^{55,56}					Wooldridge & Muzzy ⁶³		
Pappas & Okuno ^{55,56}	Peterson et al ⁵⁷							
Romanenko & Kharchenko ⁵⁸								
Simpson et al ⁵⁷								
Smith ⁵⁹								
Whitten et al ³⁷								
Wooldridge & Muzzy ⁶³								

incomplete in the nonreactive foreign gas injection category, with Bartle and Leadon's study (reference 43), where no profile information was taken, being perhaps the most exhaustive.

Finally, the category of most interest for heat shield ablation or transpiration applications is the reactive blowing data. Work is just getting underway in low speed flows with the University of Utah duplication (references 41, 49, and 59) of the original Wooldrige and Muzzy experiments (reference 63). There is little basic data of interest in supersonic or hypersonic flows.

2. CRITERIA USED FOR DATA SELECTION

The criteria used for judging the usefulness of experimental data must of course depend on what use is to be made of the data. For turbulent model studies, it is of interest to model the details of the flow through the entire boundary layer, therefore profiles of the important boundary layer variables become of primary importance. In the usual experiment, state-of-the-art instrumentation is used to measure stagnation pressure and stagnation temperature behind a normal shock (created by the probe itself) for supersonic flows, although for adiabatic wall conditions local total temperature can be assumed equal to the reservoir temperature with only a small error. These pressure and temperature data are used to arrive at other more fundamental variables such as velocity and temperature or enthalpy. Thus, data selected for these turbulent model studies must at least include measured profiles of one or more of the important boundary layer variables.

Other criteria on which to judge the data are more subtle and can only be described in a fairly general way. Herein is presented a list of items that have been considered in viewing a set of experimental data.

- The wind tunnel should provide a shock-free, low freestream turbulence isentropic flow.
- The boundary layer flow upstream of the test section should be well characterized if it eventually forms the boundary layer for testing (as in wind tunnel wall boundary layer testing).
- The test section or model should be of known flatness and hydraulically smooth.
- Leading or trailing edge effects should be examined to determine their influence.
- The two-dimensionality of the model - wind tunnel - test section combination should be considered.

- The flow should be fully turbulent at the test section, free of any transitional or boundary layer trip effects.
- Where transpiration effects are investigated, the injection must be uniform or known to within a few percent.
- The displacement effects of the boundary layer flow on the inviscid flow must be completely known - particularly with injection.
- Probe sizes must be small compared to boundary layer sizes.
- Disturbance of the flow at the wall by wall instrumentation must be held to a minimum.
- The data should appear relatively smooth and consistent with a minimum of scatter.
- Where possible, the integral conservation equations should be checked and satisfied experimentally to a reasonable percent error.

The points mentioned above are essentially the desired features of an acceptable boundary layer experiment. No attempt was made, however, to develop a rating system for the various data sets. Rather, an overall impression gathered from reading about each experiment was formed, notes were made regarding each data set where necessary, and in many cases, telephone or personal interviews were held with principal investigators. Important features of each data set have been noted in the "Remarks" column of Tables I and II.

3. SELECTED DATA SETS

A minimum of five data sets was desired for turbulent model comparisons. The approach used in selecting these data sets was an attempt to provide data which test the turbulent model in a variety of flow situations which are encountered in flight. This obviously means that comparison could not be carried out for each category of Tables III and IV since there are more than five categories containing good data. The five data sets selected were:

1. Coles' JPL experiments (reference 8 - Supersonic flow with zero pressure gradient.
2. NOL experiments by Lee, et al. (reference 17) and Brott, et al. (reference 6) - Hypersonic flow with and without pressure gradient.

3. TRW experiments run at AEDC (reference 18) - Hypersonic flow with highly nonsimilar wall conditions.
4. Stanford experiments by Simpson, et al. (reference 33) - Low speed flow with nonreactive blowing, including steps in blowing.
5. Cambridge experiments by Jeromin (reference 48) - Supersonic flow with nonreactive blowing.

Details on the five selected data sets are presented in the remainder of this section. The descriptions below are supplemented by three more tabular comparisons. Table V presents the particular test conditions for each test run used for comparisons. Table VI presents further information on the instrumentation used in each of the five data sets, while Table VII compares the data reduction techniques.

a. Coles - Supersonic Flow with Zero Pressure Gradient

Coles' data (reference 9) at two Mach numbers, $M = 2.6$ and $M = 3.7$, were selected as baseline cases. Coles' experiments were carried out in the Jet Propulsion Laboratory 29-inch supersonic wind tunnel, whose flexible nozzle walls were adjusted to give a nearly constant pressure flow over the adiabatic flat plate model. The test model consisted of a 30-inch long flat plate sharpened with a half-wedge on the upper surface at each end; the lower test surface was flat over the entire length. This plate was inserted into the tunnel, located on the centerline and pitched 0.17 degrees nose down. Various types of boundary layer trips were employed by Coles. For the two comparison runs cited herein, the trip, or fence, consisted of 0.014-inch diameter wires spaced 1/4 inch apart which projected about 0.1 inch beyond the leading edge of the plate.

This experiment emphasized accurate evaluation of the skin friction coefficient with a floating element gage. Only total pressure profiles were measured; total temperature was assumed to be constant to determine velocity profiles across the boundary layer for the adiabatic plate, as described in Tables VI and VII. Freestream conditions were assumed based on isentropic expansion of a $\gamma = 1.4$ fluid. Profile measurements were taken at only one station 21.5 inches from the leading edge. Skin friction gages were placed at 5.5, 13 and 24 inches. Static pressure taps in the plate were used to determine axial pressure variations.

TABLE V
TEST CONDITIONS (NOMINAL) FOR BLIMP COMPARISON DATA SETS

Test	Stagnation Conditions		Edge Conditions				Wall Conditions			
	P ₀ (atm)	T ₀ (°R)	M _e	P _e (atm)	T _e (°R)	u _e (ft/sec)	T _w (°R)	T _w /T _{aw}	F	
COLES #27, M=2.5	0.935	556	2.568	0.049	240	1950	522	1.000	0.0	
	1.355	561	3.701	0.0134	150	2219	512	1.000	0.0	
NOL Lee, 5 atm 10 atm Brott, 5 atm 10 atm	5.1	784	4.70	0.0135	144	2766	520	0.74	0.0	
	10.2	747	4.74	0.0241	136	2711	524	0.74	0.0	
	5.1	762	3.89 +4.55	0.039 +0.016	190 +149	2628 +2720	557	0.82	0.0	
	10.2	762	3.93 +4.56	0.073 +0.033	186 +148	2633 +2719	556	0.82	0.0	
TRW Step-Up in T _w Step-Down in T _w	4.86	569	4.00	0.032	136	2280	17C +565	0.33 +1.085	0.0	
	4.89	573	4.03	0.031	135	2295	560 +185	1.09 +0.36	0.0	
STANFORD #2367, F=0.000 #122366, F=0.002 #122066, F=0.004 #121966, F=0.008 #5867, Step-Up in F	1.005	525	0.0375	1.004	525	42.2	525	1.000	0.0	
	1.003	545	0.0403	1.002	545	46.1	534	0.980	0.00190	
	0.0997	548	0.0402	0.996	548	46.2	532	0.970	0.00385	
	1.000	546	0.0402	0.999	546	46.0	527	0.964	0.00780	
	1.000	529	0.0380	0.999	529	42.6	532	1.010	0.00400	
JEROMIN #2.5-0.0 #2.5-1.2 #3.6-0.0 #3.6-2.1	5.21	530	2.55	0.28	230	1900	514	1.035	0.0	
	5.21	536	2.55	0.28	235	1905	522	1.070	0.00127	
	8.28	533	3.57	0.097	149	2150	517	1.055	0.0	
	8.30	527	3.52	0.105	152	2125	524	1.11	0.00211	

TABLE VII
REPRESENTATION OF KEY PARAMETERS AND METHODS OF DATA REDUCTION

TEST	STAGNATION PRESSURE	STAGNATION TEMPERATURE	FREE STREAM PRESSURE	FREE STREAM TEMPERATURE	PROFILE TOTAL TEMPERATURE	PROFILE STATIC TEMPERATURE	PROFILE VELOCITY	WALL PROPERTIES	HEAT TRANSFER COEFFICIENT	SURFACE FRICTION COEFFICIENT	WALL PRESSURE	TEMPERATURE
COALS	MEASURED DIRECTLY	MEASURED DIRECTLY	ASSUMED CONSTANT	ASSUMED CONSTANT	ASSUMED CONSTANT	ASSUMED CONSTANT	ASSUMED CONSTANT	MEASURED DIRECTLY	MEASURED DIRECTLY	MEASURED DIRECTLY	MEASURED DIRECTLY	MEASURED DIRECTLY
NOX	MEASURED DIRECTLY	MEASURED DIRECTLY	ASSUMED CONSTANT	ASSUMED CONSTANT	ASSUMED CONSTANT	ASSUMED CONSTANT	ASSUMED CONSTANT	MEASURED DIRECTLY	MEASURED DIRECTLY	MEASURED DIRECTLY	MEASURED DIRECTLY	MEASURED DIRECTLY
TM	MEASURED DIRECTLY	MEASURED DIRECTLY	ASSUMED CONSTANT	ASSUMED CONSTANT	ASSUMED CONSTANT	ASSUMED CONSTANT	ASSUMED CONSTANT	MEASURED DIRECTLY	MEASURED DIRECTLY	MEASURED DIRECTLY	MEASURED DIRECTLY	MEASURED DIRECTLY
STAMPED	MEASURED DIRECTLY	MEASURED DIRECTLY	ASSUMED CONSTANT	ASSUMED CONSTANT	ASSUMED CONSTANT	ASSUMED CONSTANT	ASSUMED CONSTANT	MEASURED DIRECTLY	MEASURED DIRECTLY	MEASURED DIRECTLY	MEASURED DIRECTLY	MEASURED DIRECTLY
ALUMIN	MEASURED DIRECTLY	MEASURED DIRECTLY	ASSUMED CONSTANT	ASSUMED CONSTANT	ASSUMED CONSTANT	ASSUMED CONSTANT	ASSUMED CONSTANT	MEASURED DIRECTLY	MEASURED DIRECTLY	MEASURED DIRECTLY	MEASURED DIRECTLY	MEASURED DIRECTLY

NOTE: WALL NOT MEASURED

b. Naval Ordnance Laboratory - Hypersonic Flow Without and With Pressure Gradient

Many reports and documents were found which presented hypersonic flow data, and most of them included profile measurements. After discussions with various investigators in this field, the recent zero pressure gradient experiments at the Naval Ordnance Laboratory by Lee et al. (reference 17) and the extension to pressure gradient flows by Brott et al. (reference 6) were selected. Both of these investigations were carried out using the NOL Mach 5 boundary layer channel, which is a two-dimensional half nozzle with a flexible wall forming the nozzle. Boundary layer measurements are carried out on the opposite, flat wall, with moderate heat transfer to the wall controlled by circulating wall coolant. This stainless steel test surface is eight feet long and tapered from 12 to 13.5 inches wide. Lee's tests were carried out at four stations between 48 and 92 inches downstream of the throat, giving naturally turbulent boundary layers from two to four inches thick. Brott's measurements were at five stations between 56 and 84 inches, giving boundary layer thicknesses of 1.3 to 3.9 inches.

A wealth of instrumentation was used in these NOL investigations. Profile instruments included a total pressure probe, a static pressure probe, an equilibrium temperature probe (measures local recovery temperature), and, in Brott's investigation, a fine wire thermocouple probe. Wall instrumentation included water-cooled skin friction balances upstream of each profile measurement location, and wall heat flux gages.

c. TRW - Hypersonic Flow with Step in Wall Temperature

The Arnold Engineering Development Center (AEDC) Supersonic Wind Tunnel "A" with a 40-inch by 40-inch test section provided the main air flow for the TRW experiments. This tunnel was operated in a continuous, closed-circuit mode. The nozzle used was an automatically driven, flexible-plate-type. Some of the test details are contained in an AEDC report, reference 67.

The test model was a 26.09-inch E.D., 49.48-inch long hollow cylinder aligned with the flow to ± 0.05 degrees in pitch and yaw about the tunnel centerline and supported by two struts attached to the downstream end. In cross section, the leading edge was a half wedge on the outer surface. The inner (test) surface was flat along its entire length with a surface finish of 100 μ -inches. Seven separately controlled cooling (heating) copper coil circuits were counter-wrapped on the outside surface. The 400°F step in wall temperature was made between 23.0 and 24.0 inches from the leading edge with four of the seven circuits forward of the step. Liquid nitrogen was circulated in the cold wall region;

pre-conditioned water was used to achieve near-adiabatic conditions in the "hot" region. For the temperature step tests, the circuits in each region were manifolded together. A 0.375-inch wide by 0.006-inch thick piece of fiberglass tape, serrated at its leading edge and located on the inner surface approximately 0.125 inches from the cylinder leading edge provided a boundary layer trip.

Profile instrumentation for these tests included a total pressure probe, static pressure probe, shielded stagnation temperature probe, and a constant current hot wire anemometer. The total temperature probe size (0.060 inch in diameter) precluded measurements very near the wall. Wall conditions were measured with static pressure transducers, surface temperature thermocouples, and Gardon heat transfer gages for wall heat flux. Skin friction was measured with 38 individual Stanton tubes.

d. Stanford - Zero Pressure Gradient, Subsonic Flow With and Without Uniform Blowing, and With a Step in Blowing

The heat and mass transfer apparatus at Stanford University's Mechanical Engineering Department, a facility built specifically for high accuracy subsonic boundary layer experiments with blowing and suction, was used by Simpson (reference 33) for the selected uniform blowing tests. A complete description of this apparatus is given by Moffat (reference 25). The main flow system was a continuous operation open-circuit consisting of an inlet filter, flow control valve, blower, heat exchanger, screens (for flow straightening), settling plenum chamber, primary nozzle, and test section. The rectangular test section was formed of two fixed side walls, a fixed flat bottom wall which included the porous test surface and an adjustable top wall of plexiglas controlled by a bank of jacks.

The test surface consisted of 24 individual, 1/4-inch thick, porous plate sections which were 20 inches wide by 4 inches long, resulting in a total length of 96 inches. The plates were constructed of 0.005-inch sintered bronze spheres which provided a surface finish of 200 μ -inches. Final assembly of the plates left a 0.032-inch gap between adjacent sections. This gap was filled and smoothed but was not porous.

The secondary, or injection, flow system consisted of an inlet filter, blower, heat exchanger, and flow header followed by 24 separate flow control valves, flow meters and delivery tubes, one set for each plate. A porous sintered bronze pre-plate was used to obtain uniform pressure in the small plenum behind each porous surface plate. Localized transpired flow rates were found to be ± 6 percent over the center 6 inches of the span. The heat exchangers in the main and secondary systems were controlled to provide equal flow temperatures

A trip of 1/8-inch wide coarse grid carbonized garnet paper was located at the exit edge of the transition section joining the nozzle to the test section. The trailing edge of the 0.041-inch thick trip was 1/8-inch upstream of the porous test section.

Considerable emphasis was placed on minimizing experimental errors in the construction of the Stanford facility, particularly in providing uniform injection mass flow, accounting for all sources or losses of energy, and in providing a low turbulence uniform main flow. Flow rates and plate temperatures were individually measured for each of the 24 porous segments. Pressure profiles were taken with a flat-based, .614-inch by .433-inch probe at four axial locations for each test, during which the freestream conditions were maintained virtually constant. Static temperatures were measured with an exposed thermocouple probe aligned with the flow. Static pressure taps located along the side walls were used to obtain the desired uniform flow contour of the upper surface. Due to the use of porous plates, skin friction was not measured directly, but was computed from the momentum integral equation and by a viscous schlieren method (see reference 53).

e. Jeromin - Supersonic Flow With and Without Uniform Blowing

Jeromin's experiments were carried out in the Cambridge University Engineering Department Supersonic Wind Tunnel, an intermittent blowdown tunnel with about 60 seconds of useful test time. The nozzle was two-dimensional with fixed side and top surfaces. The top surface was contoured but not adjustable; the lower surface which contained the flush mounted test surface was flat and could be adjusted vertically and in a pitch mode. The rectangular test section was 6.5 inches by 4.5 inches.

Jeromin used two test plates: a solid plate for the zero blowing tests and a 1/4-inch thick rolled, "porosint," sintered bronze plate made from 2.5 micron spheres for blowing tests. These plates were 3.38 inches wide by 15.6 inches long and were inserted into the bottom side of the nozzle with the leading edge 3.4 inches downstream of the nozzle throat. The junction between the nozzle wall and test surface was filled with paste and ground glass. A boundary layer trip was not employed.

Injection air was taken from the main tunnel supply, passed through a flow control valve and a metering orifice. No ducts carried the flow into separate plenum chambers upstream of a porous pre-plate. A single plenum on the other side was common to the entire test surface plate. Mass flow variations among 2.5-inch diameter samples of the test surface material (not the test surface itself) were ± 5 percent. No local variation measurements of the actual test plate were reported.

Jerome used a pitot probe and an equilibrium cone recovery temperature probe (similar to the BCU design) to obtain the boundary layer profiles. After several measurements which showed excellent agreement with the static temperature relation

$$T = T_w + (T_r - T_w) \left(\frac{u}{u_e} \right) - (T_r - T_e) \left(\frac{u}{u_e} \right)^2 \quad (1)$$

total temperature profiles were not measured. Velocity and temperature profiles were determined iteratively using the above relation and the Mach number profiles. Skin friction was not measured directly, but calculated from the momentum integral equation, the Sommer and Short T' method, and a transformation method described by Jerome (reference 18). The mass flow through the entire plate was measured with a single calibrated orifice.

SECTION III
TURBULENT MODEL SELECTION

The BLIMP code solves the partial differential equations expressing the conservation of mass, momentum, energy, and species for a viscous fluid. In turbulent flows, the equations are written with velocity, enthalpy, and species concentrations expressed in terms of mean and fluctuating components, i.e.,

$$u = \bar{u} + u' \quad (2)$$

The time averaged equations of motion then include time averaged products of fluctuating quantities such as $\overline{u'^2}$, which distinguish the equations of motion from their laminar flow counterparts. Turbulent modeling involves the mathematical description of these new flow variables such that the number of governing equations matches the number of unknowns.

The BLIMP code has been written to accept eddy viscosity or mixing length descriptions of the turbulent fluctuation terms. The eddy viscosity approach characterizes the turbulent velocity fluctuation as being related to local velocity gradient:

$$-\overline{(\rho v)' u'} = \rho \epsilon_m \frac{\partial \bar{u}}{\partial y} \quad (3)$$

Mixing length is related to eddy viscosity by the relation

$$\epsilon_m = l^2 \frac{\partial \bar{u}}{\partial y} \quad (4)$$

Many eddy viscosity and/or mixing length models have been reported in the recent literature (references 68 to 74). In this section of the report three widely used models are reviewed briefly and a "best" combination of eddy viscosity and mixing length relations and associated constants is chosen for the data comparisons of Section IV.

1. DESCRIPTION OF LEADING TURBULENT MODELS

a. Aerotherm Model (reference 1)

The Aerotherm turbulent model was formulated specifically for boundary layer flows with blowing. It was first reported in reference 2, and was limited to incompressible flows. Turbulence is described in the wall region by a mixing length equation, which approaches Prandtl's expression, $l = k_m y$, far from the wall. The incompressible expression is

$$\frac{dl}{dy} = (k_m y - l) \frac{\sqrt{\tau/\rho}}{y_a^+ v} \quad (5)$$

The constant k_m is taken as 0.44, while y_a^+ , related to a laminar sublayer thickness, is held constant at 11.823. Shear stress τ is taken to be the local value rather than the wall stress, τ_w . This expression allows a smooth transition from zero turbulence at the wall to large turbulence in the "law of the wall" region of the boundary layer. The mixing length distribution is automatically changed for blown flows due to the blowing effect on shear stress. Constants y_a^+ and k_m remain the same with or without blowing.

For compressible flows, equation (5) was changed to deal with the products ρl and ρy :

$$\frac{d\rho l}{dy} = \left(k_m \int_0^y \rho dy - \rho l \right) \frac{\sqrt{\tau/\rho}}{y_a^+ v} \quad (6)$$

Constants y_a^+ and k_m are left at their incompressible values of 11.823 and 0.44, respectively. As with incompressible flows, mixing length distribution is changed for blown flows implicitly, by the influence of blowing on local shear stress, τ .

The equation for mixing length is solved and then used to find eddy viscosity from equation (4). This wall region eddy viscosity is used from the wall on out into the boundary layer until it exceeds the wake region eddy viscosity expression

$$\epsilon_m = 0.018 u_e \epsilon_i^* \quad (7)$$

at which point the constant wake ϵ_{∞} value is adopted for the remainder of the boundary layer. In equation (7), u_e is the local boundary layer edge velocity and δ_i^* is the kinematic displacement thickness,

$$\delta_i^* = \int_0^{\infty} \left(1 - \frac{u}{u_e} \right) dy \quad (18)$$

In the energy and species equations, terms involving time averaged fluctuations of enthalpy and species concentrations appear and are related to the mean flow variables by definitions of eddy conductivity and eddy diffusivity:

$$\overline{\rho c_h} = - \frac{\sum_i \overline{(\rho v) h_i'}}{\sum_i \overline{K_i \frac{\partial h_i}{\partial y}}} \quad (19)$$

$$\overline{\rho c_{D_i}} = - \frac{\overline{(\rho v) K_i'}}{\overline{K_i \frac{\partial y}{\partial y}}} \quad (20)$$

In the Aerotherr model, eddy conductivity and diffusivity are simply related to eddy viscosity by constant turbulent Prandtl and Schmidt numbers.

$$\overline{\rho \tau_c} = \frac{\epsilon}{\nu} \quad (21)$$

$$\overline{\rho c_c} = \frac{\epsilon}{\nu} \quad (22)$$

A value of 0.75 for each of these was recommended in reference 1.

The Aerotherr model has not had the open literature exposure that the other two models considered here have had. Therefore, in order to verify its usefulness, some results from previously run program predictions are included here. Figures 1 to 4 present comparisons with flat plate, unblown, incompressible flow data taken by Wieghardt and Tillman (reference 38). The Wieghardt and Tillman case was included in the 1968 AFOSR-Stanford-TR

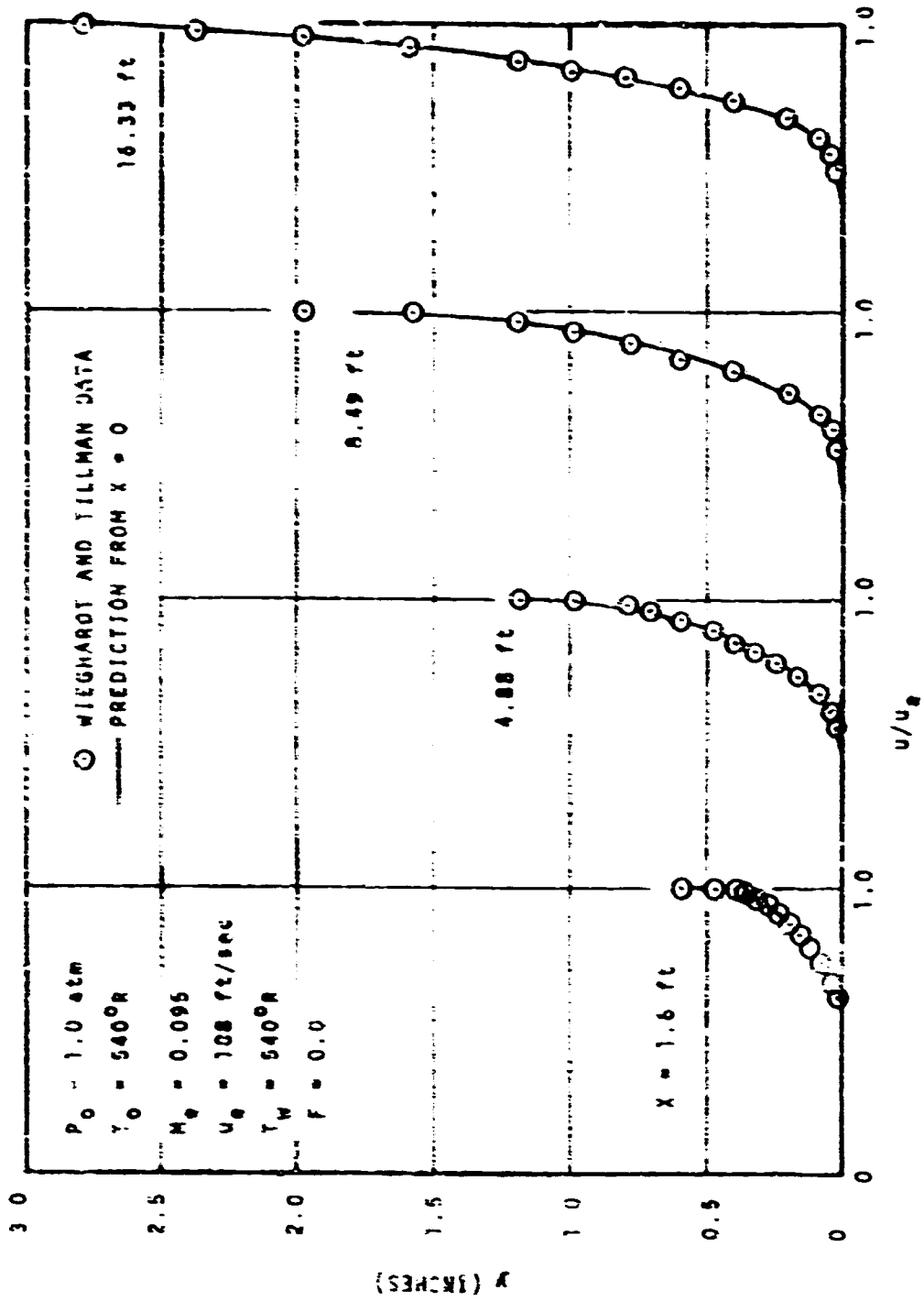


Figure 1. Velocity Ratio Profile
 Wieghardt, Subsonic Flow, Zero Pressure Gradient

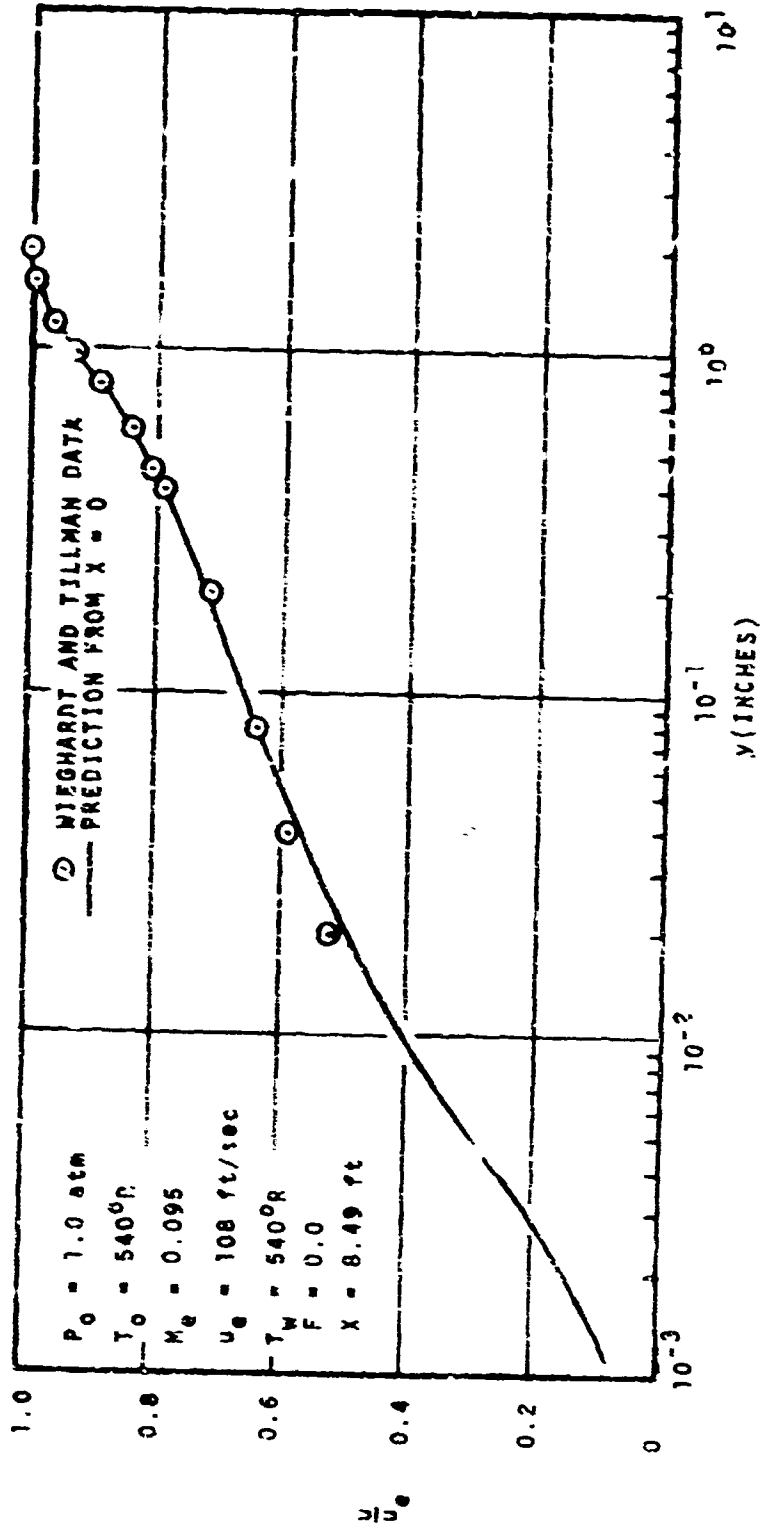


Figure 2. Linear u_e Velocity Ratio Profile
 Wieghardt, Subsonic Flow, Zero Pressure Gradient

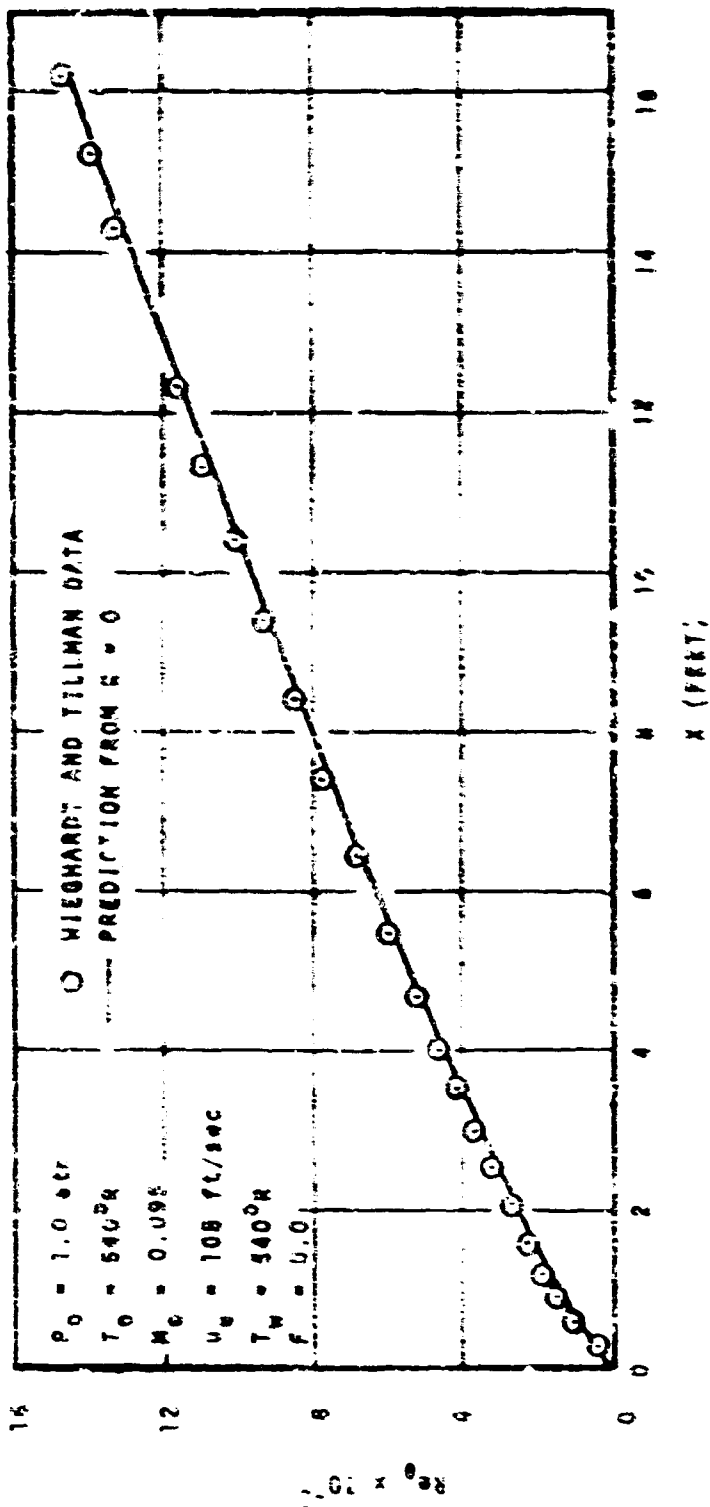


Figure 1. Momentum Reynolds Number vs. Distance from Inlet for Wieghardt, Subsonic Flow, Zero Pressure Gradient.

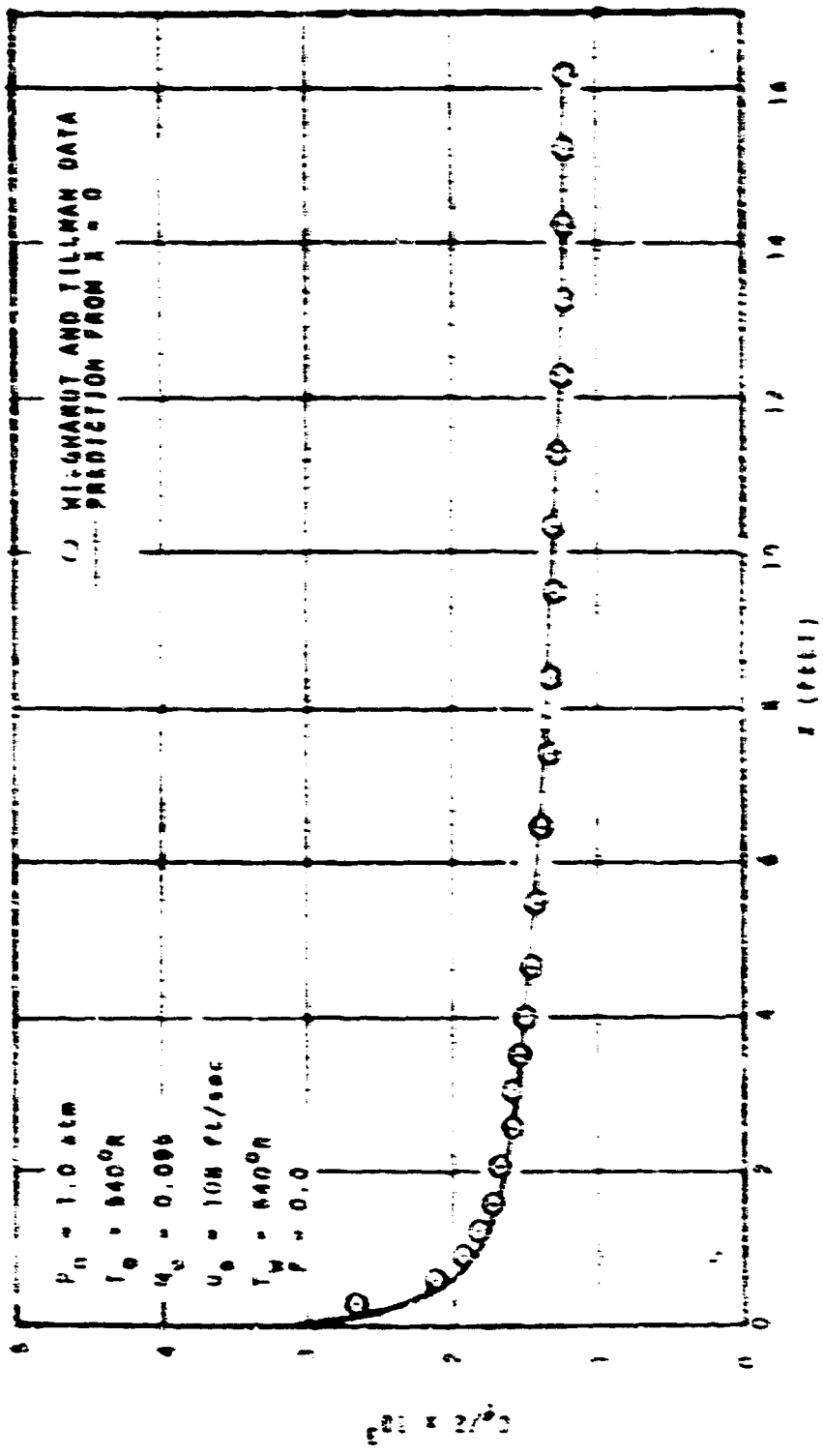


Figure 4. NACA Prediction Coefficient vs. Reynolds Number
Wilghamut, Subsonic Flow, Zero Pressure Gradient

Turbulent Boundary Layer Conference, and is regarded as a top quality flat plate experiment. The excellent agreement between the Aerotherm model and these data, both in profile and drag prediction, is apparent from these figures. Comparisons with subsonic, blown boundary layer data taken at MIT by Kendall (reference 66) are shown in Figures 5 to 8. These data were essentially the basis for the Aerotherm wall law model, although comparisons with other data have been shown to be equally good. As with the unblown case, profile comparisons are excellent. Drag is underpredicted by about 10-20% in comparison to the reported $C_f/2$ values for this case; however the prediction is well within the error bands associated with these values.

b. The Cebeci - Smith Model (reference 68)

In the Cebeci-Smith model, the boundary layer is also characterized by inner and outer regions. In the inner region, a mixing length approach is used, based on the Prandtl mixing length law as modified by Van Driest (reference 75). Cebeci and coworkers have extended and modified the basic Van Driest law to include pressure gradient, blowing, and variable turbulent Prandtl number effects. The inner region mixing length expression is

$$l = k_m y [1 - \exp(-y/A)] \quad (13)$$

where

$$A = \frac{26\nu}{\sqrt{\frac{\tau_w}{\rho_w}}} \left(\frac{\rho_w}{\rho}\right)^{1/2} \left(\frac{\mu}{\mu_w}\right) \left(\frac{1}{N}\right) \quad (14)$$

$$N = \left\{ \frac{\mu}{\mu_e} \left(\frac{\rho_e}{\rho_w}\right)^2 \frac{P^+}{v_w} \sqrt{\frac{\tau_w}{\rho_w}} \left[1 - \exp\left(11.8 \frac{\mu_w}{\mu} \frac{v_w}{\sqrt{\frac{\tau_w}{\rho_w}}}\right) \right] + \exp\left(11.8 \frac{\mu_w}{\mu} \frac{v_w}{\sqrt{\frac{\tau_w}{\rho_w}}}\right) \right\}^{1/2} \quad (15)$$

$$P^+ = \frac{v \frac{du_e}{dx}}{\left(\frac{C_f}{2}\right)^{1/2}} \quad (16)$$

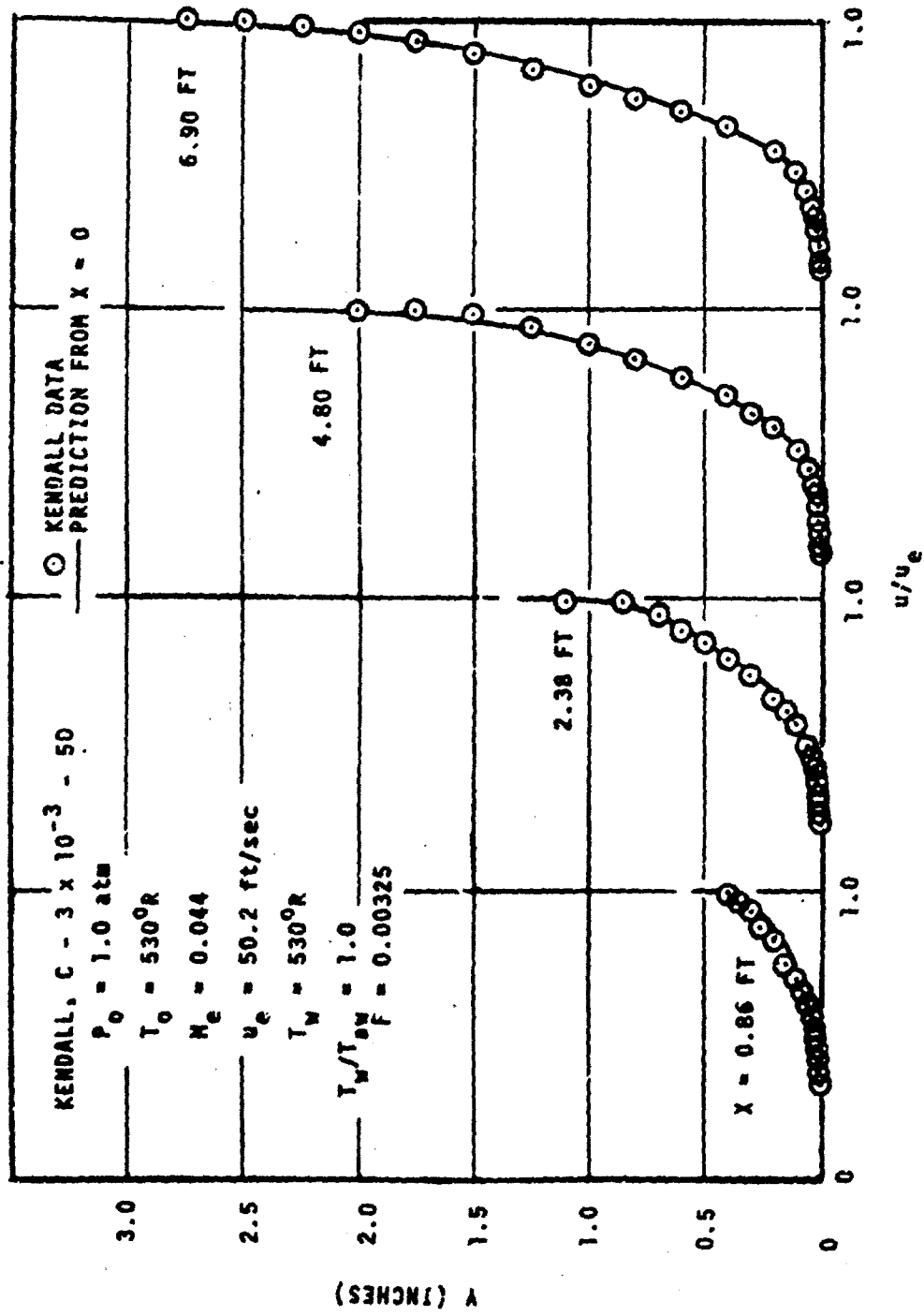


Figure 5. Velocity Ratio Profiles
 Kendall, Subsonic Flow, $F = 0.00325$

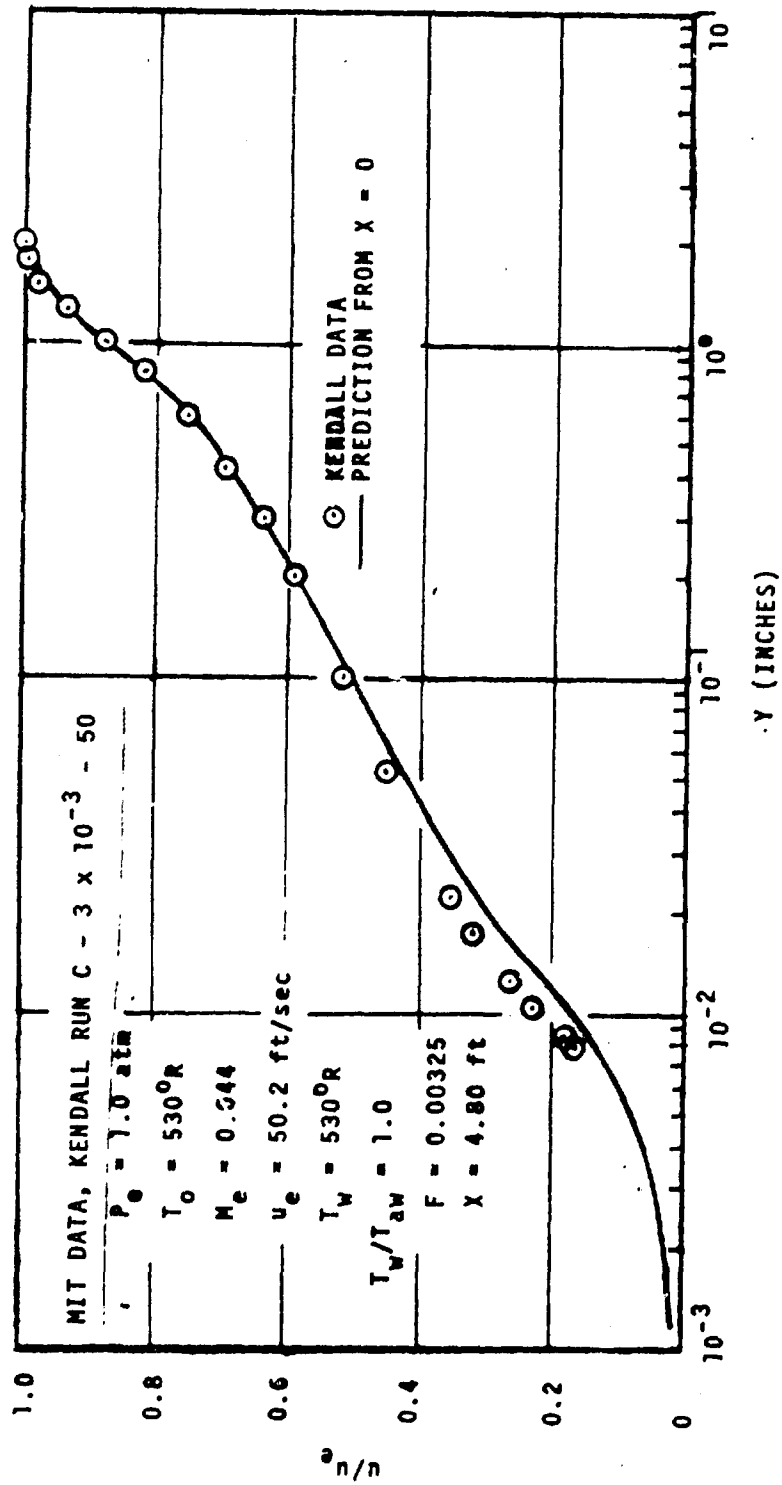


Figure 6. Linear-Log Velocity Ratio Profile
Kendall, Subsonic Flow, $F = 0.00325$

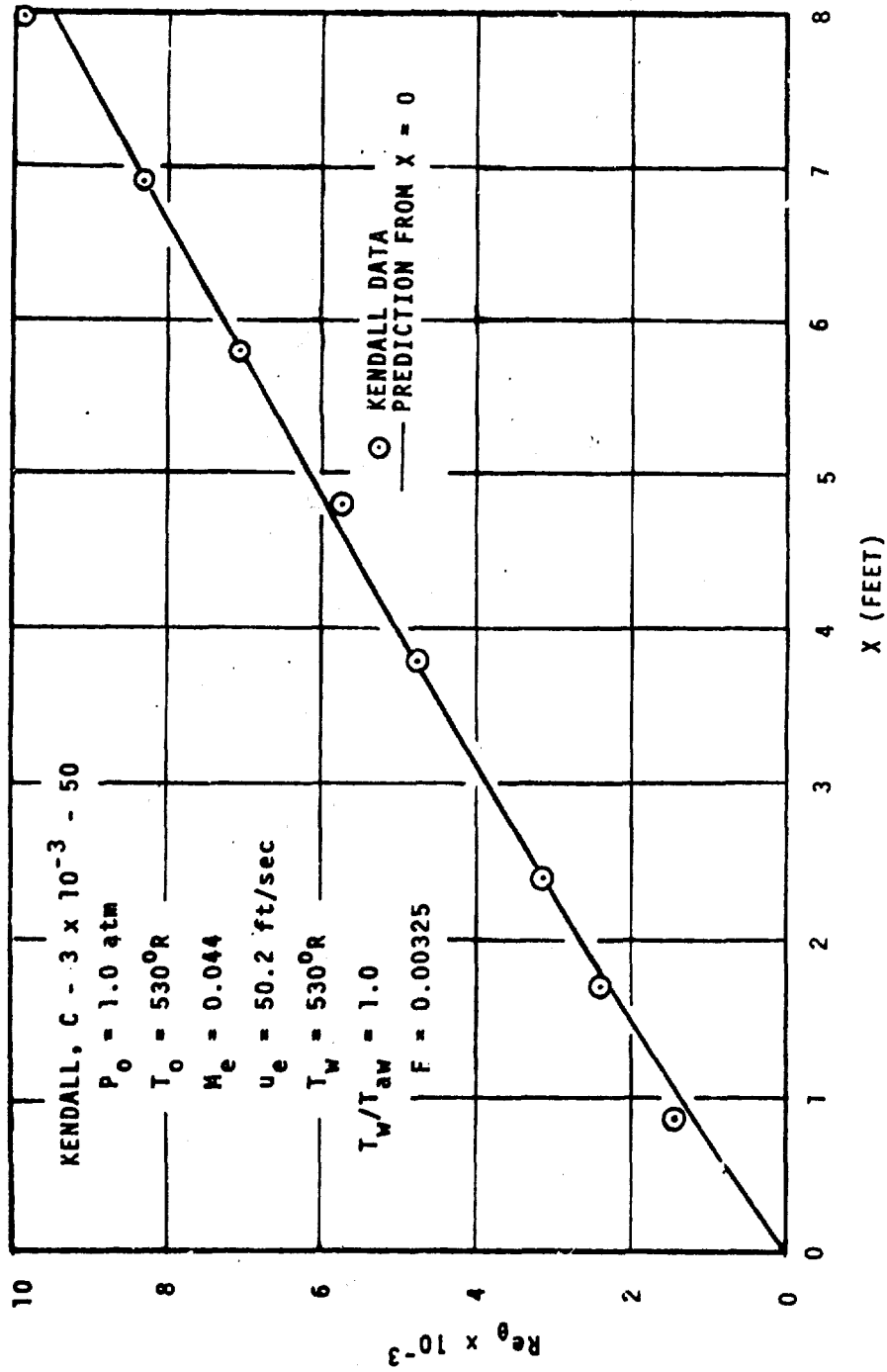


Figure 7. Momentum Thickness Reynolds Number vs. Streamwise Location
 Kendall, Subsonic Flow, $F = 0.00325$

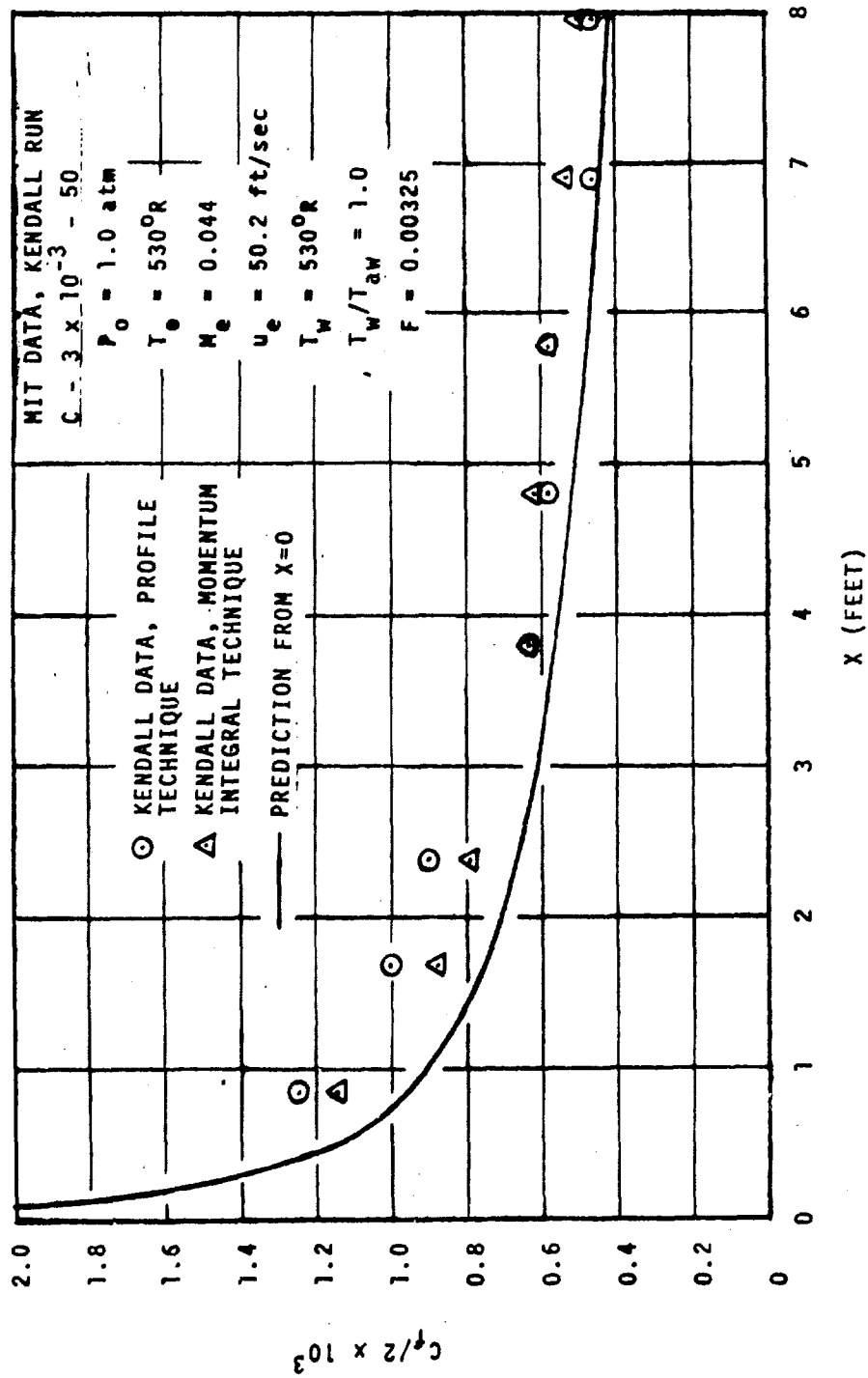


Figure 8. Skin Friction Coefficient vs. Streamwise Location
 Kendall, Subsonic Flow, $F = 0.00325$

$$k_2 = \text{Prandtl constant, taken as 0.46} \quad (17)$$

The effect of blowing is reflected in the value of N , which in turn affects the damping constant λ . Increasing the amount of blowing decreases λ , which results in less damping, or a more rapid approach to the Prandtl mixing length expression.

In the outer region, a constant eddy viscosity expression similar to equation (7) is used:

$$\epsilon_m = 2.9168 \frac{u^2}{s} \quad (18)$$

This eddy viscosity is multiplied by Elstanoff's (reference 76) intermittency factor,

$$\gamma = \left[1 - 5.5 \left(\frac{z}{\delta} \right)^4 \right]^{-1} \quad (19)$$

where δ is the boundary layer thickness. As in the Aerochem model, the inner region ϵ_m expression is used until it exceeds the outer region expression, at which point the outer region ϵ_m is used.

The Gebert model for eddy conductivity is based upon an examination of the one-dimensional nonsteady energy equation subject to an oscillatory boundary condition, similar to his derivation of eddy viscosity. This analysis results in a constant model for turbulent Prandtl number:

$$Pr_t = \frac{k_2 [1 - \exp(-\gamma/\lambda)]}{k_2 [1 - \exp(-\gamma/\sqrt{\pi}/3)]} \quad (20)$$

where

$$\lambda = \frac{34\nu}{\sqrt{\frac{v}{\rho}}} \left\{ -\frac{Pr^+}{\sqrt{\frac{v}{\rho}}} \sqrt{\frac{v}{\rho}} \left[\exp\left(11.8 \frac{v}{\sqrt{\frac{v}{\rho}}}\right) - 1 \right] + \exp\left(11.8 \frac{v}{\sqrt{\frac{v}{\rho}}}\right) \right\} \quad (21)$$

$$k_2 = \text{an energy mixing length constant, taken as 0.44} \quad (22)$$

$$Pr = \text{molecular Prandtl number} \quad (23)$$

Since Cebeci does not consider nonhomogeneous flows, he does not have a model for turbulent Schmidt number.

The Cebeci-Smith turbulent model validity is well documented in numerous open literature publications (references 77 to 79).

c. Bushnell and Beckwith Model (reference 69).

Bushnell and Beckwith use a mixing length model for the entire boundary layer. Near the wall (to $y/\delta = 0.1$), Prandtl's mixing length expression modified by Van Driest's damping function is used:

$$l = 0.4y[1 - \exp(-y/\lambda)] \quad (24)$$

where

$$\lambda = \frac{u^*}{\sqrt{\tau_w}} \quad (25)$$

Local shear and density are included rather than wall values. The λ^* value is taken from a fit of experimental data on blown, subsonic boundary layers, as shown in Figure 3. The experimental data are those of Simpson, et al. (reference 33) and the data reported in reference 2.

In the far wall region ($y/\delta > 0.3$), mixing length is assumed to be a function of boundary layer thickness and the incompressible form factor, $\beta_1^* = \rho_1^*/\rho_w$, where

$$\beta_1^* = \int_0^{\delta} \frac{u}{u_e} \left(1 - \frac{u}{u_e}\right) dy \quad (26)$$

Figure 19 shows the curve used to determine l/δ . This curve is the "quadratic variation" of reference 69, which has been adopted as the standard model at NASA/Langley (reference 80). The use of an l/δ variation as a function of incompressible form factor is an attempt to account for nonequilibrium* effects in the profile shape. Thus, it is most useful in strongly nonsimilar flow situations.

A straight line segment for l/δ is used to join the inner and far wall regions between $y/\delta = 0.1$ and $y/\delta = 0.3$.

*Nonequilibrium as used here refers to the fluid mechanical state rather than chemical state.

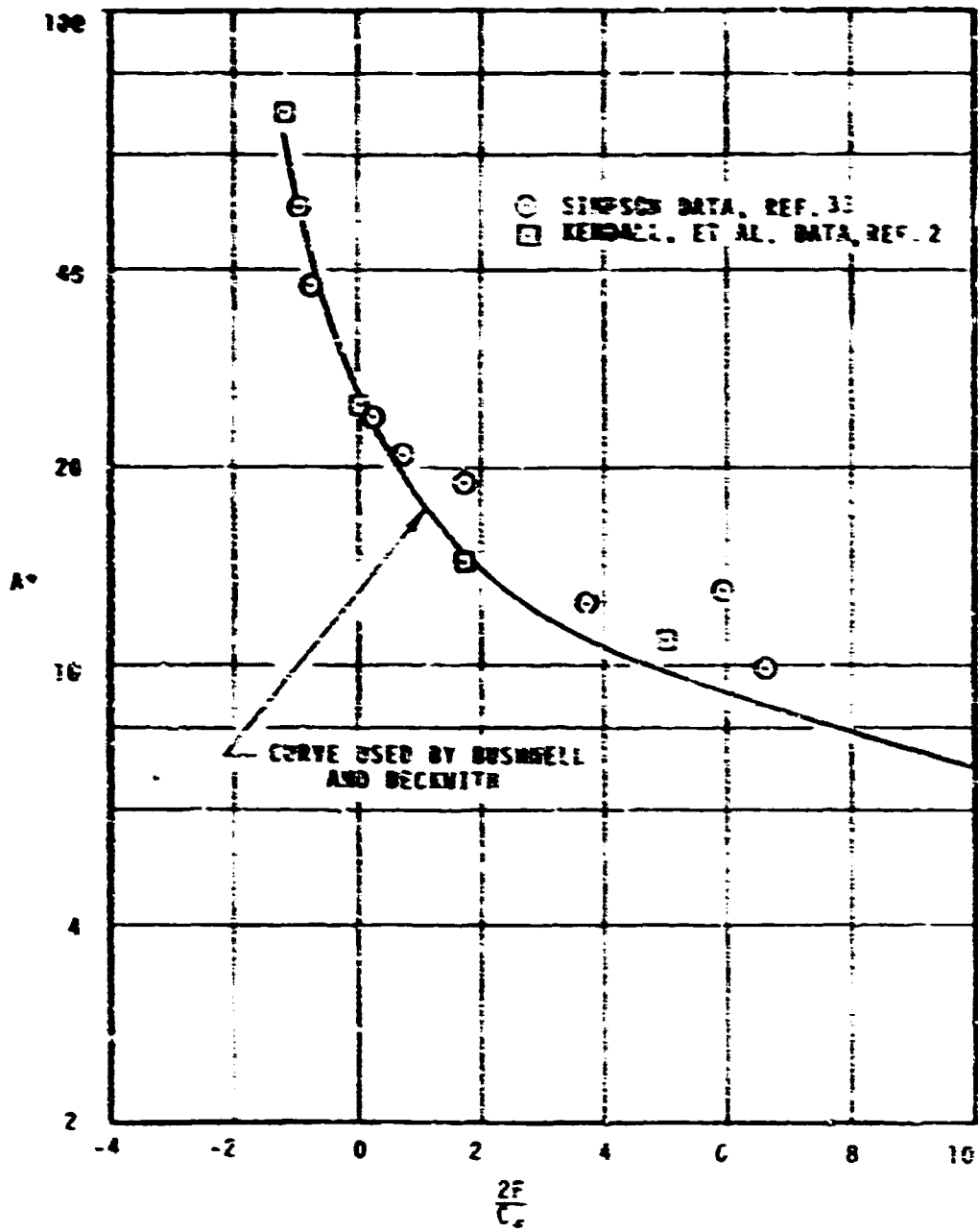


Figure 9. Variation of Damping Constant for Bushnell-Beckwith Wall Model

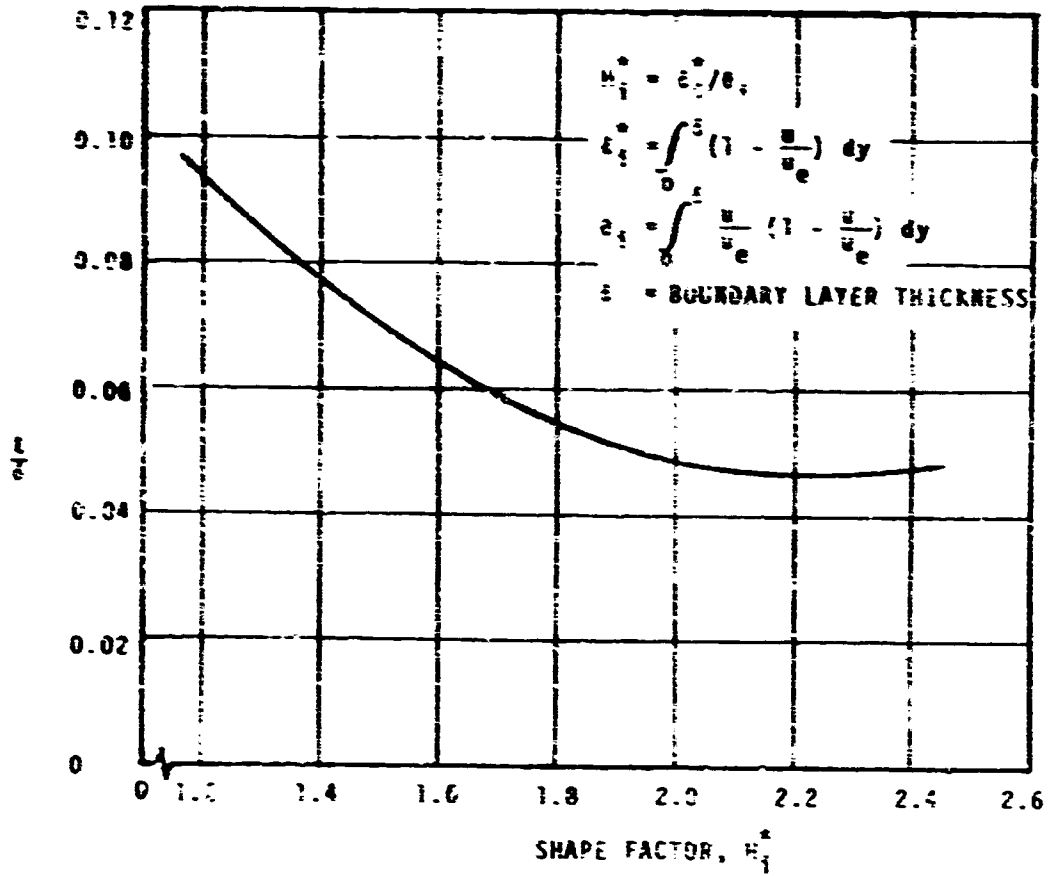


Figure 10. Variation of Mixing Length for Bushnell-Beckwith Wake Model

Bushnell and Beckwith use a constant turbulent Prandtl number but base it on total enthalpy fluctuations rather than static enthalpy fluctuations. That is,

$$\text{Pr}_T = \frac{\epsilon_h}{\epsilon_{H_T}} = \left(\frac{(\overline{\rho v})' \bar{u}}{(\overline{\rho v})' H_T'} \right) \left(\frac{\partial \bar{H}_T}{\partial y} \right) \quad (27)$$

Since no species equations are solved, no turbulent Schmidt number is specified.

The validity of the Bushnell-Beckwith model under several different kinds of flow conditions has been presented in reference 69.

2. TURBULENT MODEL COMPARISONS FOR THE LAW OF THE WALL REGION

a. WALAW Program

In order to examine the differences between the near wall mixing length formulations, a small computer code (WALAW) was written which solves the one-dimensional continuity, momentum, and energy equations. These equations, written for the wall region where streamwise changes are small compared to changes normal to the wall, are

continuity

$$\rho v = \rho_w v_w \quad (28)$$

momentum

$$\rho_w v_w u = \rho (u + \epsilon_m) \frac{du}{dy} - \tau_w \quad (29)$$

energy

$$\rho_w v_w \left(h + \frac{u^2}{2} - h_w \right) = \rho (v + \epsilon_m) \frac{d(u^2/2)}{dy} + \left(k + \frac{\rho \epsilon_m c_p}{\text{Pr}_t} \right) \frac{dT}{dy} - q_w \quad (30)$$

A perfect, ideal gas equation of state is assumed, and Runge-Kutta integration is used. Inputs to the code are τ_w , q_w , T_w , and $(\rho v)_w$. Also, a law for the eddy viscosity variation must be included in the set of equations. The code includes the three wall region eddy viscosity relations described above, however a constant turbulent Prandtl number equal to 0.9 has been assumed in all three models.

b. Results for Three Near Wall Models

The differences between the three near-wall mixing length models are exemplified by the curves of Figures 11 through 15. The WALAW code was run for a 50 ft/sec, adiabatic flat plate flow with three different blowing rates, $\rho_w v_w / \rho_e u_e = 0.0, 0.004, \text{ and } 0.010$. The turbulent models in these figures are labeled as follows:

- A = Aerotherm model
- B = Bushnell-Beckwith model
- C = Cebeci-Smith model

In Figure 11 where no blowing is included it is seen that all three models result in nearly the same mixing length variations. The Prandtl mixing length equation is essentially matched at about $y^+ = 100$. In Figure 12 where a moderate-to-strong blowing rate of 0.004 has been input, all three l^+ curves have shifted toward the Prandtl law, but the Bushnell and Cebeci models show more shift than the Aerotherm model. In Figure 13 where a very strong blowing rate of 0.010 is included, Models B and C have adopted the Prandtl line, $l = k_m y$, over the entire range of interest. Model A shows a similar trend with blowing, but does not respond as readily. Thus, it can be expected from these results that, under no blowing conditions, there will be very little difference between near wall predictions with the three mixing length models. As blowing increases, differences will become apparent. When constrained to the same wall shear value, the Aerotherm law will give lower turbulence levels which in turn result in larger gradients ($\partial u / \partial y, \partial T / \partial y$, etc.) than the Cebeci and Bushnell models.

These conclusions about the similarities between predictions for unblown flows are borne out by the WALAW results of Figure 14 through 19. Figure 14 includes a velocity profile comparison with the Wieghardt and Tillman data (reference 38). All three models show good agreement in the "law of the wall" region, which extends to about 0.5 inch for the station selected. Beyond that point, the one-dimensional equations of motion are no longer valid. Figure 15 includes comparisons with Coles (reference 8) Mach 3.7 adiabatic flat plate data, which shows how well these laws apply to compressible flows. At least for adiabatic flows, any of the three models appears to be satisfactory in the supersonic range.

For hypersonic flows, the experimental data uncertainties become greater since the flow itself is more difficult to work with. Figure 16 includes predictions from the three theoretical models compared to an experimental Mach number profile measured by Lee, et al. (reference 17). Mach number comparisons are shown since this information can be calculated directly from the pitot tube

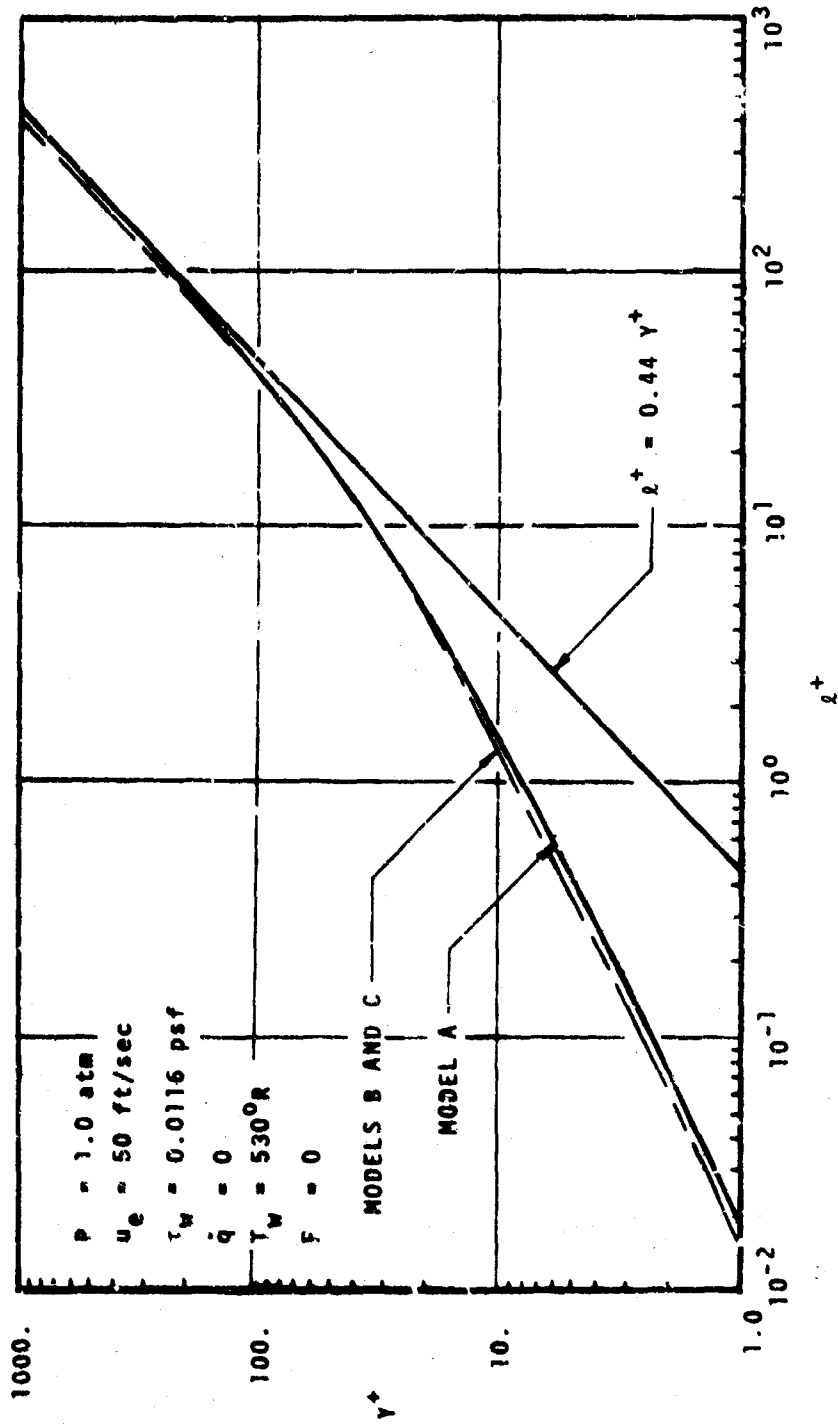


Figure 11. Mixing Length Variation with No Blowing

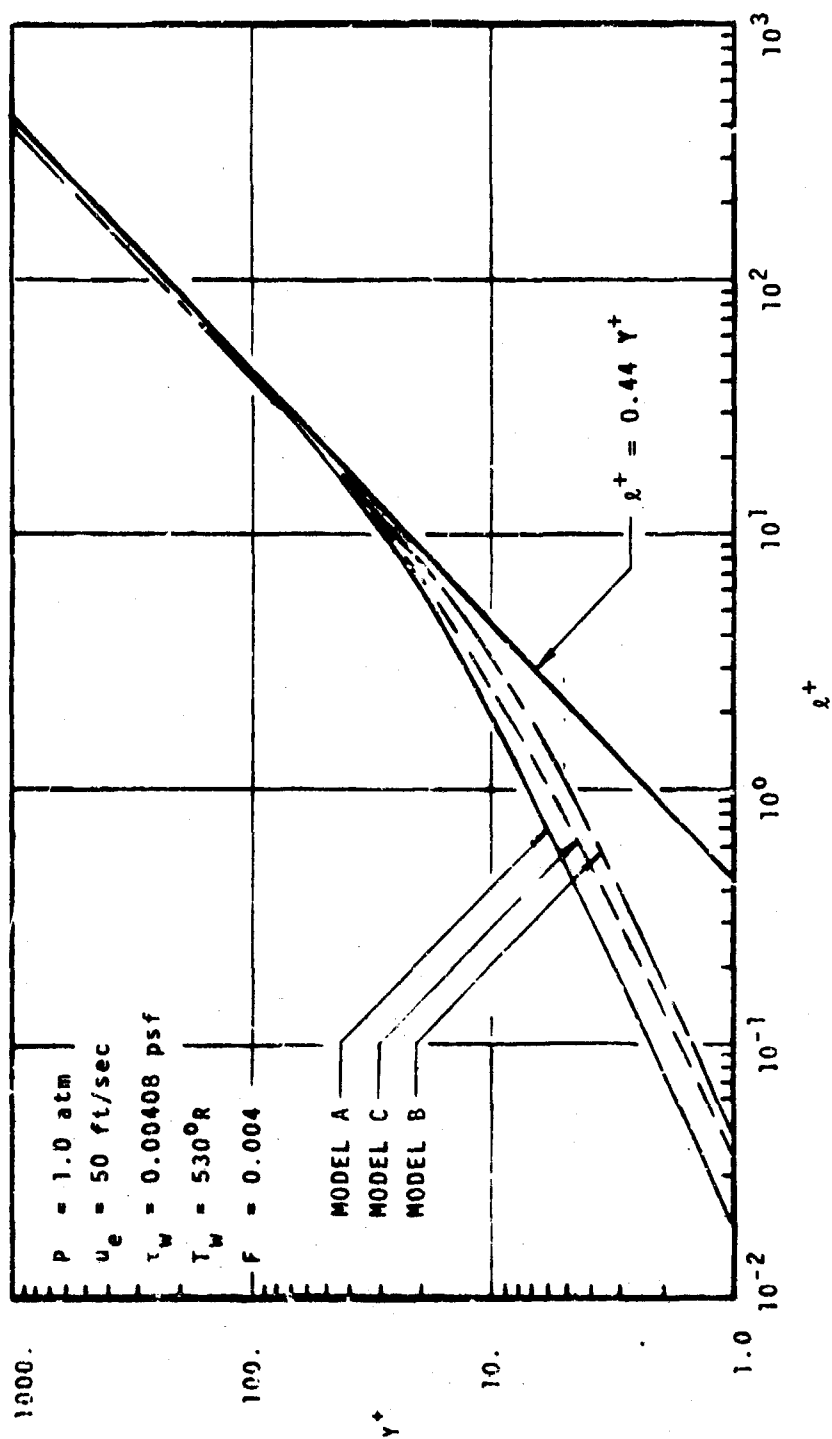


Figure 12. Mixing Length Variation With $F = 0.004$

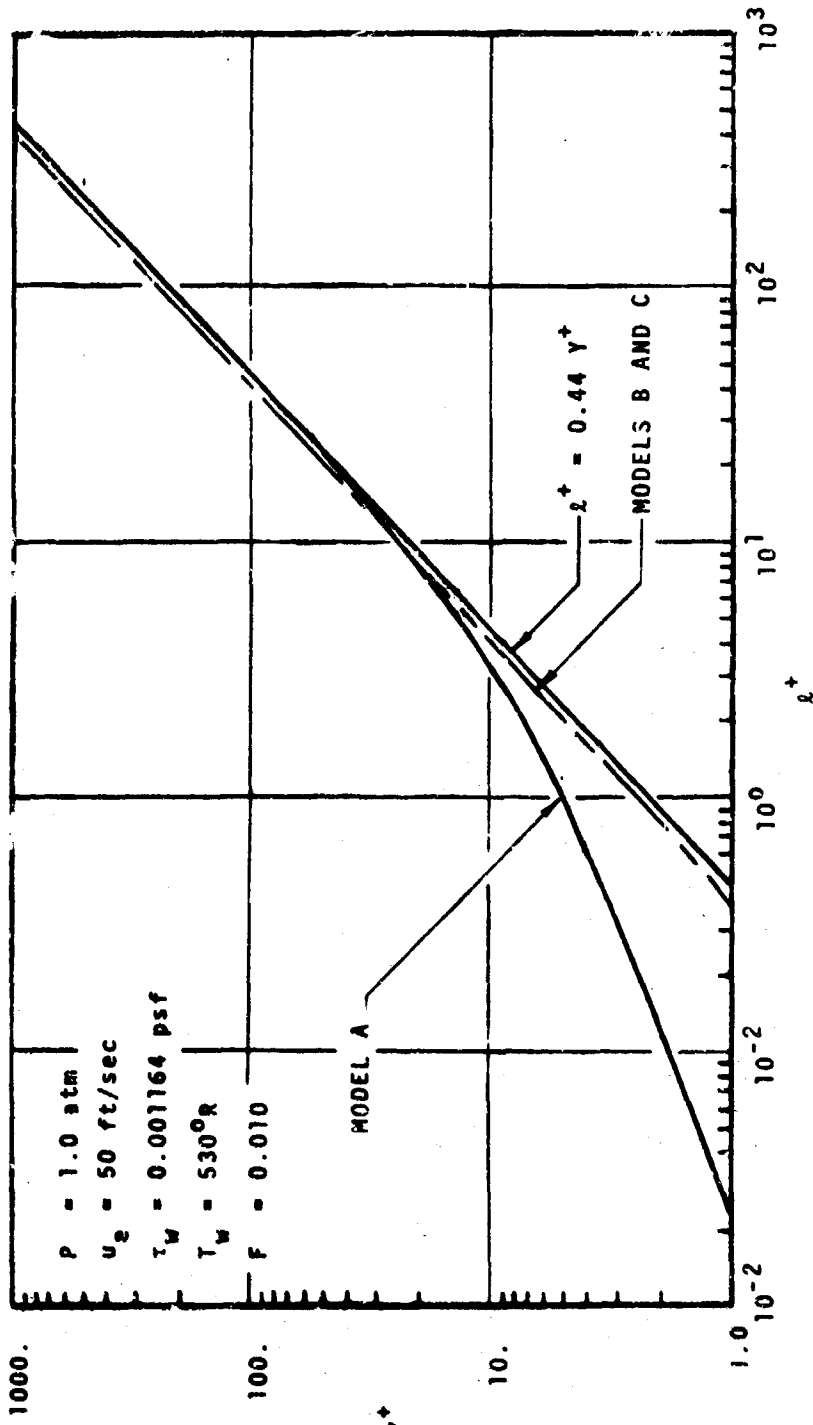


Figure 13. Mixing Length Variation With $F = 0.010$

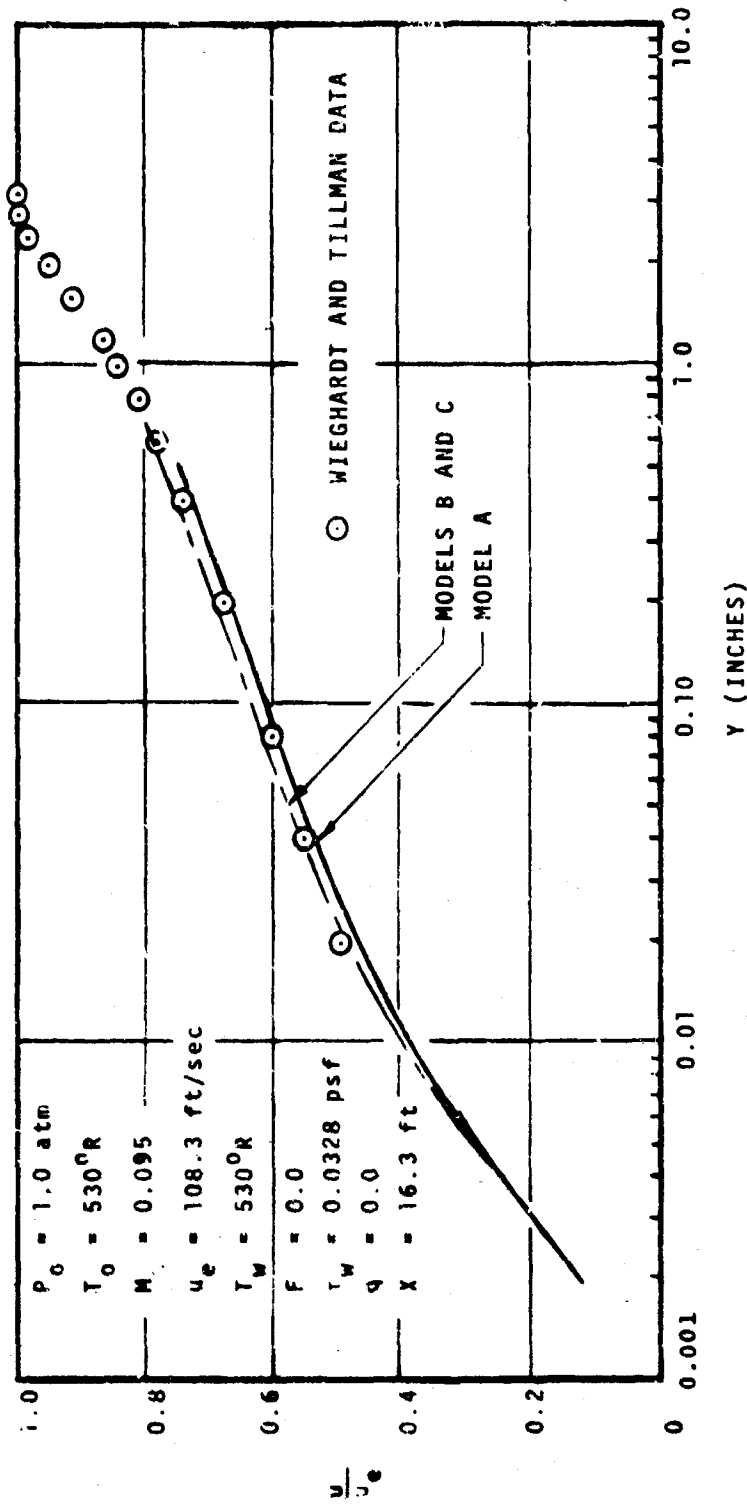


Figure 14. Linear-log Velocity Ratio Profiles
 Wieghardt, Subsonic Flow, Zero Pressure Gradient

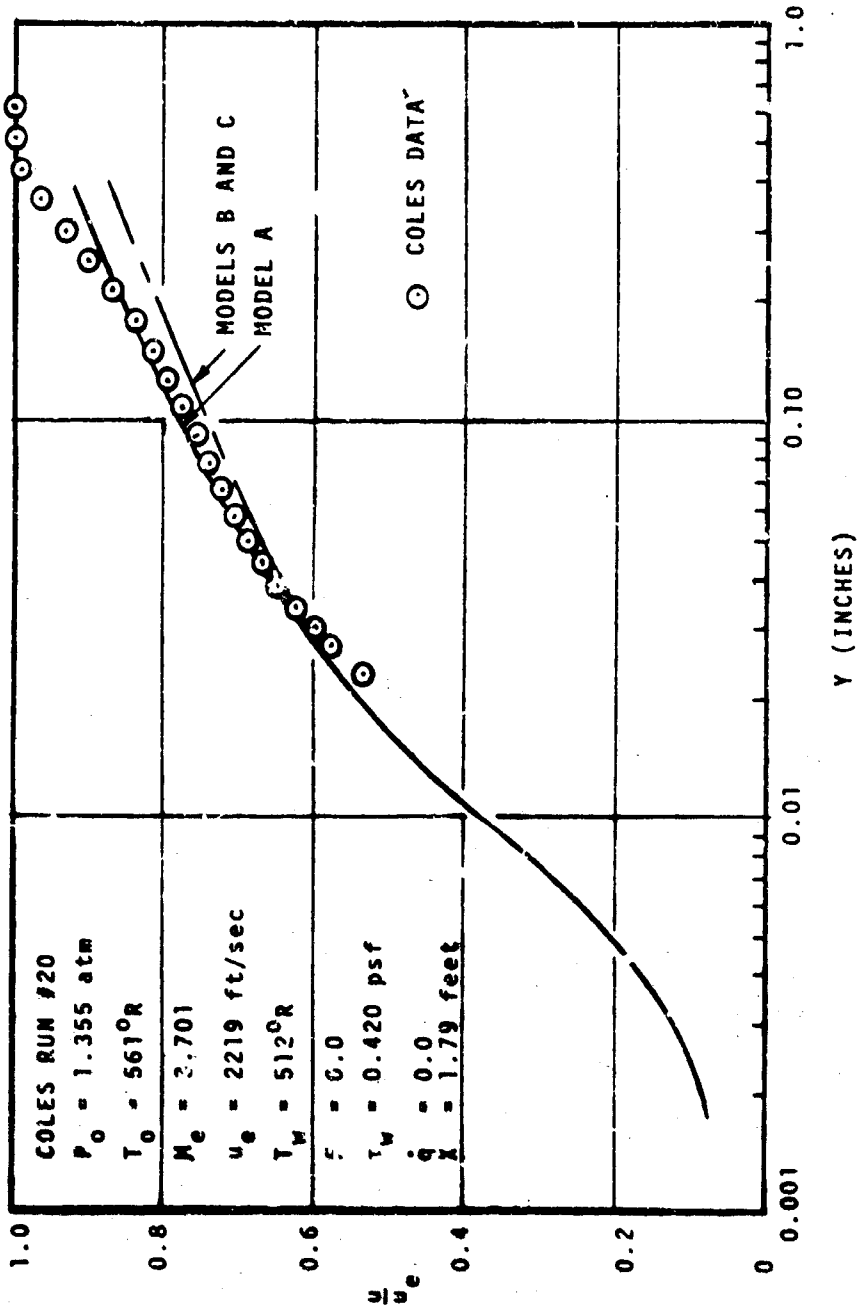


Figure 15. Linear Log Velocity Ratio Profile
 Coles Run #20, Supersonic, Zero Pressure Gradient Flow

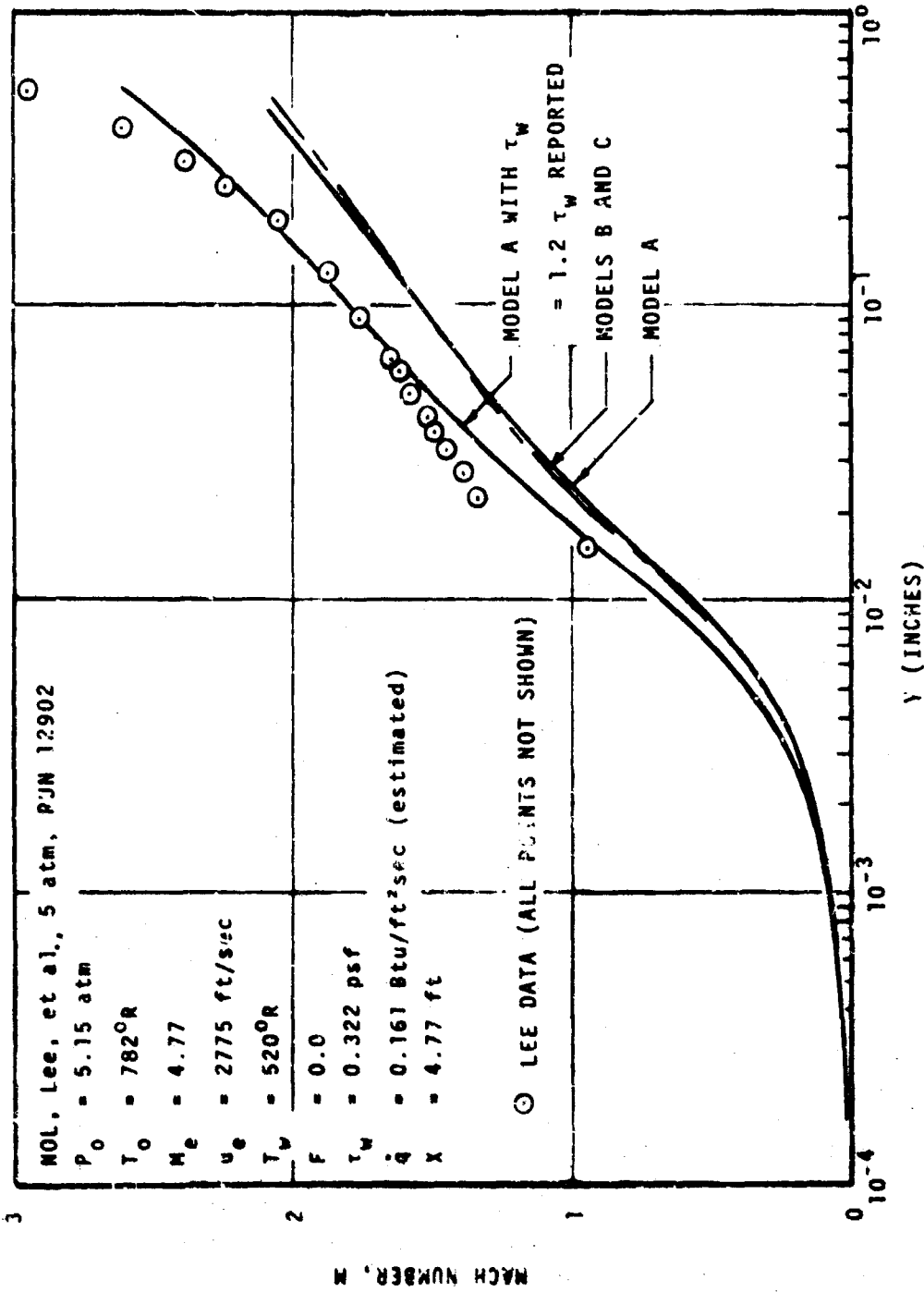


Figure 16. Linear-Log Mach Number Profile
 MOL, Lee, et al., Run 12902, Hypersonic, Zero Pressure Gradient Flow

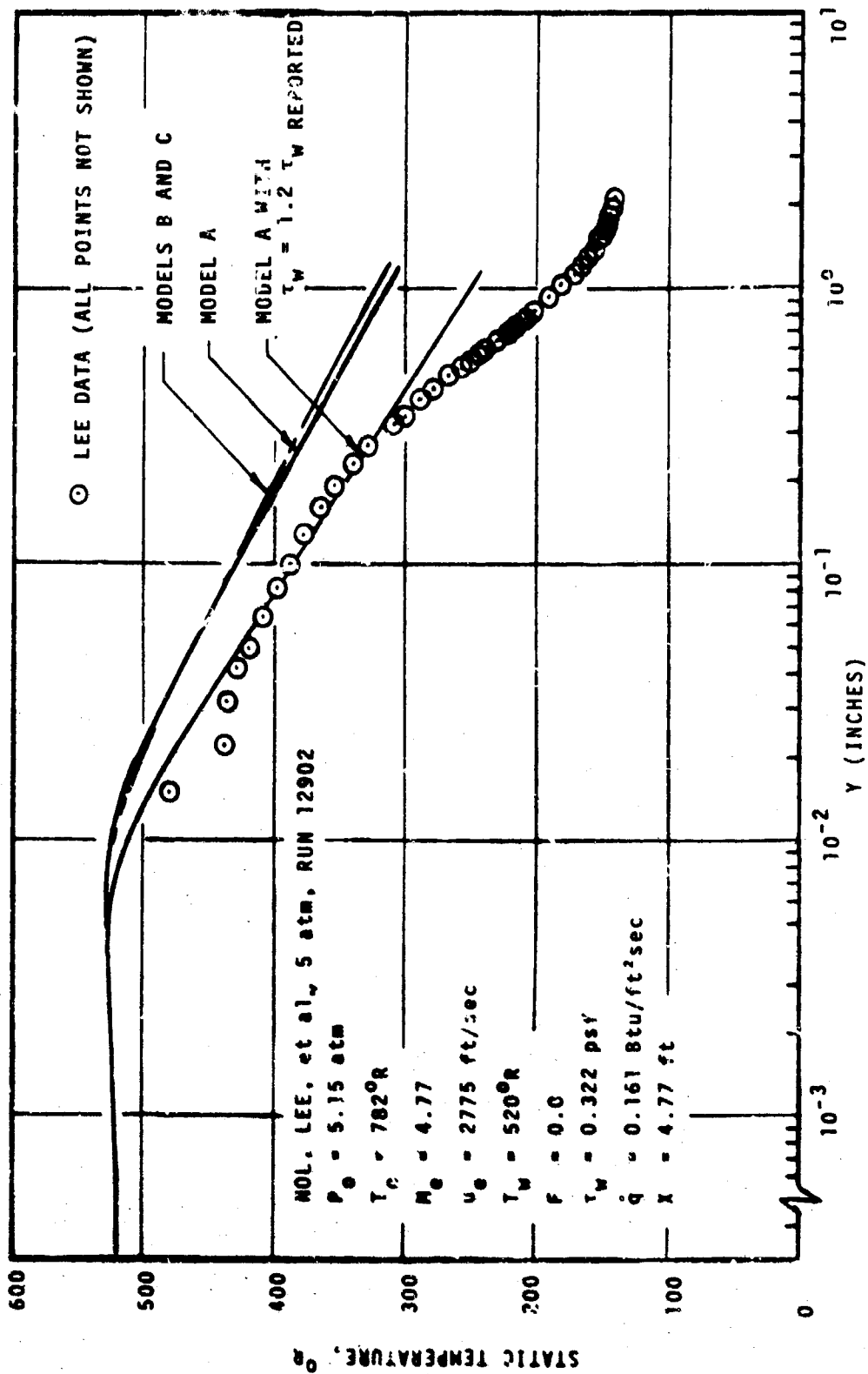


Figure 17. Linear Log Static Temperature Profile
 NOL, Lee, et al., Run 12902, Hypersonic, Zero Pressure Gradient Flow

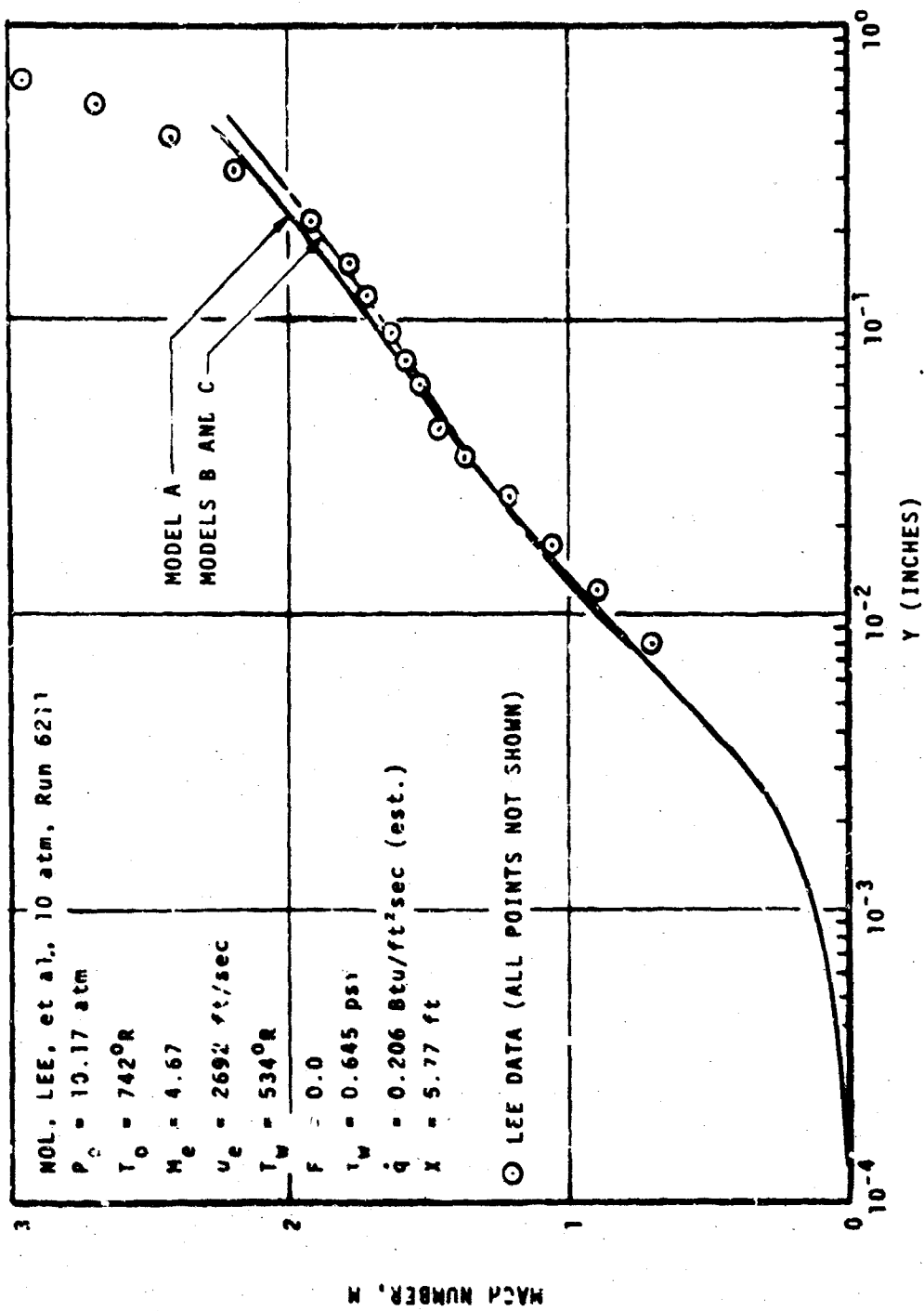


Figure 18. Linear-Log Mach Number Profile
 NOL, Lee et al., Run 6211, Hypersonic, Zero Pressure Gradient Flow

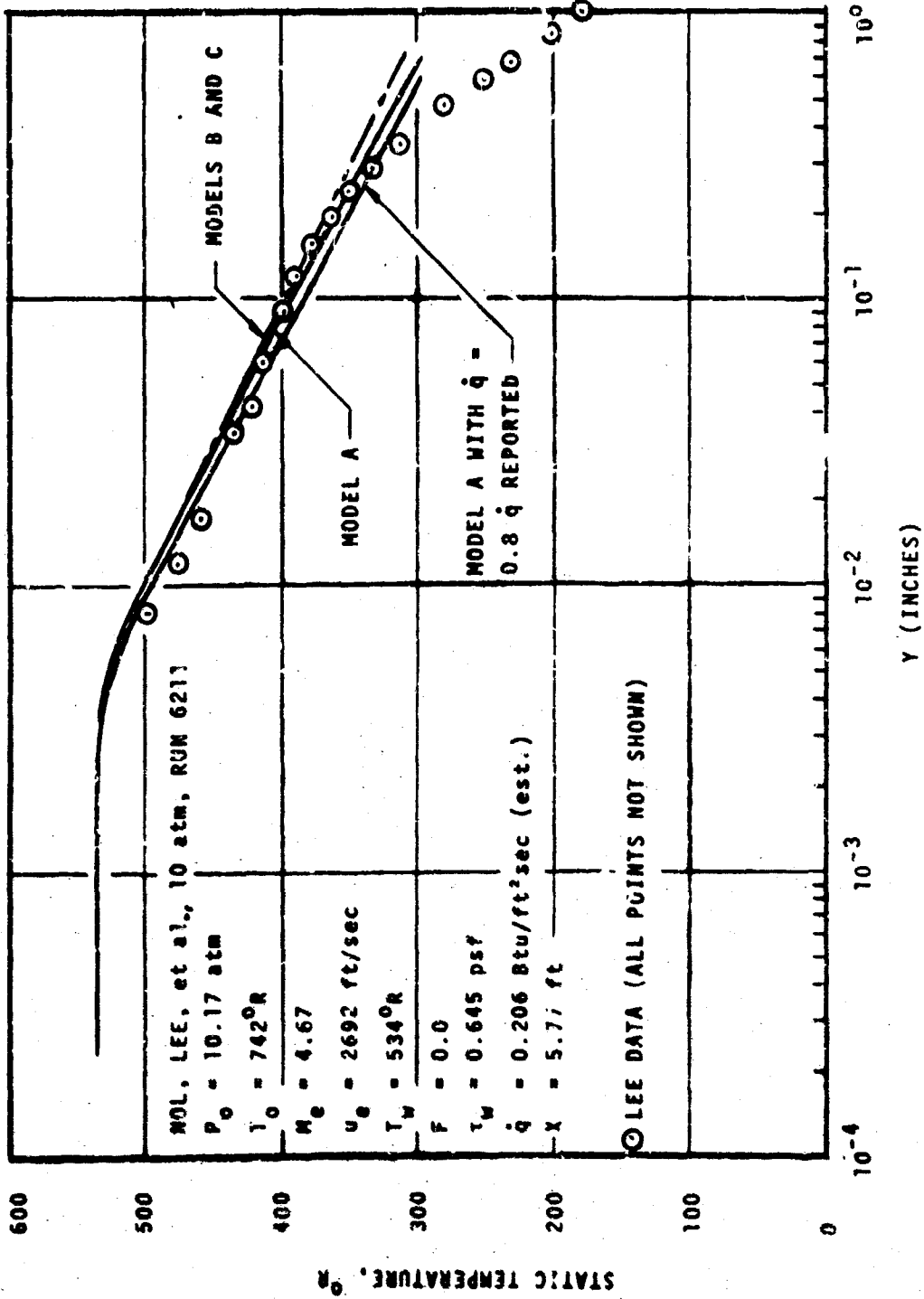


Figure 19. Linear-Log Static Temperature Profile
 NOL, Lee, et al., Run 6211, Hypersonic Zero Pressure Gradient Flow

readings, thereby introducing the least possible instrument error. Skin friction values were measured using a floating element shear stress gage. As can be seen in Figure 16, Mach number is underpredicted by about 15 percent by all the theories when this measured shear stress level is input to the WALAW program. A value of τ_w approximately 20 percent higher would give much better agreement, as shown in the figure. Similar results are obtained for the static temperature prediction, as shown in Figure 17. Static temperature is overpredicted using the reported wall shear; a τ_w value 20 percent larger gives more correct predictions with all theories considered. More will be said of the agreement with Lee's data later in this report.

Lee's higher stagnation pressure experiments show better agreement with theoretical predictions using the reported shear values. Figure 18 shows Mach number data and predictions for a $P_0 = 150$ psia run, the highest pressure reported by Lee. Agreement between Mach number data and profiles is excellent for all three theories, as are the static temperature predictions (Figure 19). The effect of a 20 percent change in wall heat flux is also shown in this figure, in order to establish the sensitivity of the one-dimensional solution to this input quantity. Thus, it can be concluded that for incompressible flows or compressible flows up to a Mach number of 5, with or without heat transfer, all three turbulent models do a satisfactory, and a very similar, job of predicting profiles in the near wall region.

As discussed earlier, Aerotherm's mixing length law has been verified by comparisons with Kendall's (reference 66) low-speed blown boundary layer data in another report (reference 2). These comparisons were rerun with the WALAW program to confirm their validity and also to obtain simultaneous predictions for the Cebeci and the Bushnell-Beckwith models. A small error was found in the original (reference 2) comparisons; however, the results remain essentially the same, as can be seen in Figures 20, 21, and 22. All results were obtained using the wall shear values reported by Kendall, determined by a wall pressure profile technique (as opposed to a $d\theta/dx$ technique). At the modest blowing rate of $F = 0.002$ (Figure 20), agreement between the Aerotherm and Cebeci models and the experimental data is excellent. The Bushnell-Beckwith model appears to react too strongly to the blowing rate, as evidenced by the very small extent of the laminar sublayer. A higher input τ_w value would shift all predictions upward, however (see Figure 16). In Figure 21, results for a stronger blowing rate of $F = 0.003$ are shown. At this blowing rate, the Aerotherm model shows the least effect of blowing, while the Bushnell model shows the most. Agreement is good for Model A and Model C. Results for strong blowing are shown in Figure 22. Using

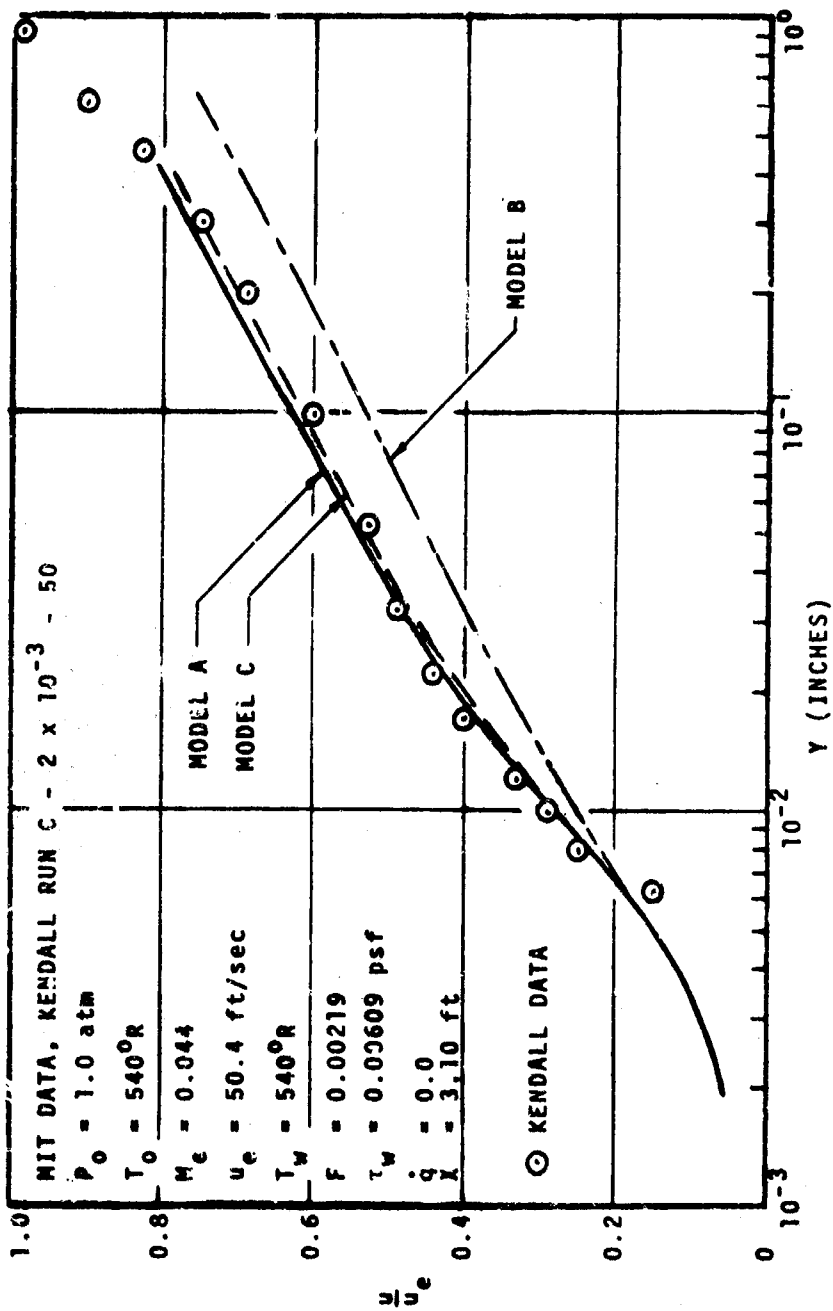


Figure 20. Linear-Log Velocity Ratio Profile
 MIT, Kendall, Run C - 2×10^{-3} - 50, Low-Speed Flow With Blowing

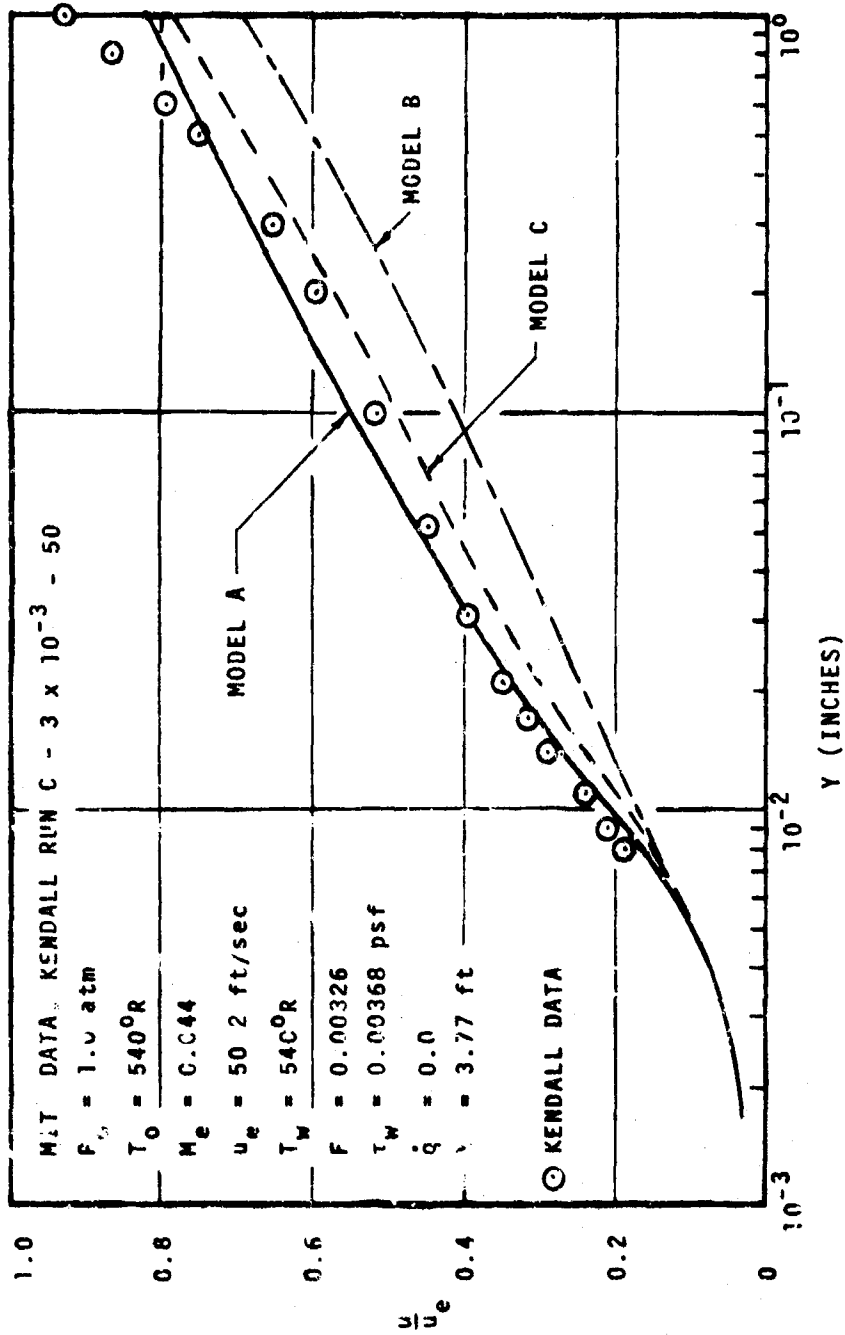


Figure 21. Linear-Log Velocity Ratio Profile
 MIT, Kendall Run C - 3×10^{-3} - 50, Low-Speed Flow With Blowing

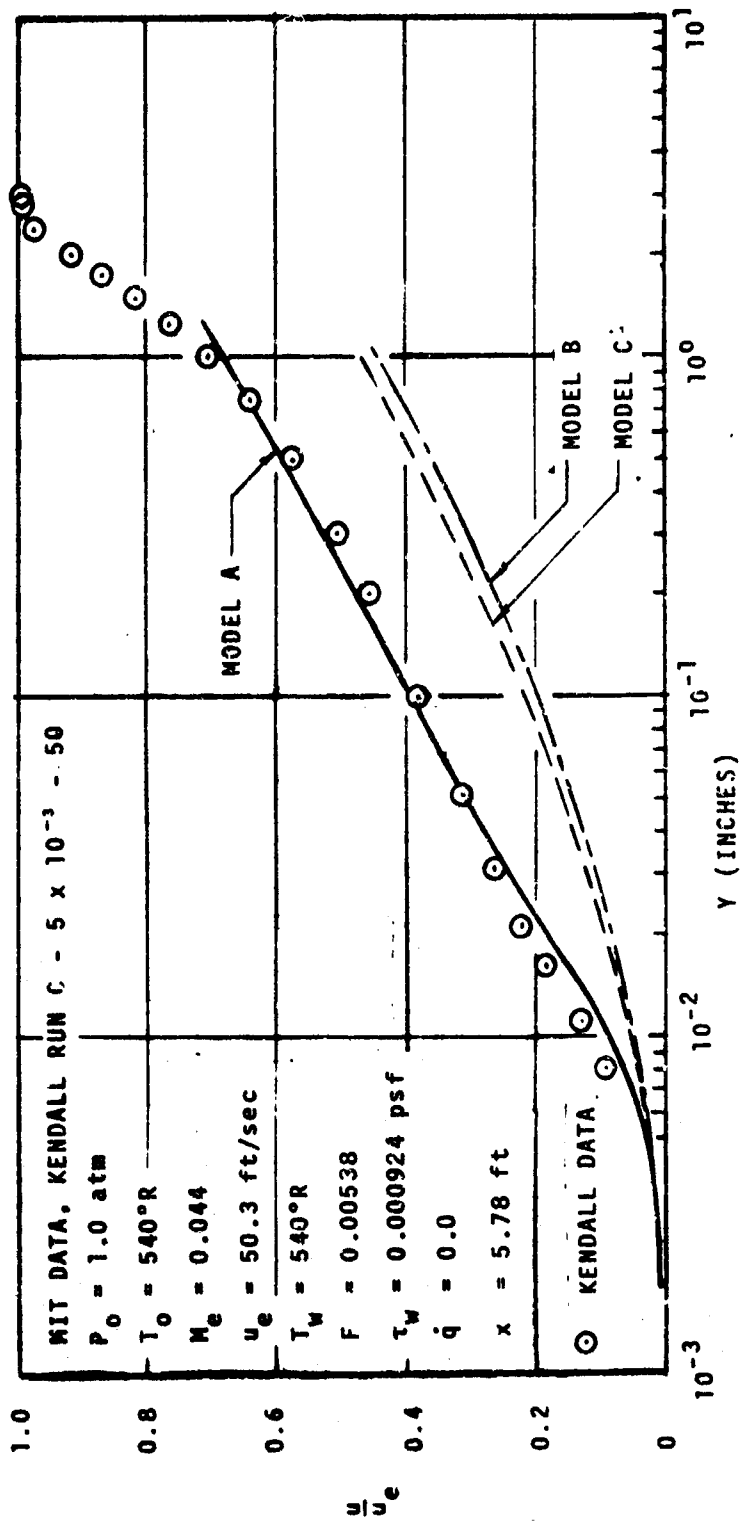


Figure 22. Linear-Log Velocity Ratio Profile
 MIT, Kendall Run C - 5×10^{-3} - 50, Low Speed Flow With Blowing

the reported wall shear stress and blowing rate, only the Aerotherm model predicts the velocity profile accurately. The Cebeci and Bushnell models result in nearly identical profiles, giving an error of 50 percent in the law of the wall region. The uncertainty in wall shear can more than account for this entire error, however.

The Stanford experimental data (reference 33) provides an independent check on the low speed blowing results presented above, since the test conditions are nearly identical. Freestream velocities of approximately 50 ft/sec with no pressure gradient were used for the reference 33 experiments, with blowing rates of $F = 0.0$ to 0.008 . Figure 23 illustrates the good agreement obtained between experiment and theory for a no-blowing case. Figures 24, 25, and 26 present data and predictions for nominal blowing rates of $F = 0.002$, 0.004 , and 0.008 , respectively. The theory trends are exactly as shown in the Kendall data comparisons. Models A and C show nearly the same results at low blowing, but diverge at stronger blowing rates. Models B and C give the same results with strong blowing. Using the reported wall shear values, the data in general follow the trends predicted by the Bushnell-Beckwith model more closely than the Cebeci model. Both of these models do a better job than the Aerotherm model. Thus, any conclusions which may have been drawn from the Kendall data comparisons must be questioned in the light of the Simpson comparisons. The difficulty lies in the requirement of an accurate C_f value, which is uncertain to ± 100 percent or more for strongly blown flows.*

One-dimensional theory and data comparisons were also carried out for the supersonic blown boundary layer experiments of Jeromin (reference 48). Jeromin experienced difficulties with axial pressure gradients and non-two-dimensionality of the flow, therefore his data must be considered less dependable than the subsonic cases. Drag coefficients were inferred from the integral momentum equation, from Stevenson's wall law technique (reference 81), and by a transformation method. In the predictions for several of Jeromin's runs shown in Figures 27 to 30, a single τ_w value was used if the three C_f determination methods were in agreement. More than one τ_w value was used (and is illustrated in the figure) if the methods gave widely divergent results. Figure 27 shows the type of agreement obtained for an unblown, Mach 2.5 flow. Agreement with the predictions is fairly good at the lower indicated shear stress value, although not as good as the Coles' comparisons in supersonic flow (Figure 15). Moderate-to-strong blowing at this Mach number (Figure 28) gives poor agreement

* The Kendall wall pressure profile technique for determining C_f was applied to several of Simpson's runs, but no identifiable trends in the alternate values for C_f were found.

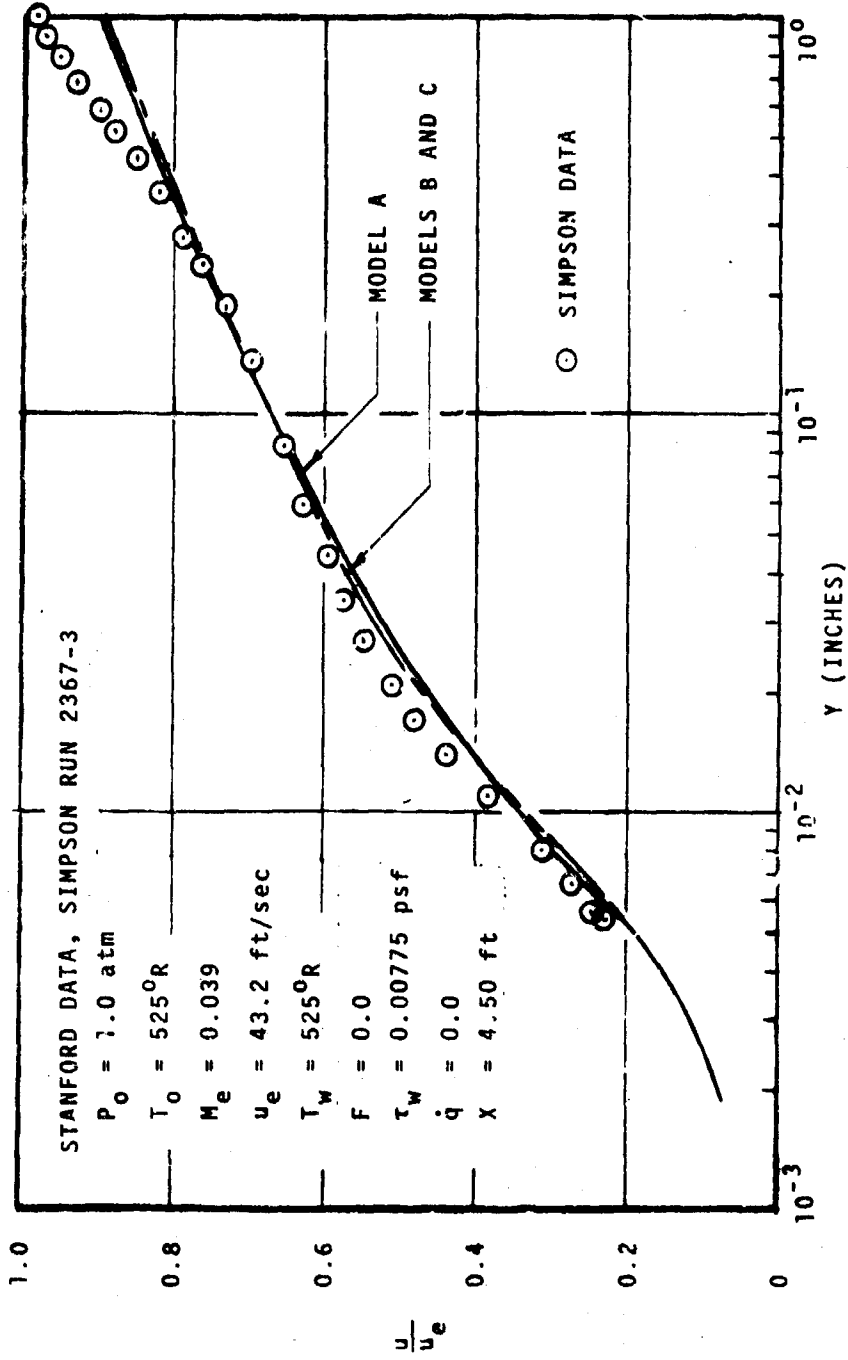


Figure 23. Linear-Log Velocity Ratio Profile
Stanford, Simpson Run 2367-3, Low-Speed Flow Without Blowing

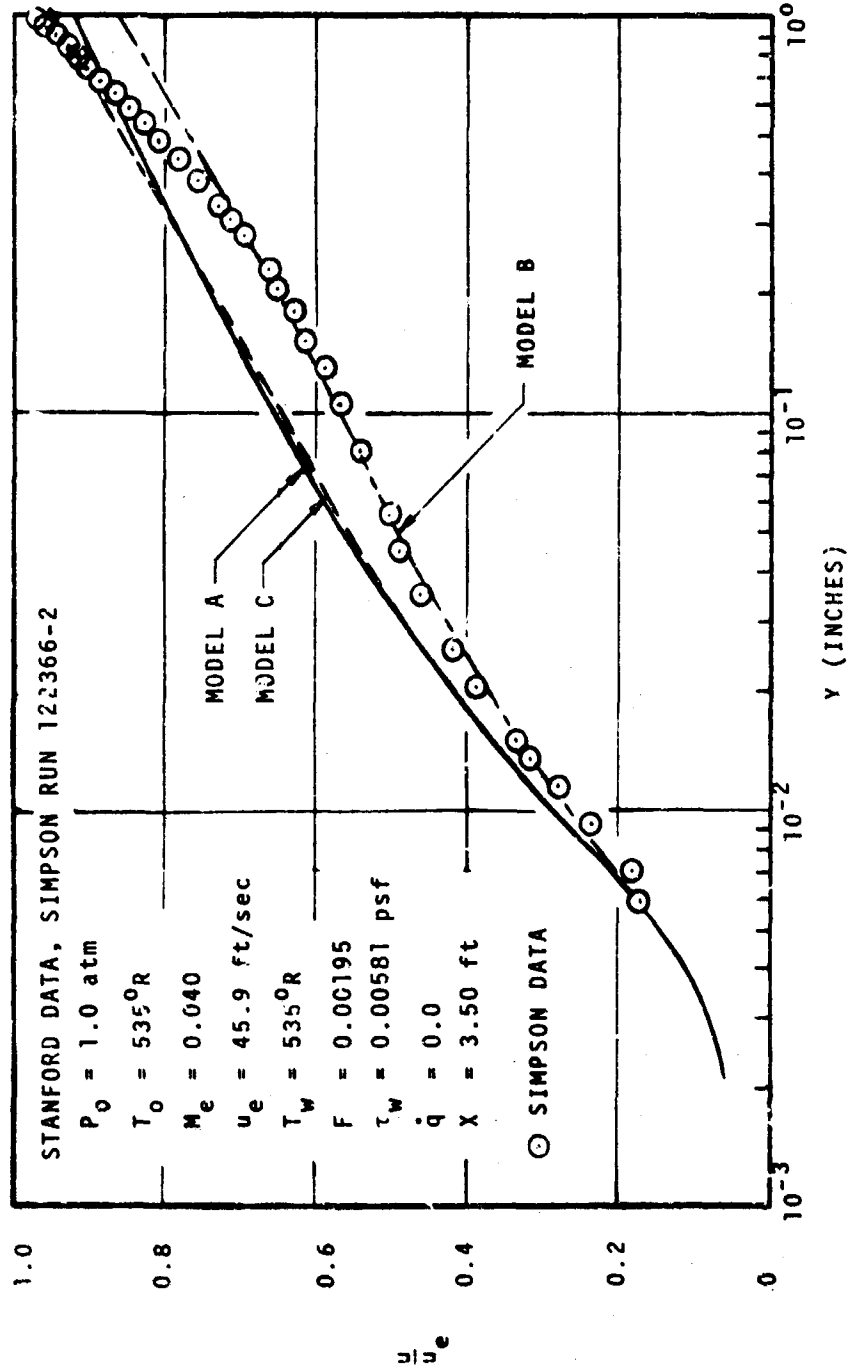


Figure 24. Linear-Log Velocity Ratio Profile
Stanford, Simpson Run 122366-2, Low-Speed Flow With Blowing

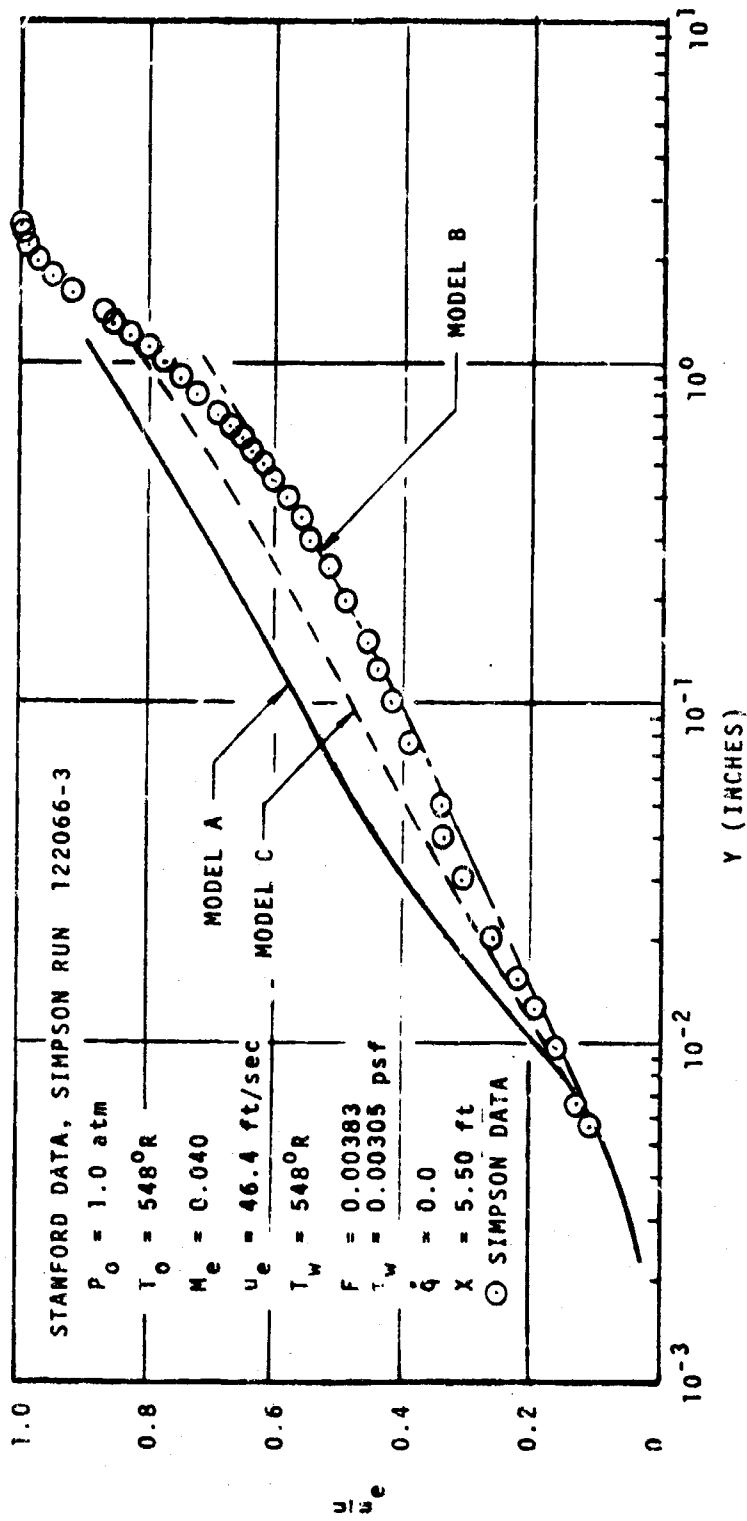


Figure 25. Linear-Log Velocity Ratio Profile
Stanford, Simpson Run 122066-3, Low-Speed Flow With Blowing

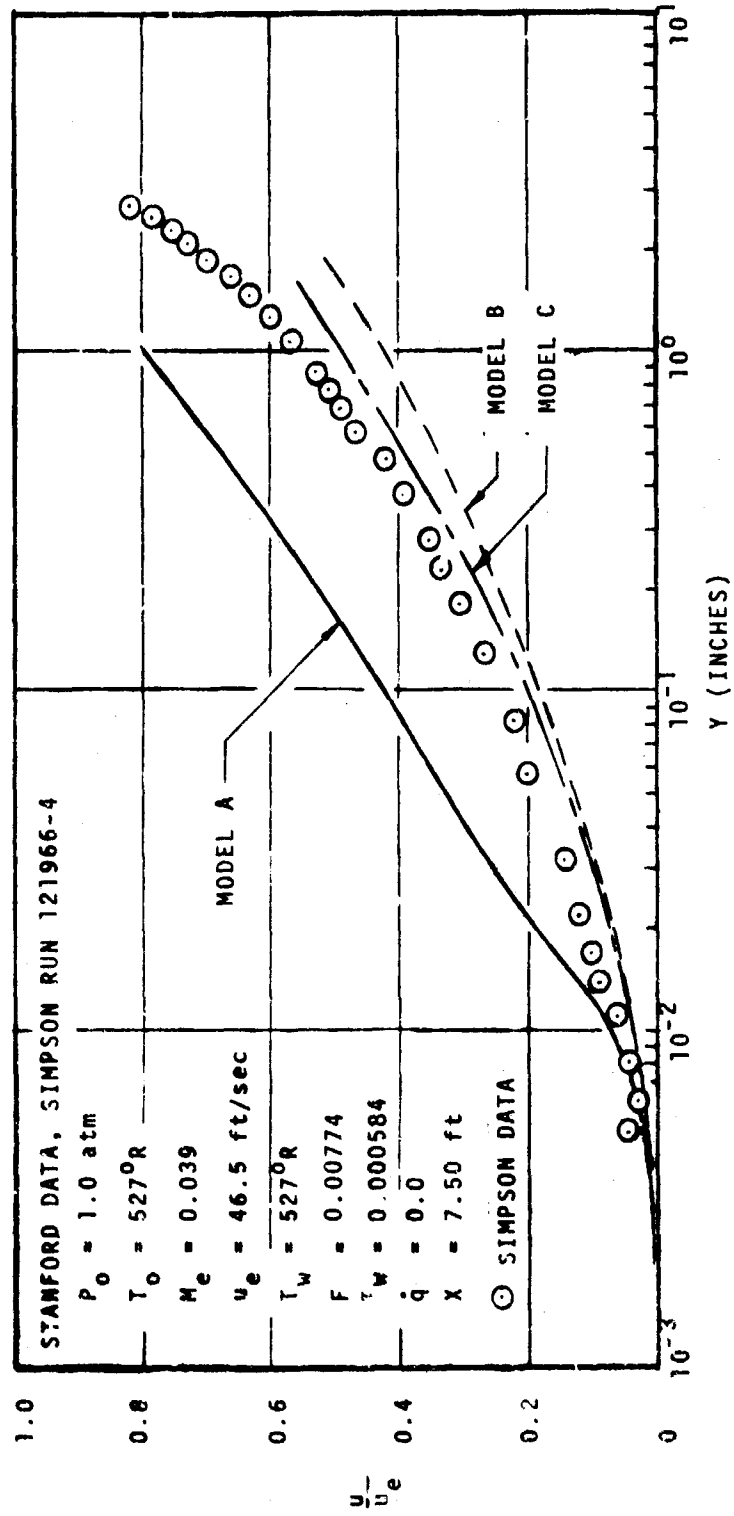


Figure 26. Linear-Log Velocity Ratio Profile
Stanford, Simpson Run 121966-4, Low-Speed Flow With Blowing

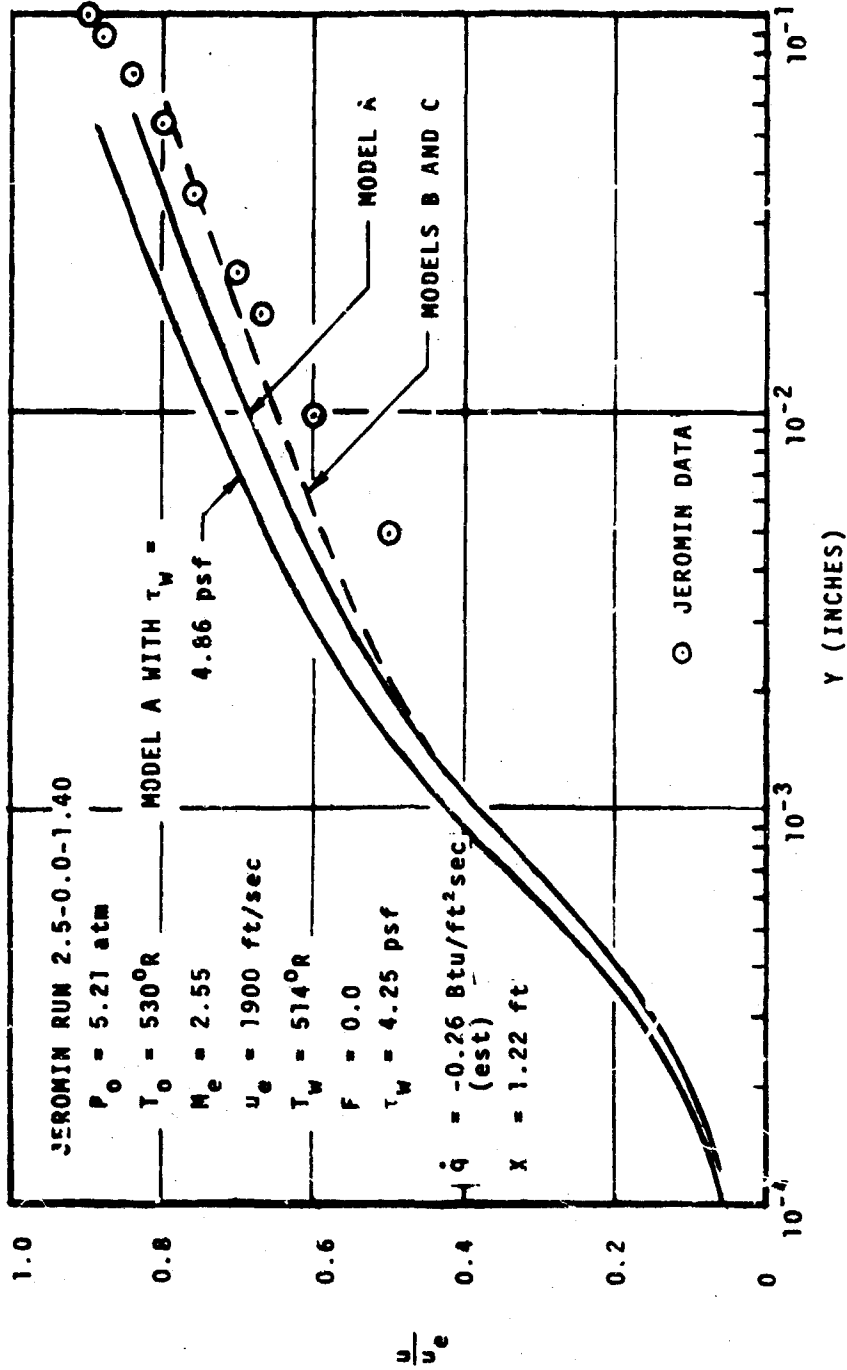


Figure 27. Linear-Log Velocity Ratio Profile
Jeromin Run 2.5-0.0-1.40, Supersonic Flow Without Blowing

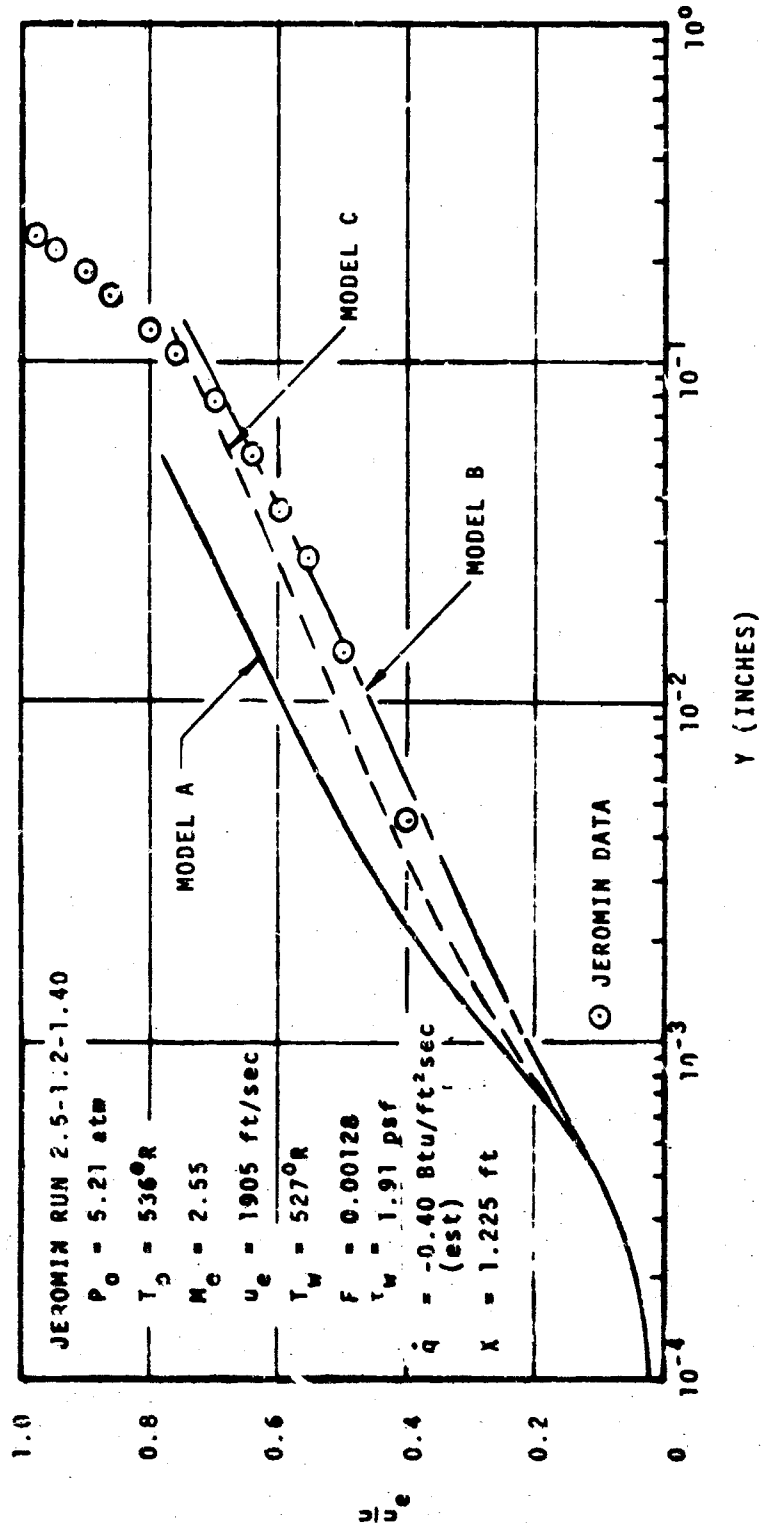


Figure 28. Linear-log Velocity Ratio Profile
 Jeromin Run 2.5-1.2-1.40, Supersonic Flow With Blowing

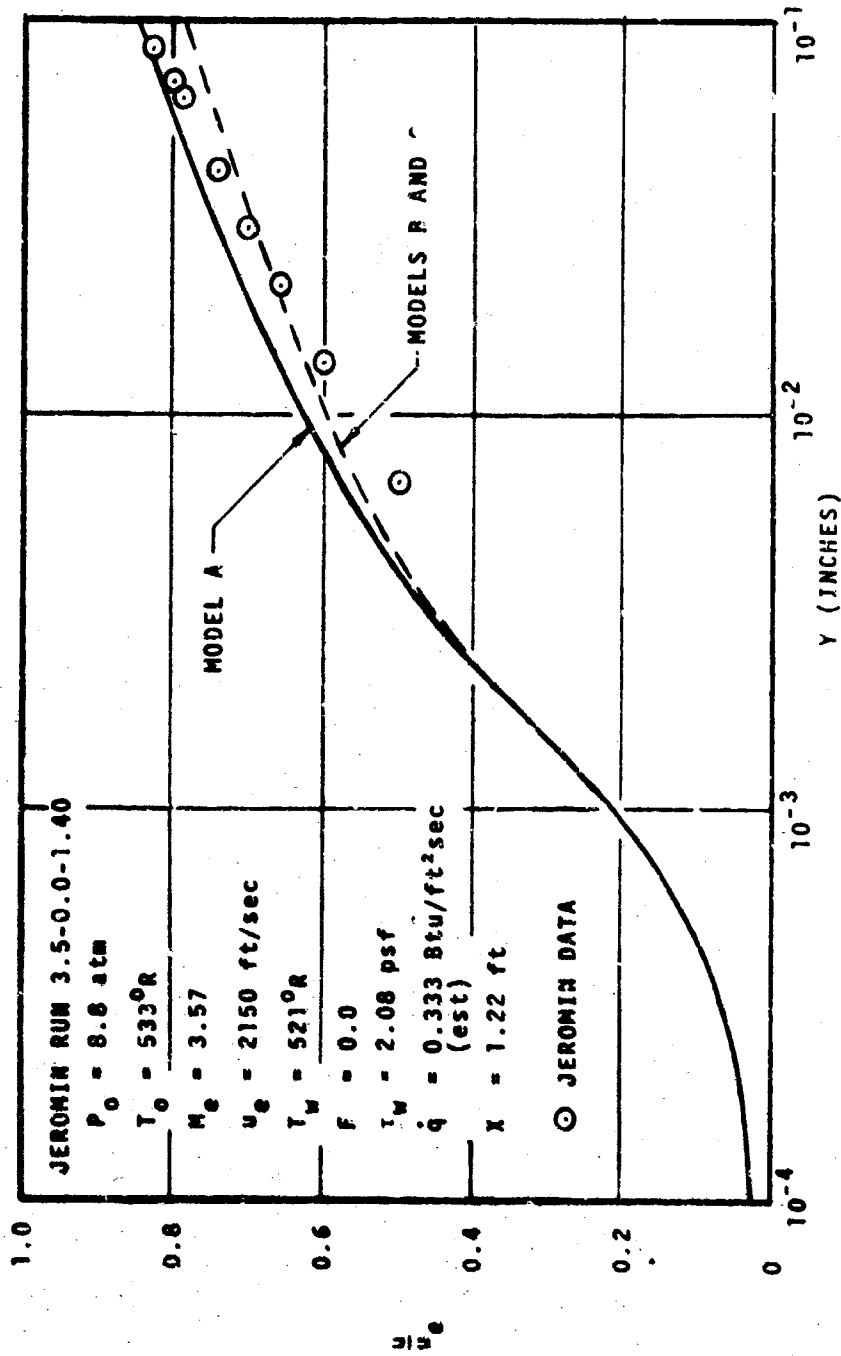


Figure 29. Linear-Log Velocity Ratio Profile
Jeromin Run 3.5-0.0-1.40, Supersonic Flow Without Blowing

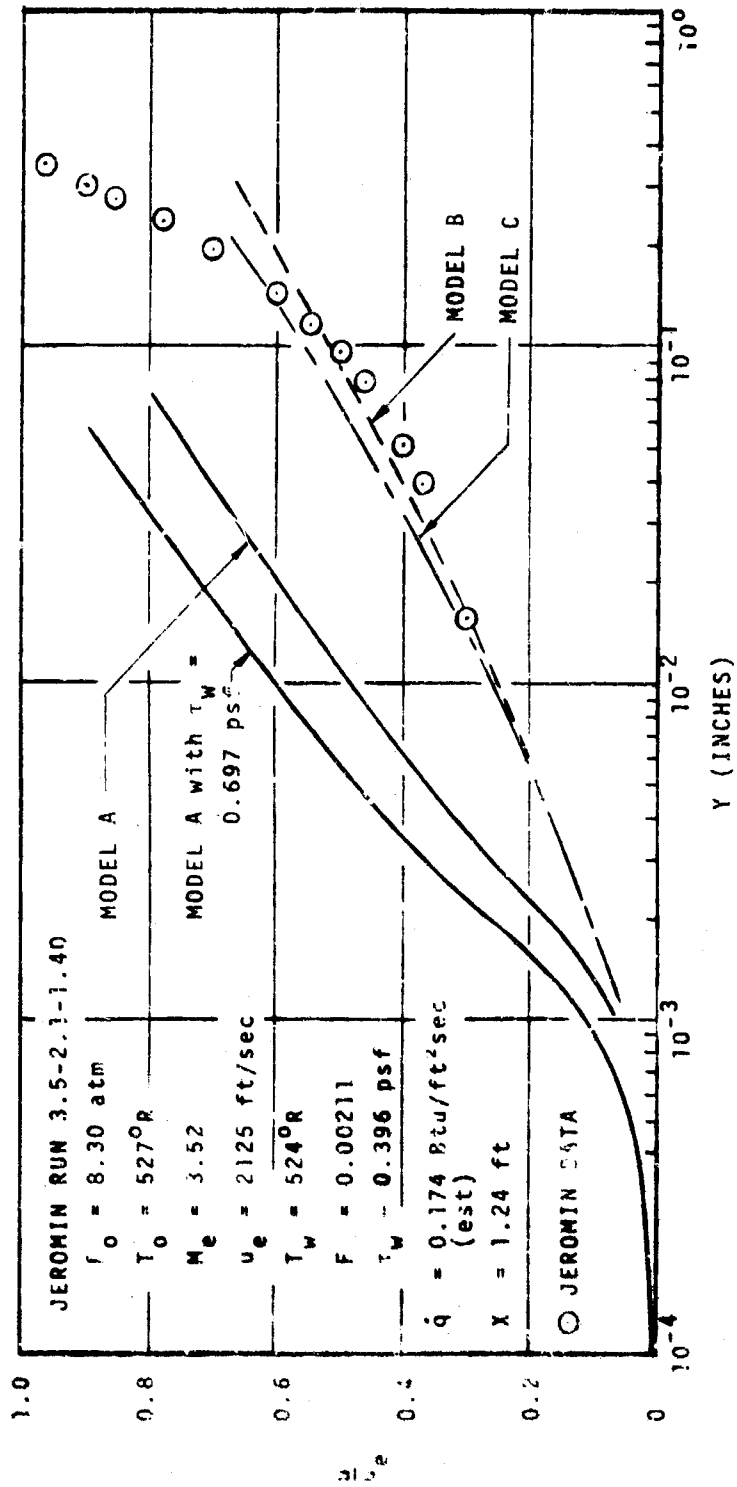


Figure 30. Linear-Log Velocity Ratio Profile
Jeromin Run 3.5-2.1-1.40, Supersonic Flow With Blowing

with Model A and good agreement with Models B and C. Results for a Mach 3.5 flow are shown in Figures 29 and 30. With no blowing, agreement is again fairly good for all theories. A very strong blowing case was selected for the last comparison, Figure 30. As with the Simpson strong blowing case, agreement with Models B and C is good, while Model A gives poor agreement. However, an uncertainty in τ_w of 100 percent for this case is not unlikely.

The preceding comparisons have shown that three leading turbulent models for near wall calculations are in substantial agreement for unblown and small-to-moderately blown flows. At larger blowing rates, with the wall shear level specified, the Aerotherm model is in substantial disagreement with the other two models and with the experimental data of Simpson and of Jeromin. On the other hand, the Aerotherm model is in agreement with the strong blowing experimental data of Kendall, which is not matched by the Cebeci and Bushnell theories. Thus, the choice of a "best" turbulent model is not at all clear.

The question of which model is best cannot actually be answered with these one-dimensional theory comparisons, since the predictions are so completely dependent on the wall shear rate. For blown boundary layers, the wall shear is generally highly uncertain. Thus, insufficient information is available to make a choice between the three models on purely technical comparison grounds. The basis for the choice which was made is presented in the next subsection.

3. THE SELECTED TURBULENT MODEL

a. Wall Law

The previous comparisons have centered on the wall law region, since this area of turbulence modeling is perhaps the most important and includes the widest disagreement between theories. The comparisons of Section III.2 have shown substantial agreement between theories for flows with no blowing or "small" blowing, but wide disagreement for flows with "strong" blowing.

In order to place the "small" blowing and "strong" blowing terminology in perspective, a practical example is presented here. Consider a 10° half-angle cone flying at sea level at Mach 10. Assume an ablating carbon or phenolic carbon surface on the cone, such that the wall temperature is about 6000°R . With all turbulent flow, the "no blowing" drag coefficients at the 1-foot and 5-foot body stations are approximately

$$C_f = 0.00042 \quad @ \quad x = 1 \text{ foot}$$

$$C_f = 0.00033 \quad @ \quad x = 5 \text{ feet.}$$

These values were calculated using the Schultz-Grunow formula corrected for compressibility:

$$C_{f_i} = \frac{0.37}{(\log_{10} Re_x)^{2.58}} \quad (31)$$

$$\frac{C_f}{C_{f_i}} = \left(\frac{\rho^*}{\rho_e}\right)^{0.8} \left(\frac{\mu^*}{\mu_e}\right)^{0.2} \quad (32)$$

$$\frac{h^*}{h_e} = 1 + 0.5 \left(\frac{h_w}{h_e} - 1\right) + (0.22)r \left(\frac{h_s}{h_e} - 1\right) \quad (33)$$

For a carbon nose tip or heat shield, the ablation rate is characterized by plateau-like behavior at a $B'_c = \dot{m}_c / (\rho_e u_e C_H) = 0.2$ (reference 82). Thus, assuming $C_H = C_f/2$,

$$\frac{(\rho v)_w}{(\rho u)_e} = 0.2 \left(\frac{C_f}{2}\right) \quad (34)$$

which results in a very small blowing rate. A similar behavior is obtained with phenolic carbon at a B'_c of approximately 0.6. Thus, the blowing rates for typical heat shield materials are quite small under ordinary flight conditions.

In light of the fact that there are only small differences between models at zero or small blowing, and that small blowing conditions are typical for flight cases, the logical choice of a wall region turbulent model for BLIMP comparisons was the reference 1 model. The reference 1 model is already incorporated in the BLIMP code, which minimized the amount of programming time required. The constants within this model were held at the incompressible flow values of

$$k_m = 0.44 \quad (35)$$

$$y_a^+ = 11.823 \quad (36)$$

The effects of changes in these constants will be demonstrated in Section IV.

b. Wake Law

There has been very little discussion in the literature about the advantages or disadvantages of a Clauser type wake law, as used in Models A and C compared to a boundary layer thickness dependent mixing length law, as used in Model B. All that seems to be required in the outer portions of equilibrium type flows is that a roughly correct eddy viscosity number be arrived at. This is borne out by the BLIMP results shown in Figure 31, where the constant in the expression

$$\epsilon_m = (\text{const.}) u_e \delta_i^* \quad (37)$$

was set at both 0.016 and 0.018, all other features of the reference 1 model remaining the same. This 12.5 percent change in the outer boundary layer turbulence coefficient over a distance of 2.75 feet in running length produced virtually no change in the velocity profile. The Clauser type formulation in terms of the kinematic or velocity displacement thickness δ_i^* , seems to be adequate for equilibrium compressible flows, therefore the reference 1 wake model was adopted for the final data comparisons using the 0.018 constant.

c. Turbulent Prandtl and Schmidt Number

The turbulent Prandtl and Schmidt numbers relate the turbulent transport of energy and chemical species to the turbulent transport of momentum. While there is only a weak basis for doing so, it is common practice to assume a constant ratio between the transport coefficients. Experimental data on actual turbulent Prandtl numbers and their variations through the boundary layer are becoming available (references 83, 84, and 85). The evidence indicates that Pr_t should vary from ~ 0.5 in the outer portions of the boundary layer, to near unity at $y/\delta = 0.1$, to ~ 1.5 or 2.0 near the laminar sublayer. Results are primarily for air boundary layers. While these results are certainly relevant to the BLIMP turbulent model, the development and incorporation of a Pr_t model which has reasonable validity for multicomponent chemically reacting flows was beyond the scope of the current effort. Thus, a constant Pr_t model was used for the current studies. A similar situation exists for turbulent Schmidt number, although fewer data are available (e.g., reference 86).

Numerical studies with the BLIMP code and the reference 1 turbulent model have shown that a turbulent Prandtl number of 0.9 results in the generally accepted value of 0.88 for the flat plate recovery factor in air. These results, shown in Figure 32, were generated with BLIMP by demanding zero heat flux to the wall as a solution boundary condition. Thus, a constant value of $Pr_t = 0.9$ was used for boundary layer predictions with the current turbulent model.

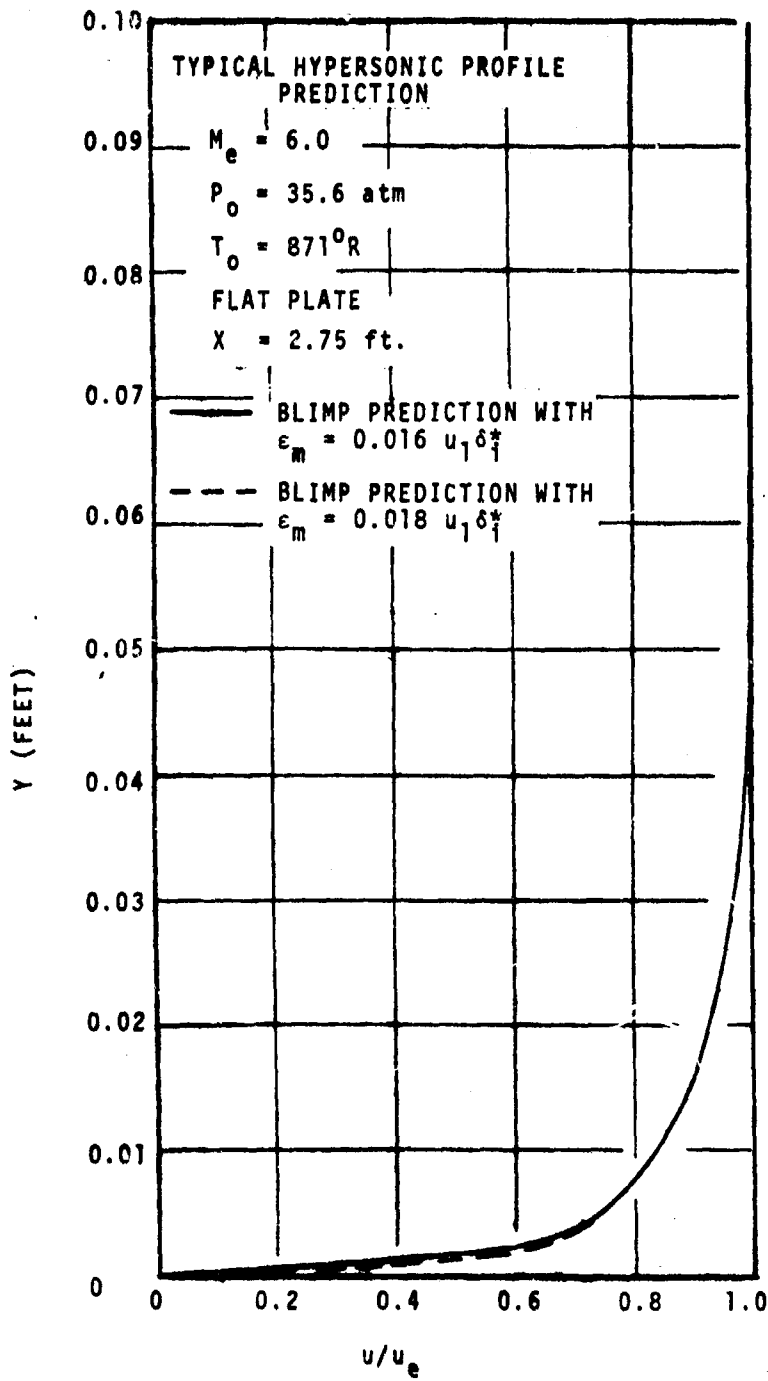


Figure 31. Effect of Constant in Wake Region Eddy Viscosity Expression

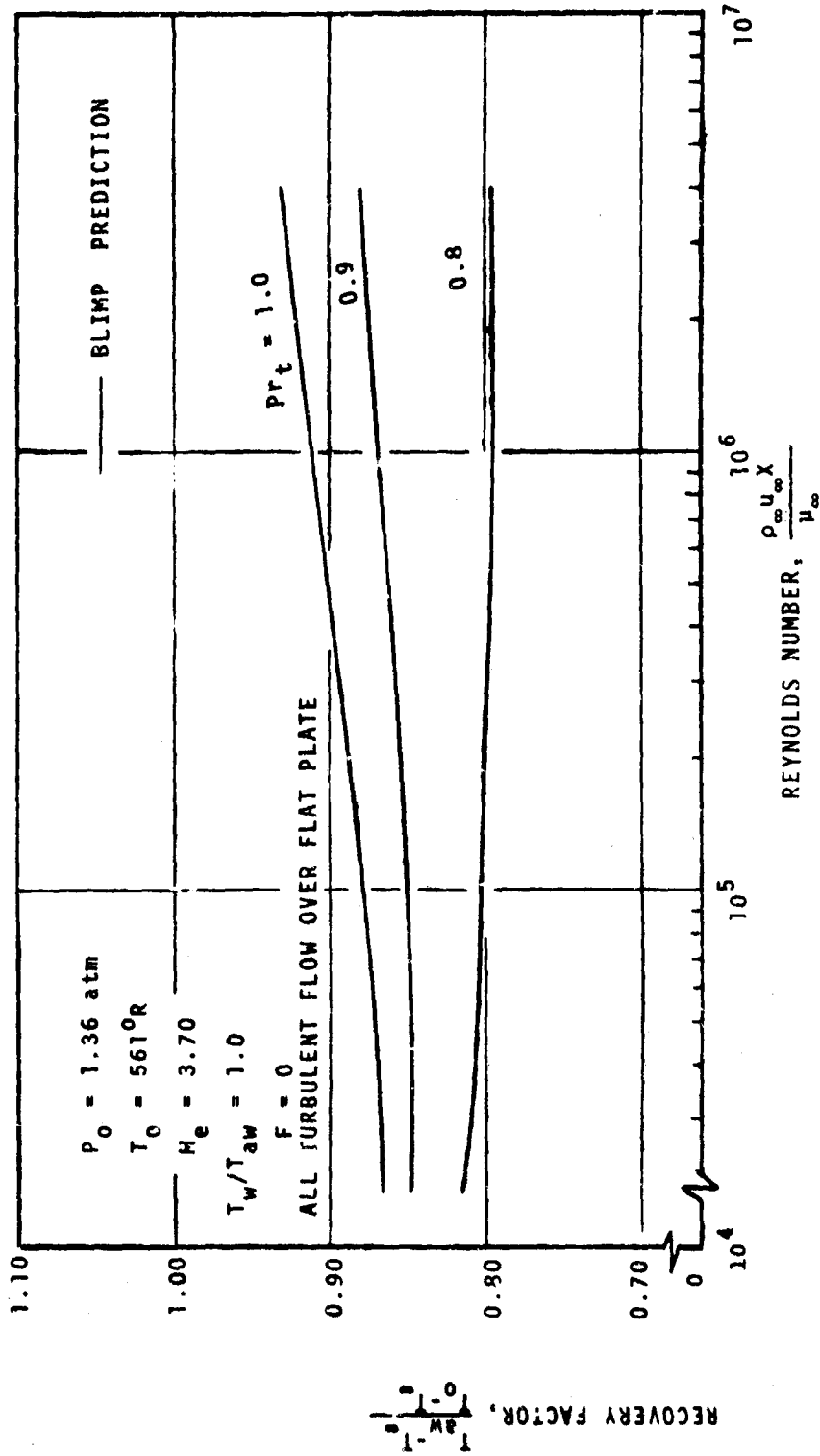


Figure 32. Effect of Turbulent Prandtl Number on Recovery Factor at $M = 3.7$

SECTION IV
PREDICTIONS AND COMPARISONS WITH DATA

1. PRESENTATION OF COMPARISONS

The comparisons between BLIMP predictions and measured data for the 17 separate data sets listed in Table V are presented in this section. The results are listed in the order of Table V. They consist of (1) a brief description of the BLIMP input* as related to the data and (2) graphical results, where applicable, in the form of linear Mach number ratio, total temperature ratio, and velocity ratio profiles as functions of y , velocity ratio profiles as functions of y in linear-log coordinates, and linear plots of momentum thickness Reynolds number, Re_θ , and skin friction coefficient, $C_f/2$, versus streamwise dimension, x . Symbolism has been standardized for all plots. Measured data are represented by circled points; where more than one set exists on a single plot, symbols are noted on that plot. BLIMP predictions started far upstream of the region of interest using an approximate starting profile (a "zero start") are presented as solid curves; predictions started at the first data station using an actual data profile (a "data start") are presented as dashed curves. Any deviations, modifications, or additions to this format are noted on the figure. In general, only one linear-log velocity plot is shown, usually the next to last of those plotted in linear coordinates.

a. Coles' Comparisons

(1) Comments on BLIMP Input

Coles' data consist of a single profile with C_f measurements at three other axial stations. Freestream and wall conditions were known to be effectively constant, thus BLIMP was started from the leading edge of the flat plate. The use of a fence trip, however, introduces an unknown initial thickness which is equivalent to the virtual origin being upstream of the leading edge. Since the data start option is not applicable with only a single station of profile data available, the only means of accounting for the trip effect was to match the profiles. The momentum thickness was selected as the appropriate

* A more complete discussion of computer code setup for these problems, including zero starts and data starts, is included in the appendix.

matching parameter. A BLIMP profile at the desired value of θ was obtained by first running the program with sufficient stations to bracket the data value, then rerunning the program including the interpolated value of x as one of the output streamwise stations (see Figure 39). Thus the profile comparisons of Figures 33-38 compare data taken at $x = 1.69$ feet to predictions at 2.46 and 2.18 feet for $M = 2.5$ and 3.6, respectively.

(2) Comments on Results

Mach number and velocity ratio comparisons in Figures 33-38 for both runs are relatively good. Temperature profiles are not included since temperatures were not measured. In general, the prediction indicates higher values of Mach number and velocity in the mid-ranges of the profile and lower values beyond $u/u_e = 0.8$ to 0.9. There is a slight indication of an inflection point in the Mach number data profile which the prediction does not seem to include. Maximum absolute differences in ratio are 0.04 to 0.05. The plot of Re_θ in Figure 39 is shown only to indicate the matching procedure. Finally the $C_f/2$ plot in Figure 40 shows the BLIMP predictions and data both referenced from the beginning of the plate. $C_f/2$ predictions for the θ -matched stations are 7.5 and 8.5 percent lower than the data for the Mach 2.5 and 3.6 cases, respectively. It should be noted, however, that improvements in the nodal distribution to be discussed in Section IV.2.b account for most or all of this error. Nodal spacing was discovered to be particularly important for θ -matched cases, in that a small improvement in $\frac{d\theta}{dx}$ brings about a new match point, which in turn gives a significantly different C_f .

b. NOL Comparisons

NOL data sets are comprised of profiles measured at four stations (Lee) and five stations (Brott) with skin friction measurements several inches upstream of each profile station. Measurements were taken over a streamwise interval from approximately 4 to 7.5 feet measured from the nozzle throat. Each profile was measured during a separate test run, thus stagnation conditions varied slightly (less than one percent) from profile to profile. Comparison to a single BLIMP run, which is based on constant stagnation conditions, is subject to some small error for this reason. In general, the BLIMP input of freestream conditions was based on the measured Mach number and average stagnation conditions for the four or five reported profiles. Wall temperatures were taken as the reported values. As a consequence of this approach, the pressure gradients at a given test station are slightly different for the prediction than actually existed. Axial pressure gradients are not discussed by

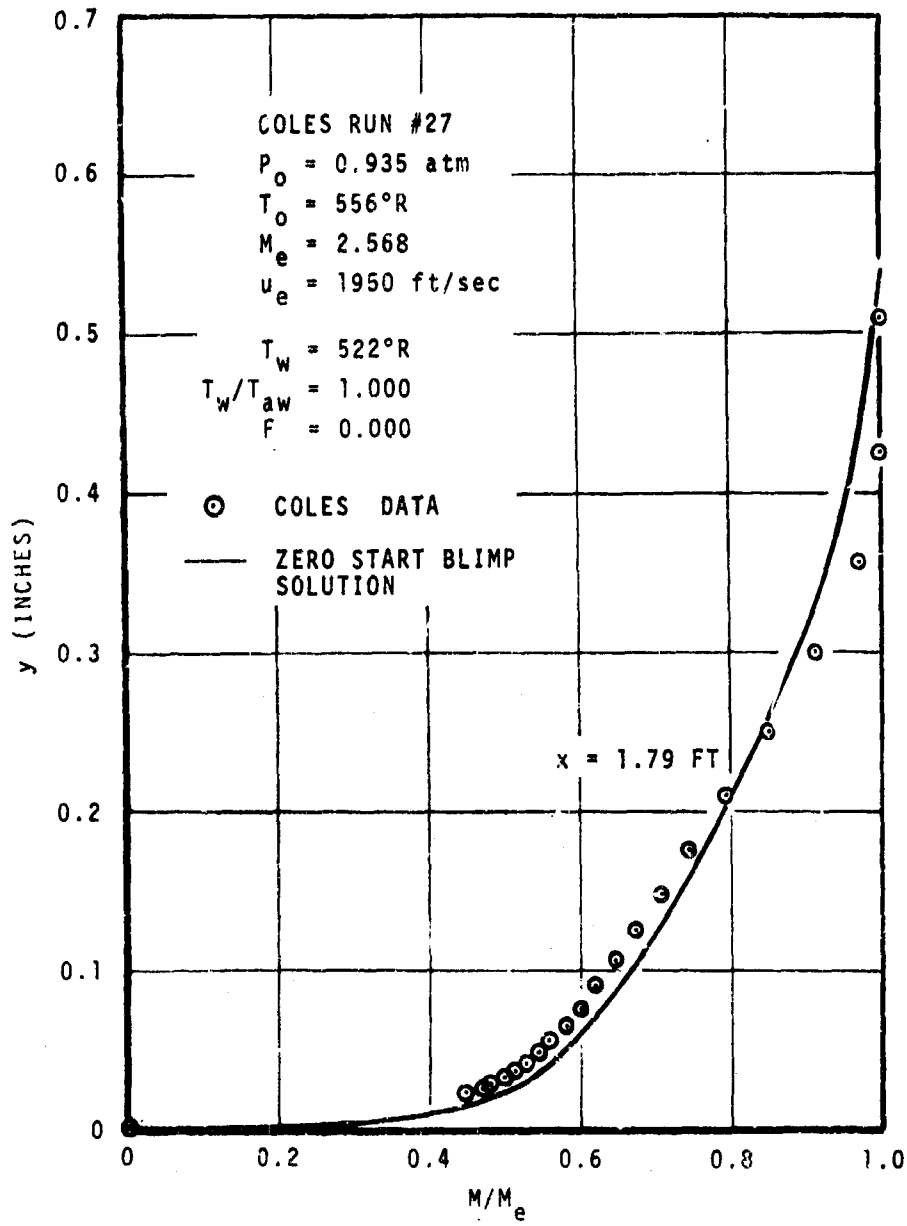


Figure 33. Mach Number Ratio Profile
 Coles Run #27, Supersonic, Zero Pressure Gradient Flow

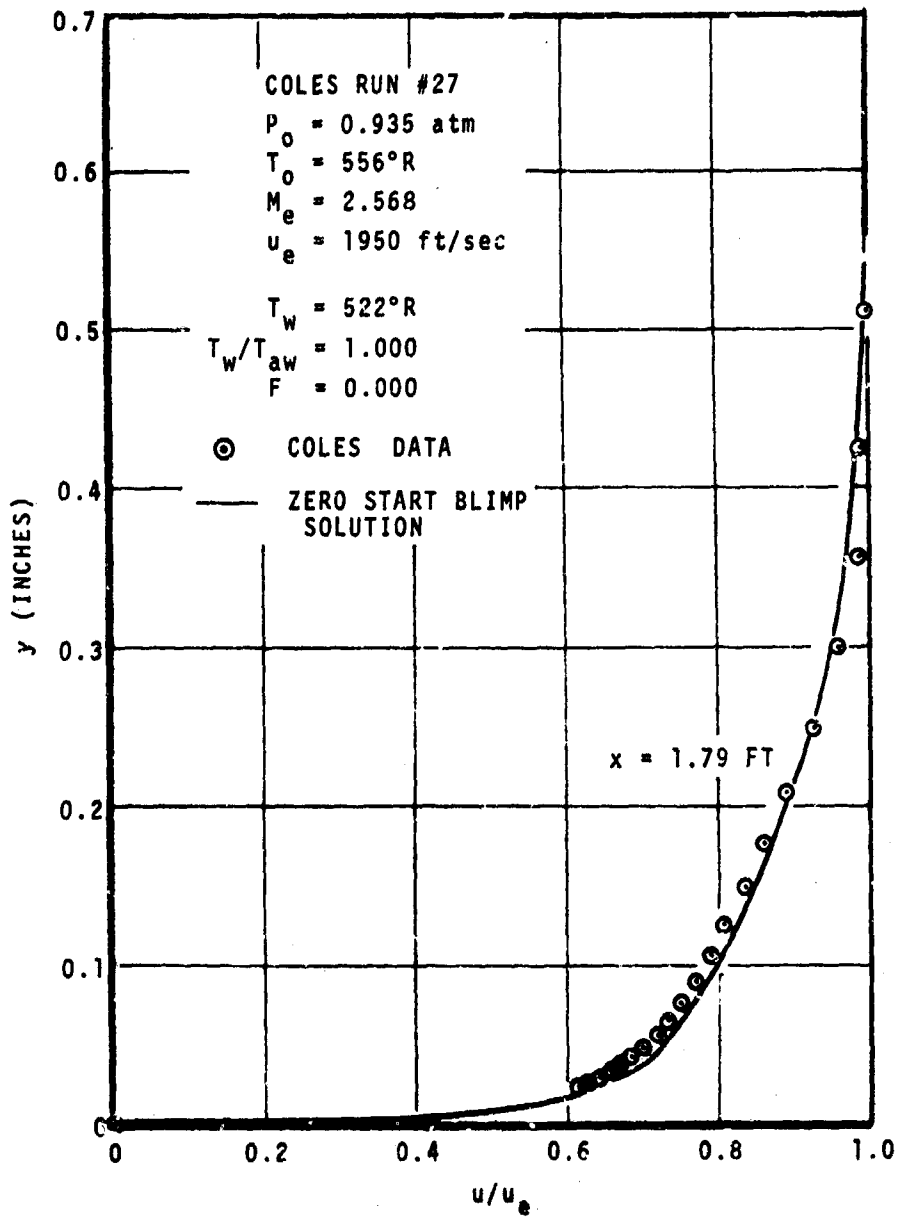


Figure 34. Velocity Ratio Profile
 Coles Run #27, Supersonic, Zero Pressure Gradient Flow

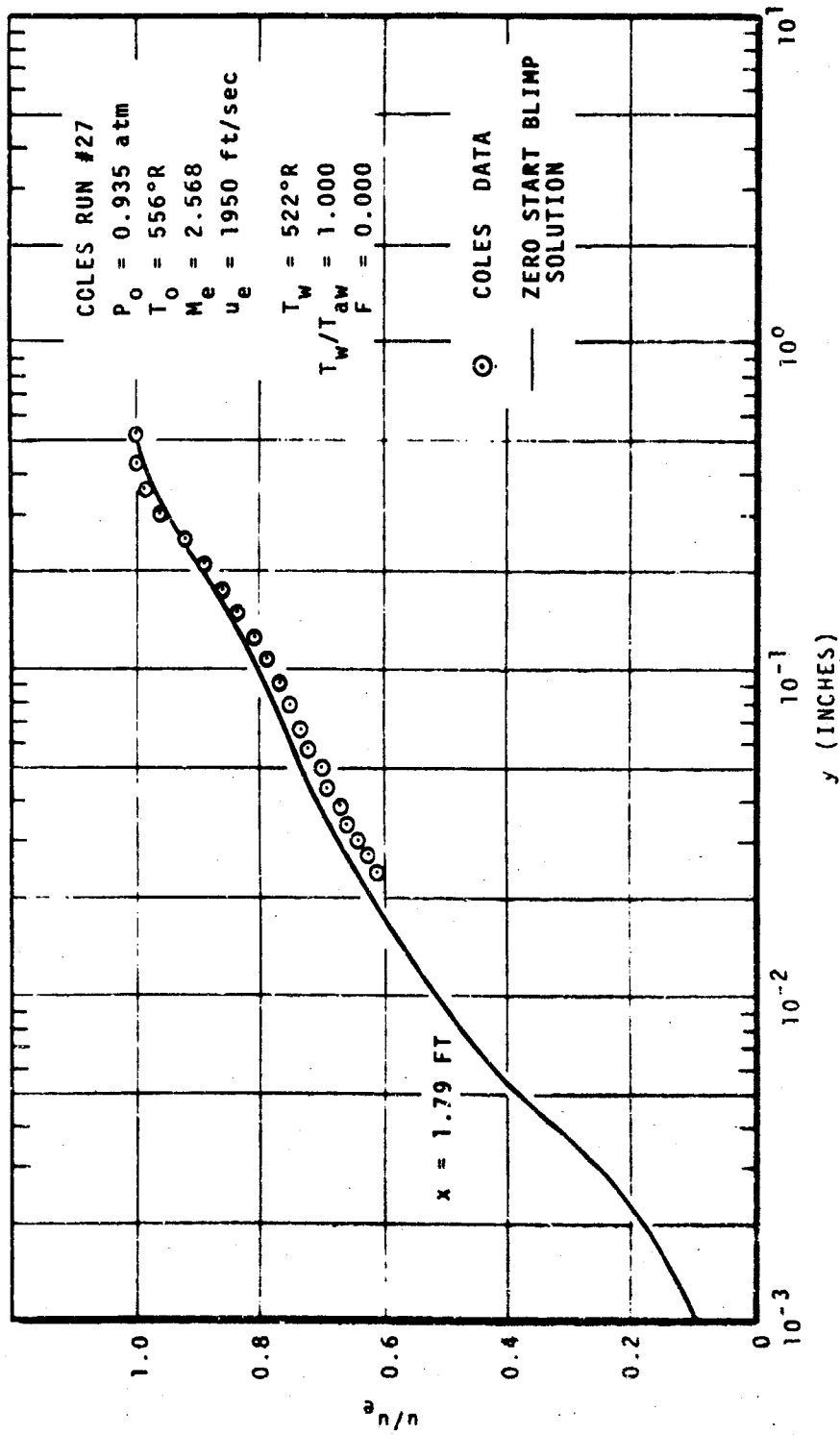


Figure 35. Linear-Log Velocity Ratio Profile
 Coles Run #27, Supersonic, Zero Pressure Gradient Flow

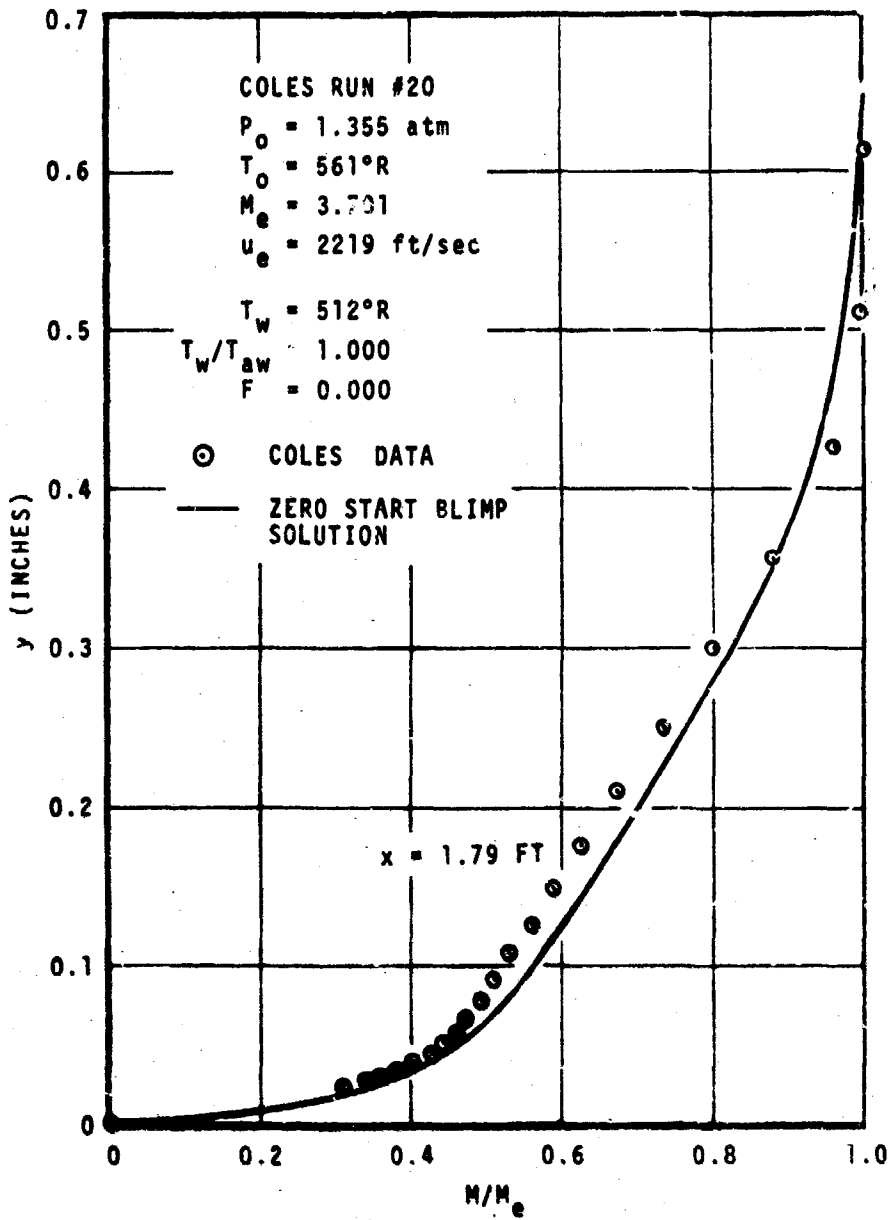


Figure 36. Mach Number Ratio Profile
 Coles Run #20, Supersonic, Zero Pressure Gradient Flow

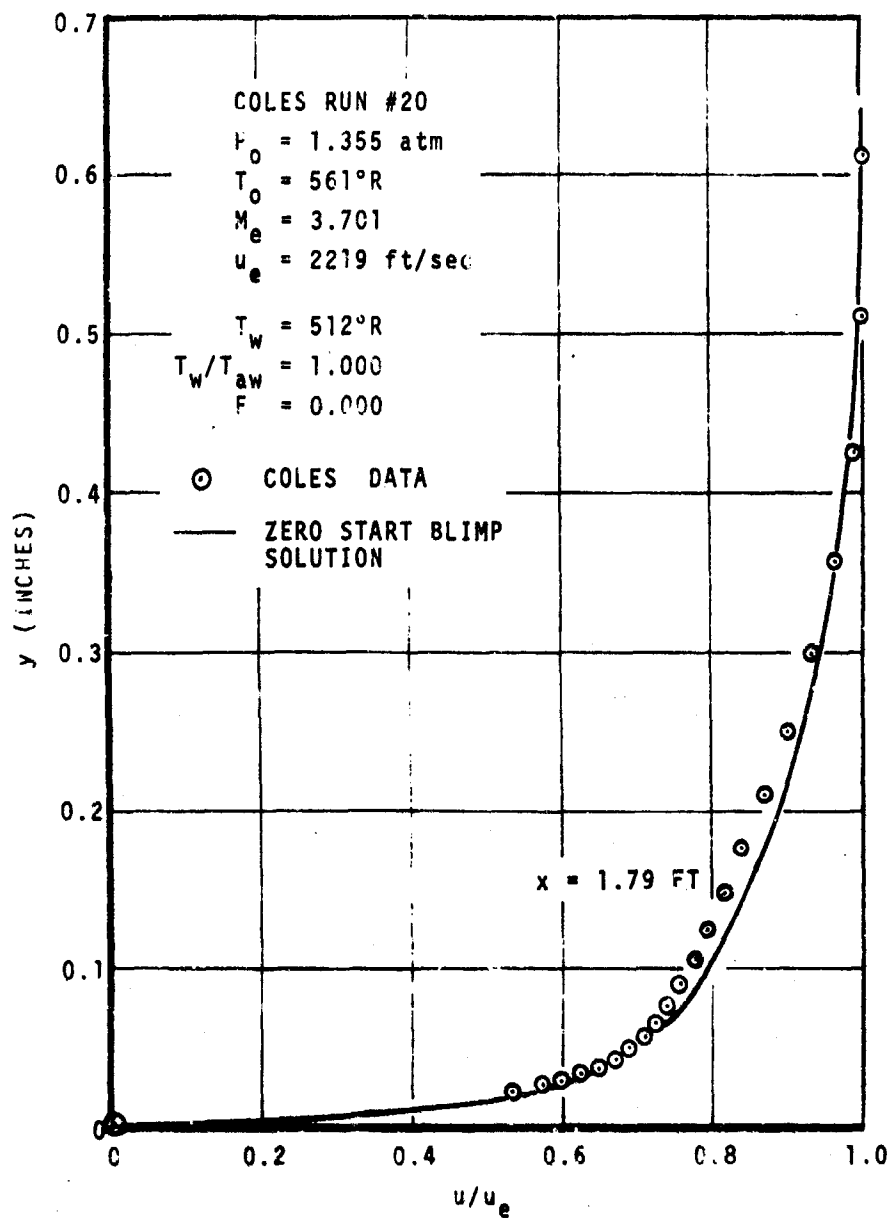


Figure 37. Velocity Ratio Profile
 Coles Run #20, Supersonic, Zero Pressure Gradient Flow

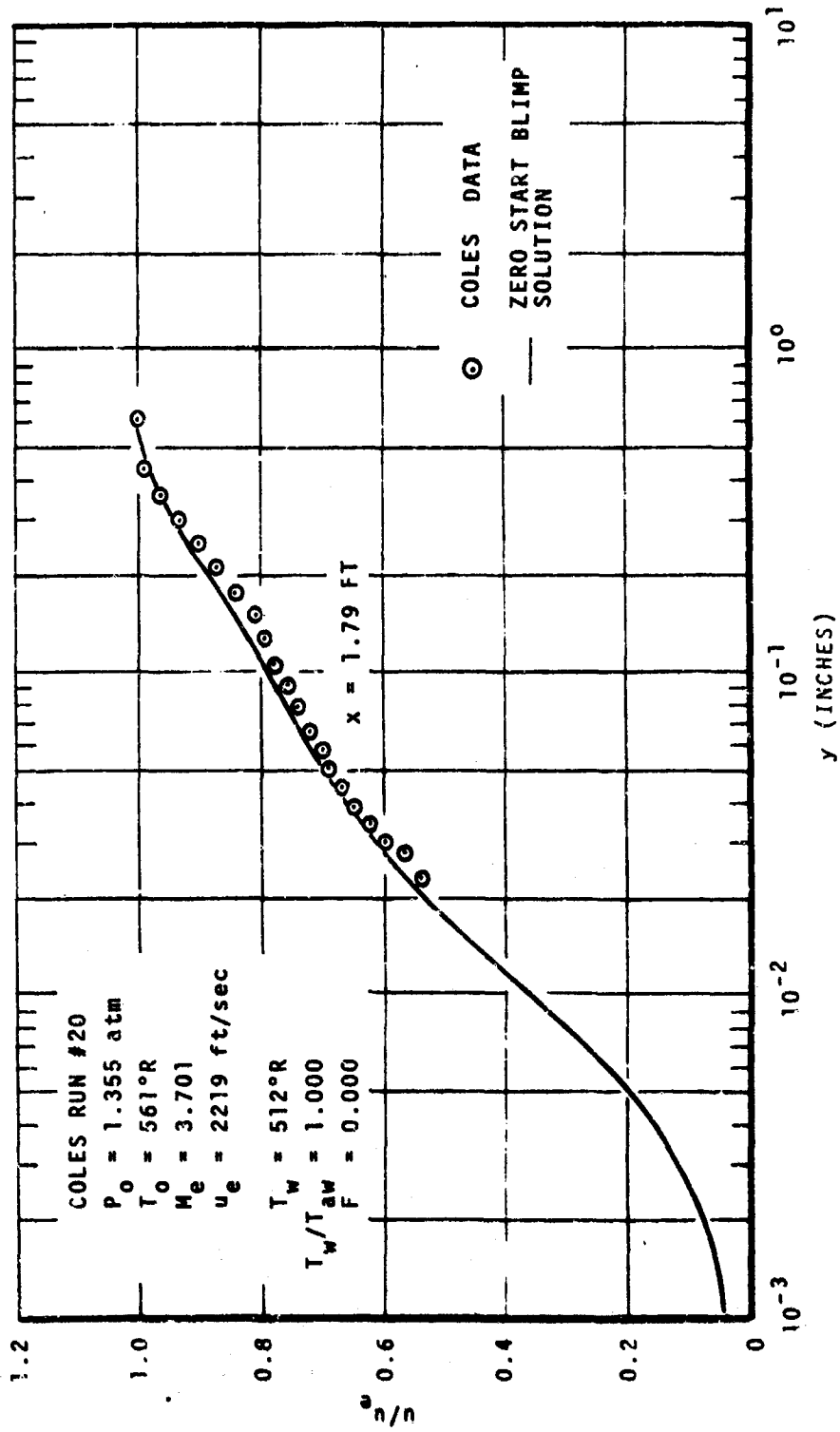


Figure 38. Linear-Log Velocity Ratio Profile
 Coles Run #20, Supersonic, Zero Pressure Gradient Flow

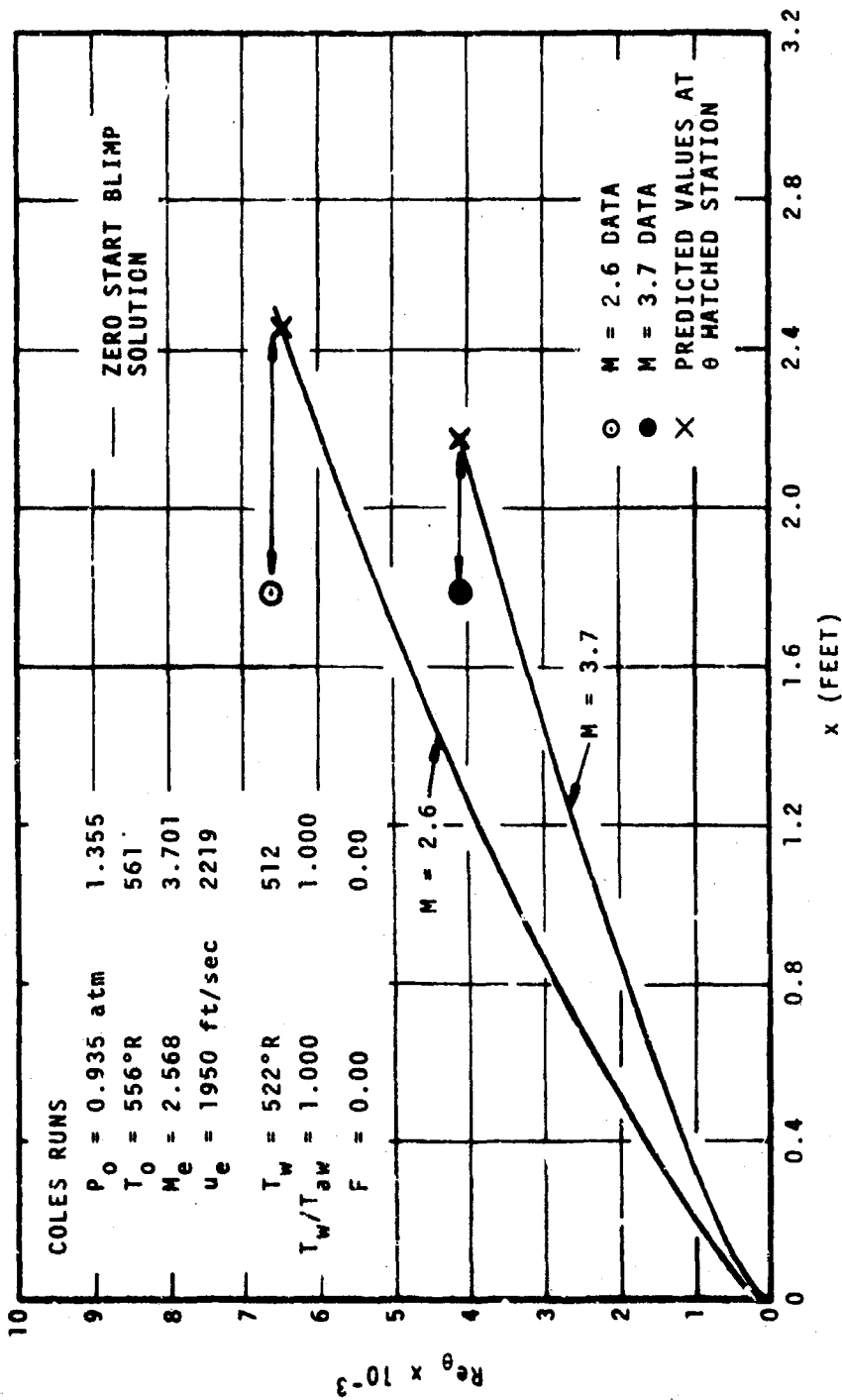


Figure 39. Momentum Thickness Reynolds Number vs Streamwise Location
 Coles Runs at Mach 2.6 and 3.7

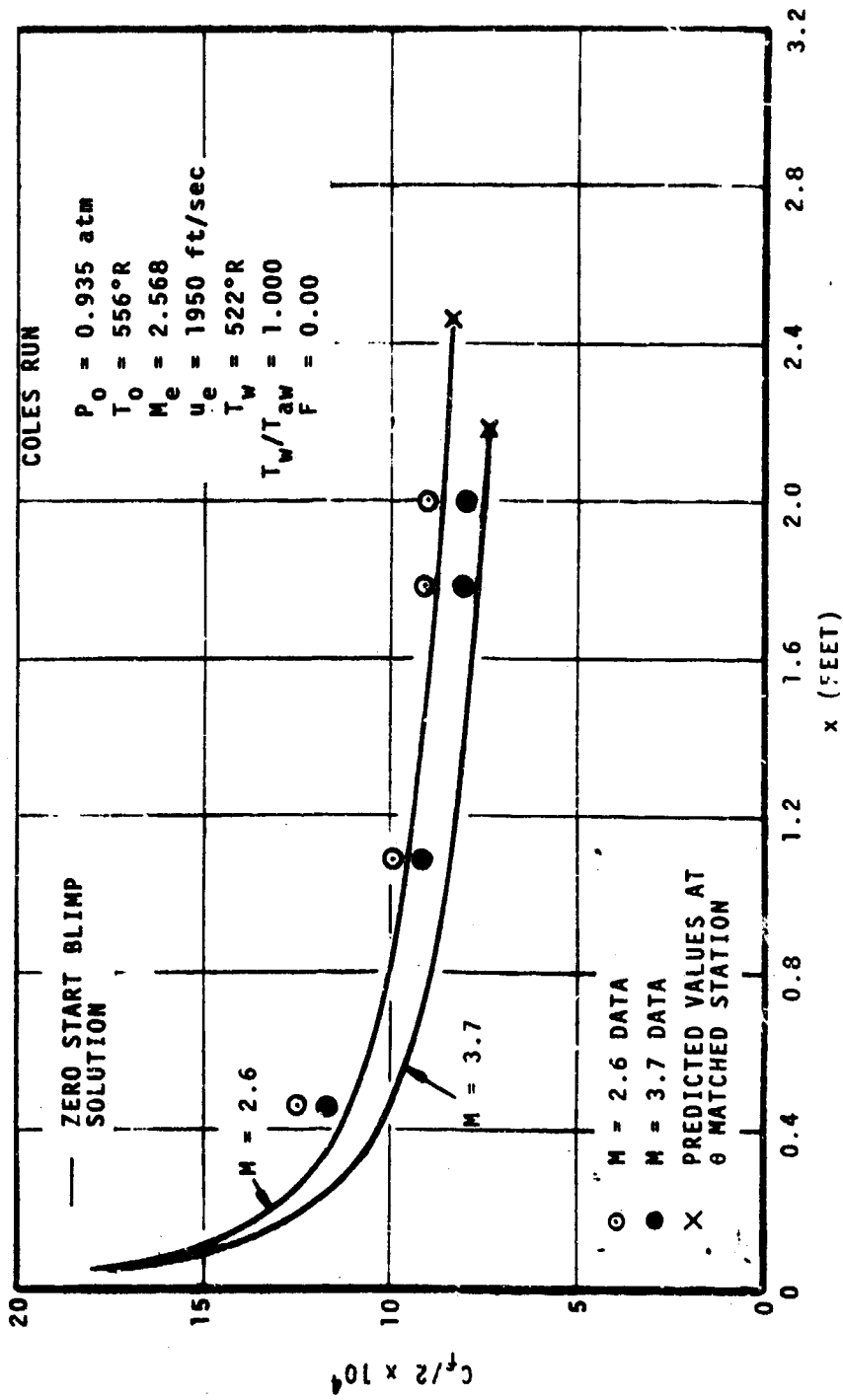


Figure 40. Skin Friction Coefficient vs Streamwise Location
Coles Runs at Mach 2.6 and 3.7

Lee, et al., except to note that the 48-inch station was located in the acceleration region, 55 inches being the beginning of the constant freestream flow where Mach number variations are constant within ± 0.75 percent. There is no indication of local gradient conditions at either the skin friction gages or profile station. Brott does list such data; however, there is currently no way to model the pressure gradients directly in the BLIMP code. Pressure gradients at the prediction stations are determined by a quadratic curve fit of the input pressure distribution which depends, of course, on the interval between stations as well as the pressures.

(1) Data of Lee, et al.

(a) Comments on BLIMP Input

To show the effects of pressure gradients, the 5 atmosphere run of Lee was set up as described above while constant freestream conditions equal to the average of those reported at the four stations were used for the 10 atmosphere run. Both cases were run with the data start option since conditions upstream of the first profile station were not reported.* Several "approximate" zero start runs were attempted for the 10 atmosphere run, one using the nozzle profile reported by Brott and the other assuming constant conditions throughout. These results bracketed the measured values of θ only in a gross sense (see Figure 51). However, as shown in Figure 52, these approximate zero start runs do define limits on the value of $C_f/2$ within which a prediction based on the actual upstream conditions can be expected to fall.

(b) Comments on Results

Figures 41-46 and 47-51 show the results for the 5 and 10 atmosphere runs, respectively. In both cases, the predicted and measured profiles for Mach number, velocity and temperature diverge from the data as the flow proceeds down the plate (after the matched data start beginning). The predictions exceed the data in the mid-region of the Mach number and velocity profiles by up to 30 percent. In Figures 41 and 47 the Mach number data profiles appear to undergo a significant change in shape that is not reflected by the predictions.

In the Re_θ plots of Figures 45 and 51, the predicted growth, starting from the matched value at the first station, is less than that measured. This is consistent with the profile plots which show progressively "thicker"

* Private communication with NOL personnel indicated these data were not measured.

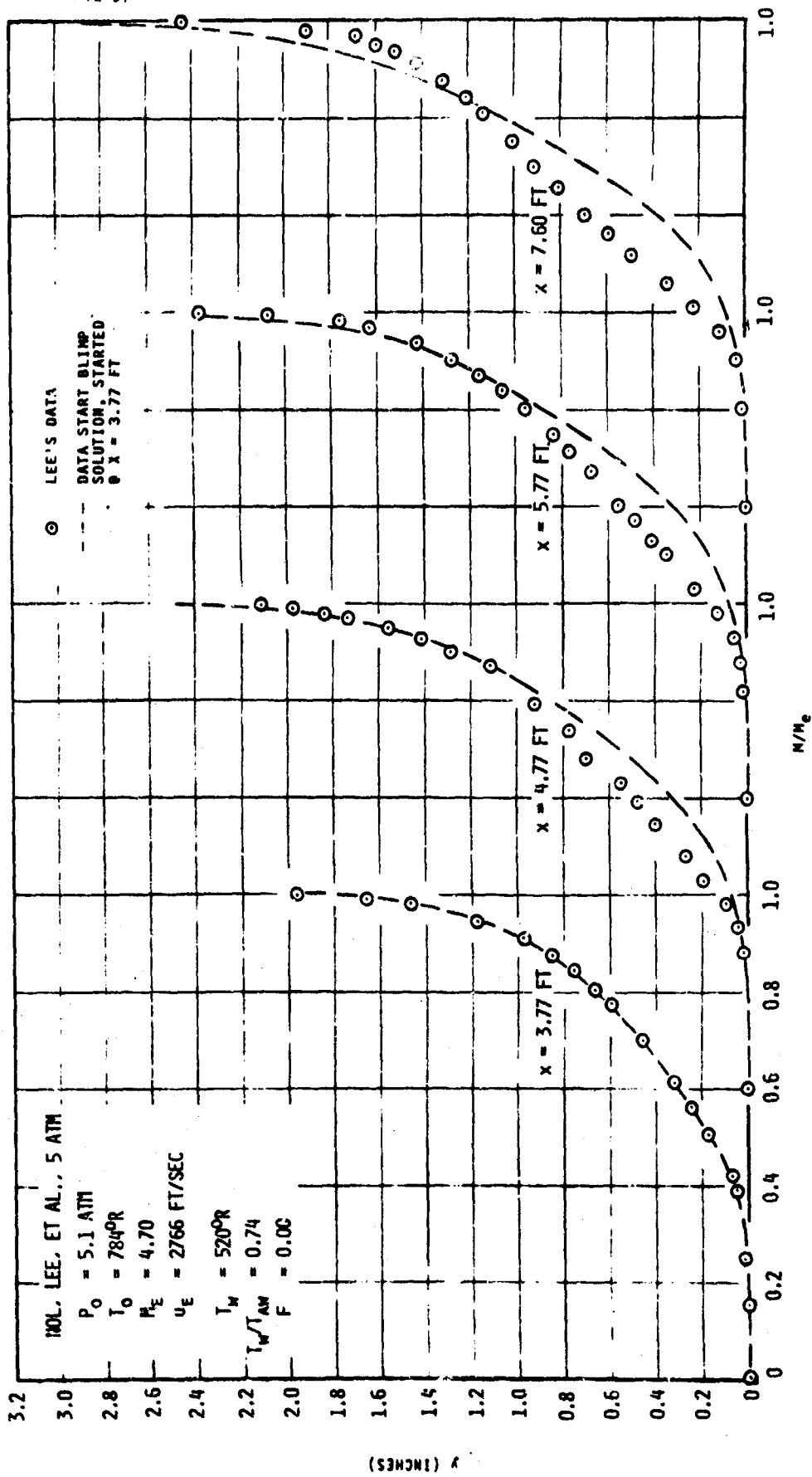


FIGURE 41. MACH NUMBER RATIO PROFILES
 INCL. LEE, ET AL., 5 ATM, HYPERSONIC, ZERO PRESSURE GRADIENT FLOW

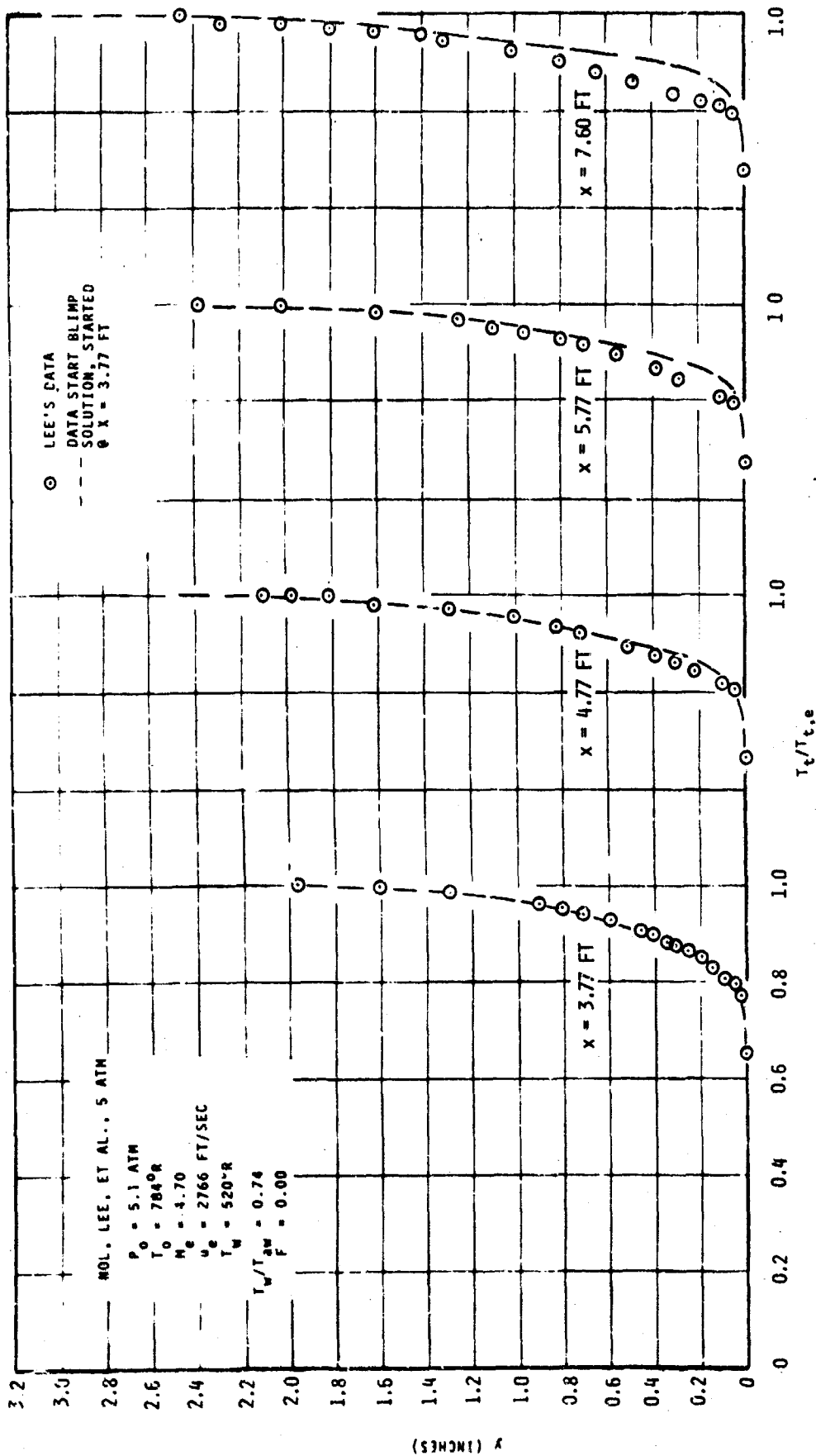


FIGURE 42. TOTAL TEMPERATURE RATIO PROFILES
 MOI. ET AL., 5 ATM, HYPERSONIC, ZERO PRESSURE GRADIENT FLOW

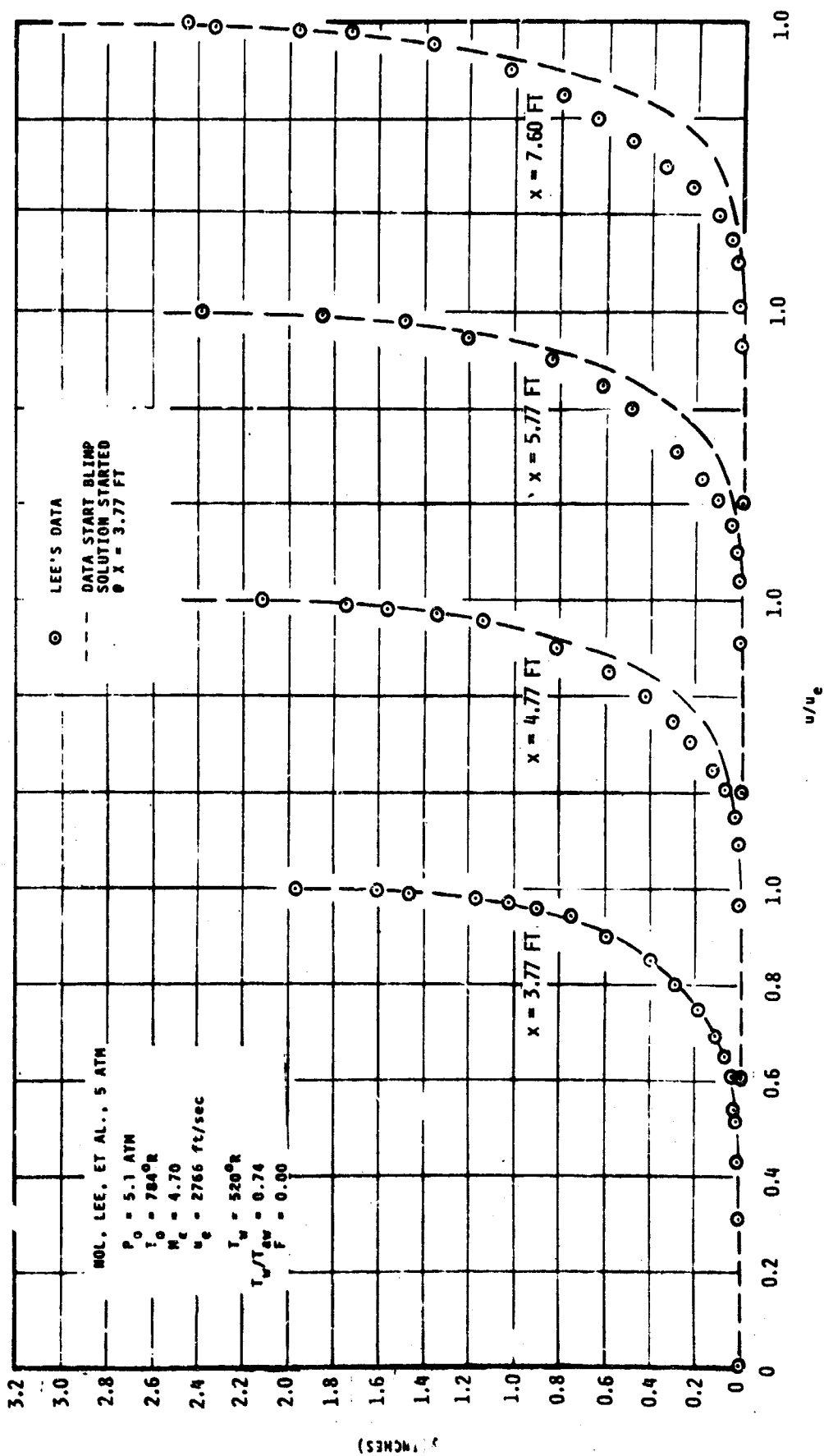


FIGURE 43. VELOCITY RATIO PROFILES
 MOL. LEE, ET AL., 5 ATM, HYPERSONIC, ZERO PRESSURE GRADIENT FLOW

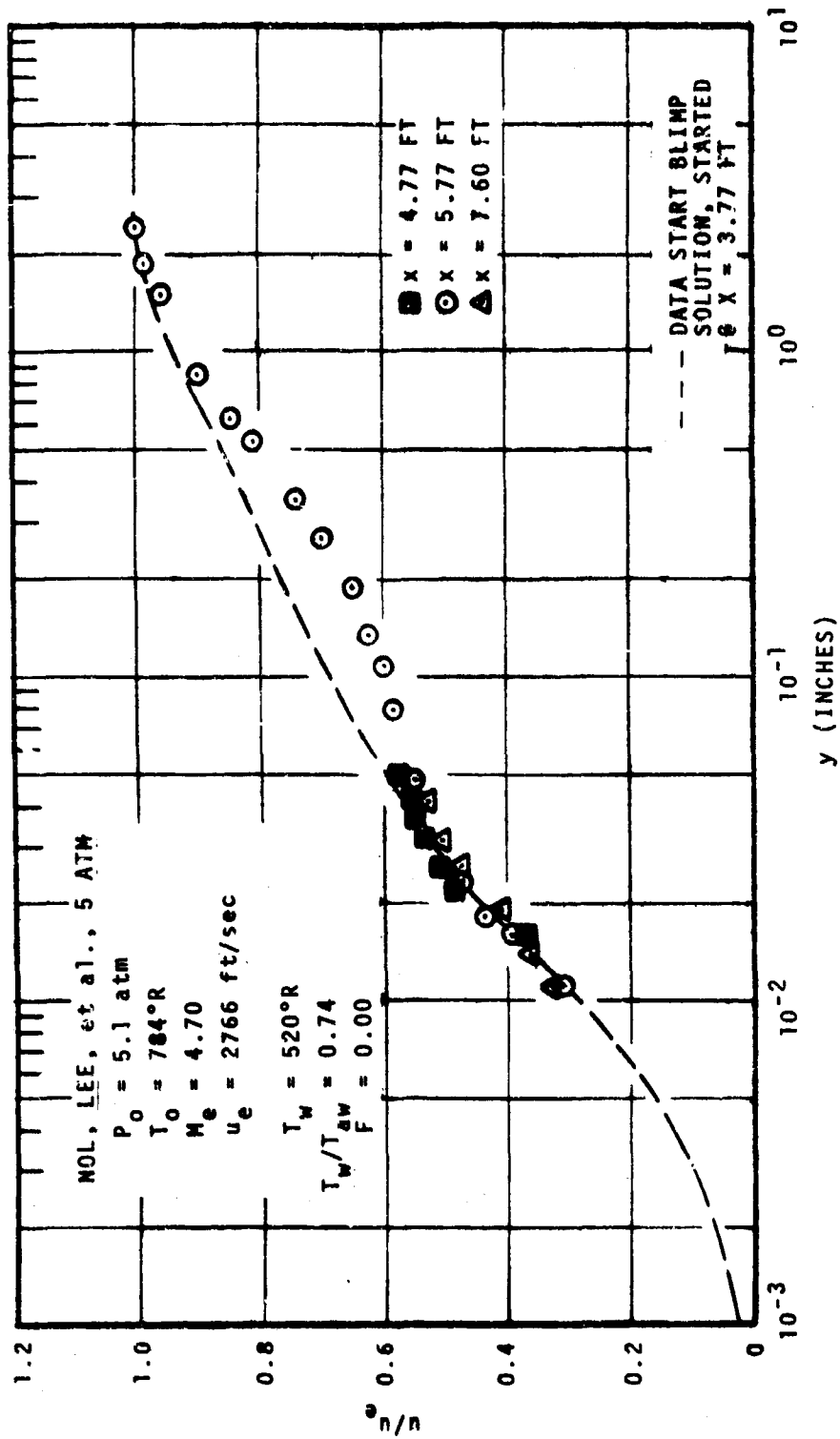


Figure 44. Linear-Log Velocity Ratio Profiles
 NOL, Lee, et al., 5 Atm, Hypersonic, Zero Pressure Gradient Flow

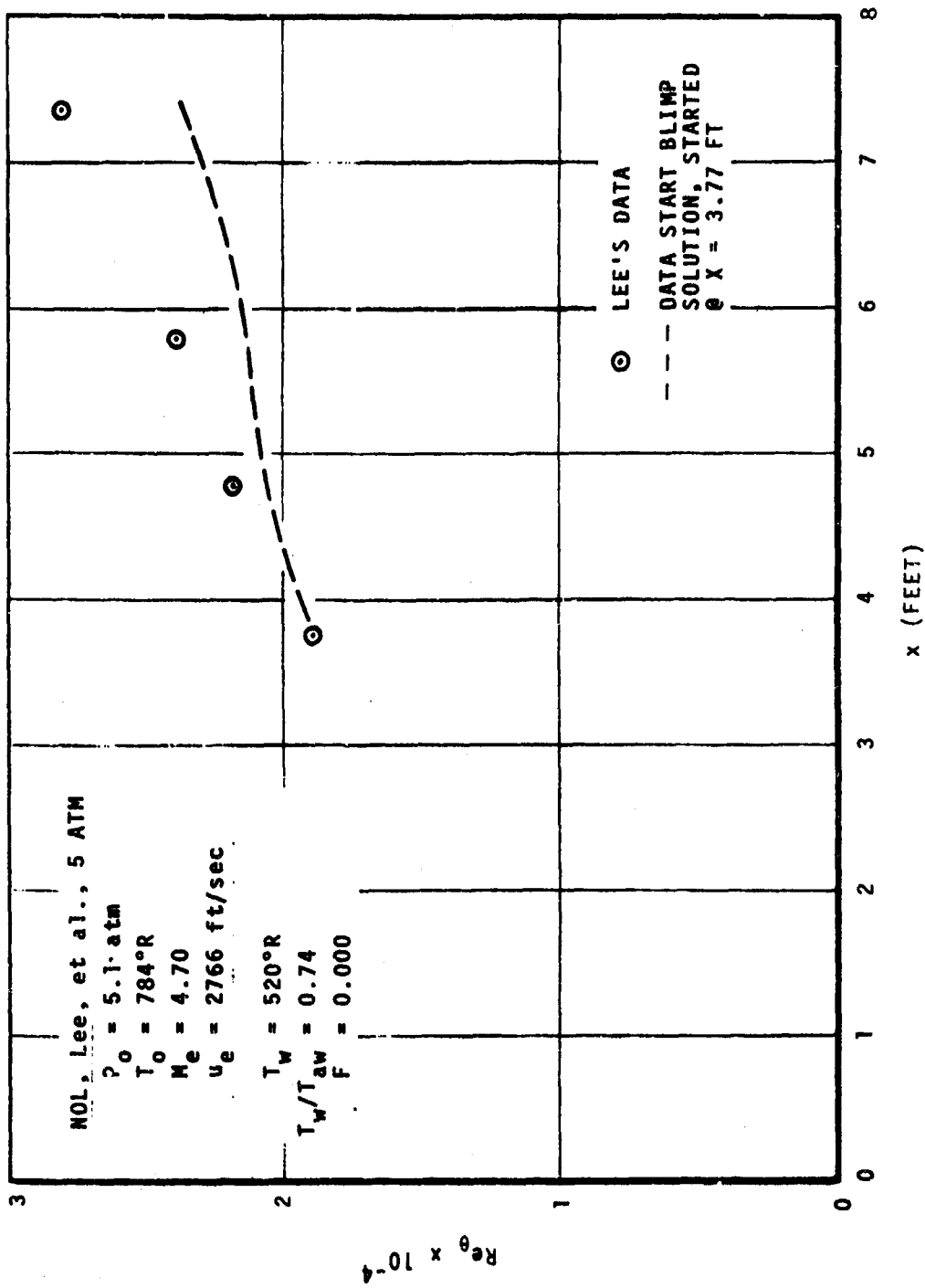


Figure 15. Momentum Thickness Reynolds Number vs Streamwise Location
 NOL, Lee, et al., 5 Atm, Hypersonic, Zero Pressure Gradient Flow

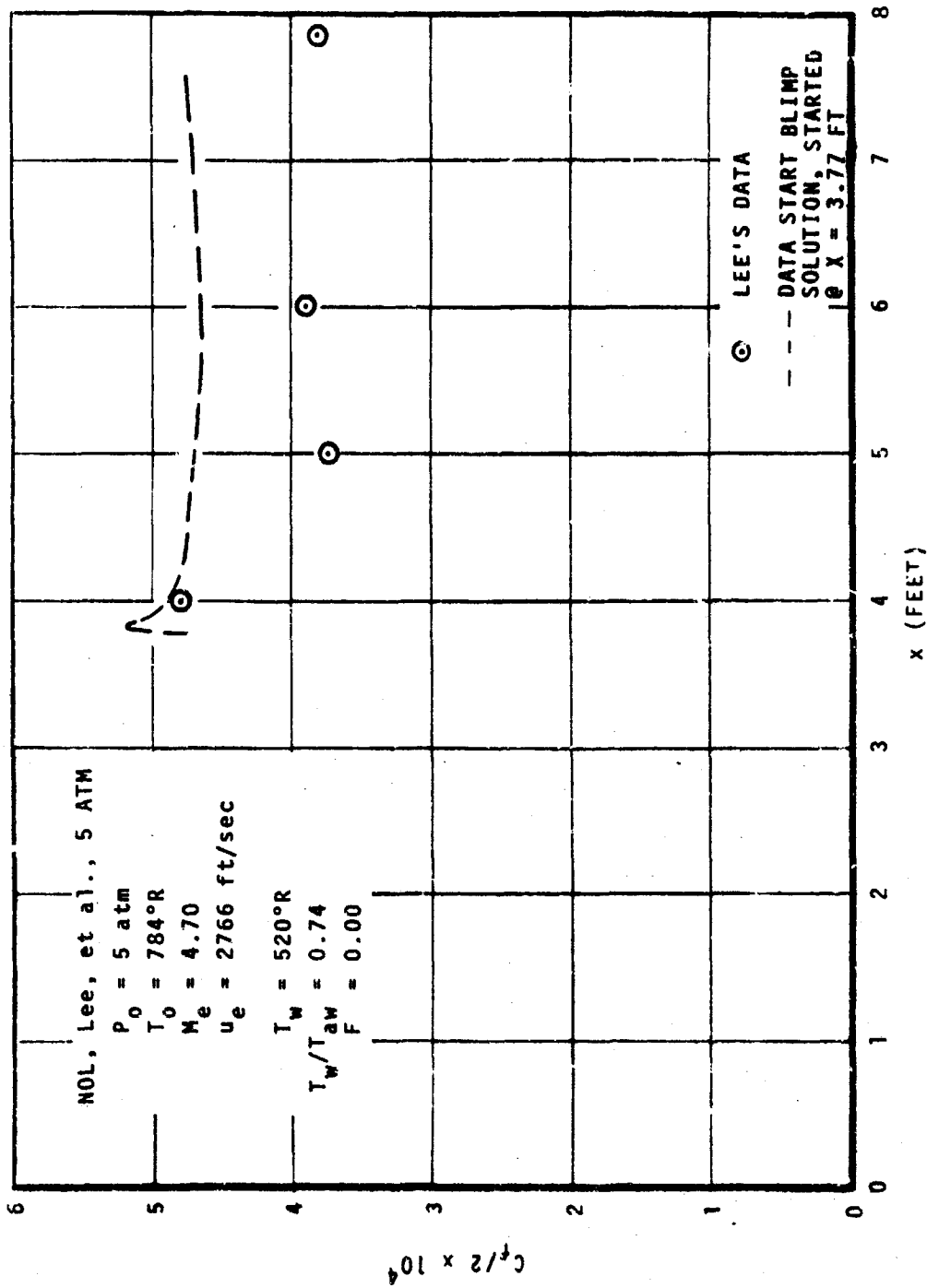


Figure 46. Skin Friction Coefficient vs Streamwise Location
 NOL, Lee, et al., 5 Atm, Hypersonic, Zero Pressure Gradient Flow

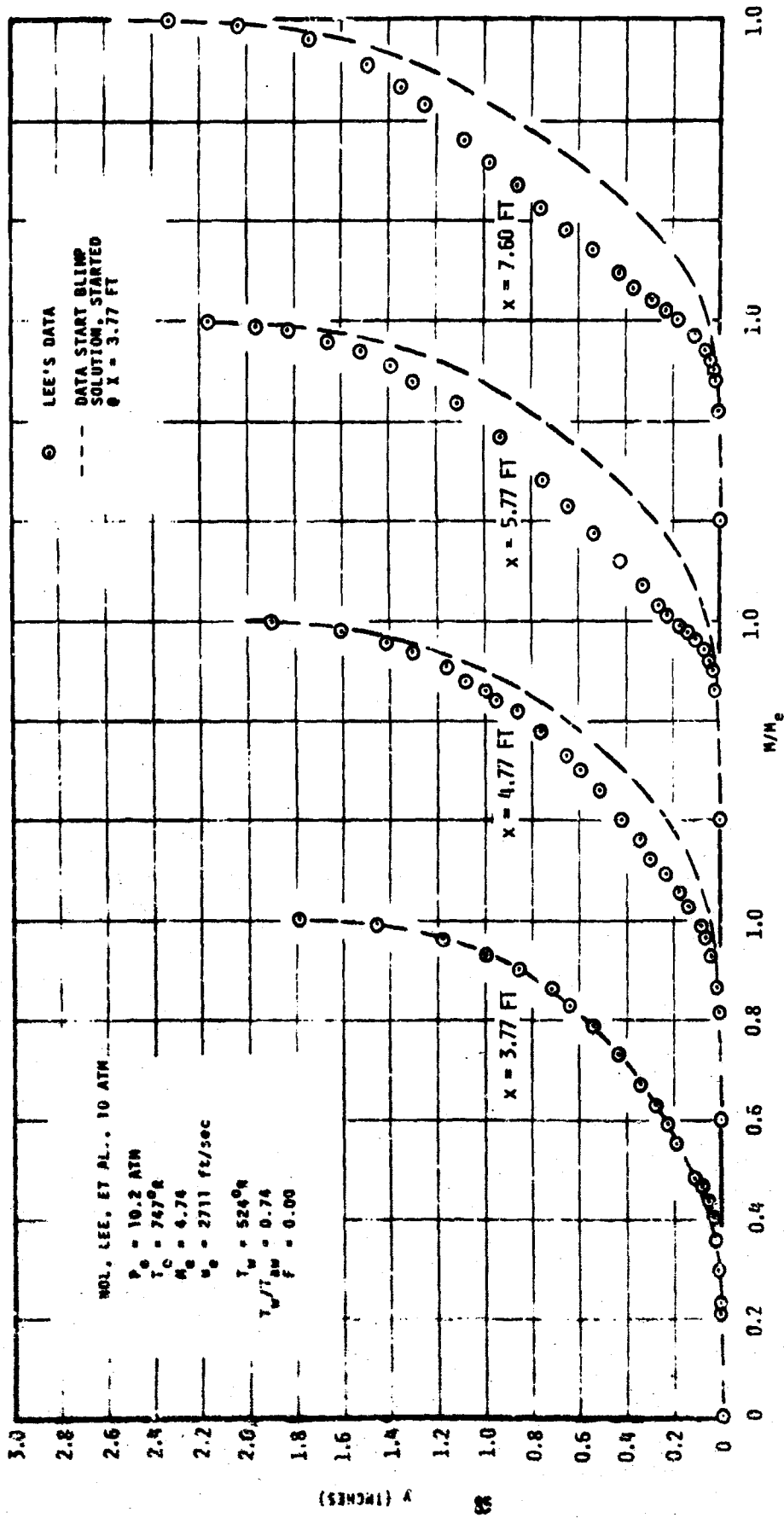


FIGURE 47. MACH NUMBER RATIO PROFILES (INCL. LEE, ET AL., 10 ATM, HYPERSONIC, ZERO PRESSURE GRADIENT FLOW)

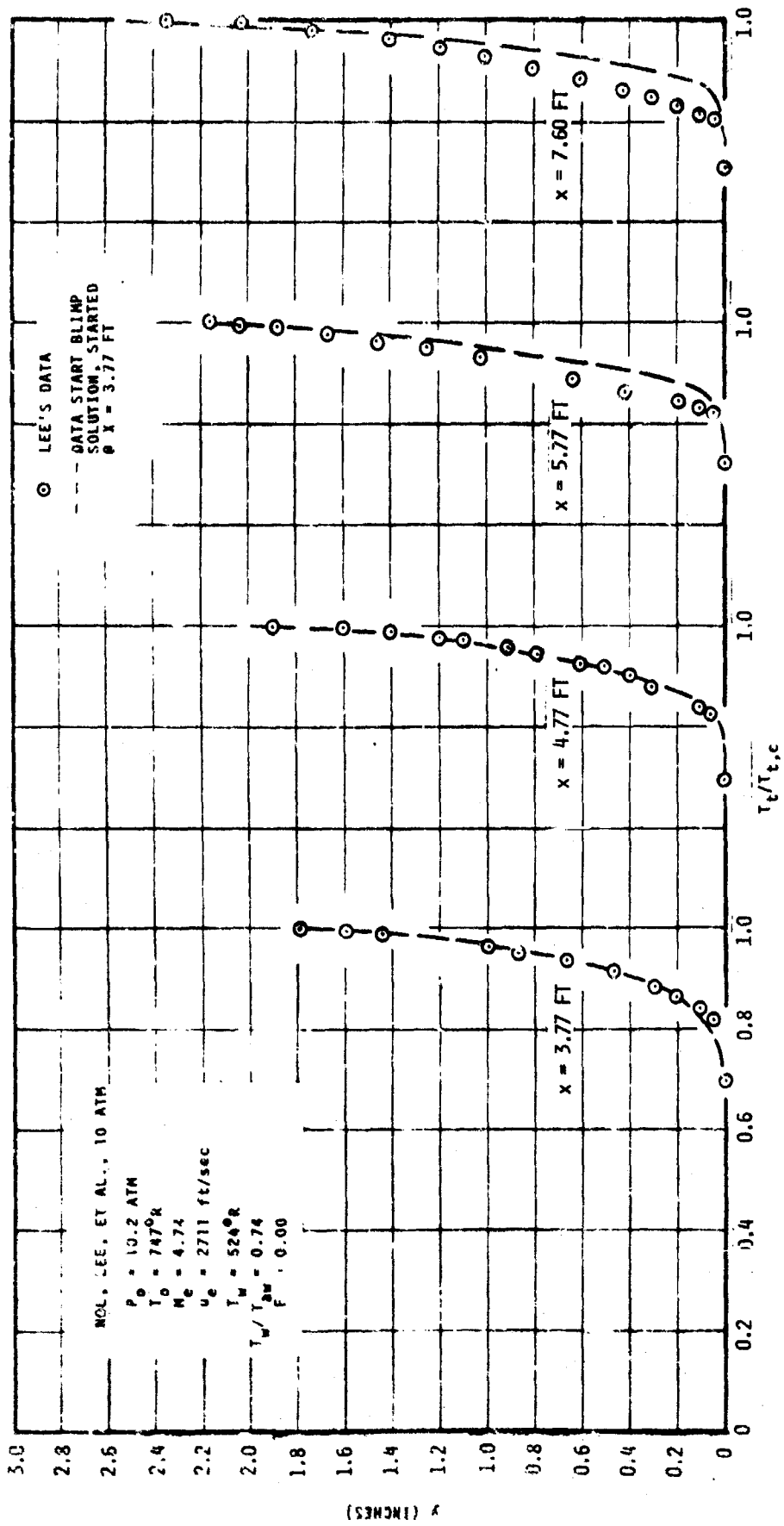


FIGURE 48. TOTAL TEMPERATURE RATIO PROFILES
 MOL, LEE, ET AL., 10 ATM, HYPERSONIC, ZERO PRESSURE GRADIENT FLOW

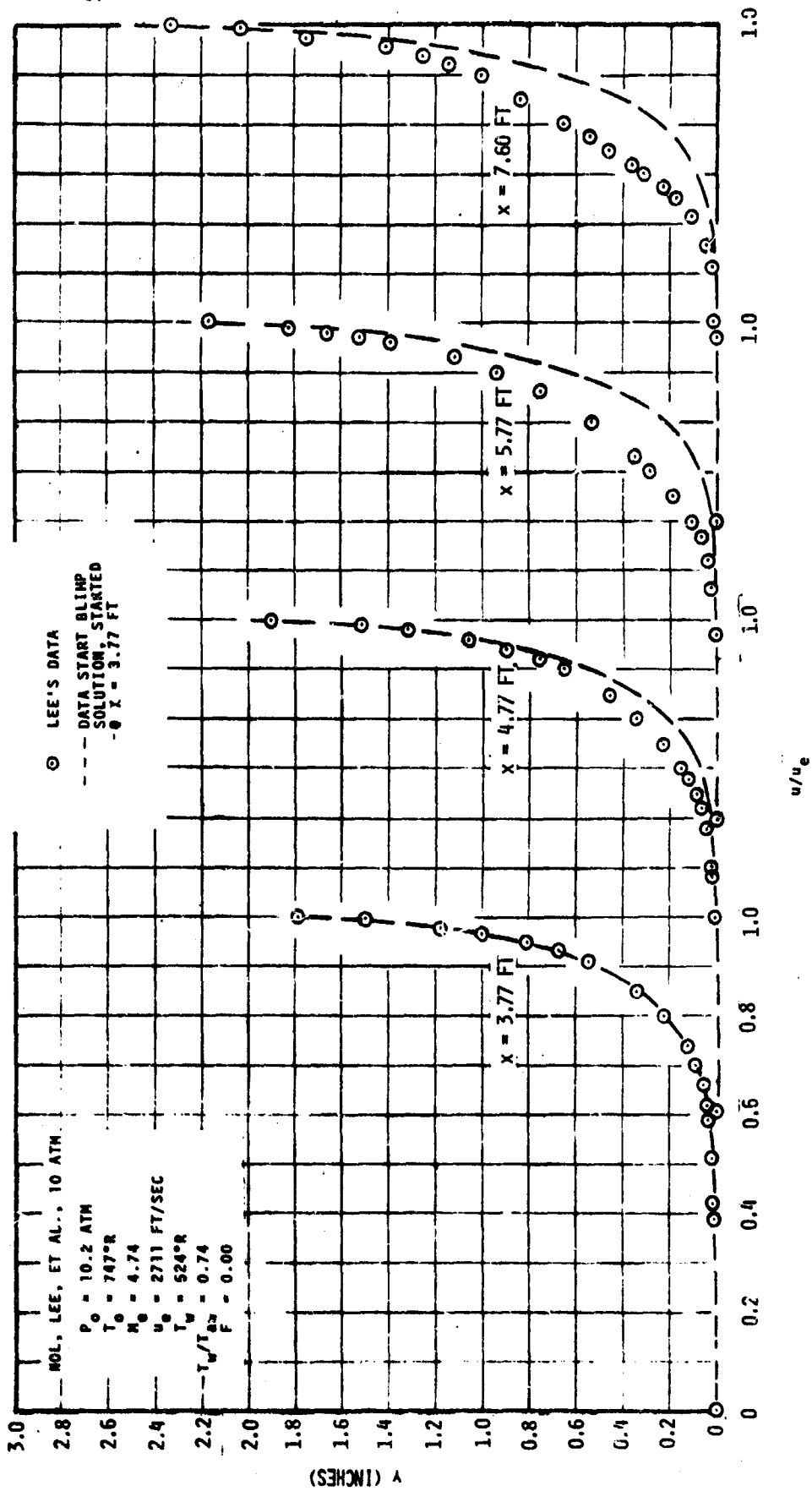


FIGURE 49. VELOCITY RATIO PROFILES
 MOI, LEE, ET AL., 10 ATM, HYPERSONIC, ZERO PRESSURE GRADIENT FLOW

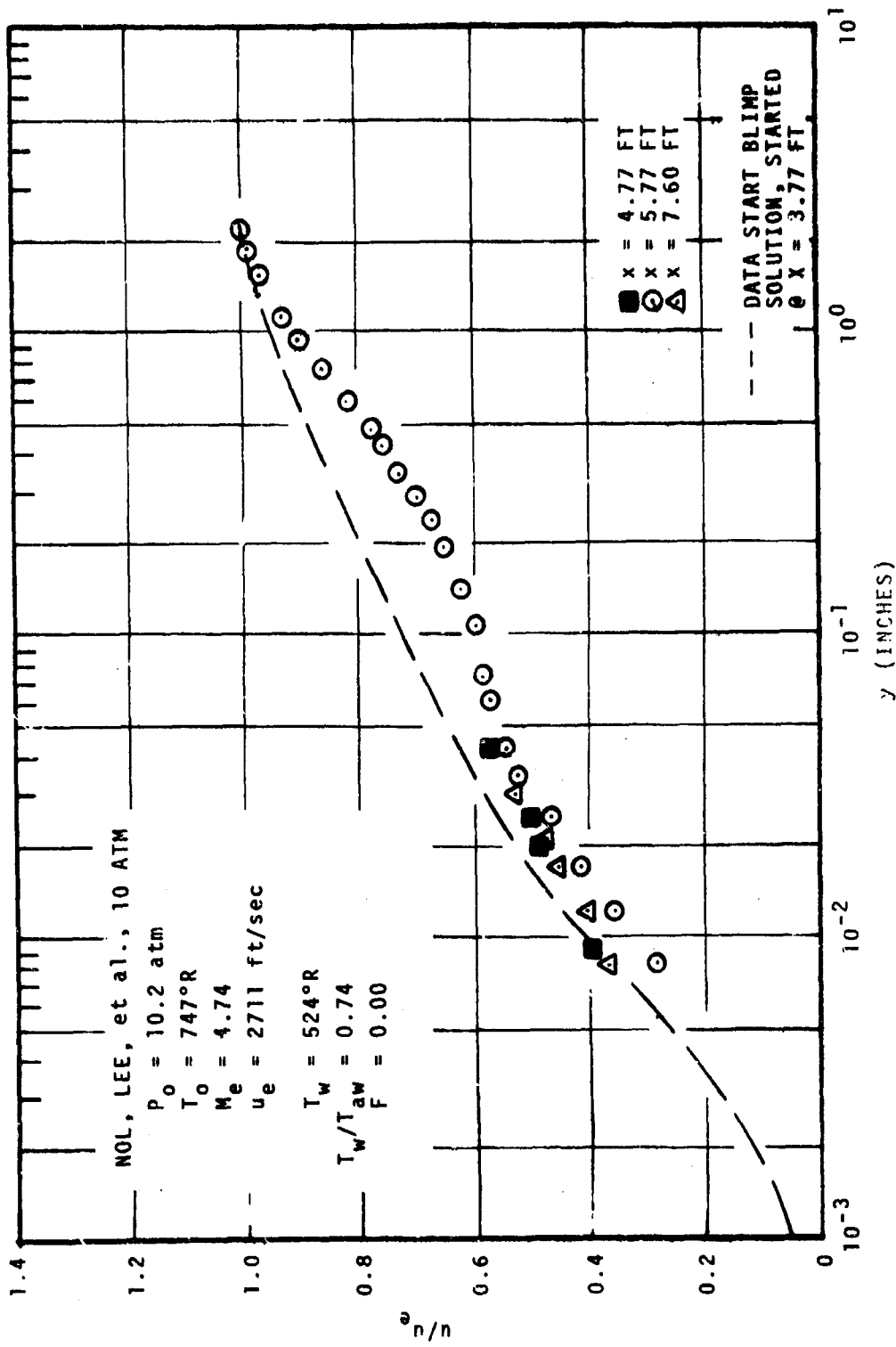


Figure 50. Linear-Log Velocity Ratio Profiles
 NOL, Lee, et al., 10 Atm., Hypersonic, Zero Pressure Gradient Flow

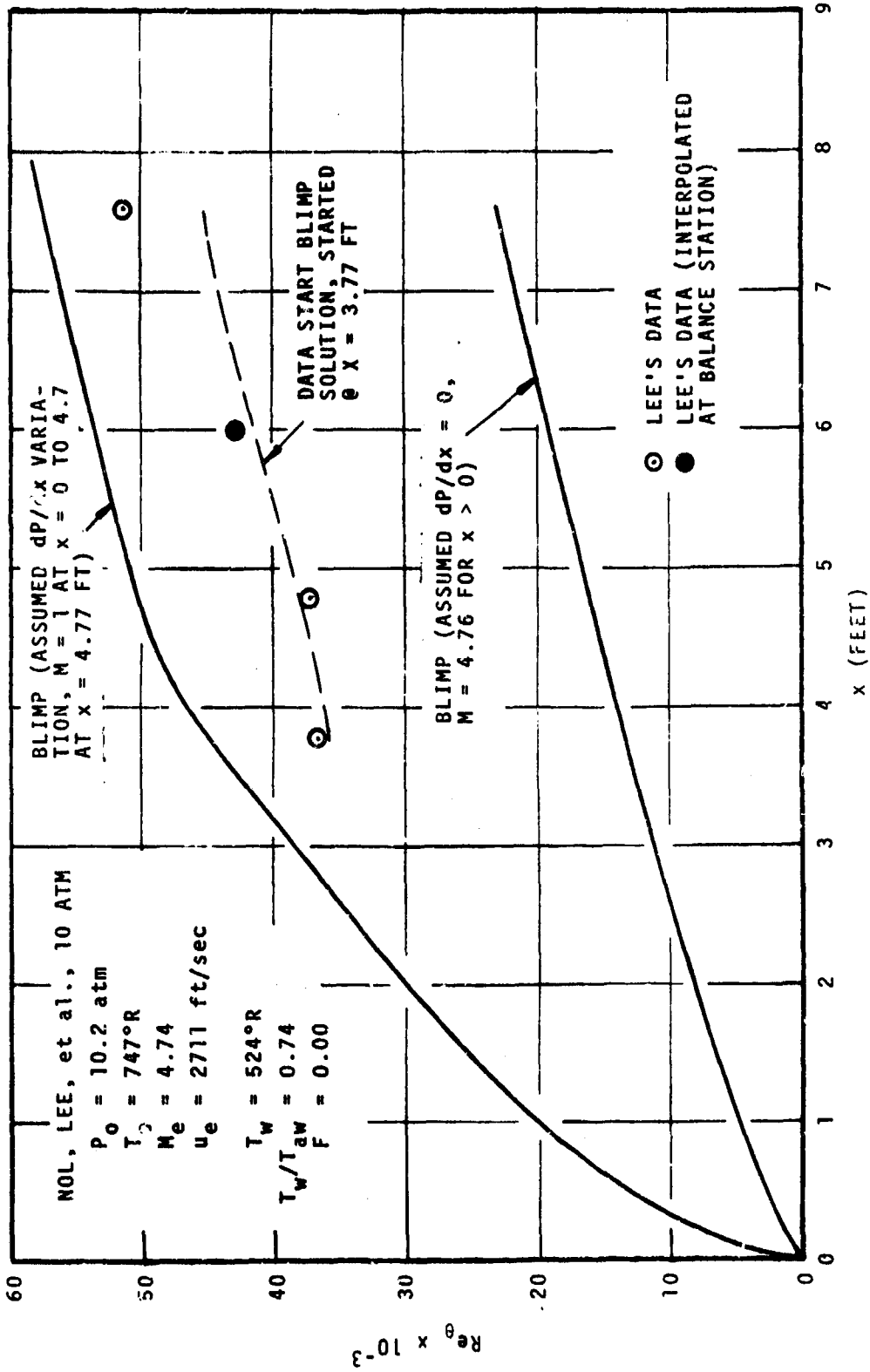


Figure 51. Momentum Thickness Reynolds Number vs Streamwise Location
 NOL, Lee, et al., 10 Atm, Hypersonic, Zero Pressure Gradient Flow

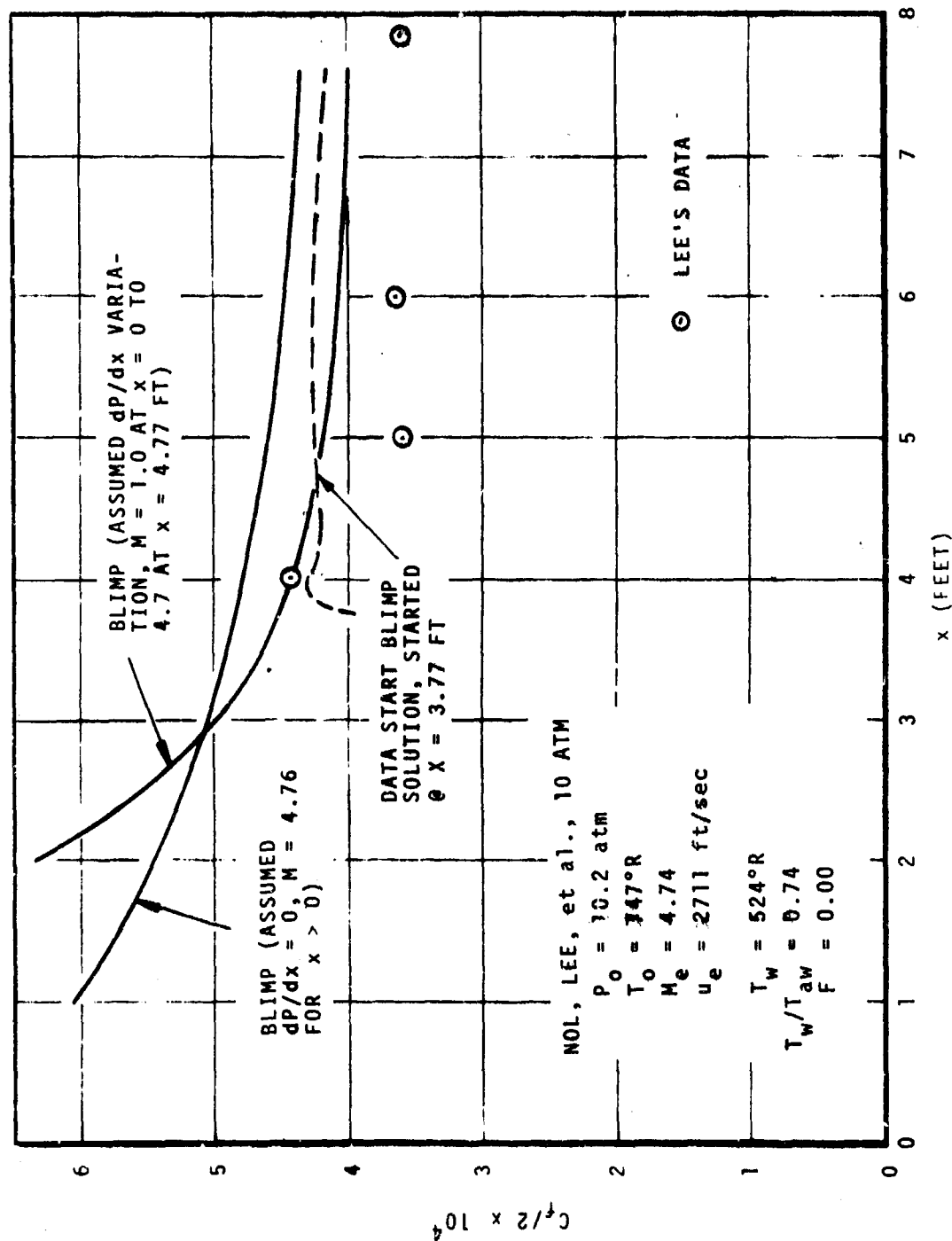


Figure 52. Skin Friction Coefficient vs Streamwise Location
 NOL, Lee, et al., 10 Atm, Hypersonic, Zero Pressure Gradient Flow

measured boundary layers in terms of θ even though the predicted and measured δ thicknesses remain essentially equal (see Figures 43 and 49). The consistency in the data appears doubtful when one considers the $C_f/2$ plots of Figures 46 and 52. For both runs, the $C_f/2$ predictions exceed the measured values after the first station (which is still within the accelerating region of the nozzle) by 16 to 24 percent. This is directly opposite to the trend seen in the Re_θ plots (Figures 45 and 51). Considering the momentum integral equation, which for zero pressure gradient and no blowing reduces to

$$\frac{C_f}{2} = \frac{d\theta}{dx} \quad (38)$$

it is clear that if $C_f/2$ is overpredicted, $\frac{d\theta}{dx}$ should also be overpredicted. The data, of course, result from skin friction gages, rather than a solution of the momentum integral equation. Calculation of $C_f/2$ using equation (38) and measured values of θ and x results in values between 8 and 9×10^{-4} as compared to skin friction data between 3.6 and 4.0×10^{-4} in the uniform flow region. On the other hand, the BLIMP predicted $C_f/2$ and $d\theta/dx$ are equal.

In view of the above comparisons, the Lee data appear somewhat questionable. This is not to say the predictions are 100% correct, but only that internal inconsistencies in the data such as three-dimensional flow are suspected. Further comment will be made in Brott comparisons to follow.

The effect of the "input" pressure gradients in the Lee data is most apparent in the Re_θ and $C_f/2$ plots of Figure 45, 46, 51, and 52. In the first set (5 atm, Figures 45, 46) pressure variations are considered in the prediction while in the latter (Figures 51, 52) they are not. The axial pressure gradient distribution computed by BLIMP is negative between 3.77 and 4.7 feet, positive up to 7.0 feet and negative thereafter. The effect on Re_θ is seen in Figure 45; $d\theta/dx$ is larger in regions of negative pressure gradient and smaller in the positive gradient regions*. The momentum integral equation accounting for pressure gradients has the form

$$\frac{C_f}{2} = \frac{d\theta}{dx} - \frac{\theta}{\rho_e u_e^2} \frac{dp}{dx} \left\{ 2 + \frac{\delta^*}{\theta} - M_e^2 \right\} \quad (39)$$

* This behavior in $C_f/2$ is directly opposite that for subsonic flow due to the change of sign of the bracket term in equation 39 at high Mach numbers.

Table VIII lists the values of each of these terms at each of seven BLIMP output stations.

TABLE VIII
MAGNITUDES OF MOMENTUM INTEGRAL EQUATION TERMS

x (ft)	$\frac{d\theta}{dx}$	Pressure Term	$\frac{C_f}{2}$
3.77	$13.00 * 10^{-4}$	$8.25 * 10^{-4}$	$4.75 * 10^{-4}$
3.82	19.18	14.00	5.18
3.90	18.58	13.60	4.98
4.20	10.24	5.45	4.79
4.77	4.41	-0.32	4.73
5.77	0.04	-4.61	4.65
7.60	9.56	4.80	4.76

From Table VIII and Figure 46, it is apparent that the predicted value of $C_f/2$ experiences only minor fluctuations even though the value of the pressure term is oscillating with an amplitude several times the value of $C_f/2$. That is, the input pressure gradient is a very important term in the momentum integral equation; however, adjustments to account for its large variations occur in the θ growth rate ($d\theta/dx$) rather than in $C_f/2$. The initial spike in $C_f/2$ is due to the incorrect input pressure gradient. The spike has no real significance since the second through the fourth stations were added only for purposes of the data start option, and the hand-interpolated pressure values resulted in locally high gradients. These pressure gradients offer no obstacle to the computer solution, and have no lasting effect on the downstream solutions; therefore, the solution was not rerun. The results do emphasize the experimental difficulties associated with accurate evaluation of local C_f values through use of the momentum integral equation.

In Figure 51 the momentum growth is essentially linear as expected for a constant axial pressure and nearly constant C_f throughout the region. The variation in $C_f/2$ in Figure 52 is due to several factors. The initial rise is the rapid recovery of the profile next to the wall following the data start profile as described in the appendix. The slow variation up to $x = 6.0$ feet is believed to be due to the readjustment of the outer portion of the profile which does have a small effect on wall gradients. Downstream of $x = 6.0$ feet, this readjustment appears to be complete and $C_f/2$ decreases slowly as expected.

for a uniform flow. These observations are further substantiated by comparison to the two solid curves which indicate the approximate zero start BLIMP predictions, assuming the upstream flow conditions noted.

(2) Data of Brott, et al.

(a) Comments on BLIMP Input

The Mach number distribution from the throat to the first profile station is presented in reference 6 for the design and the measured values. Using this information, zero start BLIMP predictions were made assigning $x = 0$ at the nozzle throat. For additional comparison, "data start" runs starting from the first reported profiles at $x = 47$ inches were made. As with the 5 atmosphere Lee run above, freestream pressures were assigned to equate the local measured and input freestream to stagnation pressure ratios.

(b) Comments on Results

Figures 53-58 and 59-64 contain the results of the 5 and 10 atmosphere stagnation pressure runs, respectively. Results are plotted for the zero start and data start predictions described above. Profiles from the data start prediction for both runs tend to readjust in shape moving down the plate. By the final station, which is nearly 3 feet downstream from the first, these profiles are quite similar to the zero start profiles. This then is a measure of the duration of the recovery process. These figures show that the adjustment of the Mach number occurs more rapidly than that of total temperature and velocity.

In comparison with the data, both forms of the prediction tend to (1) indicate higher values of Mach number, total temperature, and velocity in the mid-range of the profiles up to Mach number ratios of 0.8 and velocity ratios of 0.9 and (2) underpredict in the far wake region, particularly the Mach number. As with Lee above, the boundary layer thicknesses, δ , are essentially equal.

The momentum thickness comparisons of Figures 57 and 63 are quite good for both starting conditions. Small differences in θ at the first data point are apparently due to differences between the Aerotherm and NOL curvefit of the profile data. This good overall agreement is in marked contrast to the results of the Lee comparisons. Figures 58 and 64 show excellent agreement between predictions and data for $C_f/2$. Note that there is no sudden change in $C_f/2$ after the first station for the data start predictions, indicating that the input, i.e., the measured wall gradient, was consistent with the BLIMP solution for the local conditions. The more gradual dips shown are probably due to

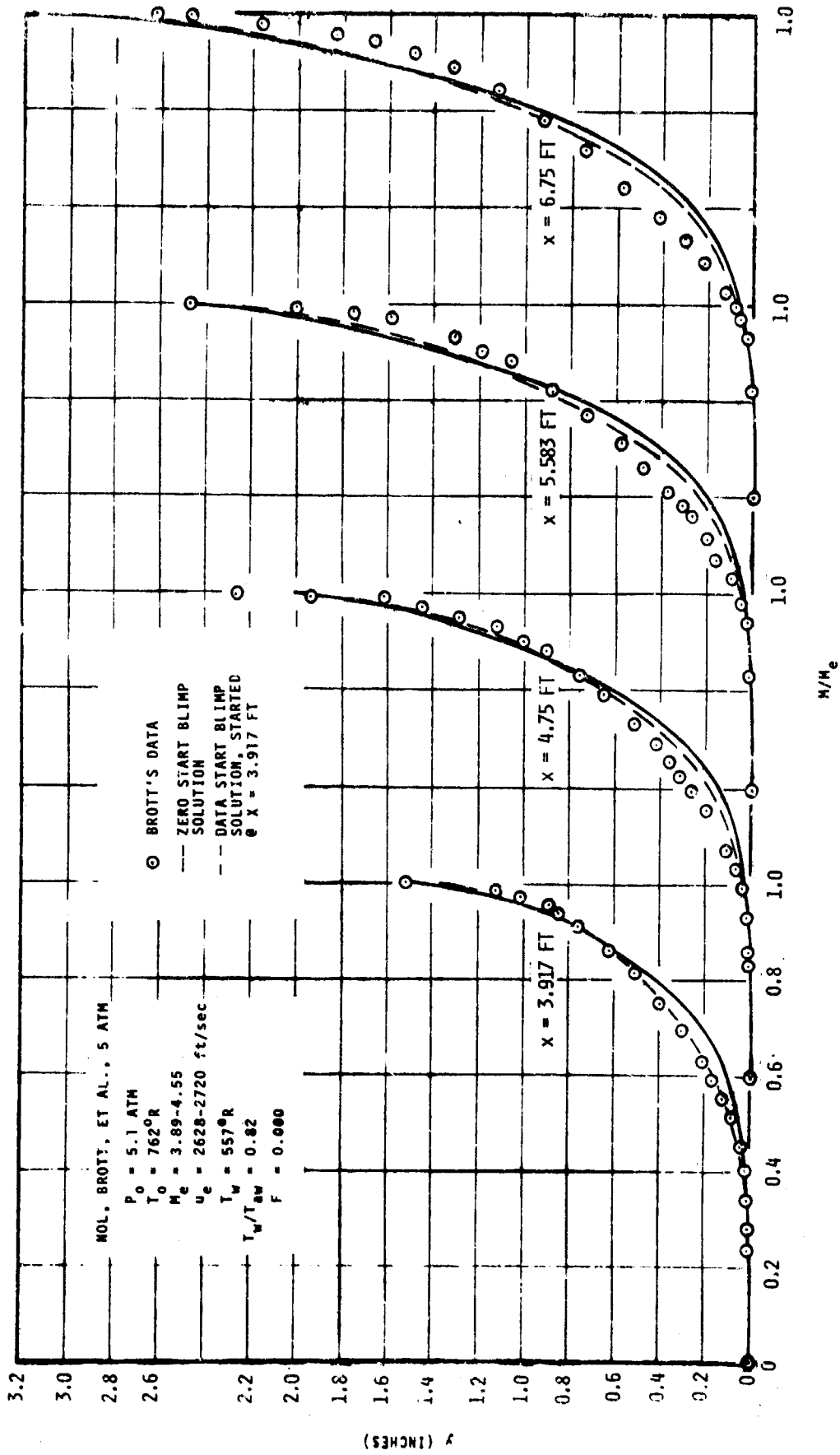


FIGURE 53. MACH NUMBER RATIO PROFILES
 MOL, BROTT, ET AL., 5 ATM, HYPERSONIC, NEGATIVE PRESSURE GRADIENT FLOW

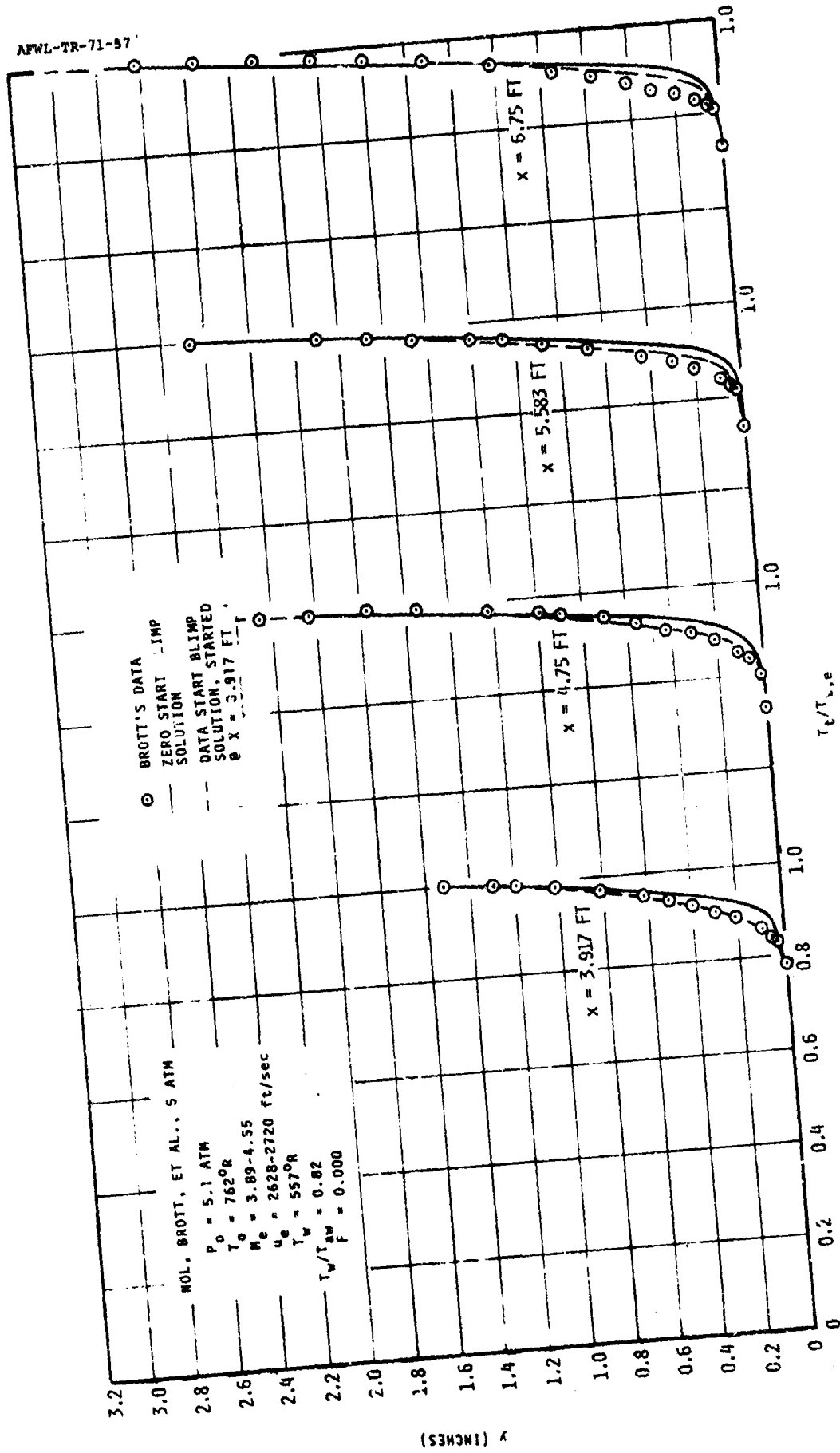


FIGURE 54. TOTAL TEMPERATURE RATIO PROFILES
 MOI., BROTT, ET AL., 5 ATM, HYPERSONIC, NEGATIVE PRESSURE GRADIENT FLOW

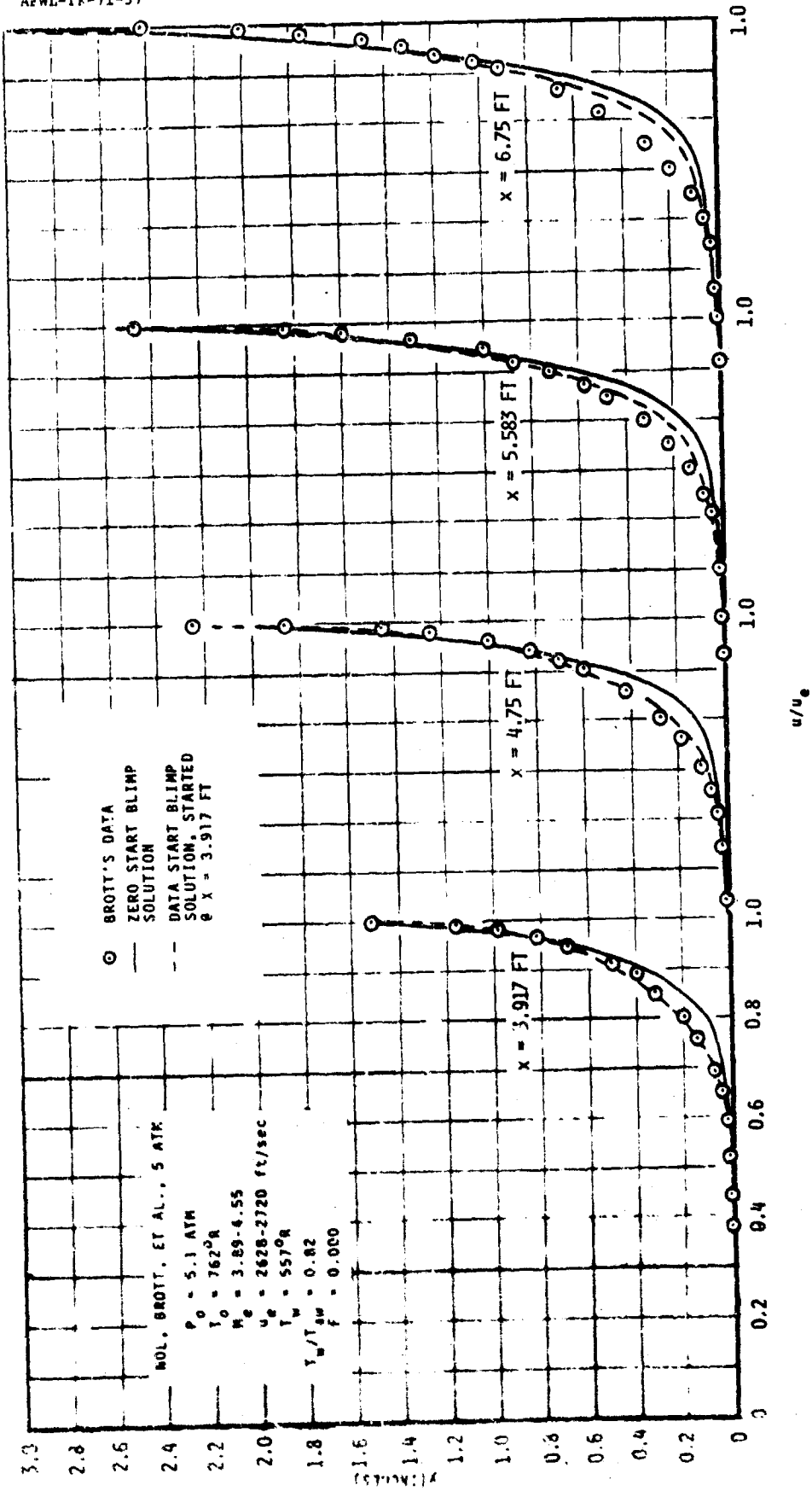


FIGURE 55. VELOCITY RATIO PROFILES
 MOL. BROTT ET AL., 5 ATK, HYPERSONIC, NEGATIVE PRESSURE GRADIENT FLOW

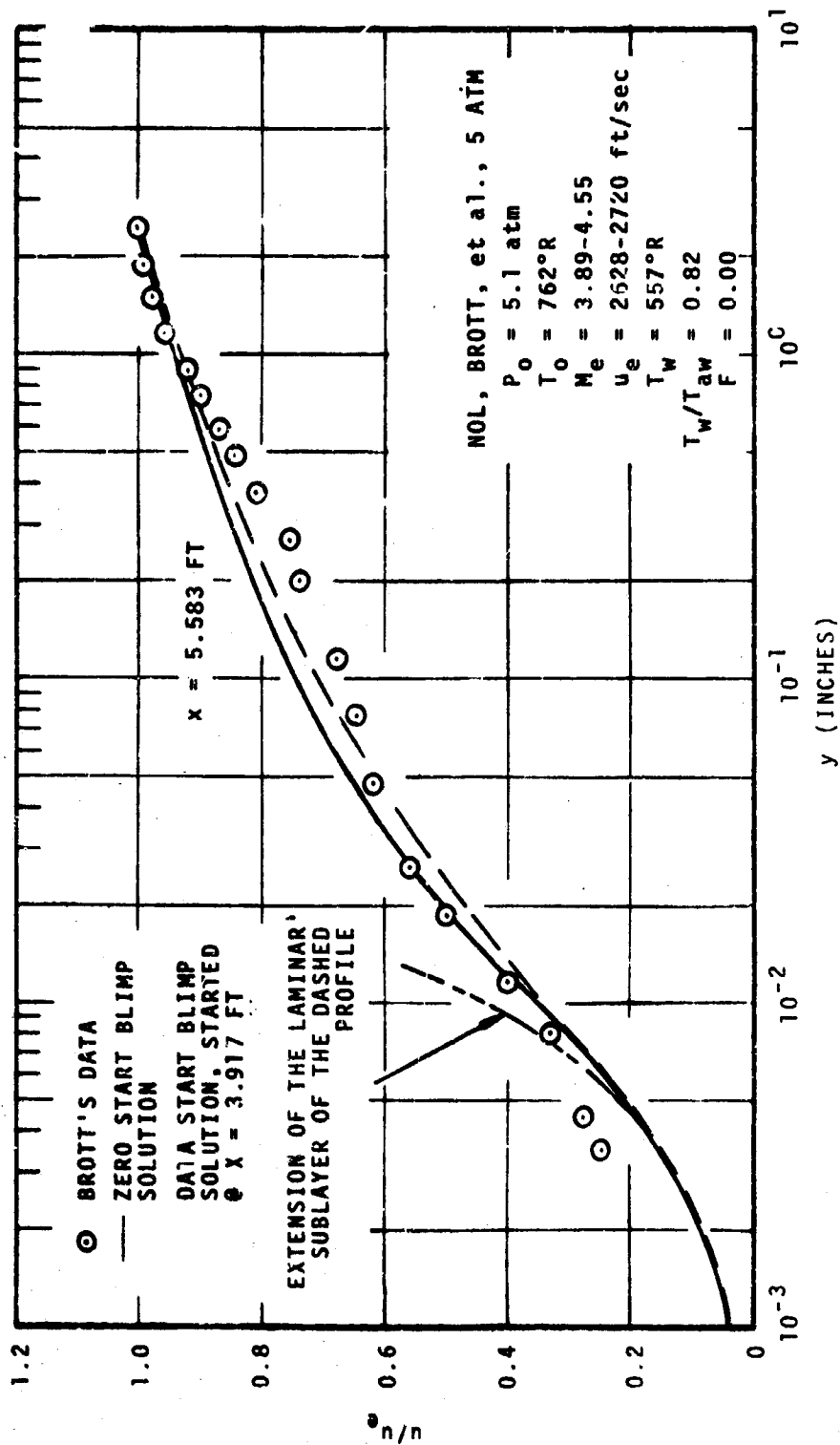


Figure 56. Linear-Log Velocity Ratio Profiles NOL, Brott, et al., 5 Atm, Hypersonic, Negative Pressure Gradient Flow

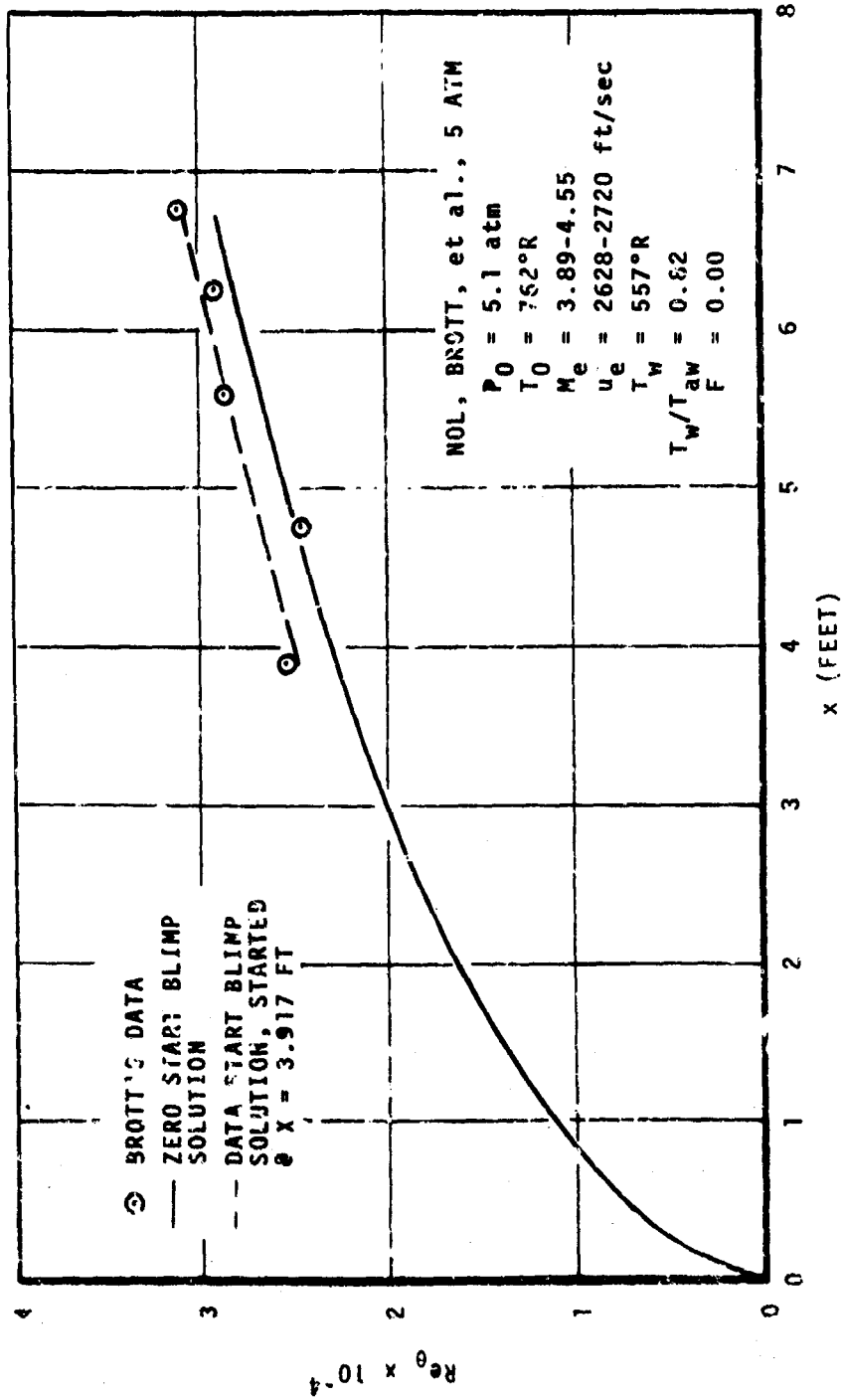


Figure 57. Momentum Thickness Reynolds Number vs Streamwise Location
 NOL, Brott, et al., 5 Atm, Hypersonic, Negative Pressure Gradient Flow

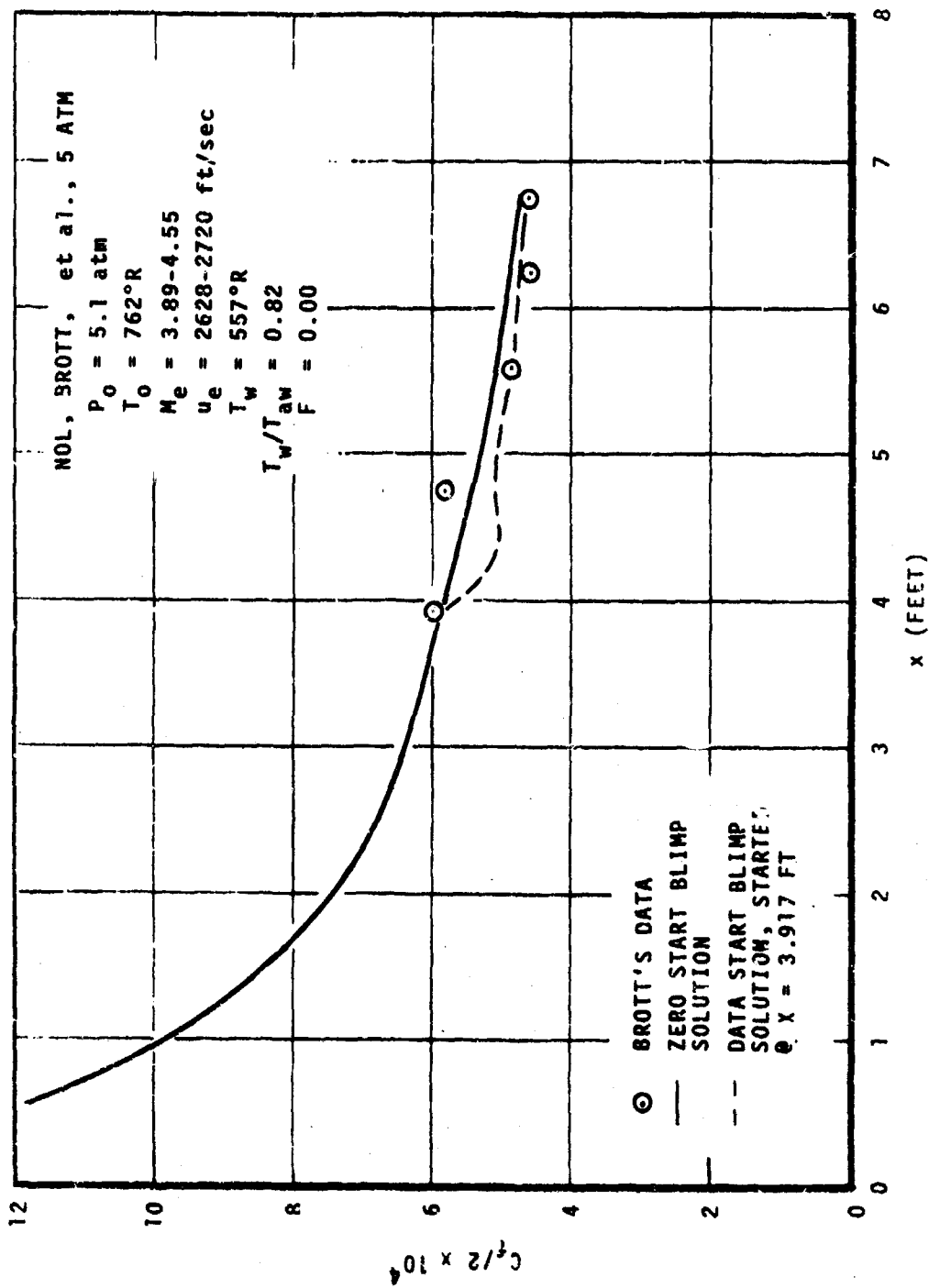


Figure 58. Skin Friction Coefficient vs Streamwise Location
 NOL, Brott, et al., 5 Atm, Hypersonic, Negative Pressure Gradient Flow

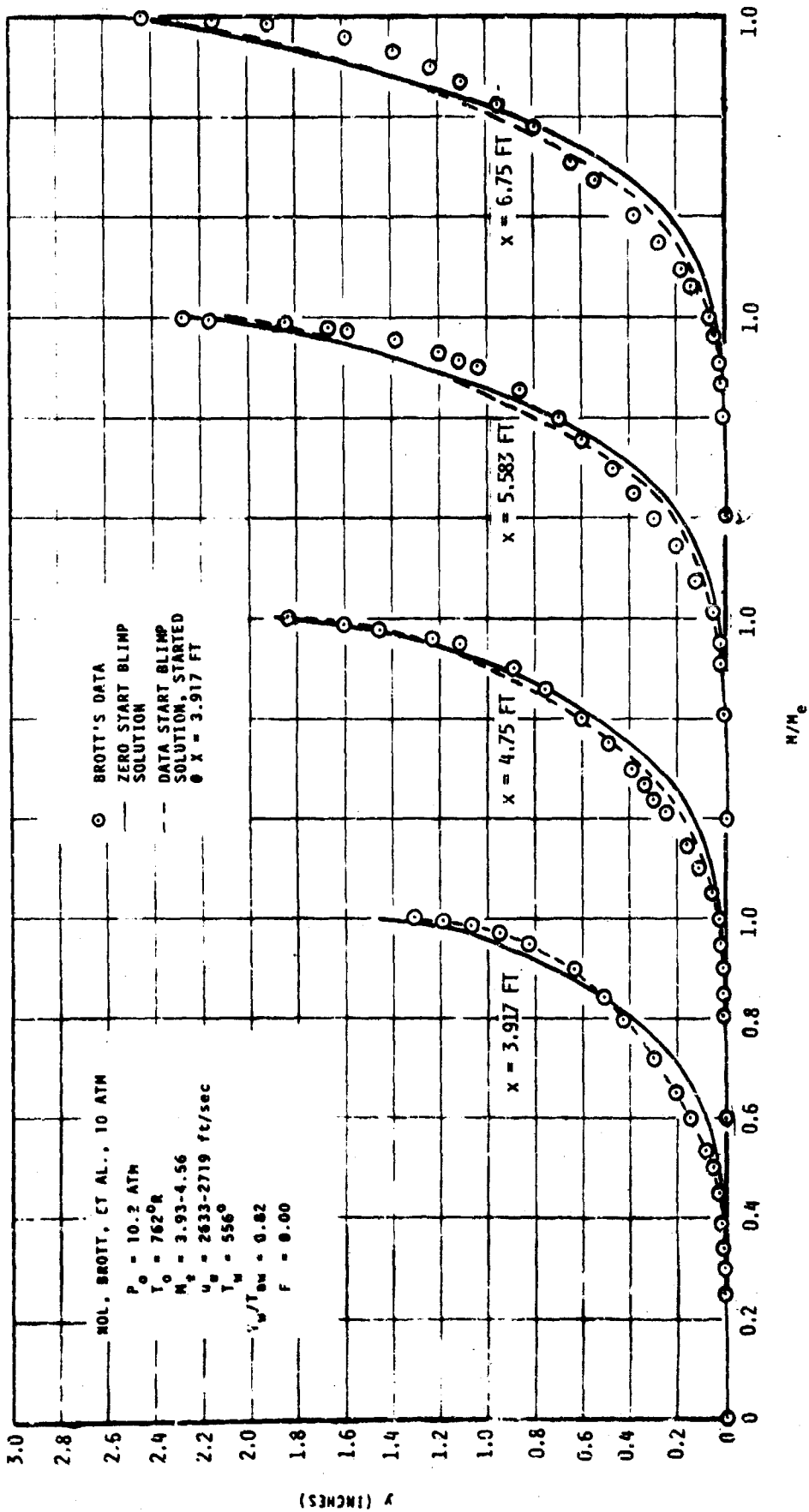


FIGURE 59. MACH NUMBER RATIO PROFILES
MOL, BROTT, ET AL., 10 ATM, HYPERSONIC, NEGATIVE PRESSURE GRADIENT FLOW

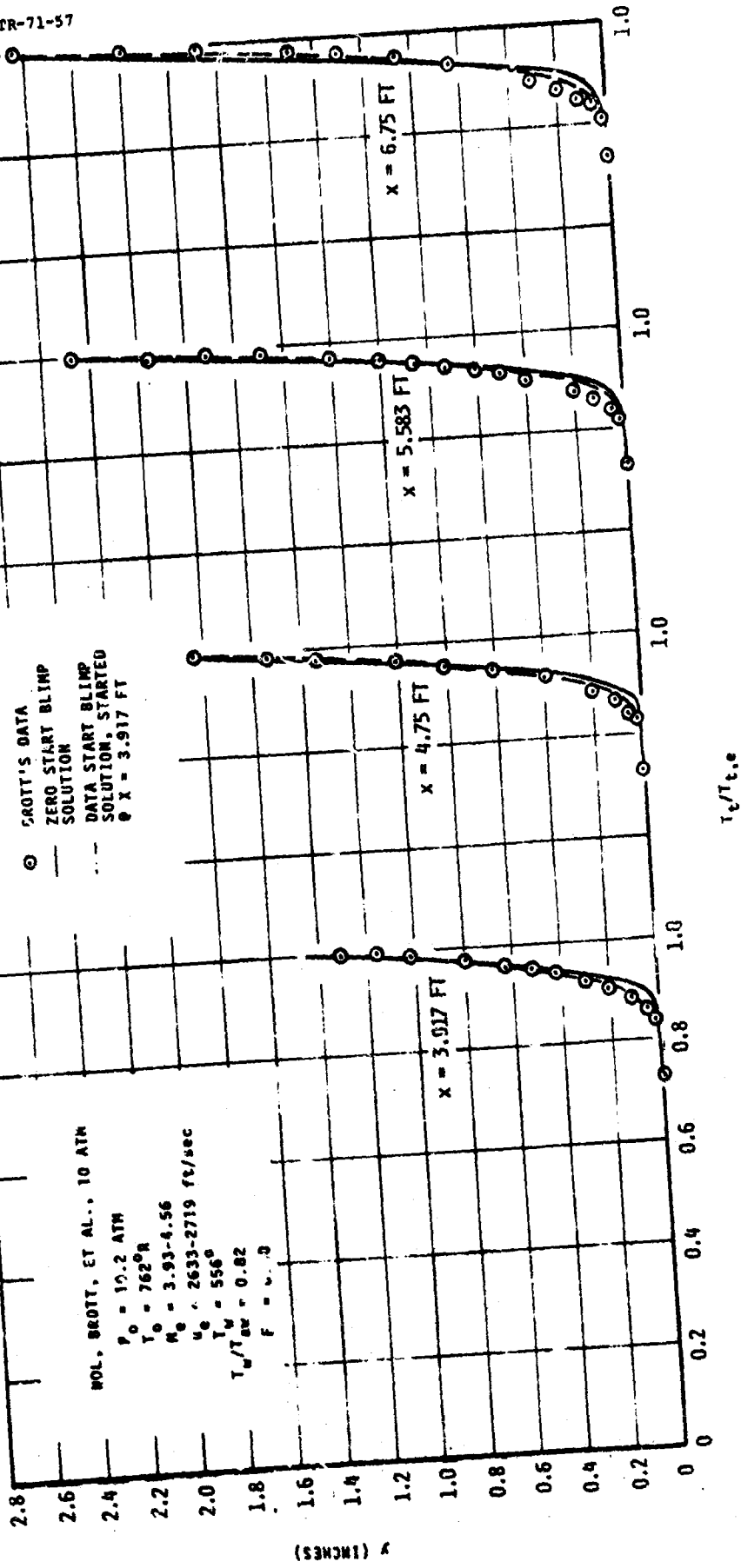


FIGURE 60. TOTAL TEMPERATURE RATIO PROFILES
 MOL. BROTT, ET AL., 10 ATM, HYPERSONIC, NEGATIVE PRESSURE GRADIENT FLOW

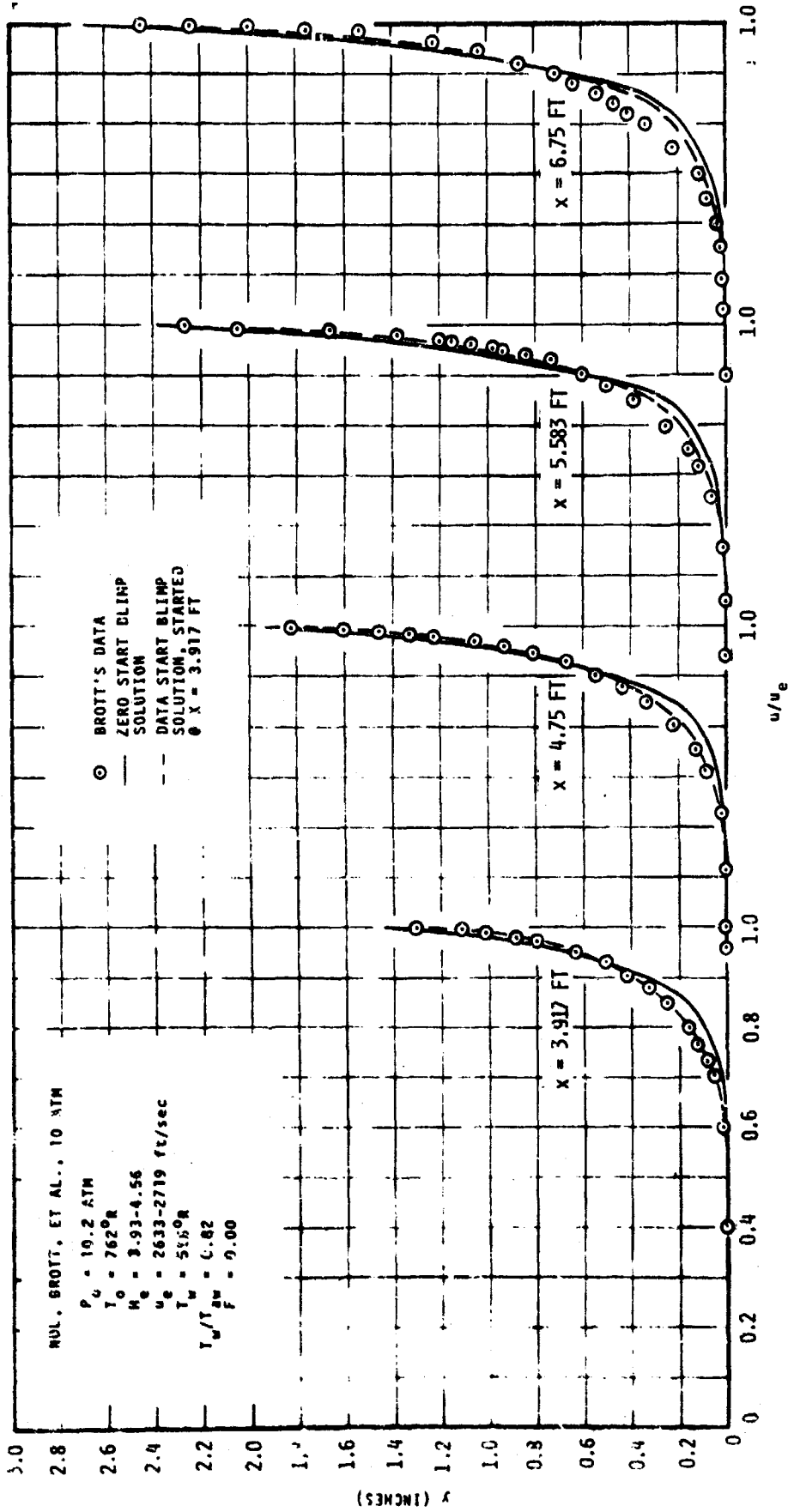


FIGURE 61. VELOCITY RATIO PROFILES
 MUL. BROTT, ET AL., 10 ATM, HYPERSONIC, NEGATIVE PRESSURE GRADIENT FLOW

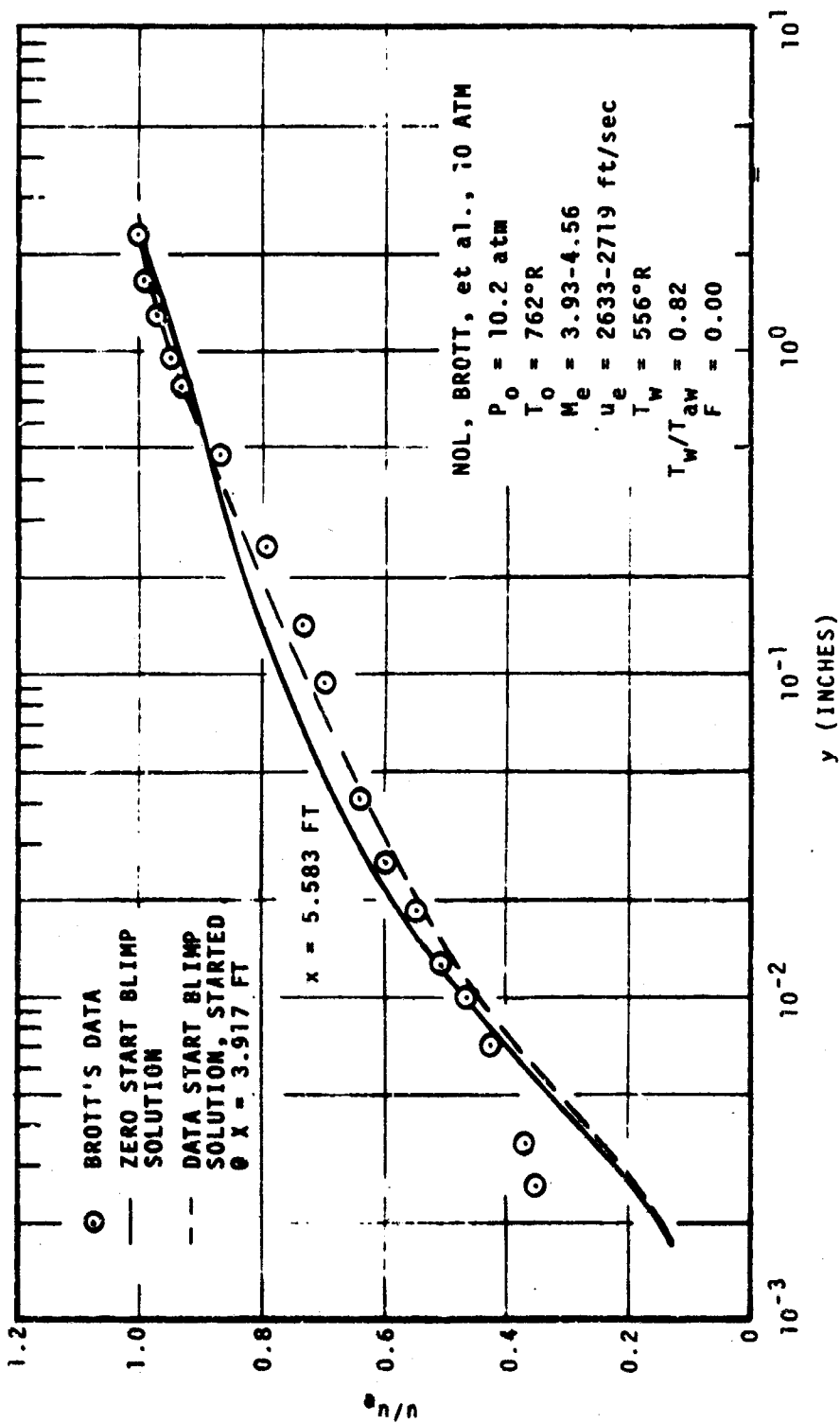


Figure 62. Linear-Log Velocity Ratio Profiles
 NOL, Brott, et al., 10 Atm, Hypersonic, Negative Pressure Gradient Flow

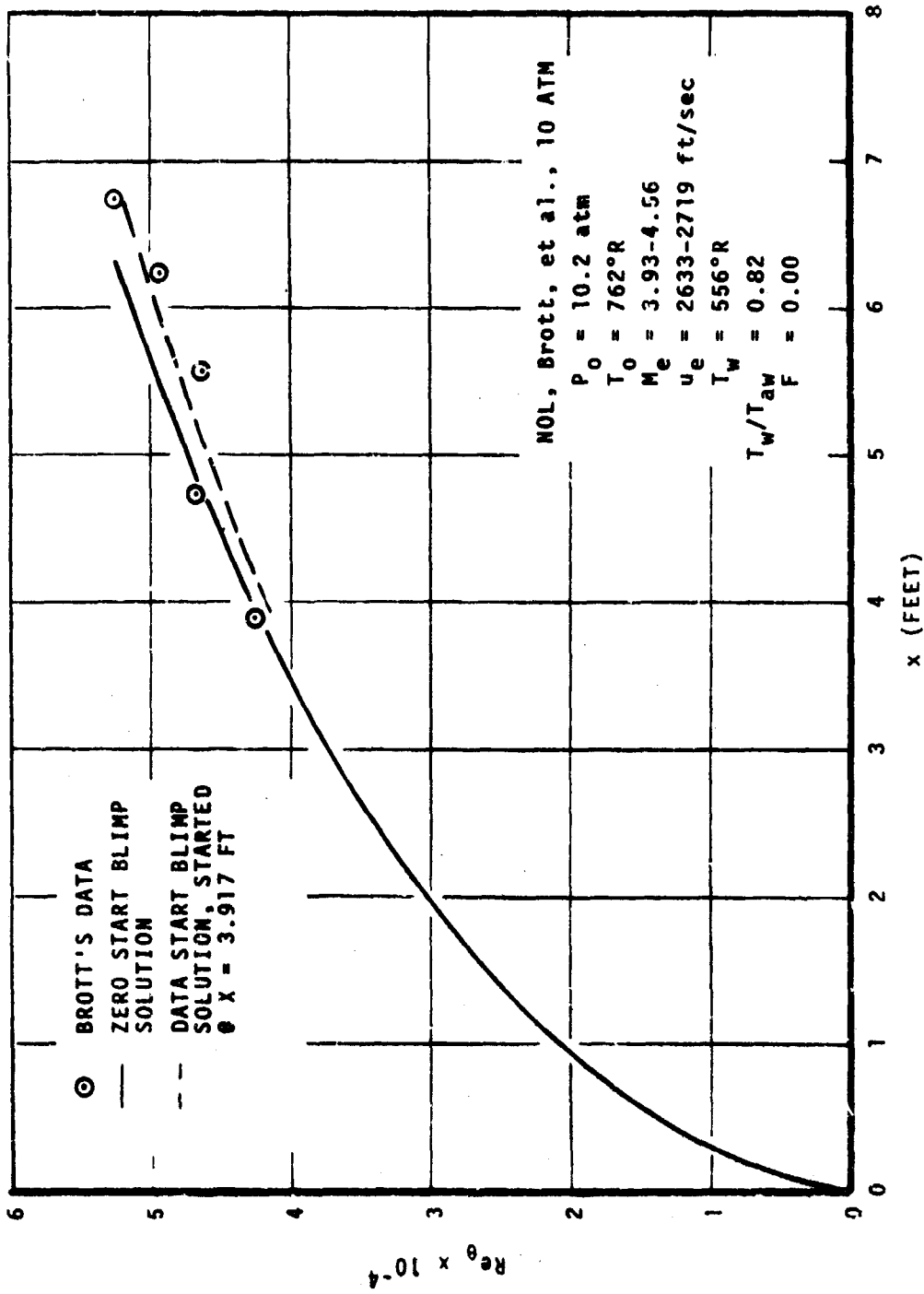


Figure 62. Momentum Thickness Reynolds Number vs Streamwise Location
 NOL, Brott, et al., 10 atm, Hypersonic, Negative Pressure Gradient Flow

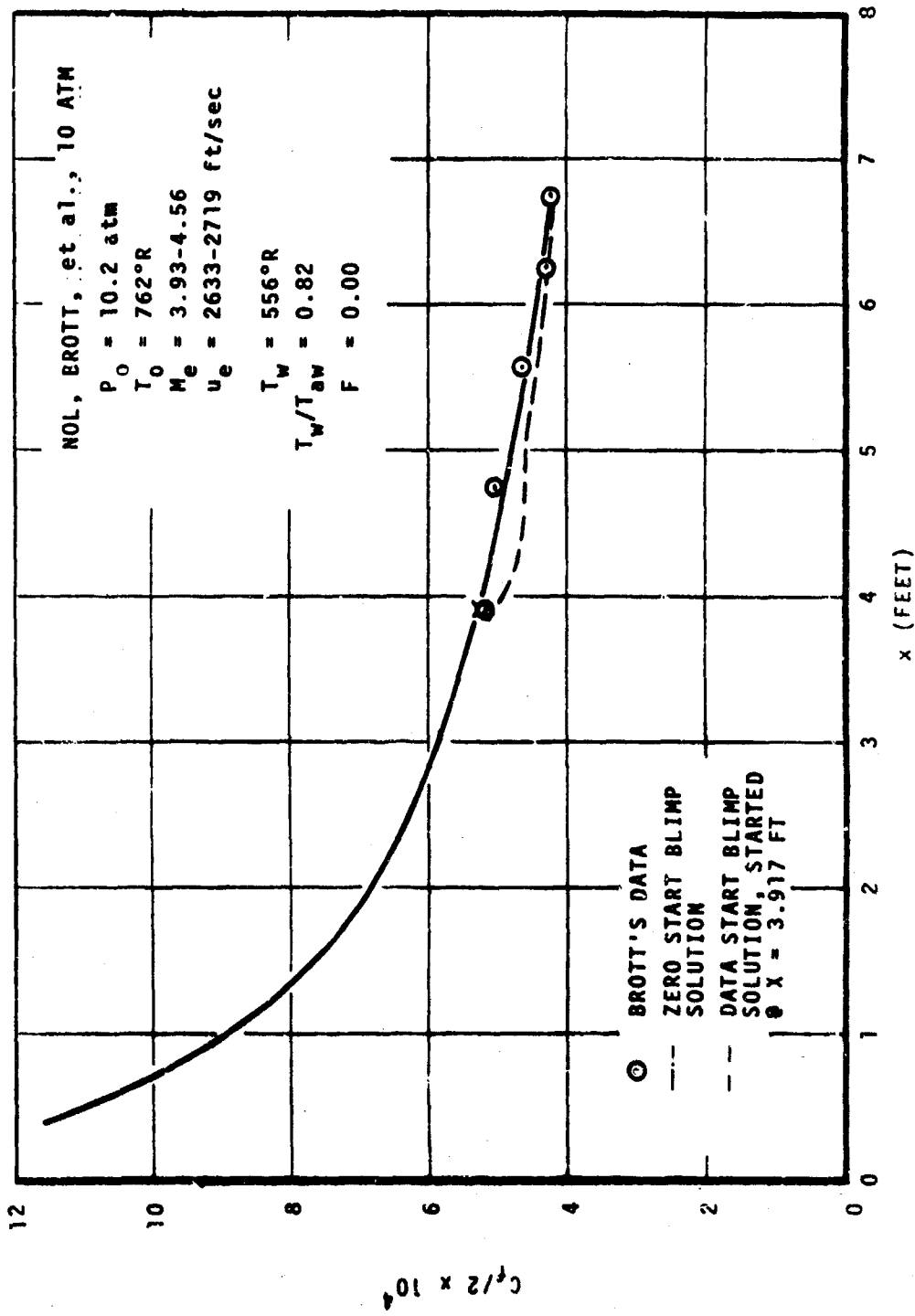


Figure 64. Skin Friction Coefficient vs Streamwise Location
 NOL, Brott, et al., 10 Atm, Hypersonic, Negative Pressure Gradient Flow

the overall profile adjustment taking place but may also be a result of the modeling of the pressure gradient in this region.

The log velocity plots of Figures 56 and 62 also show good agreement over the law of the wall region. The two data points nearest the wall in both of these figures are assumed to be in error since they are inconsistent with the skin friction balance data and the BLIMP prediction. These data points were taken with a very small probe (0.005 inch high) at very low pressures, and are subject to numerous sources of error.* Referring back to the Lee log velocity plots (Figures 44 and 50), near wall measurements show better agreement with theory, perhaps since a larger (0.016 inch) probe was used. When the near wall readings from three stations are superimposed (Figures 44 and 50), the 5 atmosphere case shows good agreement while the 10 atmosphere case does not. This merely confirms the idea that the near wall data, even with the larger probe, are questionable. Farther away from the wall, over the bulk of the profile, the Lee data are in much poorer agreement with theory than Brott's data.

In conclusion, the Brott data appear to be much more consistent in terms of profile shape, θ growth, and reported $C_f/2$ values, both internally and in comparison to the predictions. The Lee data lack this internal consistency, particularly when $d\theta/dx$ is compared to the $C_f/2$ values. Also in the Lee experiments, the rapidly changing profile shape in an essentially "similar" flow region is disturbing.

c. TRW Comparisons

(1) Comments on BLIMP Input

Since tunnel operation was continuous, variations in stagnation and freestream conditions from profile to profile were quite small. Constant input conditions were determined as averages of the reported station values. Wall temperatures were input as measured.

An experimental difficulty that might have affected the profile data was the formation of a frost layer on the cold wall section. This was not detected until after the step-up run. A change was made in procedure, namely, data were taken during only the first 15 to 20 minutes once the wall was cooled. The model was then warmed and re-cooled until measurements were complete. This procedure was employed for the step-down tests. Due to the frost formation, Stanton tube data in cold wall regions were judged to be erroneous and thus, not reported.

* Personal communication with Roland Lee at NOL indicated that correction curves for near wall measurements like these are currently being generated.

Figures 65 and 71 present the axial wall temperature distributions for the step-up and step-down runs. BLIMP comparisons were made at the stations marked by checks. For the zero start predictions, freestream and wall conditions upstream of the first reported station were assumed constant and equal to the values at the first station. In handling step changes in streamwise properties, BLIMP contains an option to treat streamwise derivatives as two point differences (linear variation) in place of the usual three point difference (quadratic curve fit). This option was applied to the step region from the first station in the step to the second station at the new wall temperature.

A data start run for the step-down case was made to model the profiles immediately upstream of the step exactly. In particular, accurate total temperature modeling was desired.

(2) Comments on Results

Profile and $C_f/2$ comparisons are presented in Figures 66-70 and 72-76 for the step-up and step-down cases. Step-down comparisons include both zero start and data start comparisons. No comparisons are shown for momentum thickness because the accuracy of these data are being reviewed by TRW*. The five plotted comparison profiles include the last station before the step, three stations within the immediate region of the step, and the final station which was approximately 1 foot downstream from the step.

Profile comparisons for both cases are quite good, particularly for the Mach number and velocity. In the total temperature comparison for the step-up case (Figure 67), the prediction follows the recovery of the profile well but has a larger "bump" near the wall in the third and fourth stations shown. Some of this is due to the initial difference in the profiles at the first station, and some may be due to the resolution of the data, that is, only the open points represent actual temperature probe data. The closest approach to the wall was 0.050 inch; all solid points shown inside this were calculated from pressure probe data. A data start prediction would have modeled the data slightly better through the step; however, the differences were not regarded as serious enough to warrant further computer solutions.

The linear-log velocity ratio profiles in Figures 69 and 75 also reflect good agreement. Comparisons for both the first and final profiles are shown.

* Personal communication with Dr. Robert Gran at TRW.

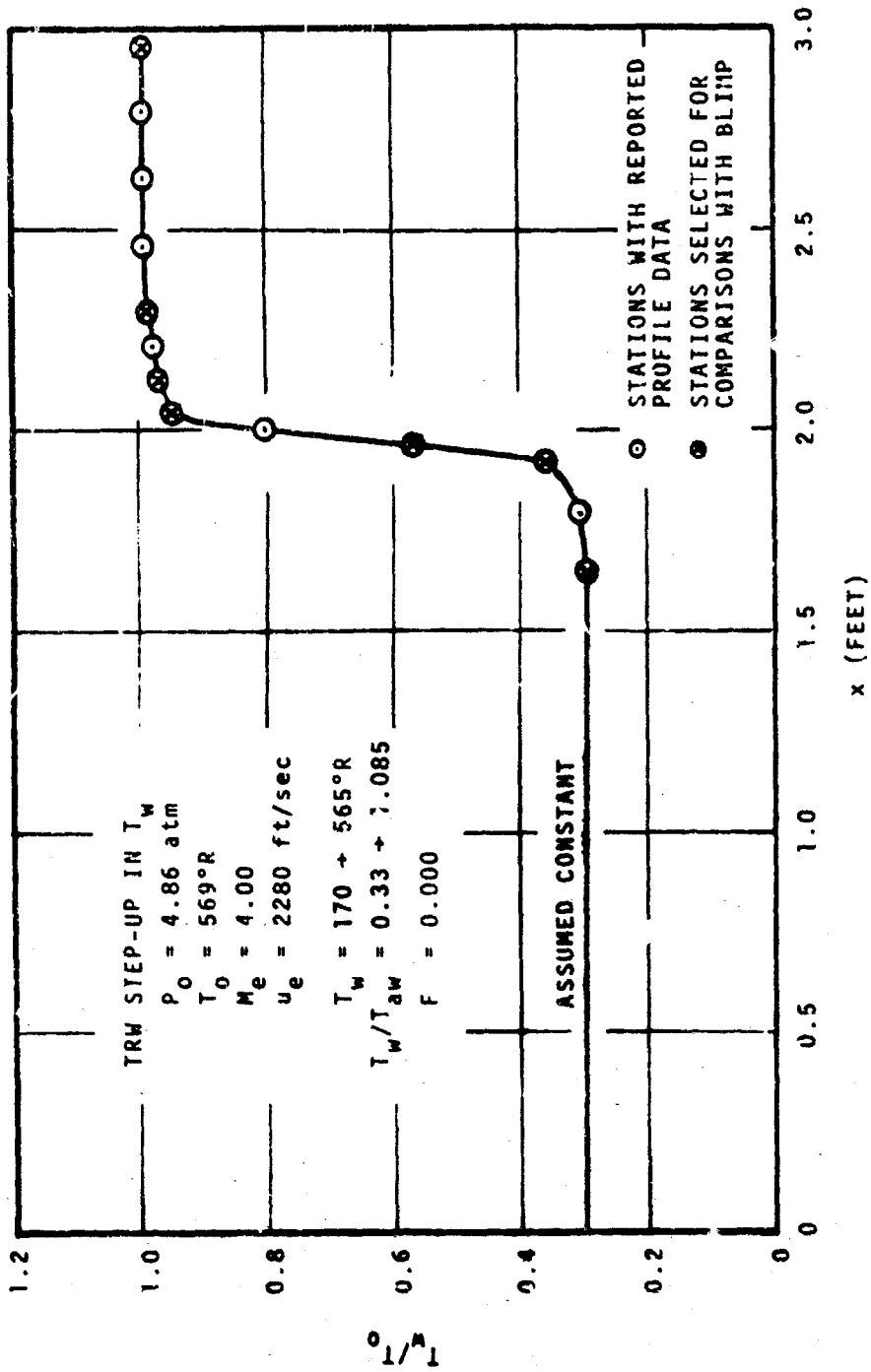


Figure 65. Wall Temperature vs X, Distance from Leading Edge of Cylinder
 TRW Step-Up in Wall Temperature

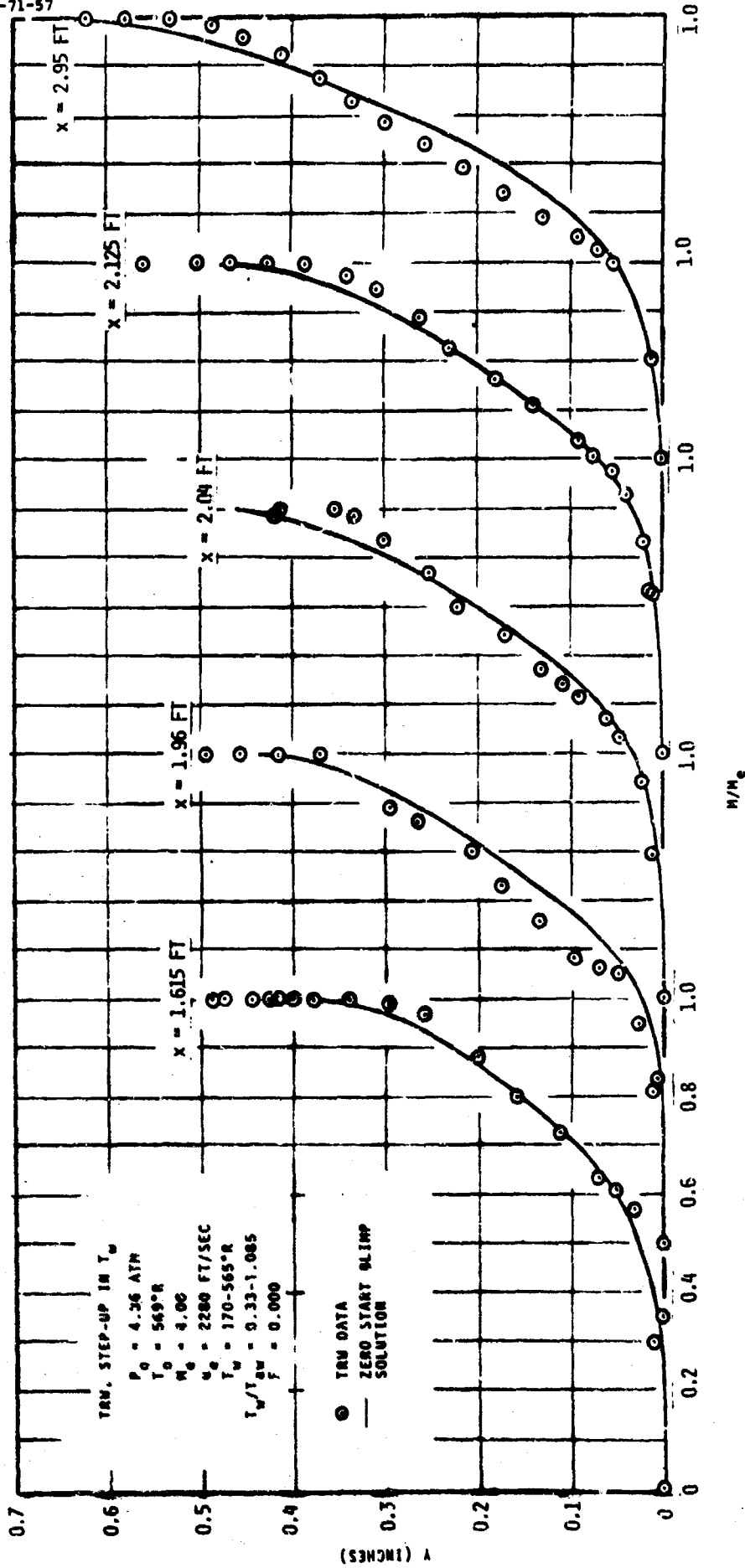


FIGURE 56. MACH NUMBER RATIO PROFILES TRW, STEP-UP IN WALL TEMPERATURE, SUPERSONIC

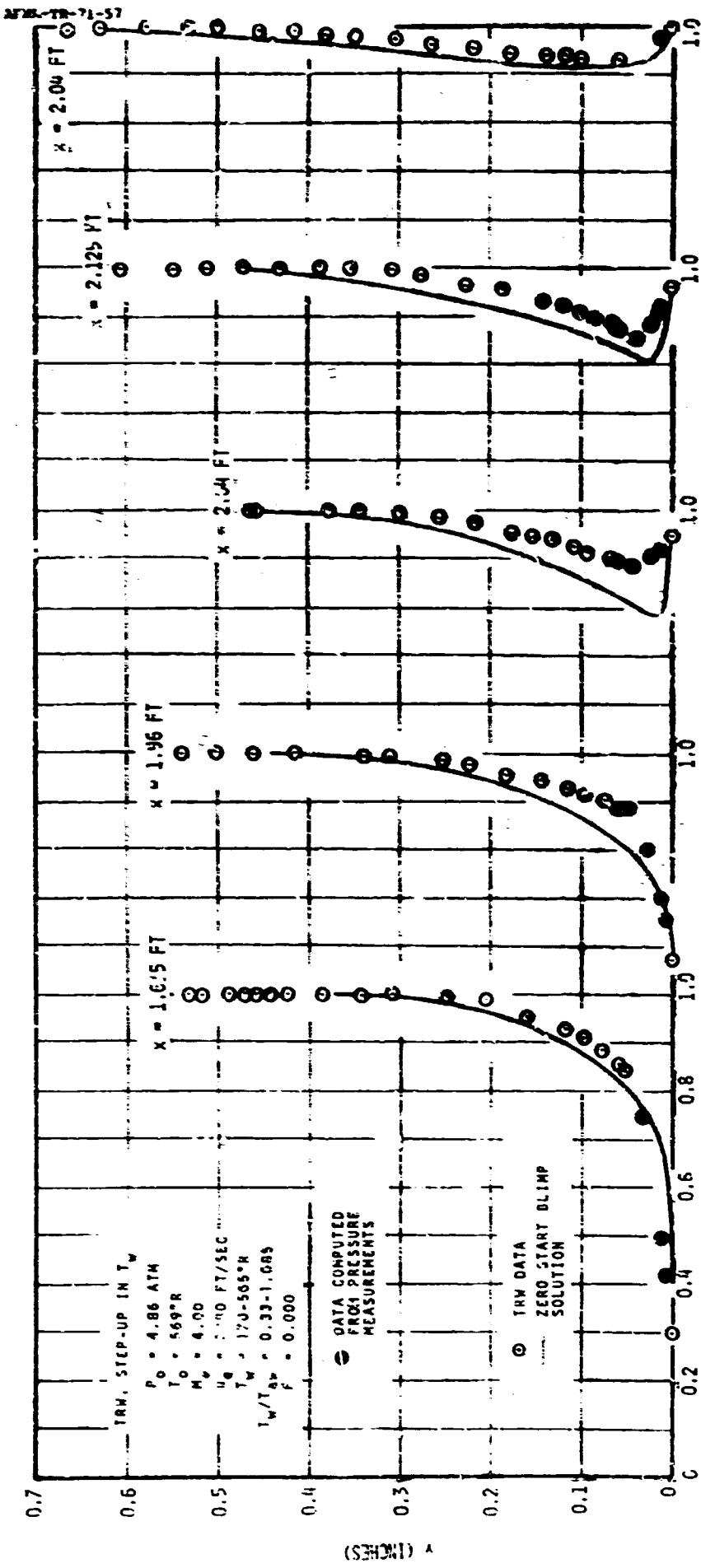


FIGURE 67. TOTAL TEMPERATURE RATIO PROFILES TRW, STEP-UP IN WALL TEMPERATURE, SUPERSONIC

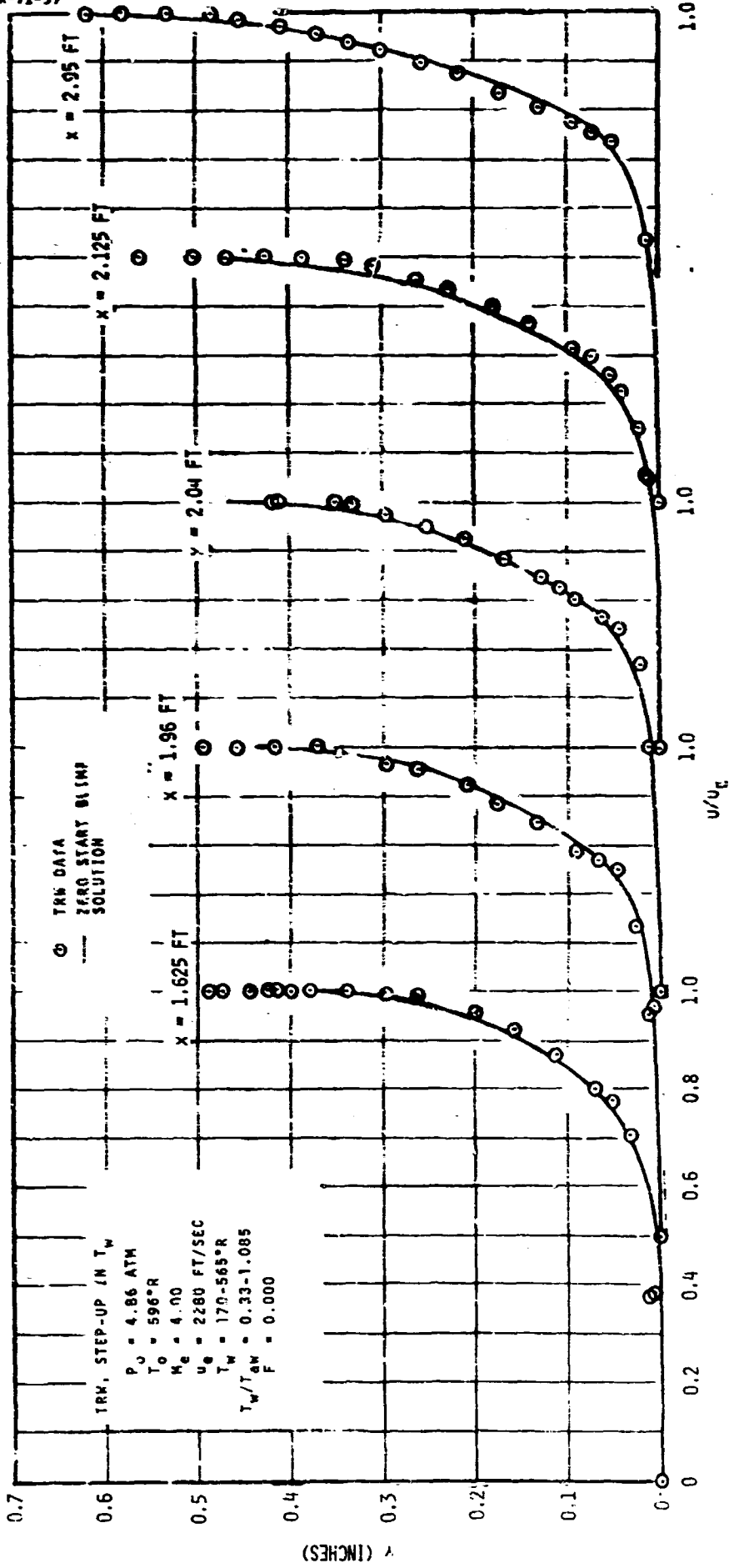


FIGURE 68. VELOCITY RATIO PROFILES TRW, STEP-UP IN WALL TEMPERATURE, SUPERSONIC

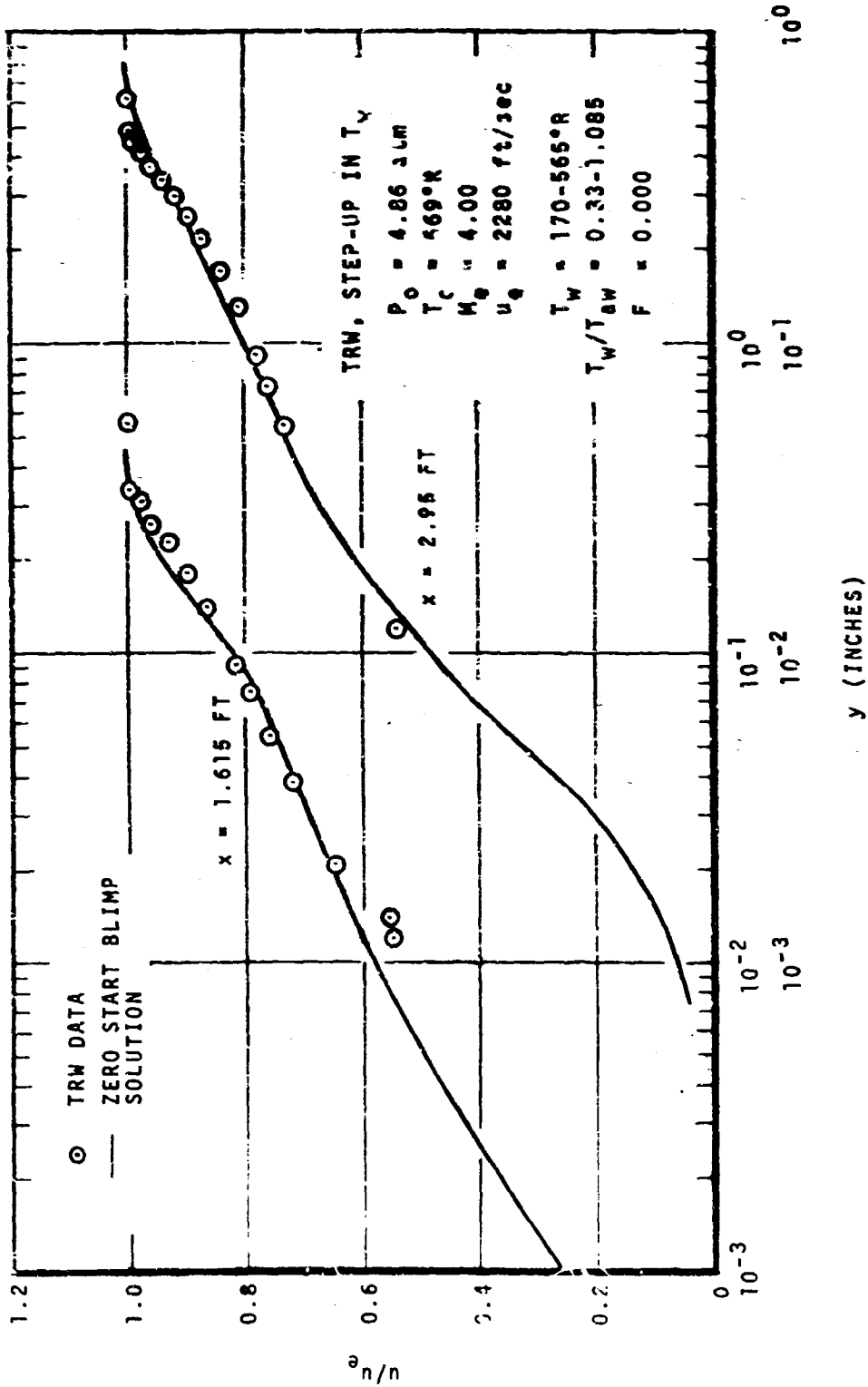


Figure 69. Linear-Log Velocity Ratio Profiles TRW, Step-Up in Wall Temperature, Supersonic

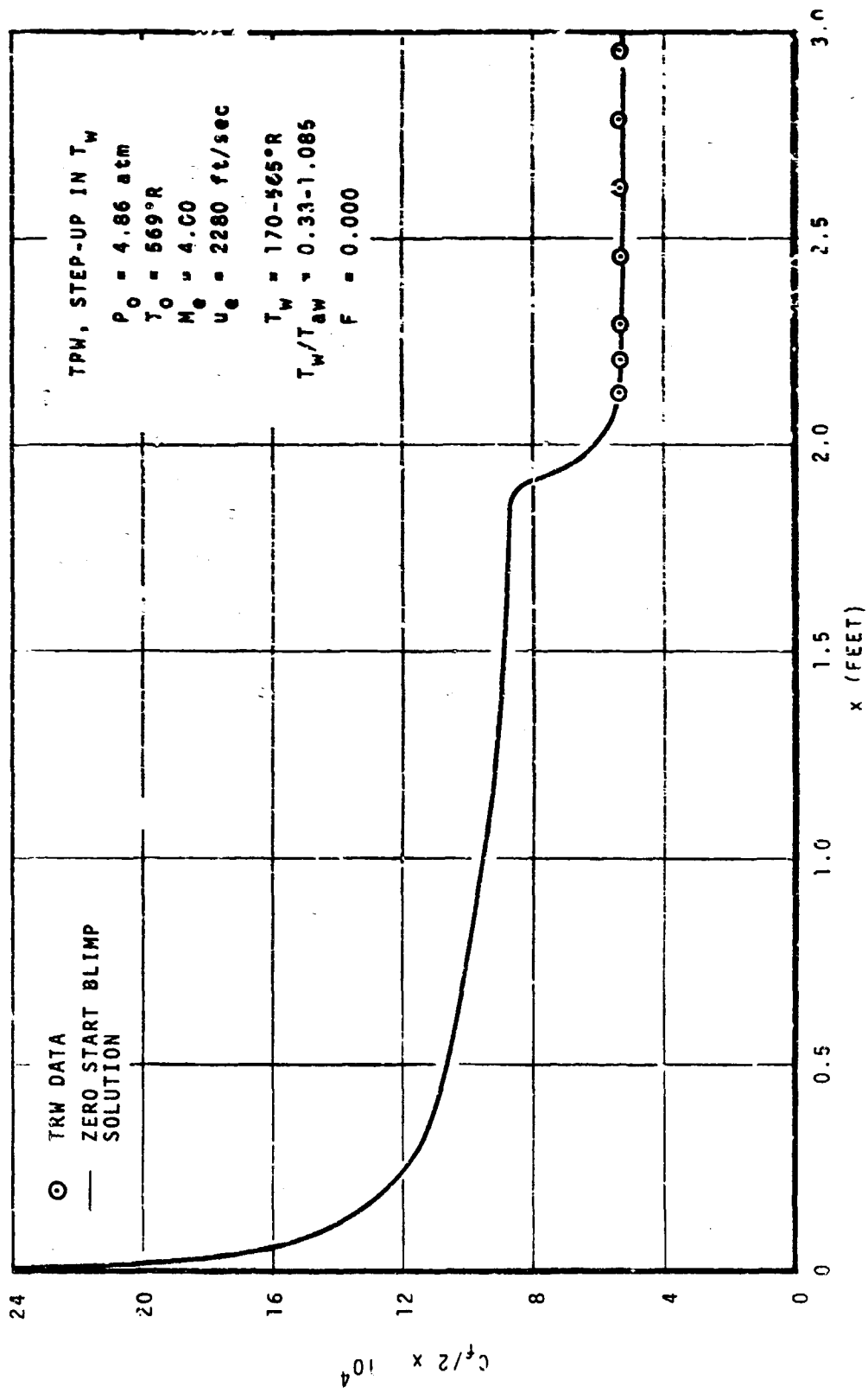


Figure 70. Skin Friction Coefficient vs Streamwise Location TRW, Step-Up in Wall Temperature, Supersonic

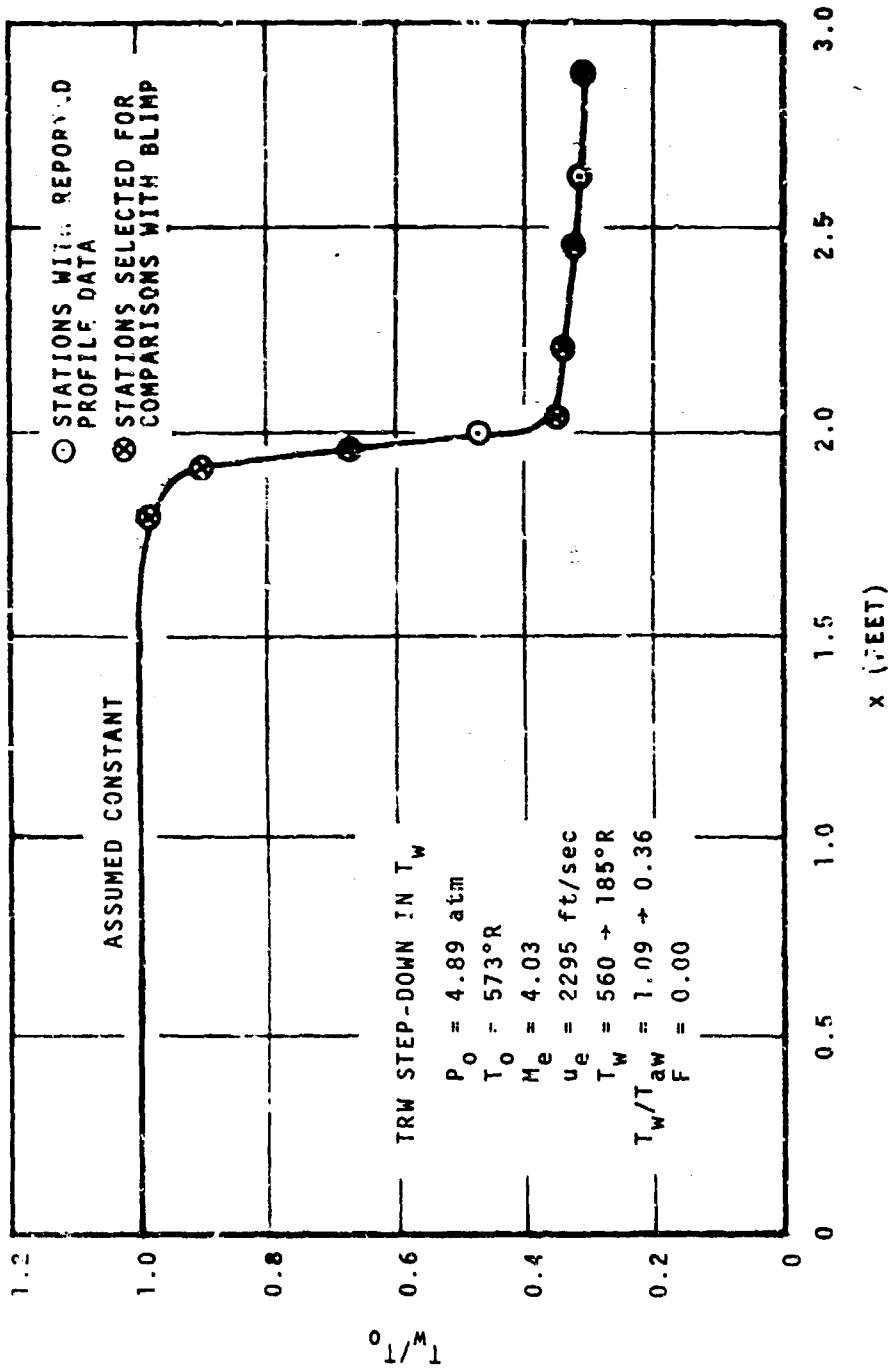


Figure 71. Wall Temperature vs X, Distance from Leading Edge of Cylinder
TRW Step-Down in Wall Temperature

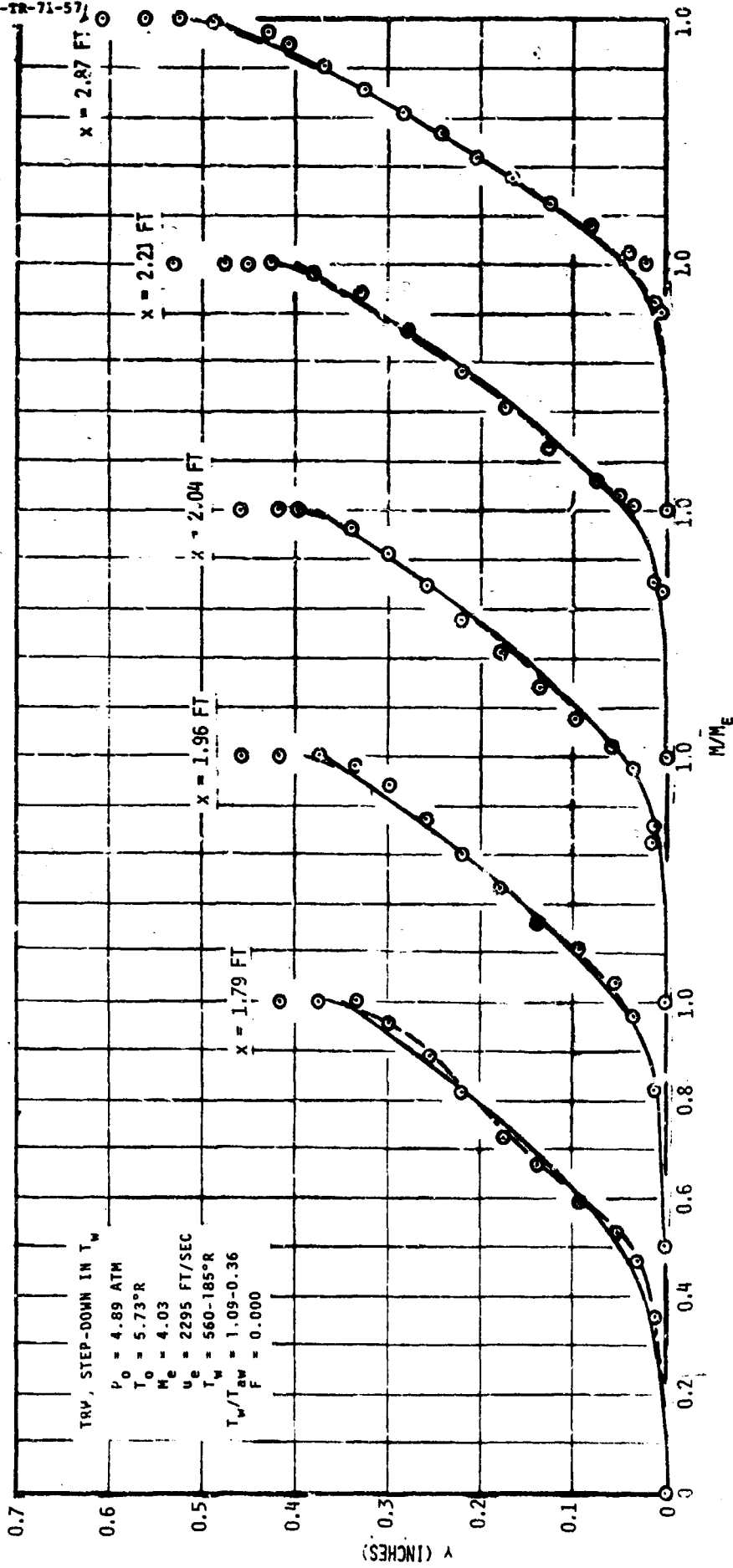


FIGURE 72. MACH NUMBER RATIO PROFILES
TRV, STEP-DOWN IN WALL TEMPERATURE, SUPERSONIC

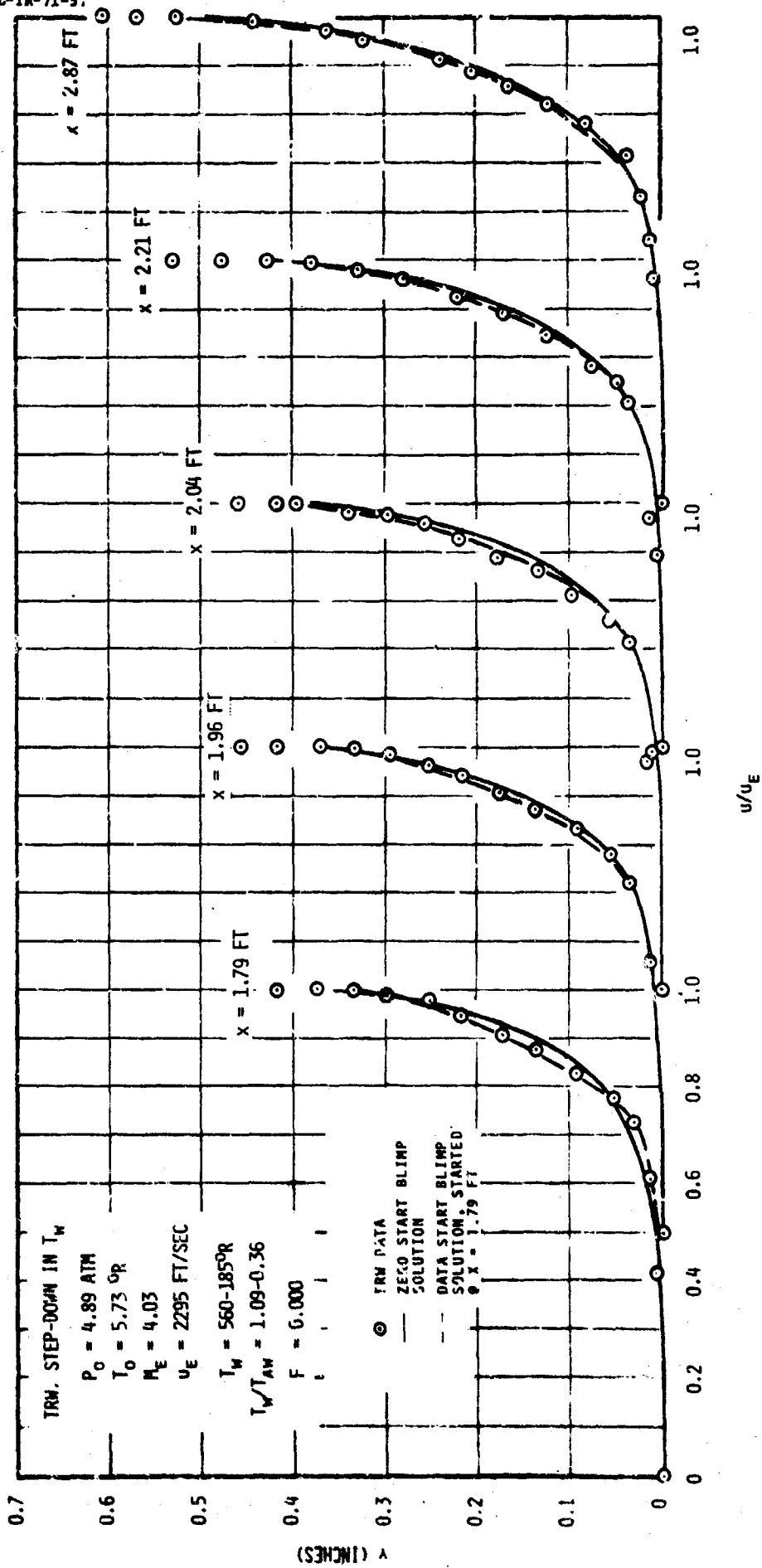


FIGURE 74. VELOCITY RATIO PROFILES
TRM, STEP-DOWN IN WALL TEMPERATURE, SUPERSONIC.

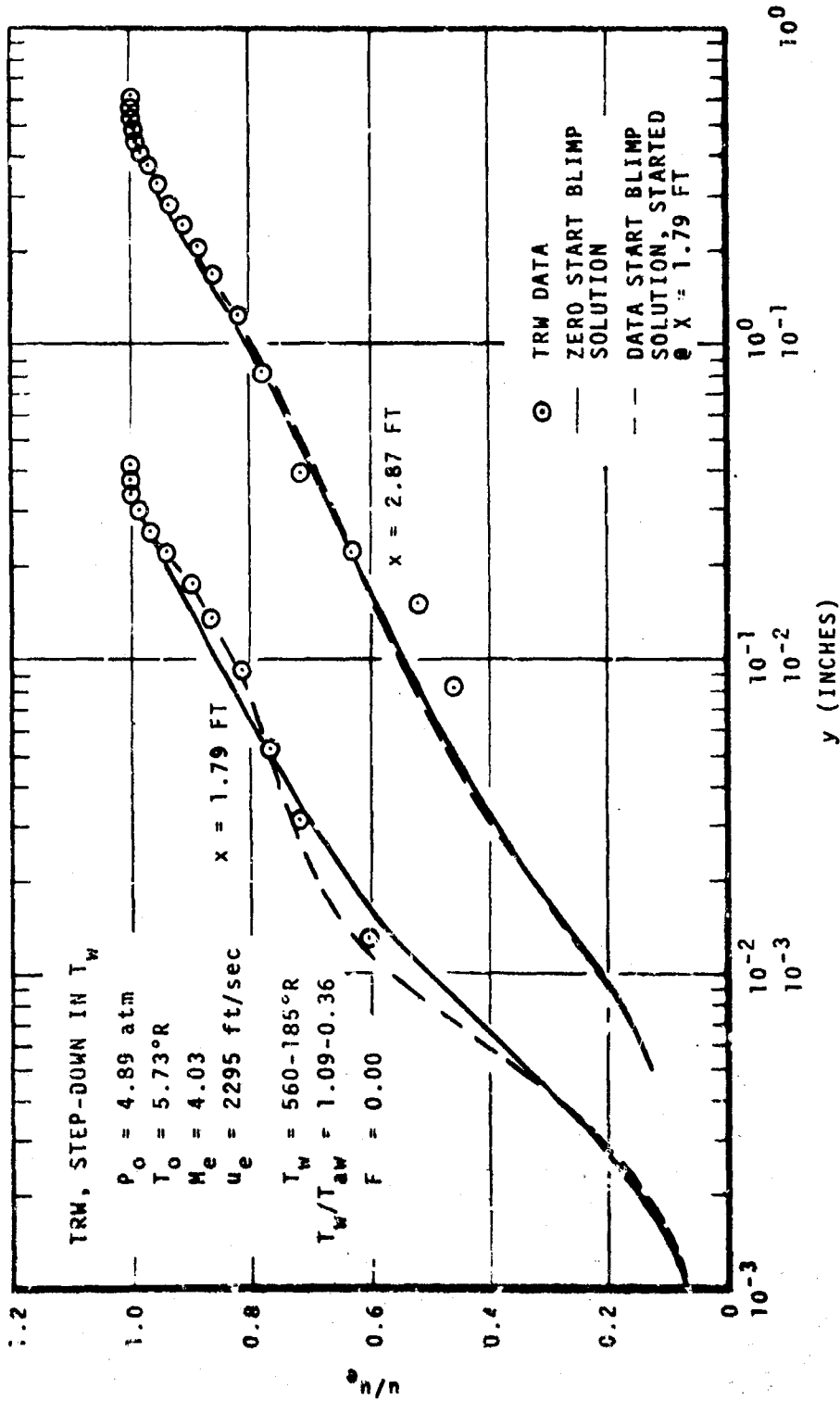


Figure 75. Linear-Log Velocity Ratio Profiles TRW, Step-Down in Wall Temperature, Supersonic

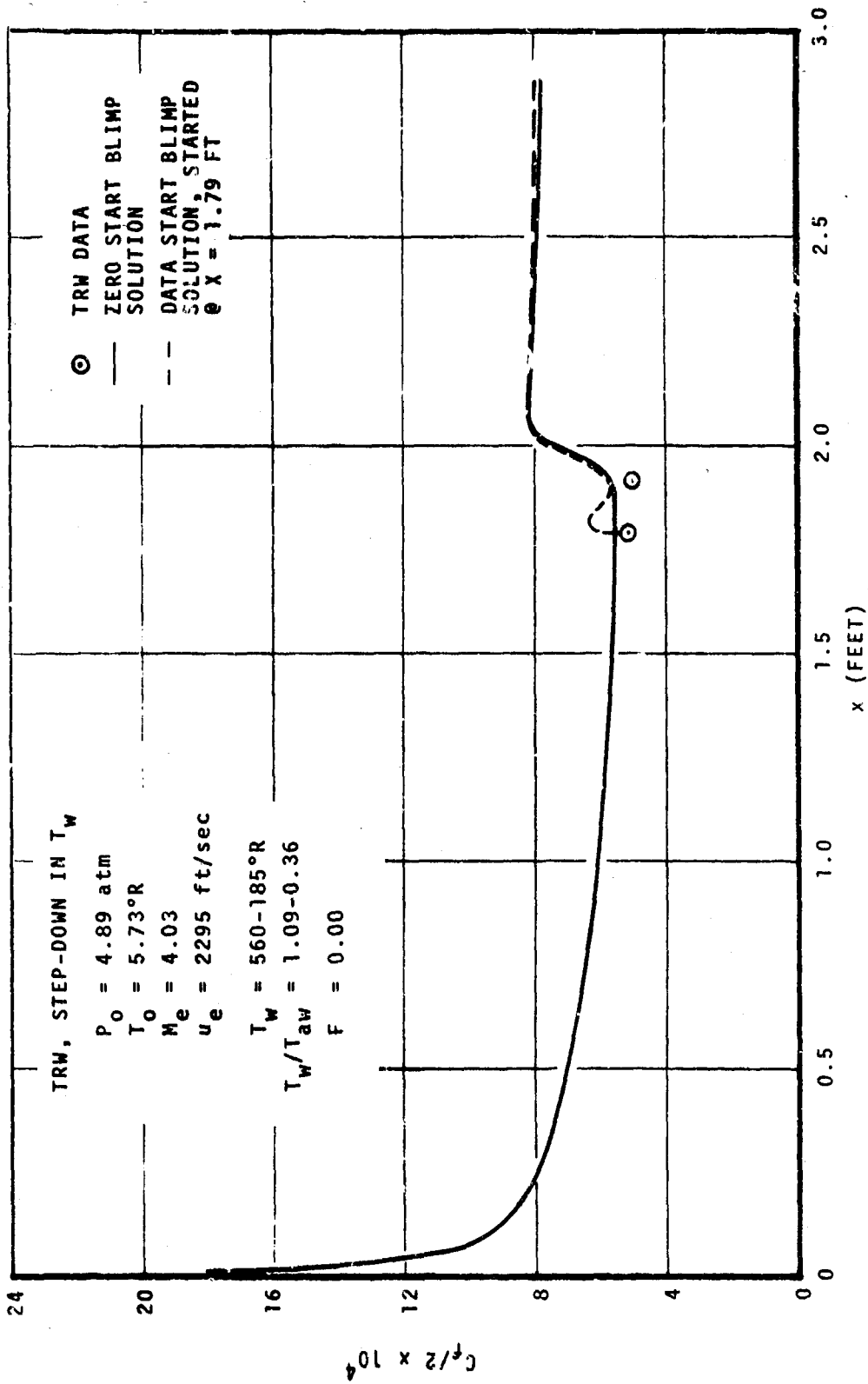


Figure 76. Skin Friction Coefficient vs Streamwise Location TRW, Step-Down in Wall Temperature, Supersonic

Note that staggered scales are used on the abscissa. Closest approach of the 3.618 inch thick total pressure probe was 0.009 inch, a distance well outside the predicted laminar sublayer.

Finally, the $C_f/2$ plots of Figures 70 and 76 show excellent agreement between the available near-wall region Stanton tube and predicted values. The response of the $C_f/2$ prediction to the step follows the variation in wall temperature (Figures 65 and 71) with no noticeable lag, indicating the weak dependence of the laminar sublayer on the outer portion of the profile.

d. Stanford Comparisons

(1) Comments on BLIMP Input

Freestream and wall conditions were maintained constant within several percent along the test section for all Simpson runs used herein. In three of these runs (no blowing, $F = 0.002$, and step-up in blowing), averaged constant streamwise pressures, wall temperatures and blowing mass flow rates were input. For the other two runs, the actual reported values at each of the four stations were used. All predictions were started at $X = 0$ defined as the leading edge of the test section. The virtual origin resulting from the use of a trip was located essentially at the leading edge of the test section.

(2) Comments on Results

Results of Stanford comparisons are plotted in Figures 77-90. Only velocity ratio profile comparisons are included since all tests chosen were essentially adiabatic at the wall with temperature variations across the boundary layer limited to a few percent. Comparisons are presented at each of the four stations reported. These are at stations between $x = 1.5$ and $x = 2.5$ feet. Station locations are not the same for every test and are noted on each plot. For Figures 85 and 86, the step in blowing occurs at $x = 5.02$ feet. Re_δ and C_f comparisons are presented in a group (Figures 87-90) following the profiles. The four constant blowing runs are plotted together in Figures 87 and 90.

Overall profile shapes are in reasonably good agreement at all blowing rates (see Figures 77-86); however, the prediction indicates progressively higher values in the mid-range of the profile as the boundary layer proceeds downstream following quite good agreement at the initial station. (Due to this initial matching, data start runs were unnecessary.) This trend is confirmed in the Re_δ plots of Figures 87 and 89 which indicate slightly higher values of δ for the measured data. It is also reflected in $C_f/2$ comparisons in Figures 89 and 90. As is well known, minor errors in δ calculation can result in enormous errors in calculated drag coefficient for flows

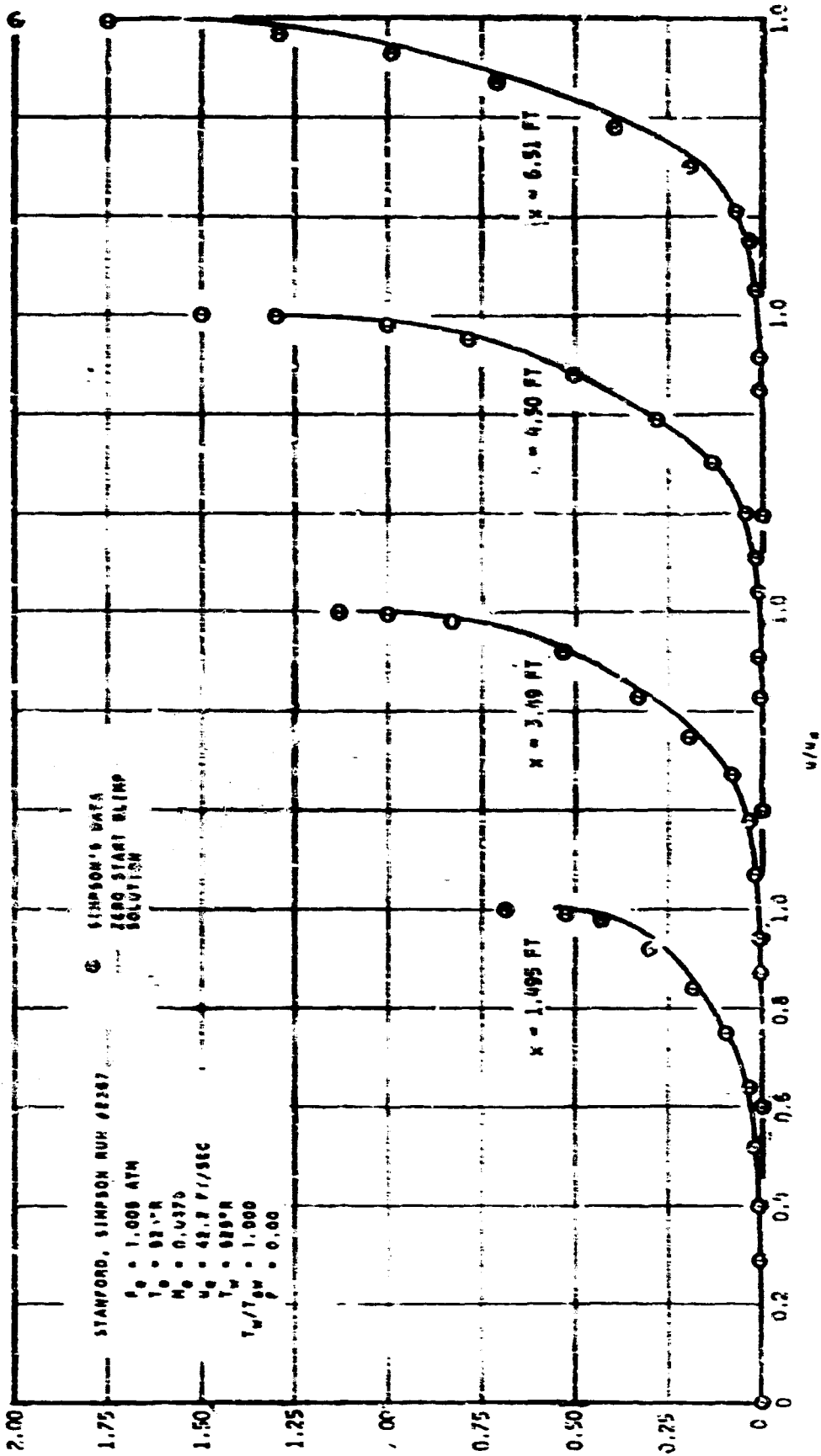


FIGURE 77. VELOCITY RATIO PROFILES
 STANFORD, SIMPSON RUI #2367, SUPSONIC, NO BLOWING

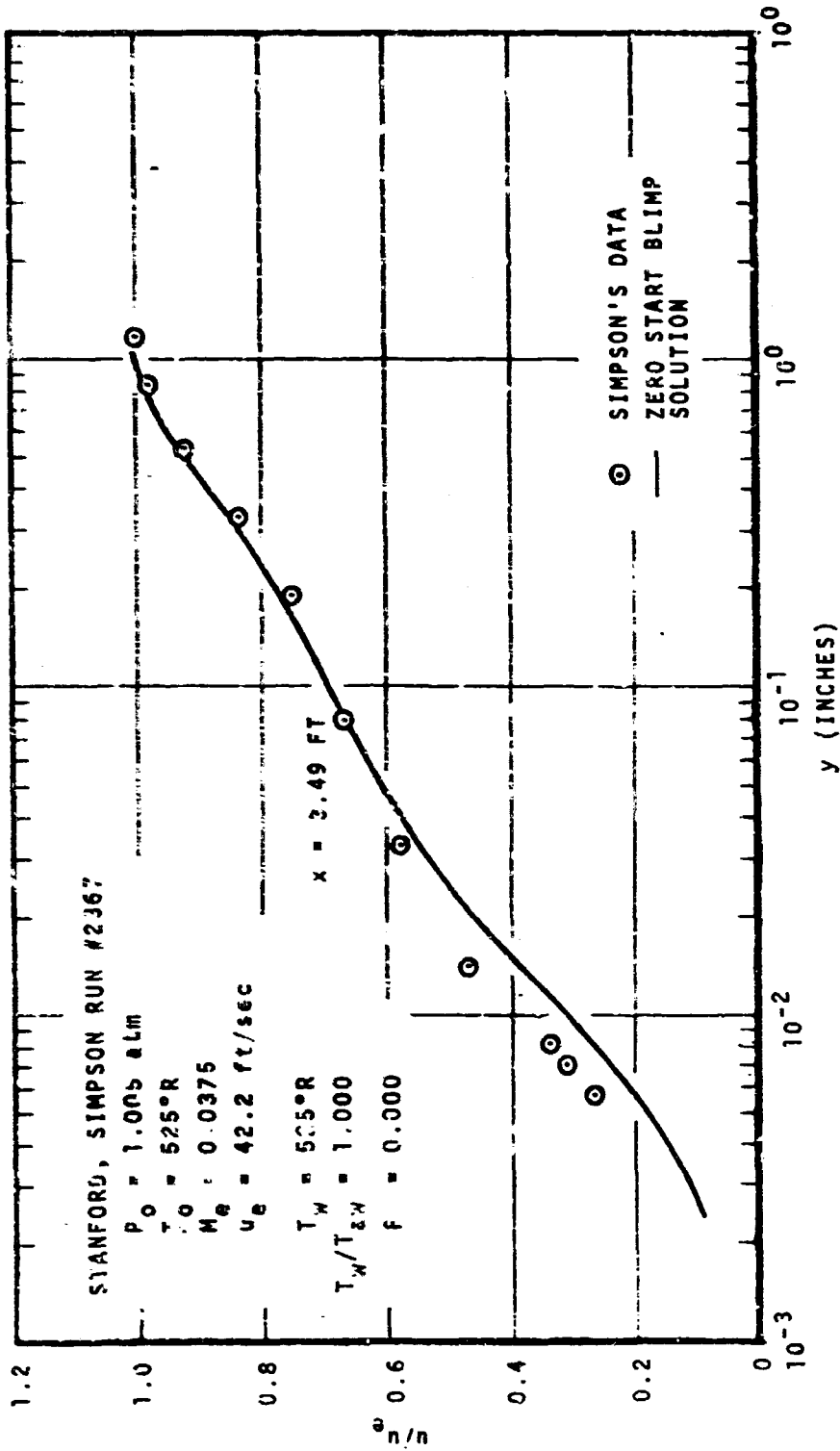


Figure 78. Linear-Log Velocity Ratio Profiles
Stanford, Simpson Run #2367, Subsonic, No Blowing

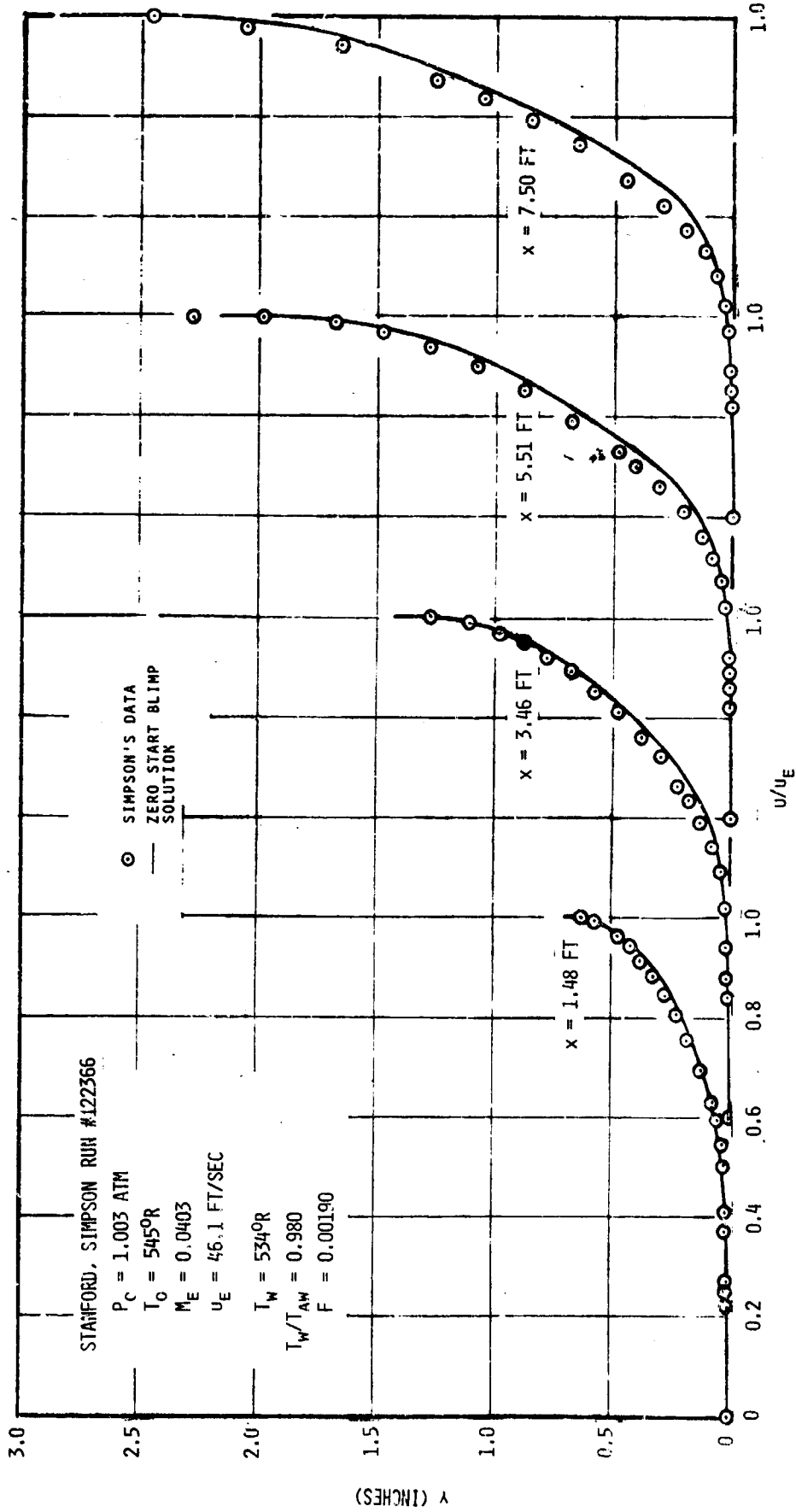


FIGURE 79. VELOCITY RATIO PROFILES
STANFORD, SIMPSON RUN #122366, SUBSONIC, $F = 0.002$

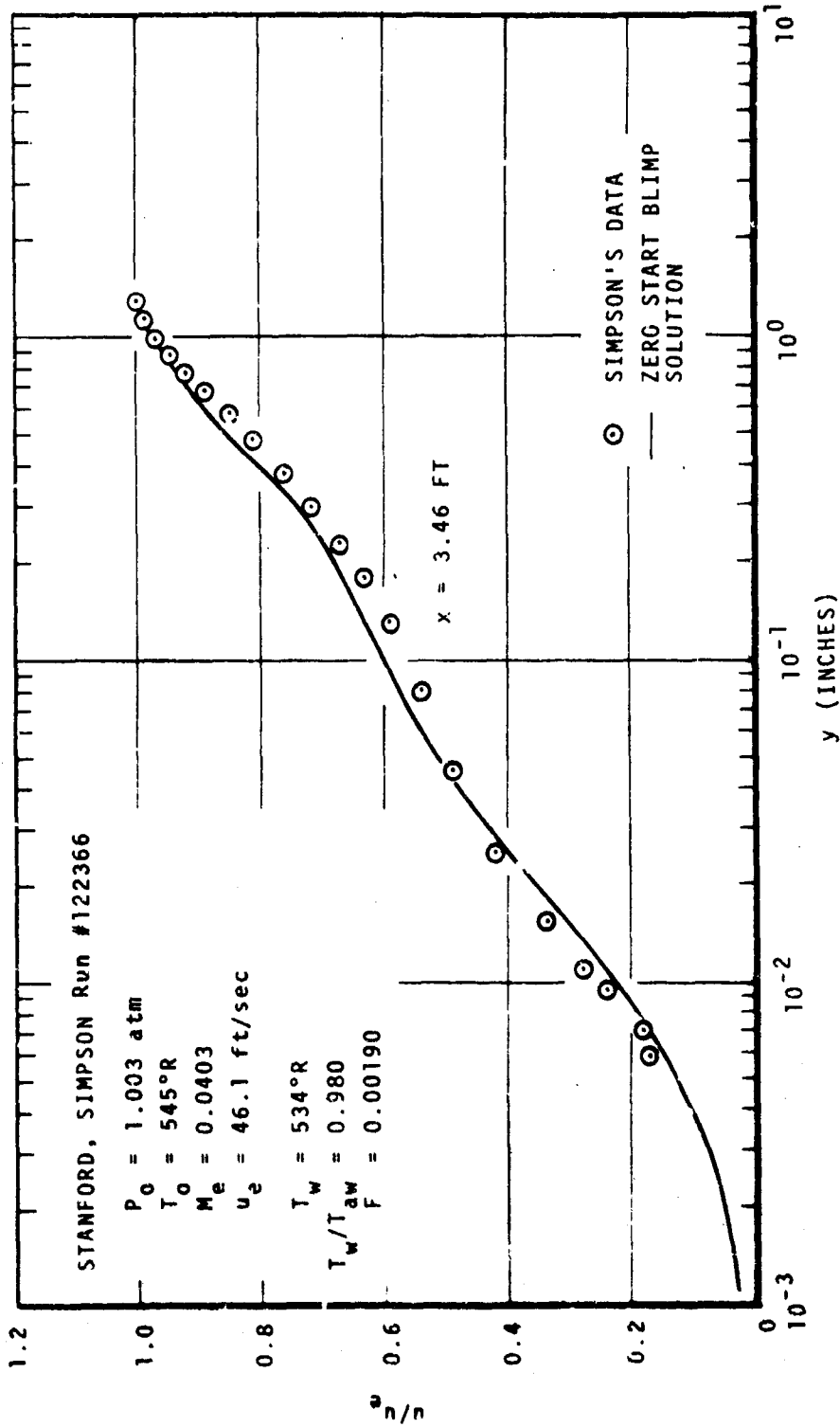


Figure 80. Linear-Log Velocity Ratio Profiles
 Stanford, Simpson Run #122366, Subsonic, $F = 0.002$

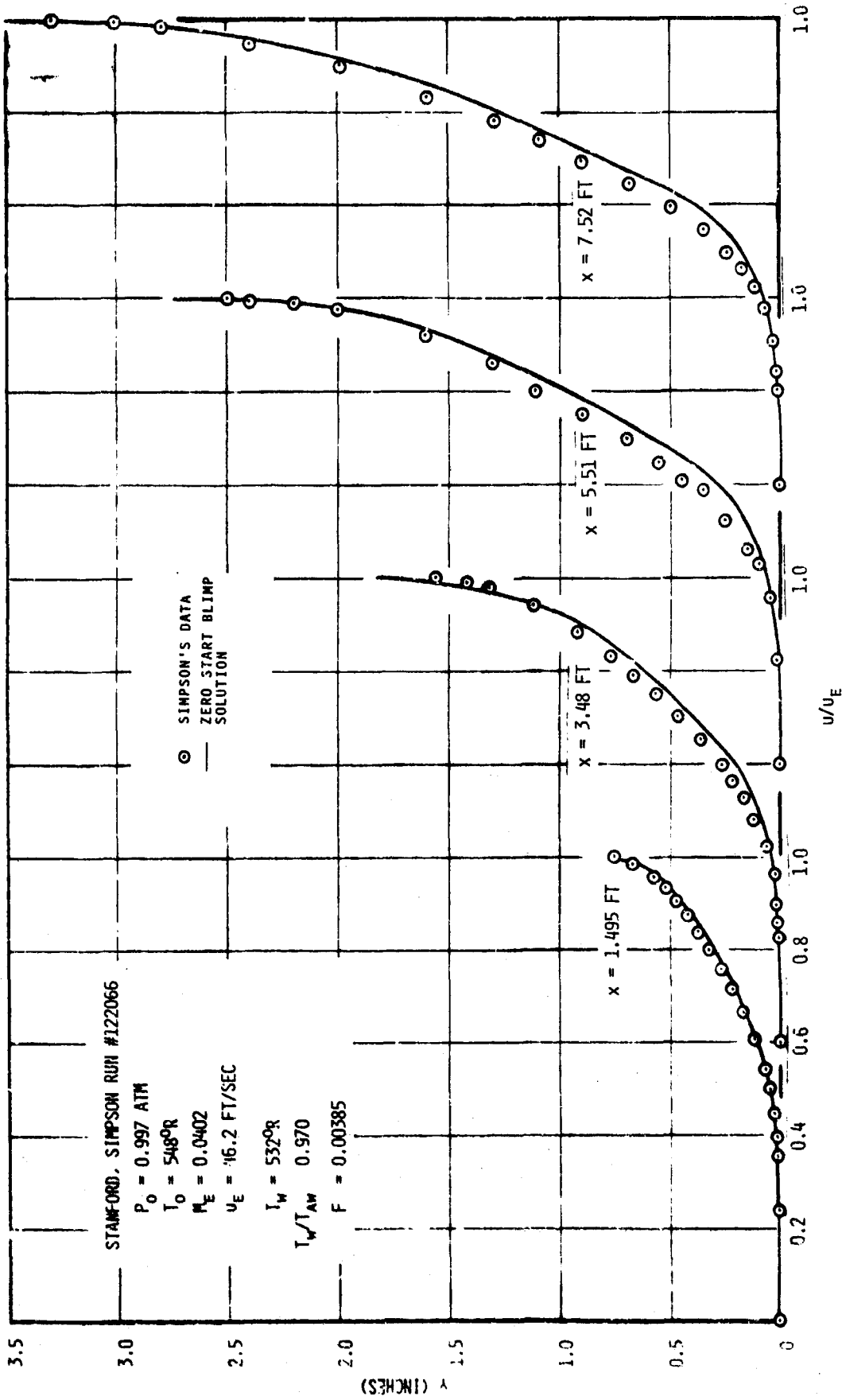


FIGURE 81. VELOCITY RATIO PROFILES
STAMFORD, SIMPSON RUN #122066, SUBSONIC, $F = 0.004$

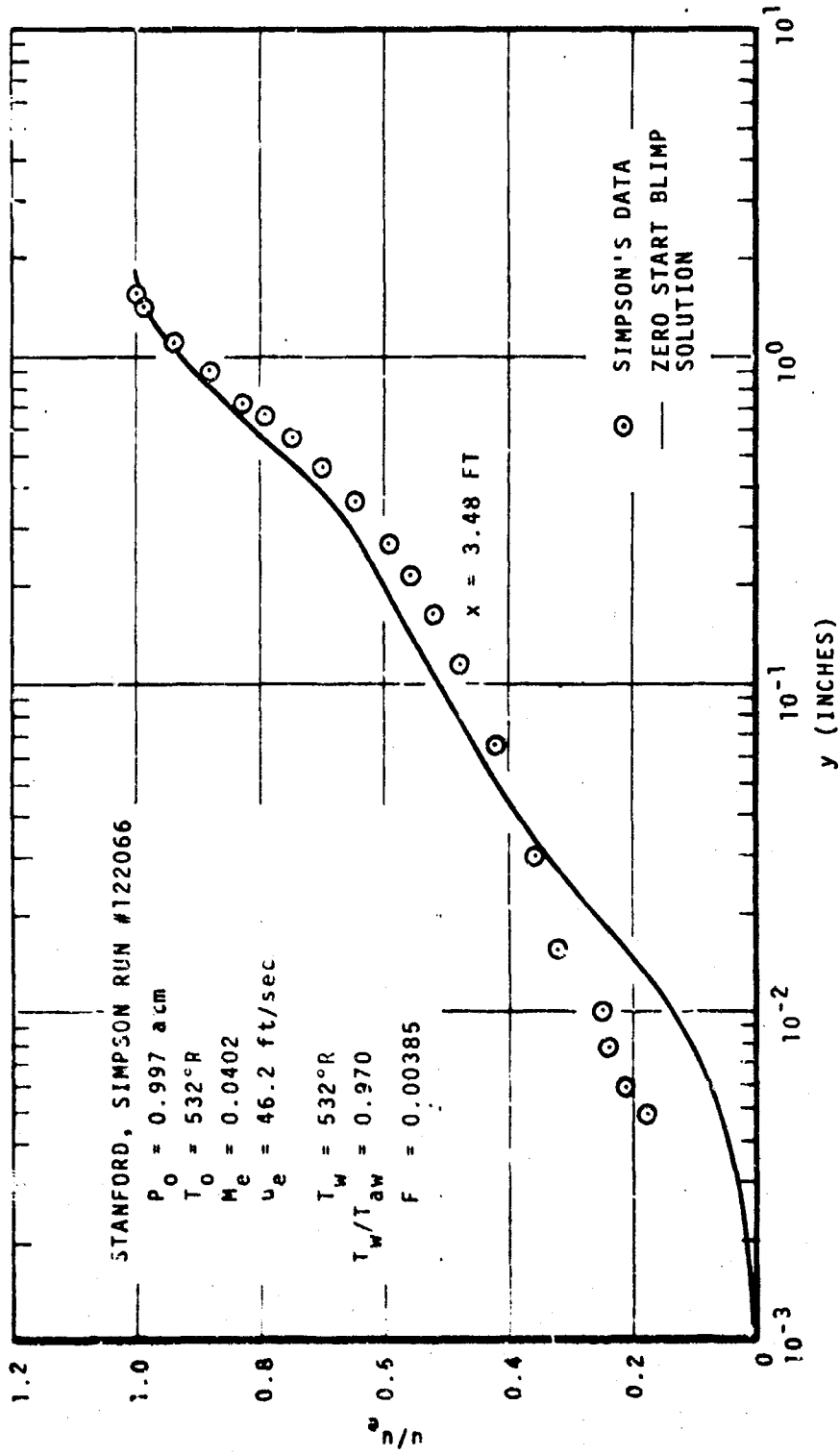


Figure 82. Linear-velocity Velocity Ratio Profiles
 Stanford, Simpson Run #122066, Subsonic, $F = 0.004$

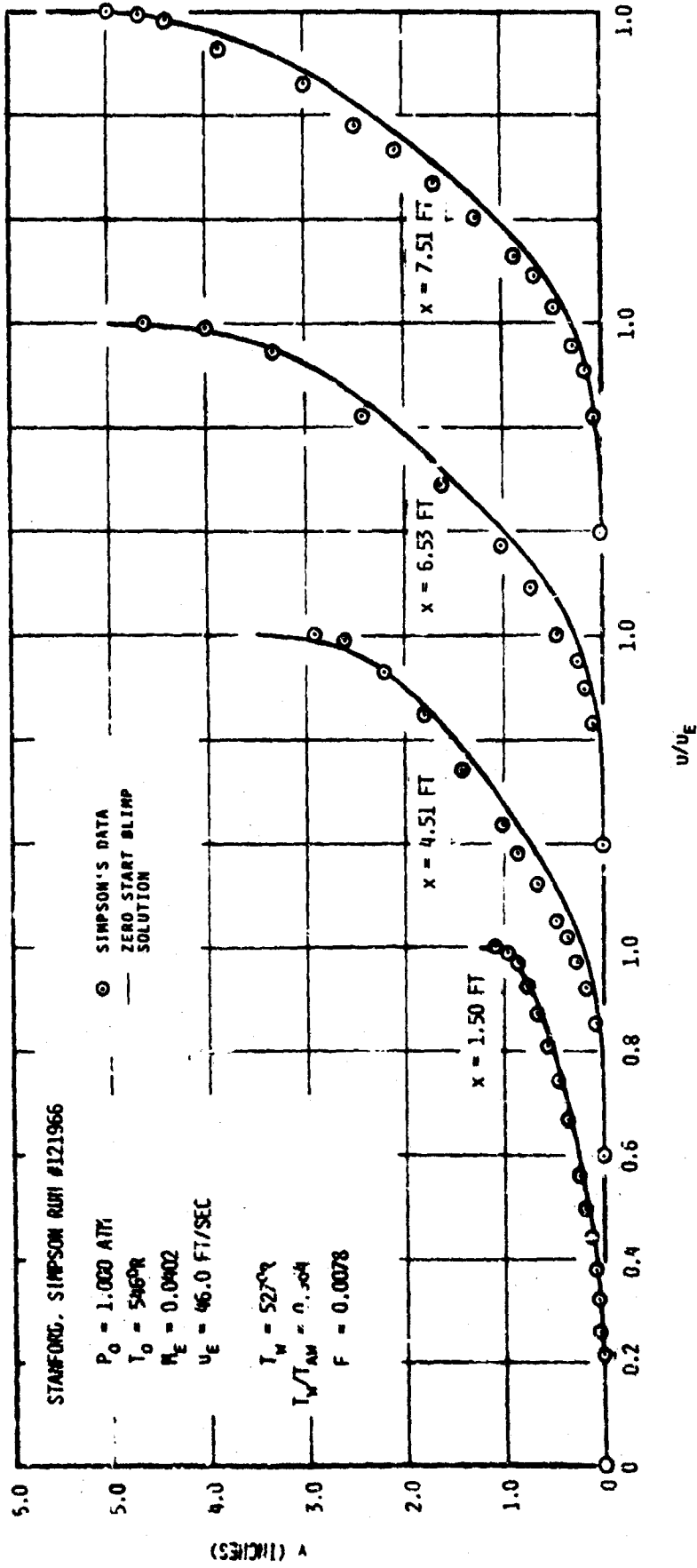


FIGURE 83. VELOCITY RATIO PROFILES
STANFORD, SIMPSON RUN #121966. SUBSONIC. $F = 0.008$

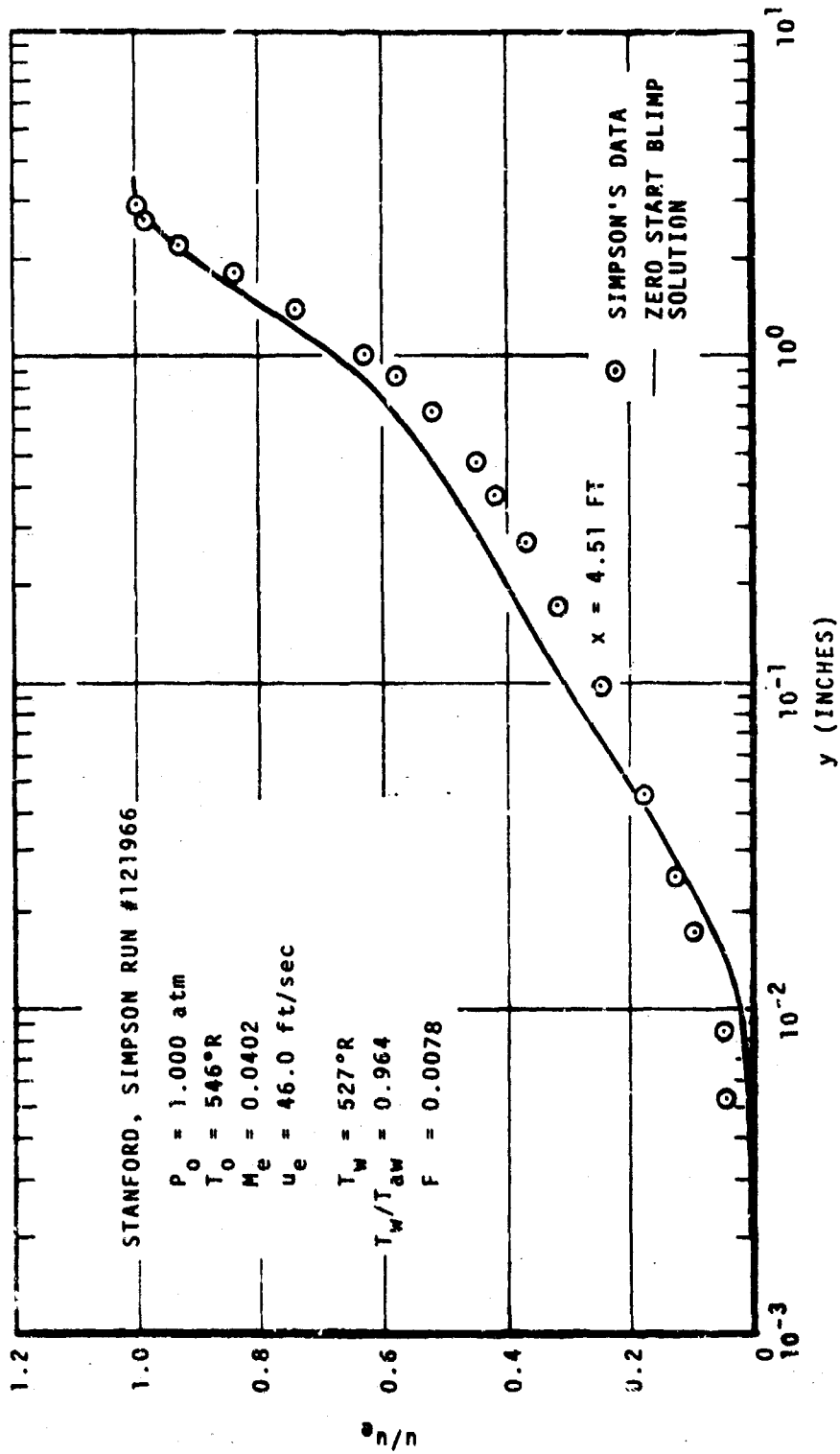


Figure 84. Linear-Log Velocity Ratio Profiles
Stanford, Simpson Run #121966, Subsonic, $F = 0.008$

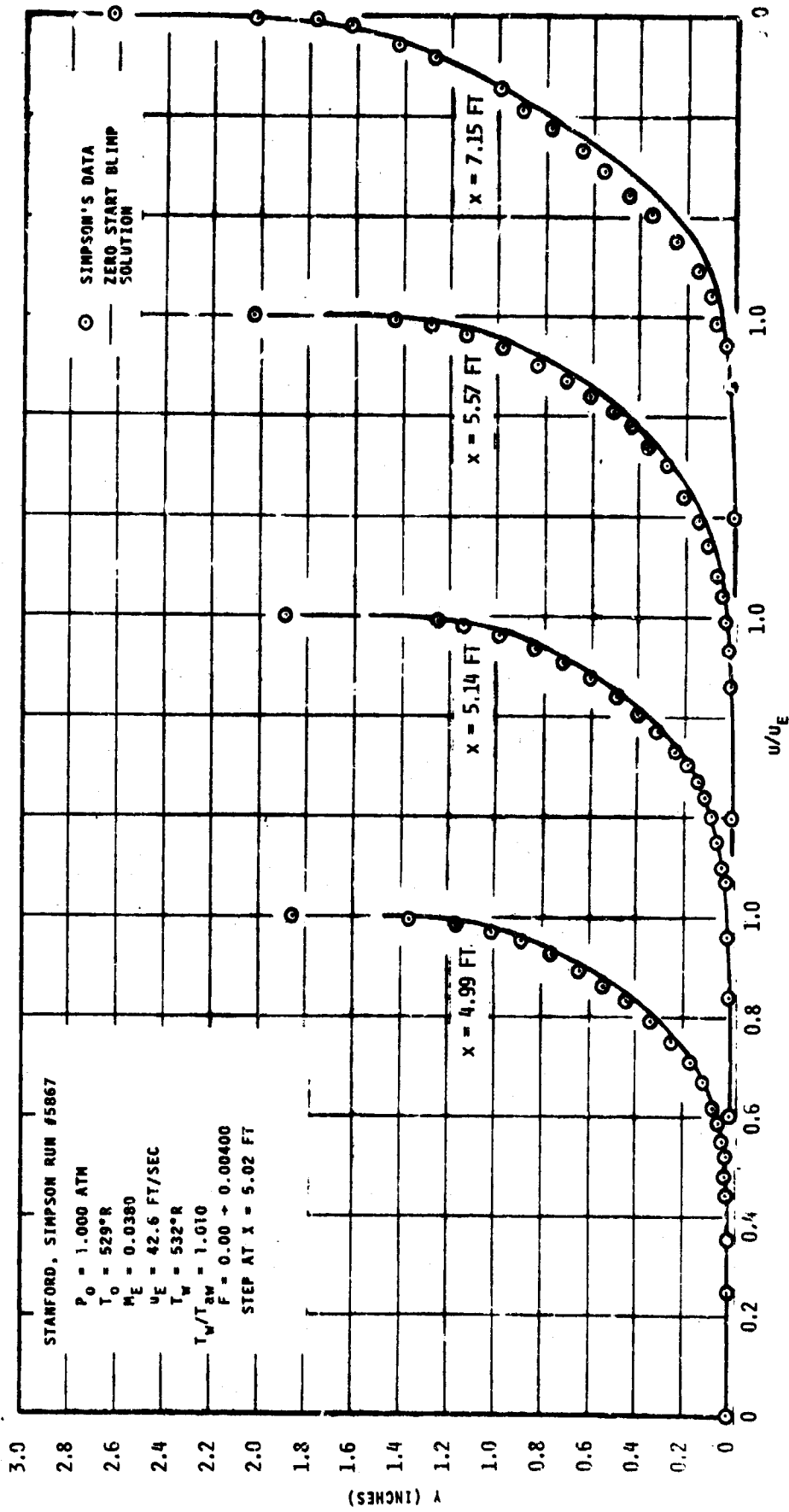


FIGURE 85. VELOCITY RATIO PROFILES
STANFORD, SIMPSON RUN #5867, SUBSONIC, STEP-UP IN BLOWING

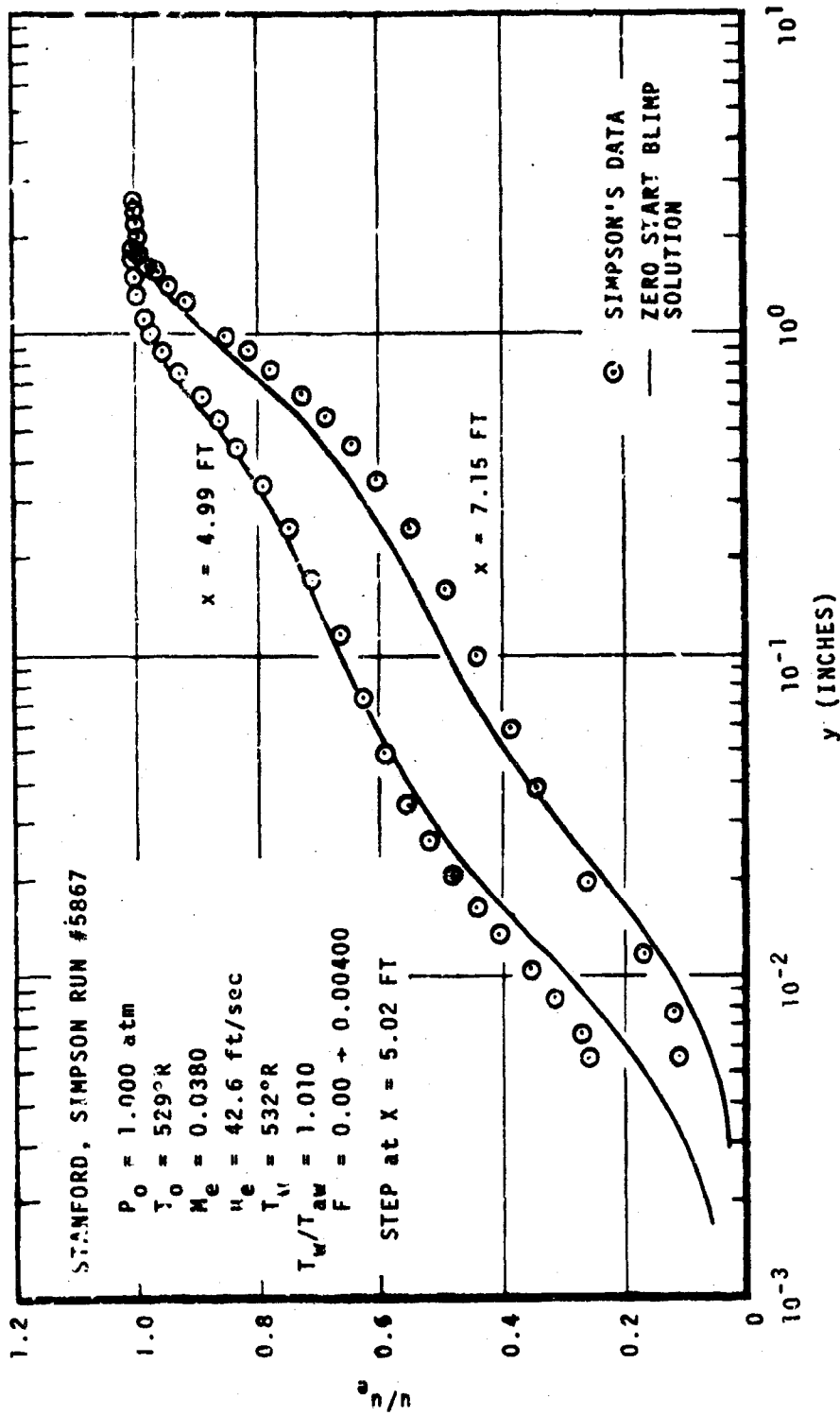


Figure 86. Linear-Log Velocity Ratio Profiles
Stanford, Simpson Run #5867, Step-Up in Blowing

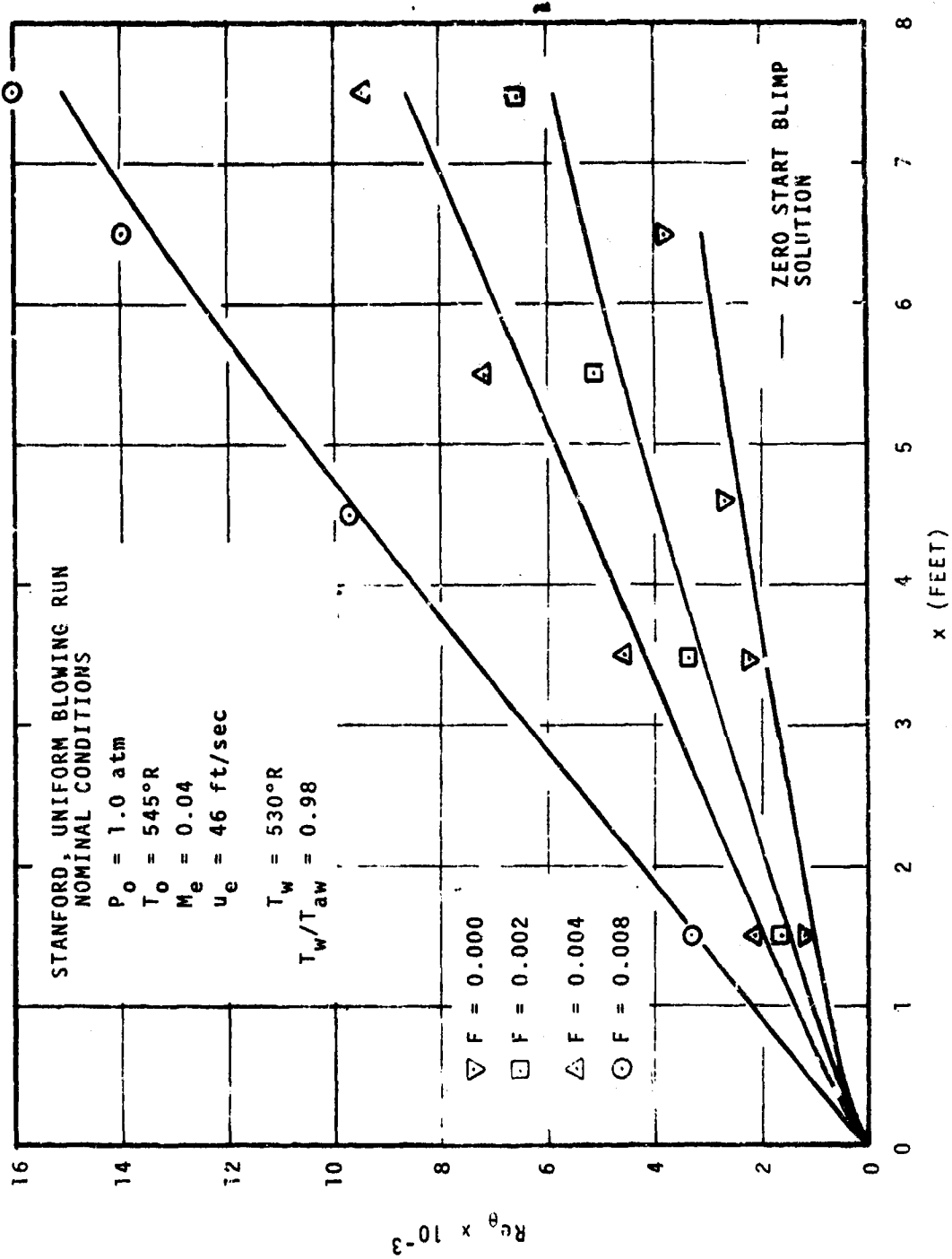


Figure 87. Momentum Thickness Reynolds Number vs Streamwise Location Stanford, Uniform Blowing Runs, Subsonic

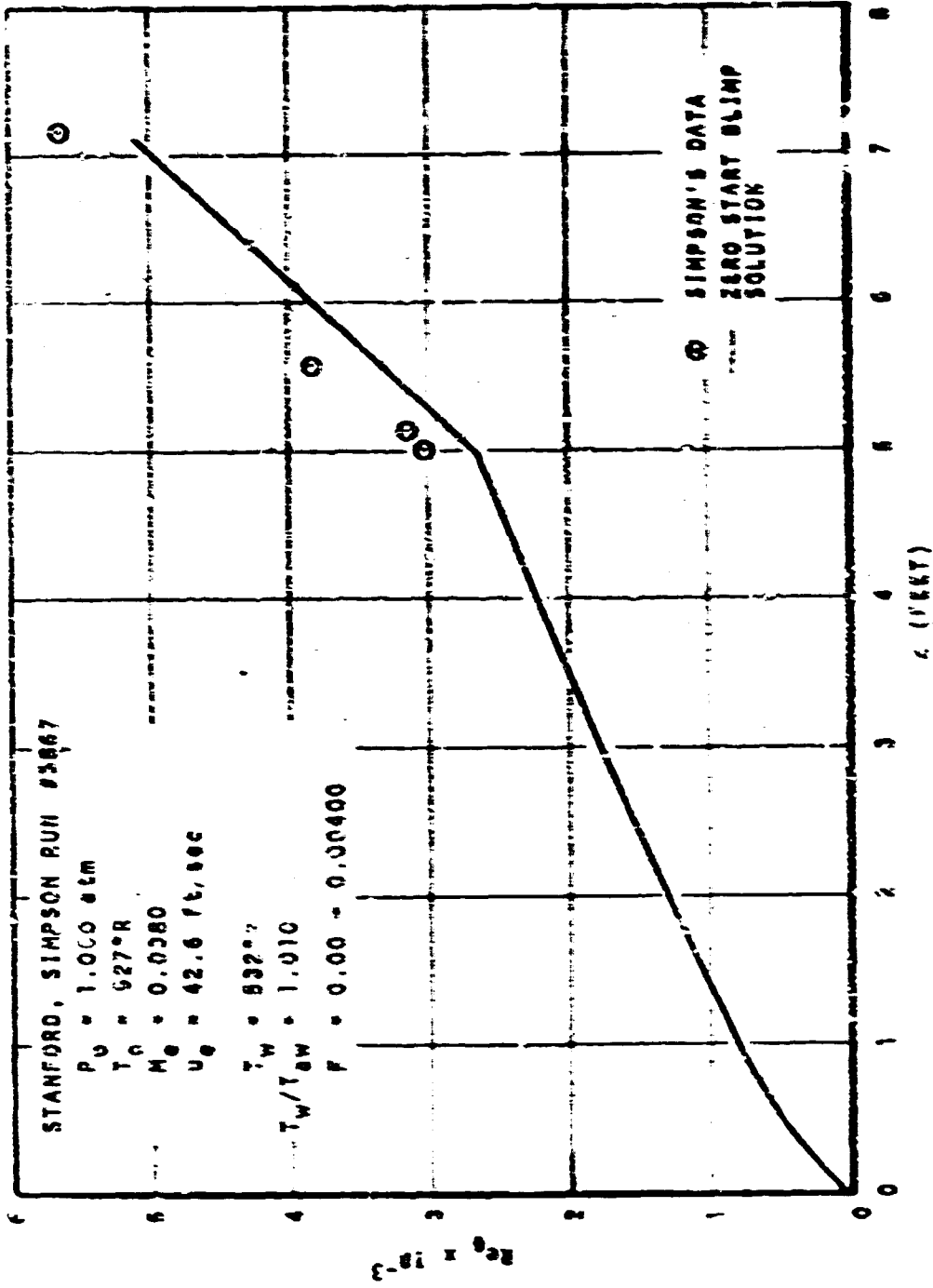


Figure 88. Momentum Thickness Reynolds Number vs Streamwise Location Beamford, Simpson Run #3867, Simulator, Step-Up in Blowing

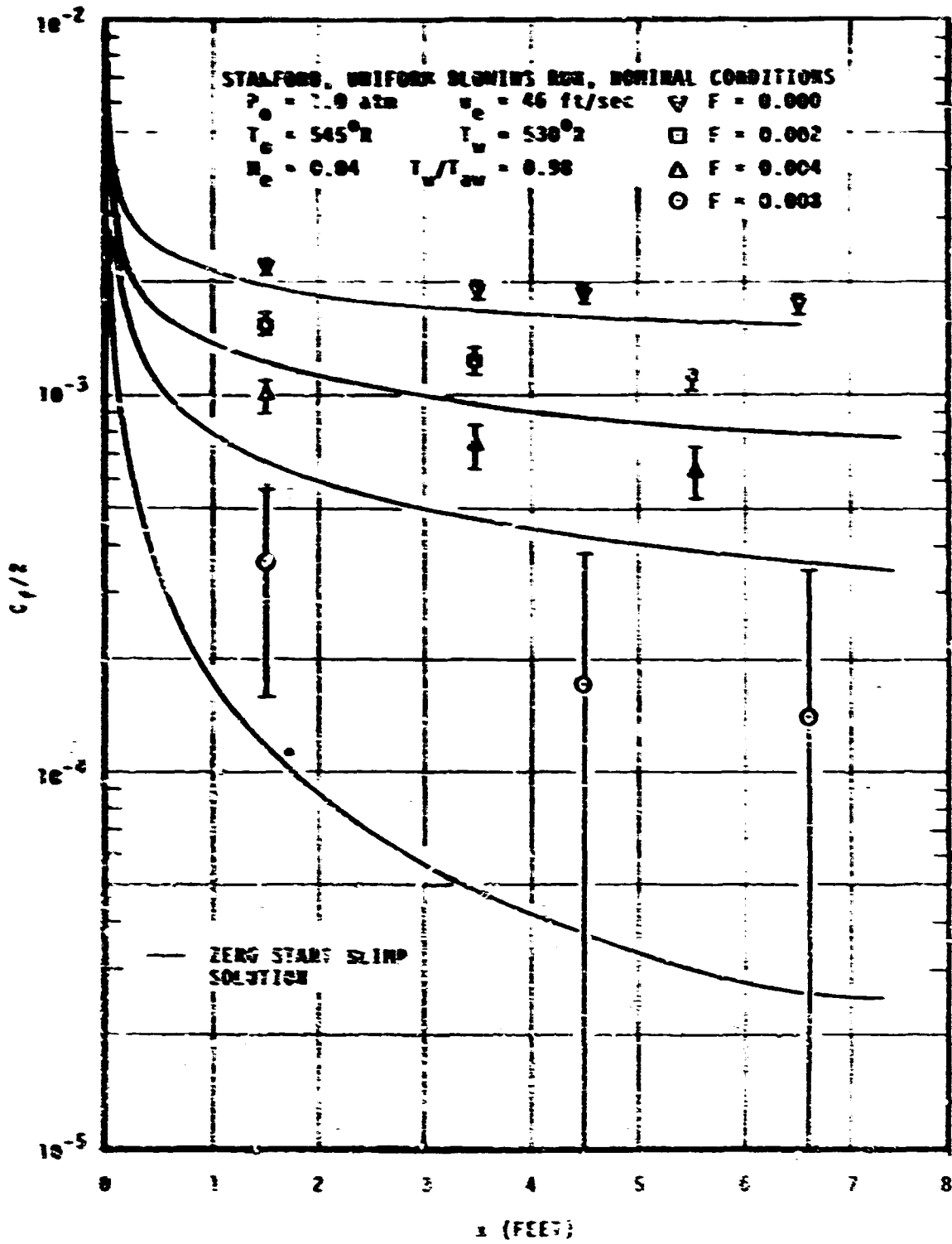


Figure 45. Skin Friction Coefficient vs Streamwise Location
 Stalford, Uniform Blowing Runs, Subsonic

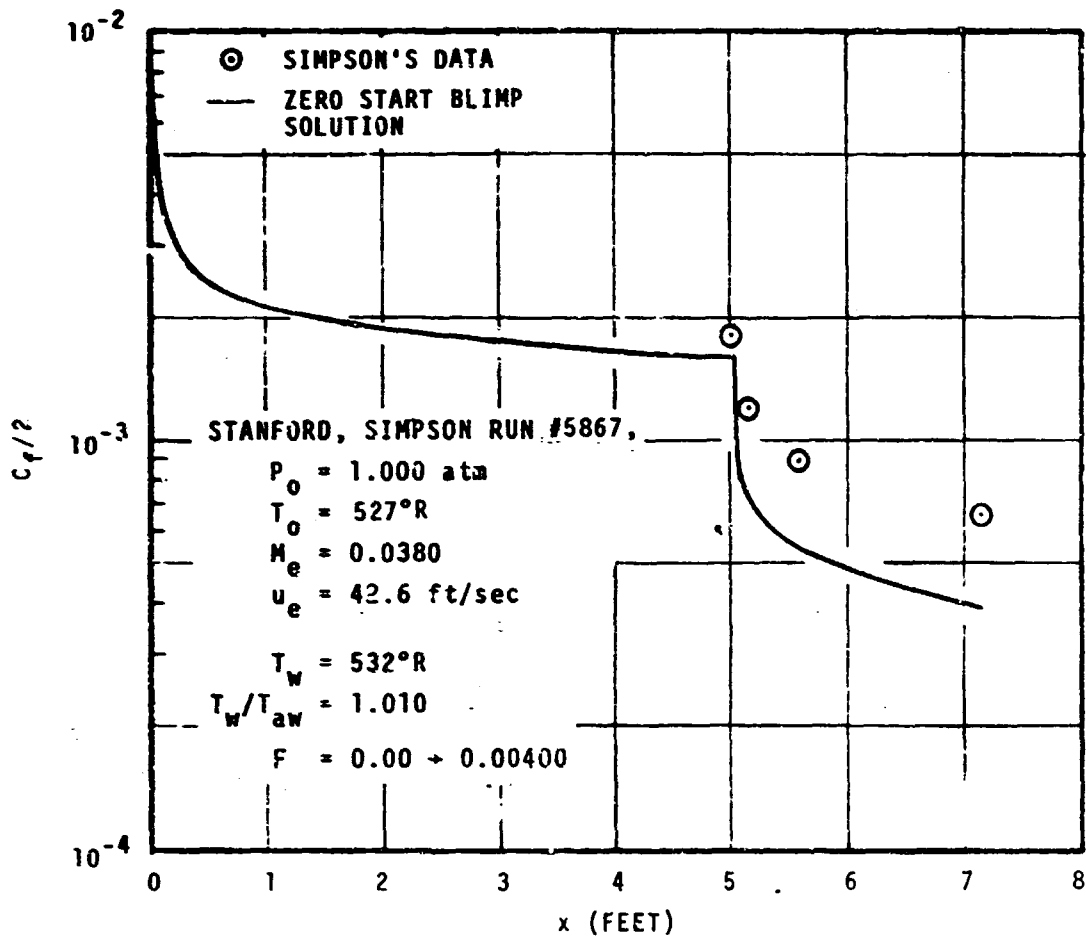


Figure 90. Skin Friction Coefficient vs Streamwise Location. Stanford, Simpson Run #5867, Subsonic, Step-Up in Blowing

with strong blowing. This holds true both for the reduction of experimental data and for prediction procedures such as BLIMP. This point will be discussed in more detail later.

The vertical bands on each data point represent the reported uncertainty intervals.* The differences between data and prediction in terms of percent of the data value are listed in Table IX.

TABLE IX
C_f/2 COMPARISONS FOR STANFORD RUNS

Simpson Run	Difference in C _f /2
F = 0.000	12% low
F = 0.002	25% low
F = 0.004	40% low
F = 0.008	80% low
F = 0.000 → 0.004	12% → 40% low

The consistency of this pattern is completed by the comparison of the near wall region in Figures 78, 80, 82, 84, and 86. In every case, the data indicate higher gradients at the wall by roughly the percentages of Table VIII.

The step in blowing causes an immediate 50 percent decrease in predicted C_f/2 and within the following 2 feet (15-20 boundary layer thicknesses) has decreased to within 10 percent of the value for constant F = 0.004 blowing from the leading edge.

e. Jeromin Comparisons

(1) Comments on BLIMP Input

All Jeromin predictions utilized the data start option since no data were presented defining the flow conditions from the nozzle throat to the first measured profile. Freestream conditions at each station were based on matching measured Mach numbers; wall conditions (temperature and mass flow) were input as reported. Initial station velocity profiles were taken from Squire (reference 88). Temperature (enthalpy) profiles were computed from equation (1) in Section II.3.c.

*These uncertainty intervals have been described as too narrow by Squire, reference 87.

(2) Comments on Results

Only velocity profile comparisons are presented because profile data were reported in that reduced form. For the runs in question, total temperature profiles were not measured but were calculated from equation (1). This procedure was justified by Jeromin based on the close agreement of preliminary measurements with equation (1). Consequently, since the measured Mach number profiles and the presented velocity profiles are directly related; no attempt was made to convert back to the Mach number form.

Figures 91-94 and 97-100 contain the velocity profiles for the runs 2.5-0.0, 2.5-1.2, 3.6-0.0, and 3.6-2.1 in that order. Comparisons are presented at four of the five profile stations reported by Squire. These latter profiles represent one-half of the number of measured profiles. Jeromin reports complete boundary condition and thickness integral data at all measured stations, which covered a streamwise range from about $x = 1.1$ to $x = 1.5$ feet. The Re_θ plots in Figures 95 and 101 include measured data at all stations. A single $C_f/2$ value obtained via the momentum integral method (by Jeromin) is shown for each test in Figures 96 and 102.

All the velocity profile comparisons indicate a recurring pattern; the BLIMP profiles progressively show higher velocity ratios in the mid-range of the profile. By the final profile, differences in velocity ratios range from 0.05 to 0.07 with the maximum occurring between $u/u_e = 0.6$ to 0.8. These differences are only slightly greater for the blown profiles than for the unblown.

The profiles reported by Squire are the actual Jeromin profiles for only the Mach 3.6 runs. Squire reran the Mach 2.5 experiments. Consequently, the Squire profiles and the Jeromin flow and wall conditions and computed profile parameters are related only in a nominal sense. This appears to be the reason for the small difference in initial data start matching of the Re_θ values for Mach 2.5 in the Figure 95 as compared to the more exact initial matching in Figure 101 for Mach 3.6. The trends are correct, however, as the Mach 2.5 profiles of Figures 91-94 clearly indicate that the measured $d\theta/dx$ should be greater than that predicted.

The nonlinear variation of Re_θ for Mach 2.5 with blowing in Figure 95 results from the recorded but unintentional axial pressure variation in the experiment. The irregularity at the downstream end of the test section in the Re_θ data in Figure 101 (Mach 3.6 with blowing) is due to apparent "blowing off"

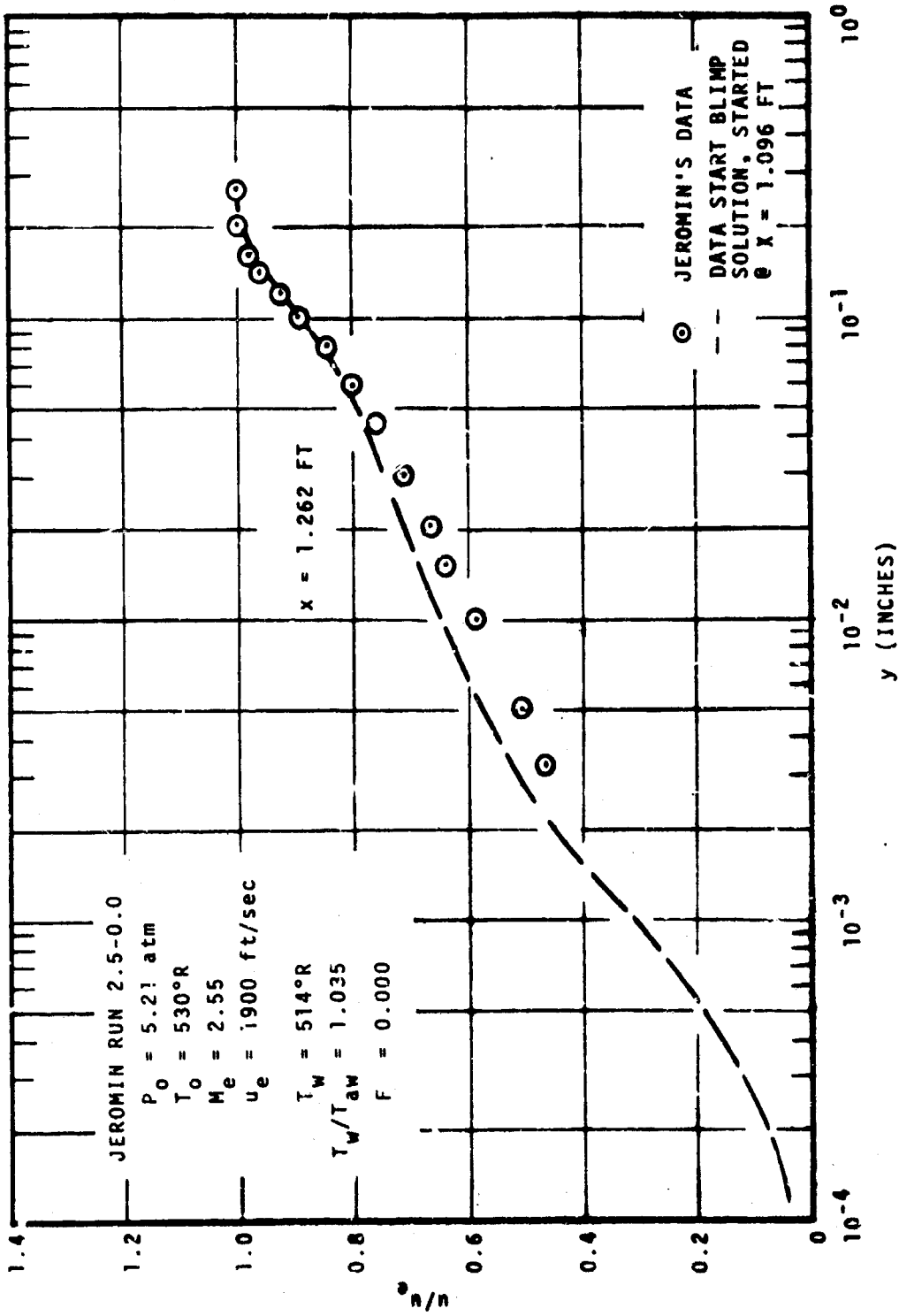


Figure 92. Linear-Log Velocity Ratio Profiles
 Jeromin Run 2.5-0.0, Supersonic, No Blowing

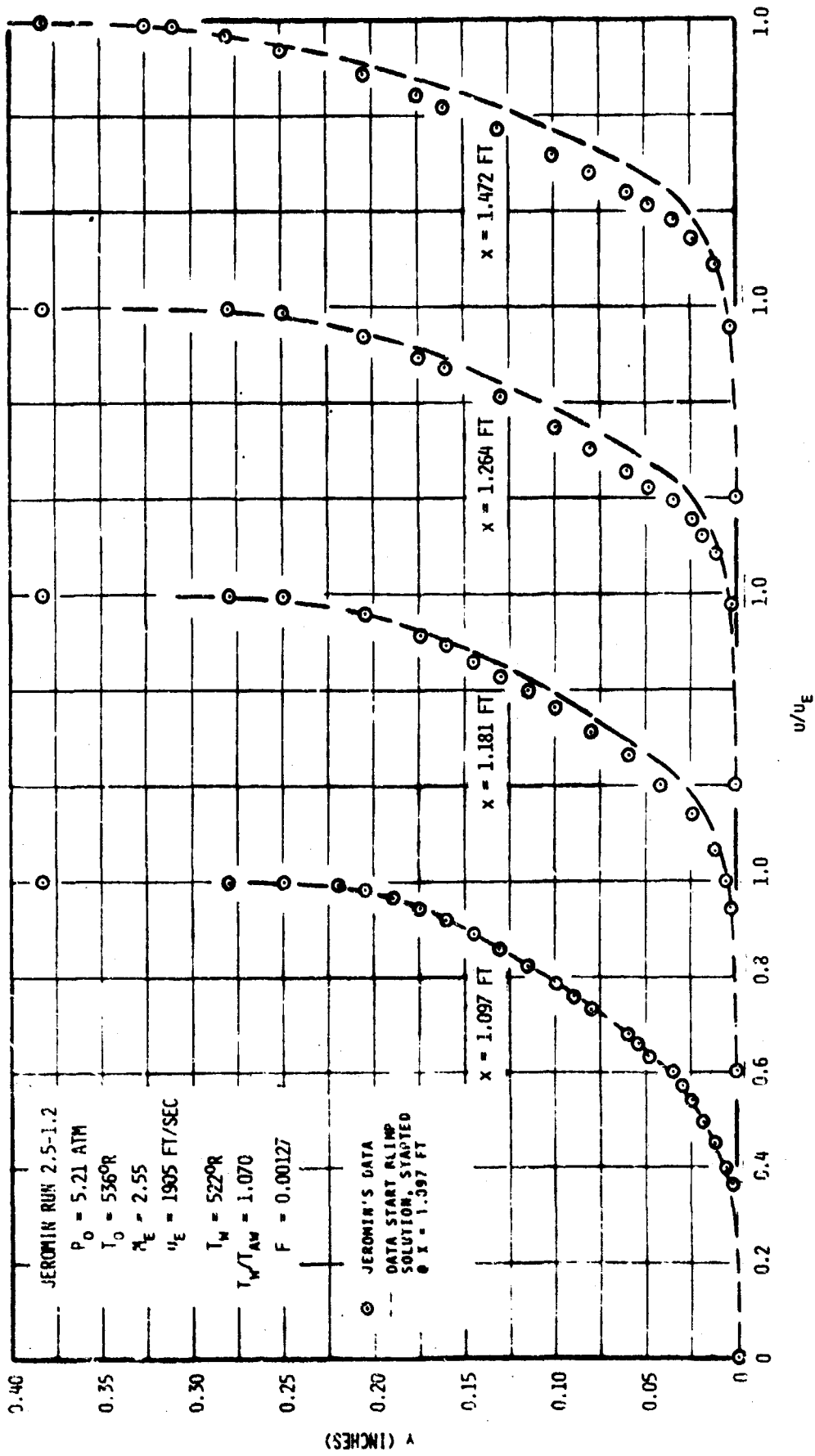


FIGURE 93. VELOCITY RATIO PROFILES
 JEROMIN RUN 2.5-1.2, SUPERSONIC, $F = 0.0012$

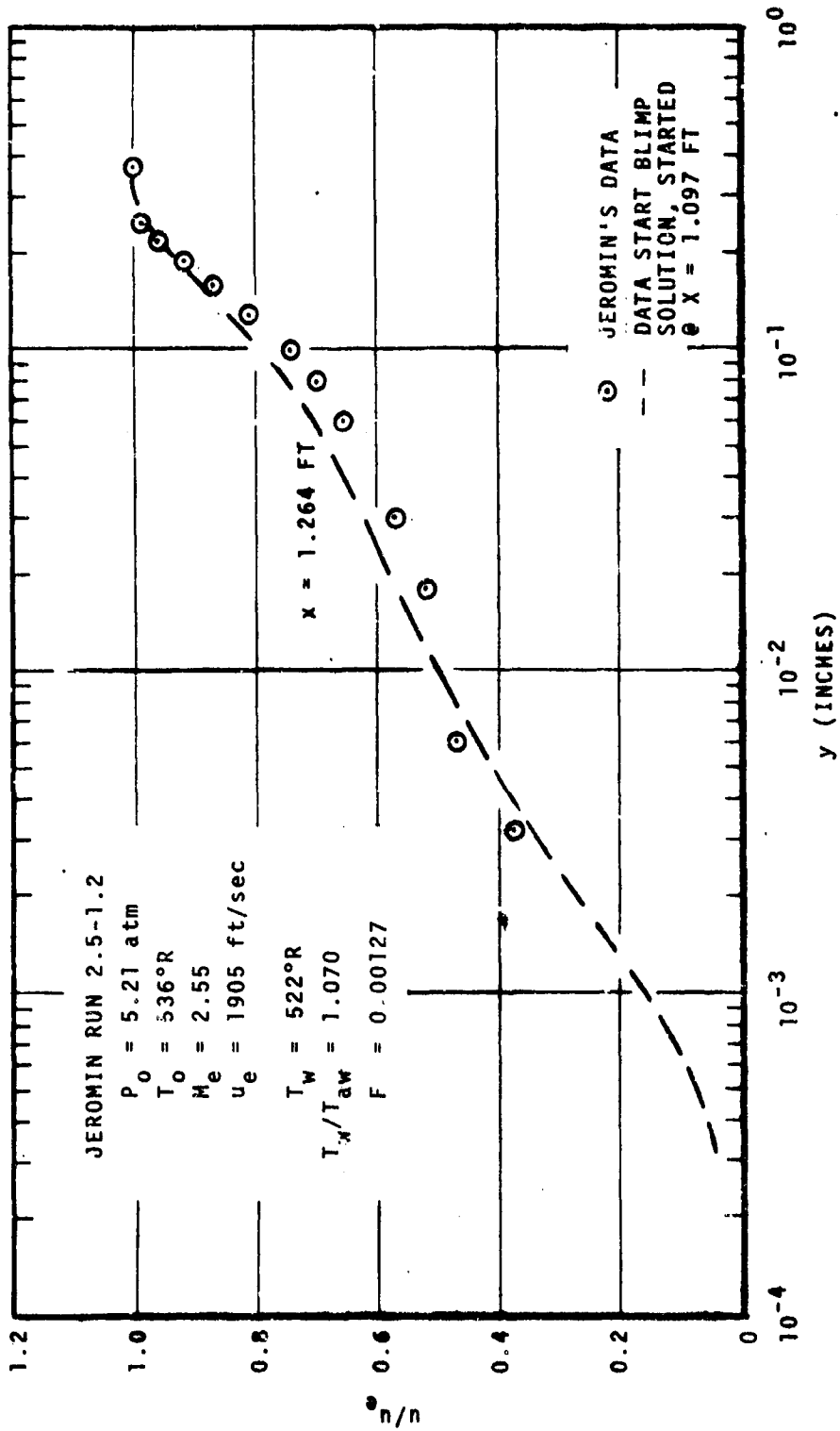


Figure 94. Linear-Log Velocity Ratio Profiles
 Jeromin Run 2.5-1.2, Supersonic, $F = 0.0012$

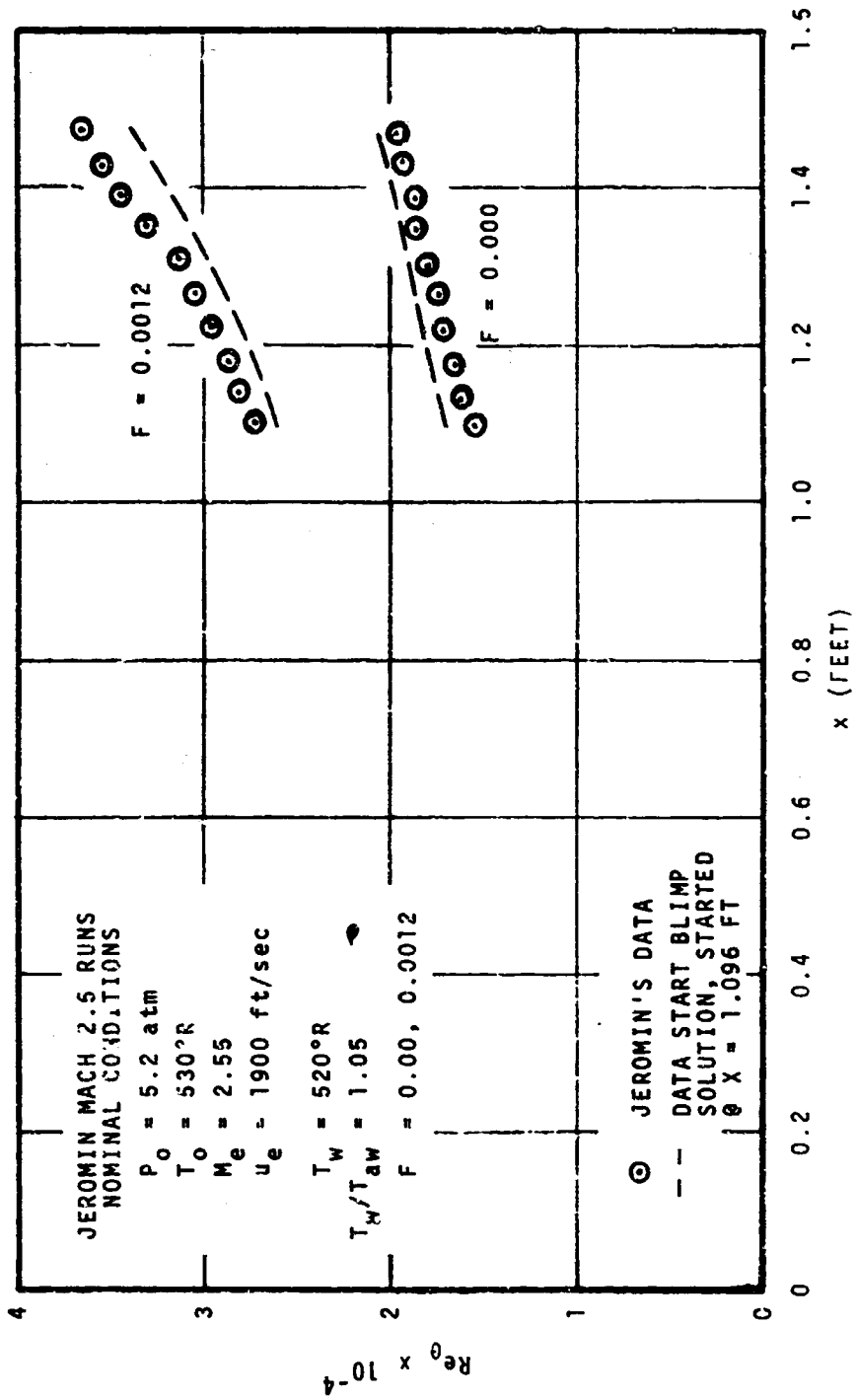


Figure 95. Momentum Thickness Reynolds Number vs Streamwise Location Jeromin Mach 2.5 Runs

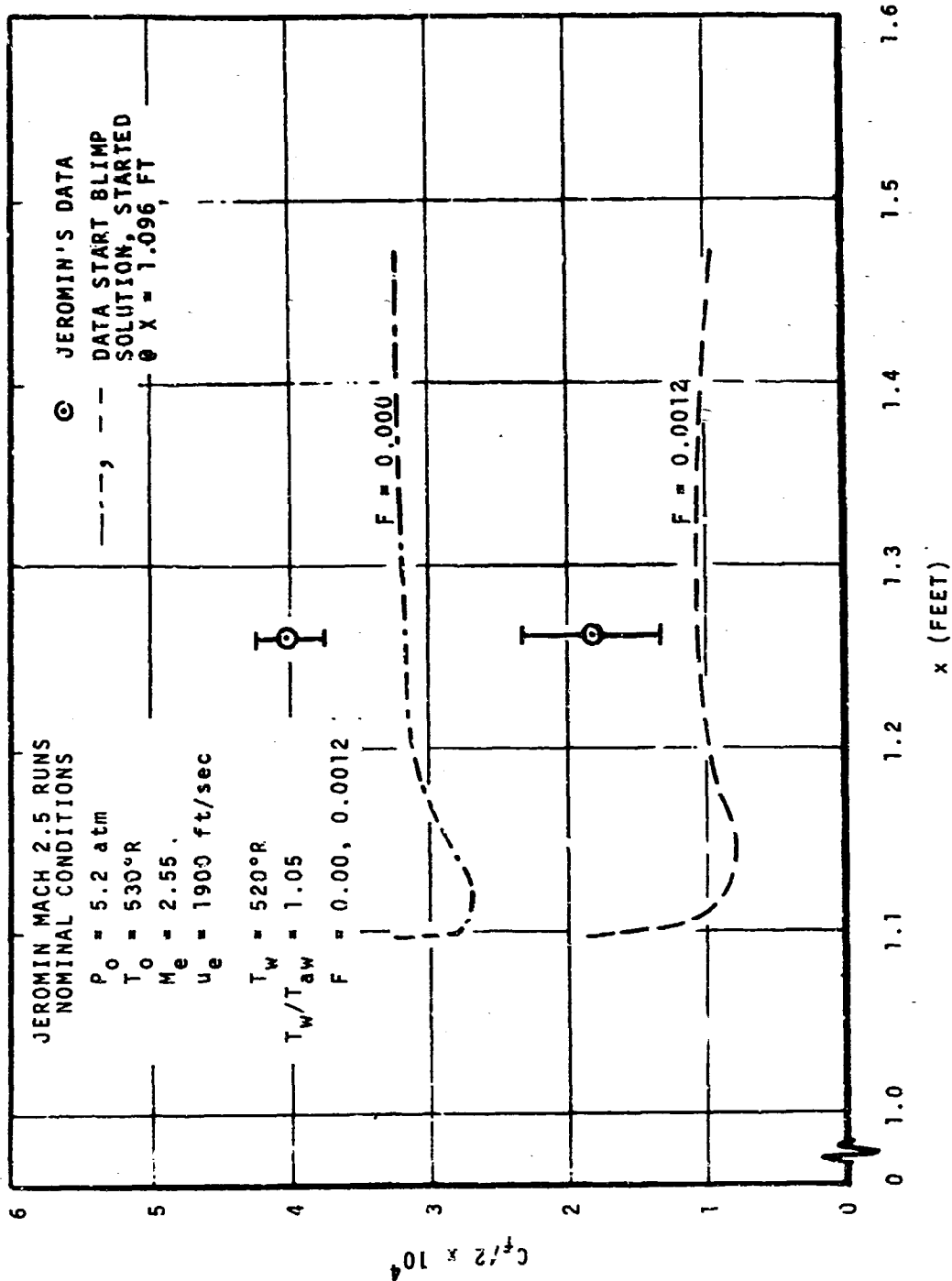


Figure 96. Skin Friction Coefficient vs Streamwise Location Jeromin Mach 2.5 Runs

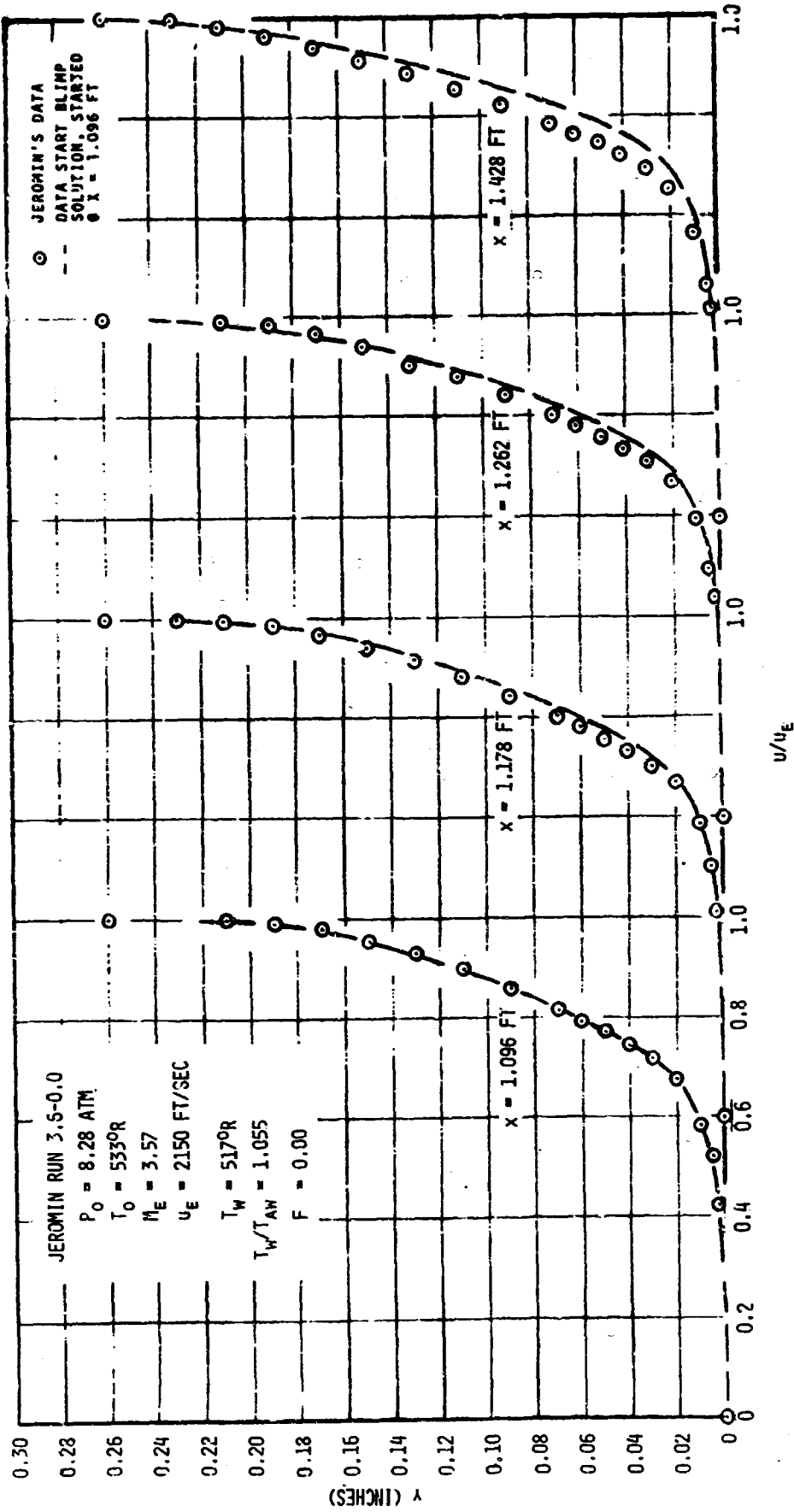


FIGURE 97. VELOCITY RATIO PROFILES
 JEROMIN RUN 3.6-0.0, SUPERSONIC, NO BLOWING

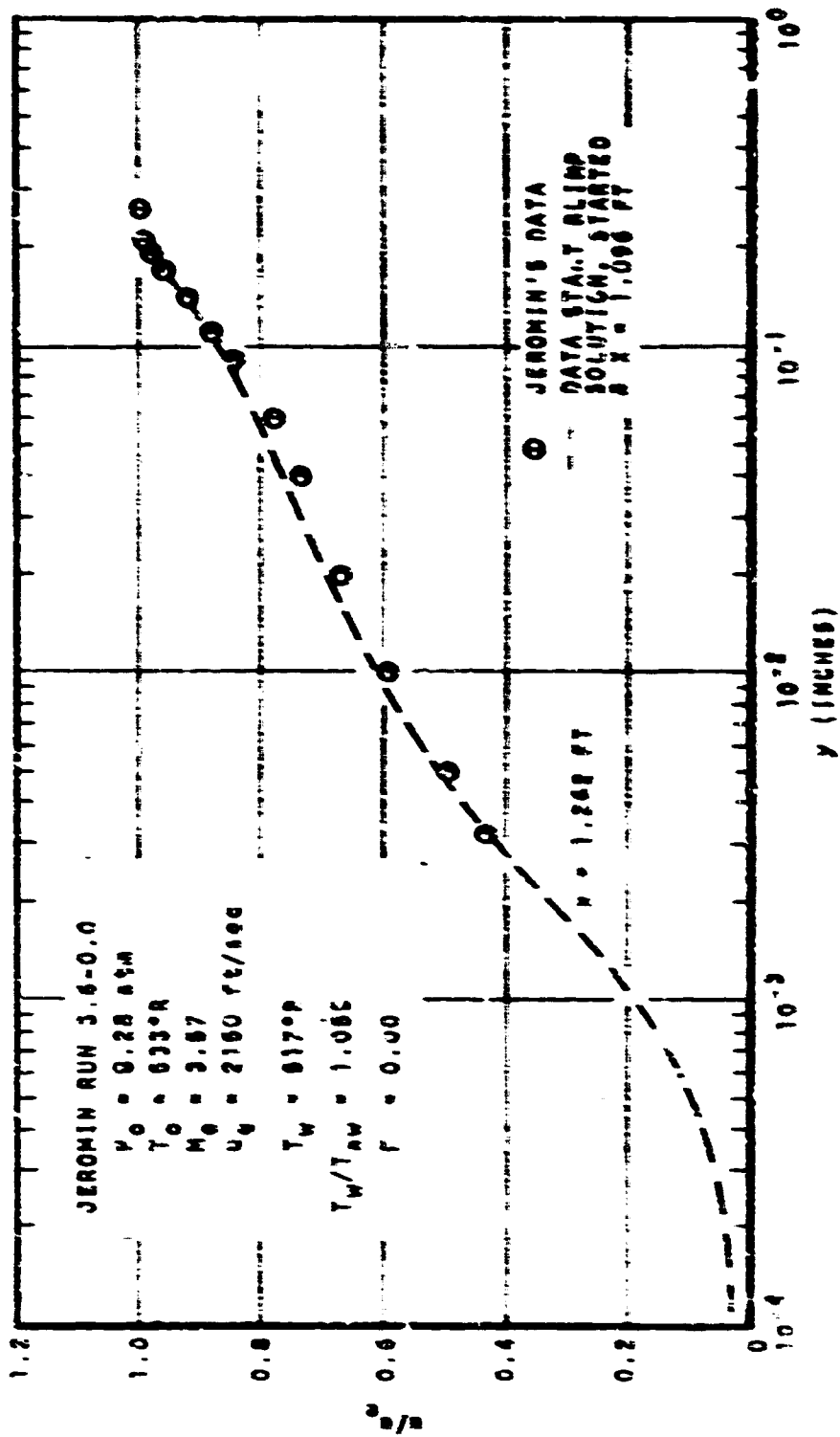


Figure 98. Minimum-Flow Velocity Ratio Profiles
 Jeromin Run 3.6-0.0, Supersonic, No Mixing

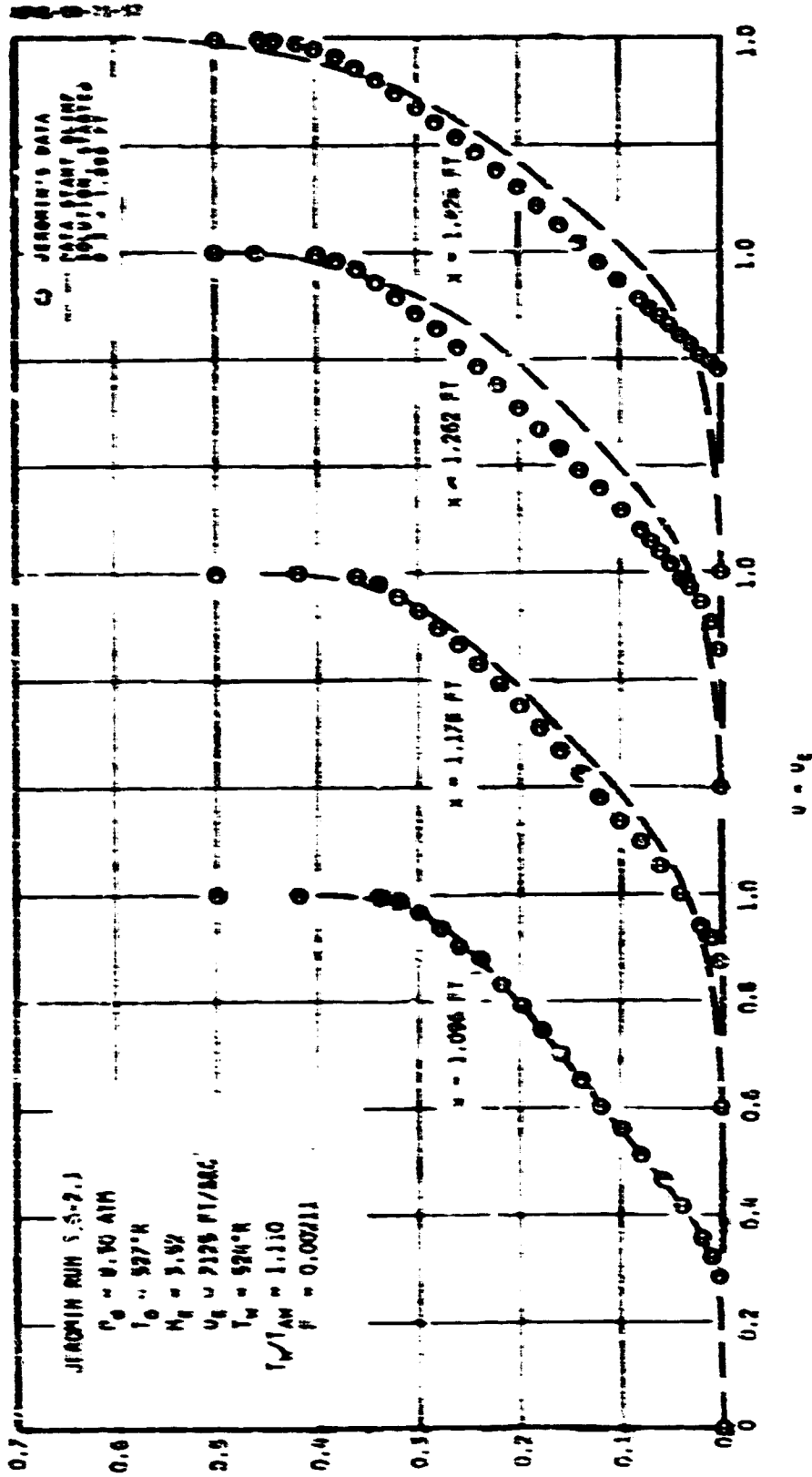


FIGURE 99. VELOCITY RATIO PROFILES
 JEROMIN RUN 5.6-2.1, SUPERSONIC, $f = 0.0021$

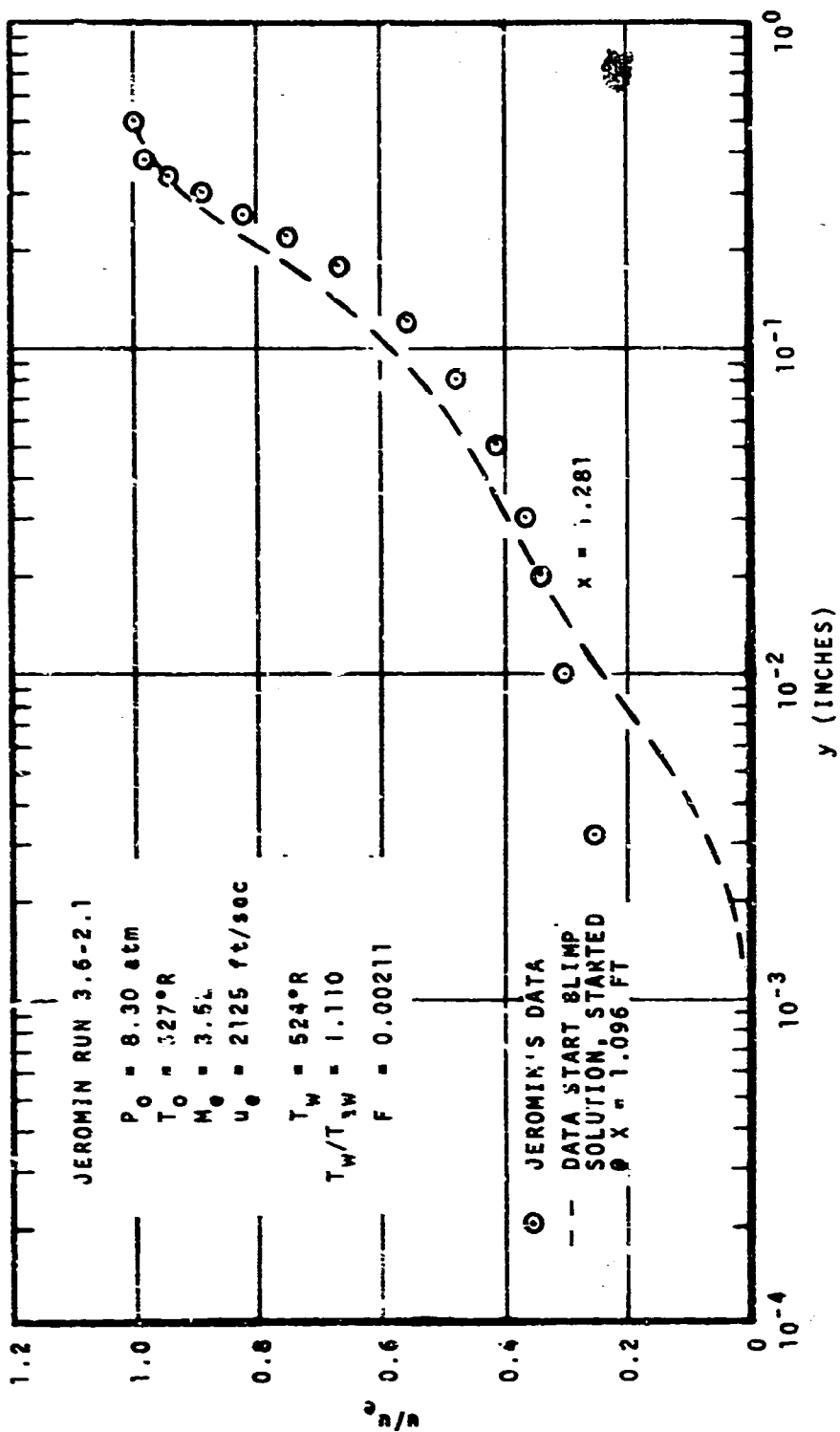


Figure 100. Linear-Log Velocity Ratio Profiles Jeromin Run 3.6-2.1, Supersonic, $F = 0.0021$

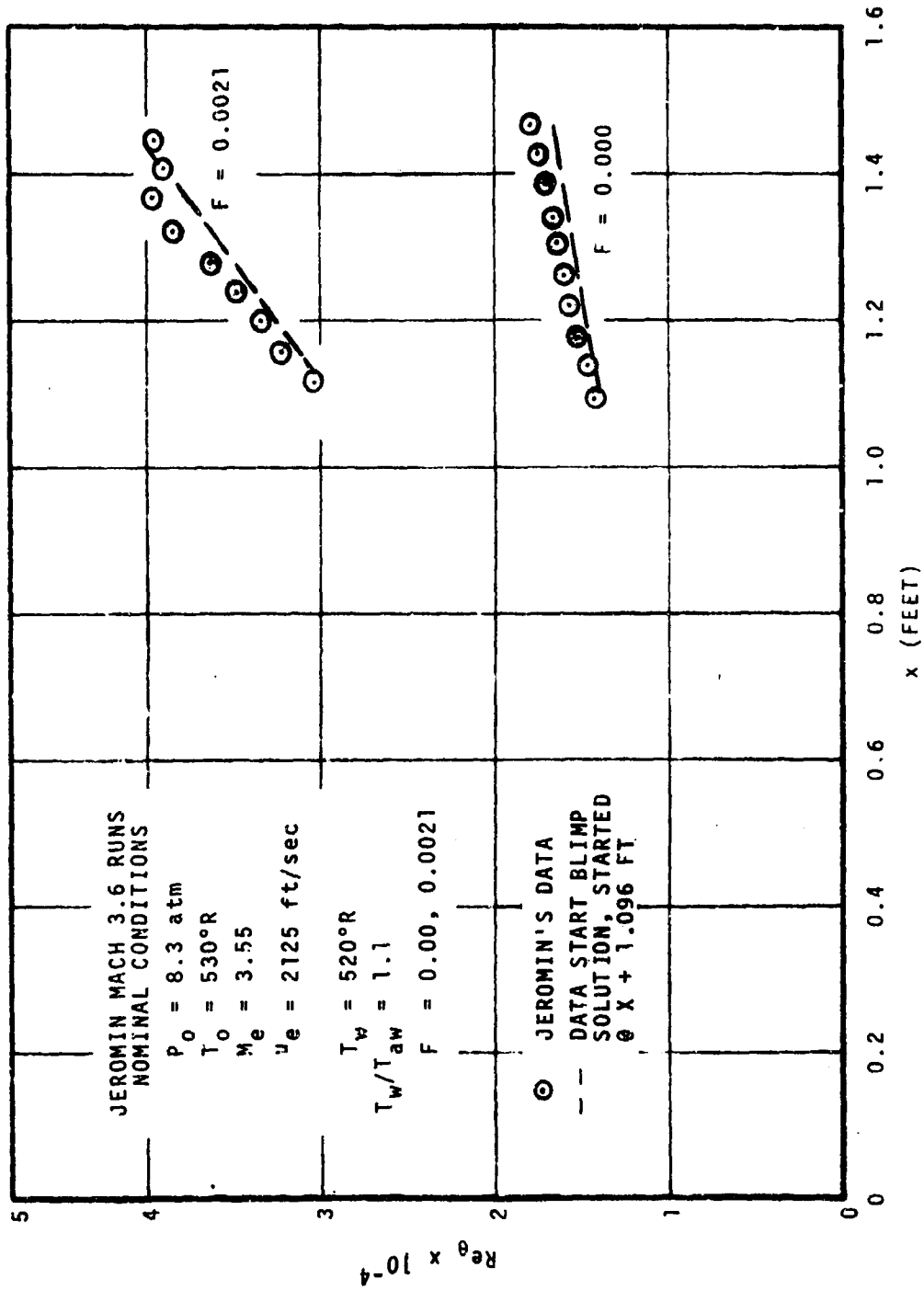


Figure 101. Momentum Thickness Reynolds Number vs Streamwise Location Jeromin Mach 3.6 Runs

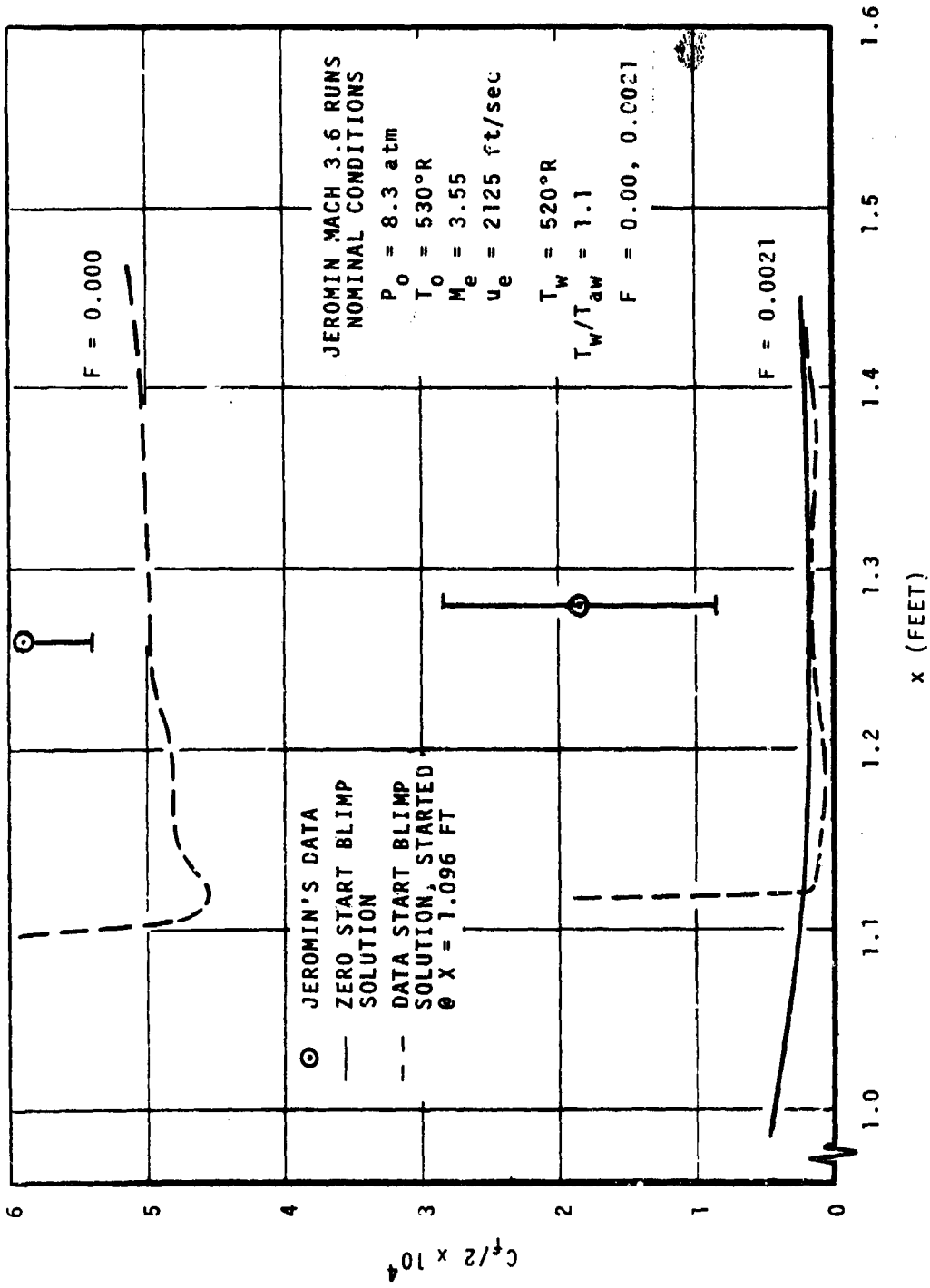


Figure 102. Skin Friction Coefficients vs Streamwise Location Jeromin Mach 3.6 Runs

of the boundary layer as discussed by both Jeromin and Squire. Difficulties in obtaining pitot pressure data near the wall under these conditions are blamed for the unusual shape of the final data profile ($x = 1.428$ feet) in Figure 99.

The $C_f/2$ comparisons of Figures 96 and 102 substantiate the profile and Re_θ comparisons in indicating lower predicted values for blowing and no-blowing. The estimated uncertainty intervals reported by Jeromin are included. The familiar data start patterns are evident again. There is an immediate change to the approximate "equilibrium" value desired by BLIMP, followed by a gradual variation caused by a combination of axial pressure gradients and, probably the more significant factor, adjustments in outer profile shape. Comparative variations in the differences between measured and predicted $C_f/2$ and $d\theta/dx$ values relative to the measured values are given in Table X.

TABLE X
VARIATIONS IN MOMENTUM INTEGRAL TERMS FOR JEROMIN COMPARISONS

Run	$C_f/2$	$d\theta/dx$
2.5 - 0.0	18% low	15% low
2.5 - 1.2	45% low	---
3.5 - 0.0	15% low	28% low
3.5 - 2.1	90% low	---

Values of $d\theta/dx$ are included only for the no-blowing cases where, neglecting the effect of pressure gradients, equation (38) applies. As discussed previously, the presence of pressure gradients does not have a significant effect on the BLIMP prediction but as noted by Jeromin, it is significant in the determination of $C_f/2$ from the momentum integral equation. This is particularly true with blowing when both $d\theta/dx$ and F are an order of magnitude greater than $C_f/2$. Considering the pressure gradients and the three-dimensional effects reported by Jeromin, combined with the difficulties in accurately measuring $d\theta/dx$, it appears likely that the reported uncertainty intervals for blowing are underestimated.

One additional prediction of $C_f/2$ is shown for Mach 3.6 with blowing on Figure 102 as a solid curve. A zero start case was run from the nozzle throat

assuming streamwise conditions based on descriptions of the nozzle and the physical dimensions of the porous plate in references 48 and 88. The matching of θ at the first station was about 20 percent off, but the $d\theta/dx$ from that point on was essentially identical to that of the data start prediction. The close agreement of the solid and dashed curves again confirms the ability of the data start procedure to respond to local wall conditions.

Figure 103 shows a comparison of static temperatures at the final station for $M = 3.6$ and no blowing. This is presented to assess the relationships among the temperature profile predicted by BLIMP (dashed curve), the temperature calculated from the Crocco relation, using the velocity profile predicted by BLIMP (triangles), and the measured Jeromin profile (circles). The close comparison between the two BLIMP determined temperatures indicates that the solution is in close agreement with the Crocco relation, and thus, in agreement with Jeromin's observations. The difference noted between Jeromin data and BLIMP predictions is consistent with the difference in the predicted and measured velocity profiles for $x = 1.428$ feet in Figure 97.

2. RATIONALIZATION OF RESULTS

Very little effort was expended to improve the turbulent model for each data set as it was run, for two reasons. First, it would be unwise to make changes without evidence from a number of cases that a change was called for. Second, the contract for this study did not call for such an optimization. Rather, once a model was selected, it was to be evaluated for all data sets. Now that all the comparisons have been completed, however, it seems appropriate to examine the results, suggest what improvements to make, and how to make them.

a. Overview of the Agreement Between Experiment and Theory

All five of the data sets which have been used for comparisons here include data for unblown, essentially zero pressure gradient flows. In addition, the comparison with the data of Wiegardt and Tillman provided a baseline case with which the others can be compared. The velocity profile comparison was given in each case and in general was very good. Only the Lee case offered any significant errors in predicted velocity profile shape; however, the validity of the Lee data is open to question. Mach number profiles for the supersonic and hypersonic data sets are not predicted as well as velocity profiles. The problem is generally one of failing to predict an inflection point near the mid-range of the Mach number ratio. In addition, M/M_e approaches 1.0 with a much greater slope than the prediction shows, which of course is related to the inflection point problem.

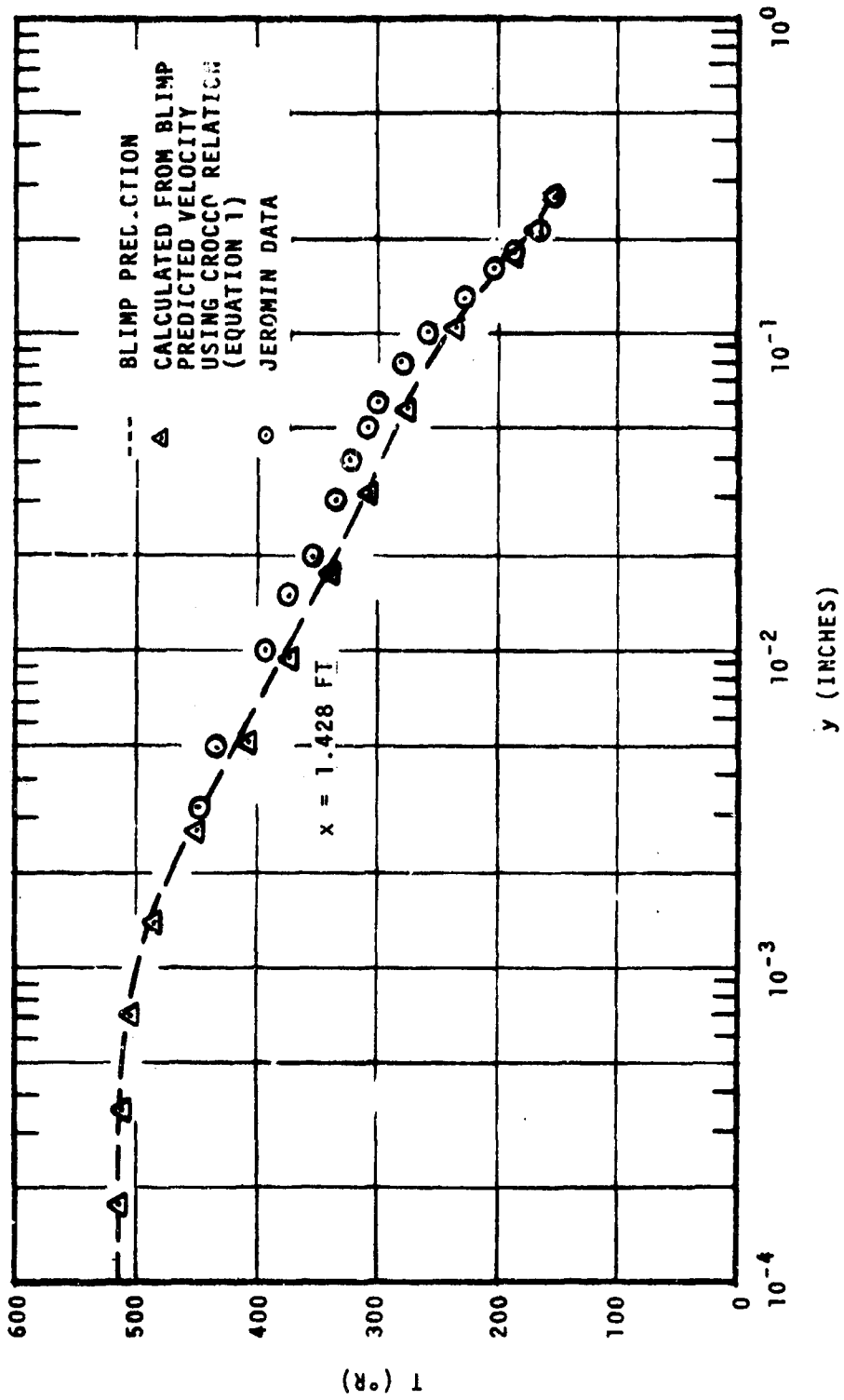


Figure 103. Static Temperature Profiles, Jeromin, $M = 3.6$, $F = 0.000$

Total temperature profiles are fairly good for NOL and TRW data, the only cases where such data were presented. The response of the prediction to the step in wall temperature in the TRW data was particularly encouraging. The $C_f/2$ and Re_θ vs. streamwise distance plots are related through the momentum integral equation. There seems to be a general trend to underpredict $C_f/2$ and θ variations slightly in several of the comparisons. This trend is disappointing in light of the excellent agreement with the Wieghardt and Tillman data. Some of this error can be eliminated by optimizing the nodal layout, as will be discussed in the next subsection, however it appears that the prediction will remain 2-3% low for the better quality data, such as Coles and Stanford. Referring back to the comparison between models of Figure 11, it is clear that all three turbulent models considered at the beginning of this report should give about the same results for unblown, low speed flows, with the Aerotherm model giving a slightly higher shear stress. Since the Cebeci model in particular has been shown to be very successful in predicting C_f for unblown flows (references 68, 77, and 78), it is hypothesized that the error observed here is a random one, and does not indicate a trend associated with the model. More will be said of this later.

For the blown flow data comparisons, velocity profile predictions are again quite good. In the Stanford data, there again seems to be a trend toward underpredicting the momentum thickness. This results in a gross underprediction of the reported drag coefficient for flows with moderate to strong blowing. This result could be anticipated from the one-dimensional analysis comparisons of Figures 24, 25, and 26. It was clear that, for the Aerotherm model, both the wall shear and the profile shape could not be predicted simultaneously. Thus, either the Simpson data are incorrect, or the Aerotherm model should be adjusted to fit it. This point is discussed further in the next subsection.

b. Changes in the Turbulent Model

For unblown flows, it has been stated above that the Aerotherm model is essentially equivalent to other, apparently successful models and there is no reason why it should not offer equivalent accuracy. A significant improvement in accuracy can be made by working with more nodes through the boundary layer, as discussed in the appendix. As more experience was gained in working with the code through the course of this contract, it became apparent that, in addition to those comments made in the appendix, the nodal distribution in the transition region (figure 104) is of primary importance. Figure 105

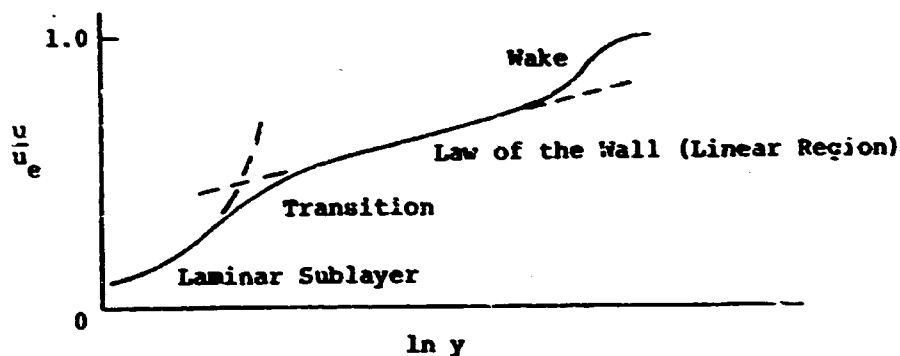


Figure 104. Diagram Showing Law of the Wall Nomenclature

shows $C_f/2$ for a 25-node model and for two 15-node runs, one with more emphasis placed on the transition region with correspondingly less on the wake region. This weighted model is in better agreement with the 25-node run which placed all the extra nodes into the transition and law of the wall regions. Figure 105 also shows $C_f/2$ values calculated from several popular theories at $Re_x = 10^6$. It is apparent that there is a certain amount of disagreement over the correct drag coefficient value even for a simple, low speed, incompressible, flat flat problem.

It is of interest to note that the weighted 15-node curve is nearly equal to the standard 15-node curve at the lower Reynolds numbers but approaches the 25-node curve at the higher Reynolds numbers. This is apparently due to the changing shape of the profile relative to the fixed $\bar{\eta}$ distribution. At the lower Reynolds numbers, the profiles are more nearly laminar with transition occurring in the outer portion of the $\bar{\eta}$ values. The 25-node model has a sufficient number of nodes to model the transition region at any of the Reynolds numbers considered. It is obvious that the 15-node model lacks this flexibility, once more emphasizing the fact that to obtain the most accurate prediction, it is necessary to evaluate the results with respect to the chosen $\bar{\eta}$ distribution and to select that distribution based upon the streamwise region of greatest interest.

These comparisons were made after the results described in Section IV were obtained and plotted. Since the differences are small percentage-wise, predictions were not rerun with the improved $\bar{\eta}$ distributions. Thus, all zero blowing $C_f/2$ predictions would appear to be about 5% low for this reason.

One obvious way to alter the turbulent model is to change the numerical values of the constants. As an indication of how the constants would affect unblown boundary layer predictions, numerical experiments were performed for

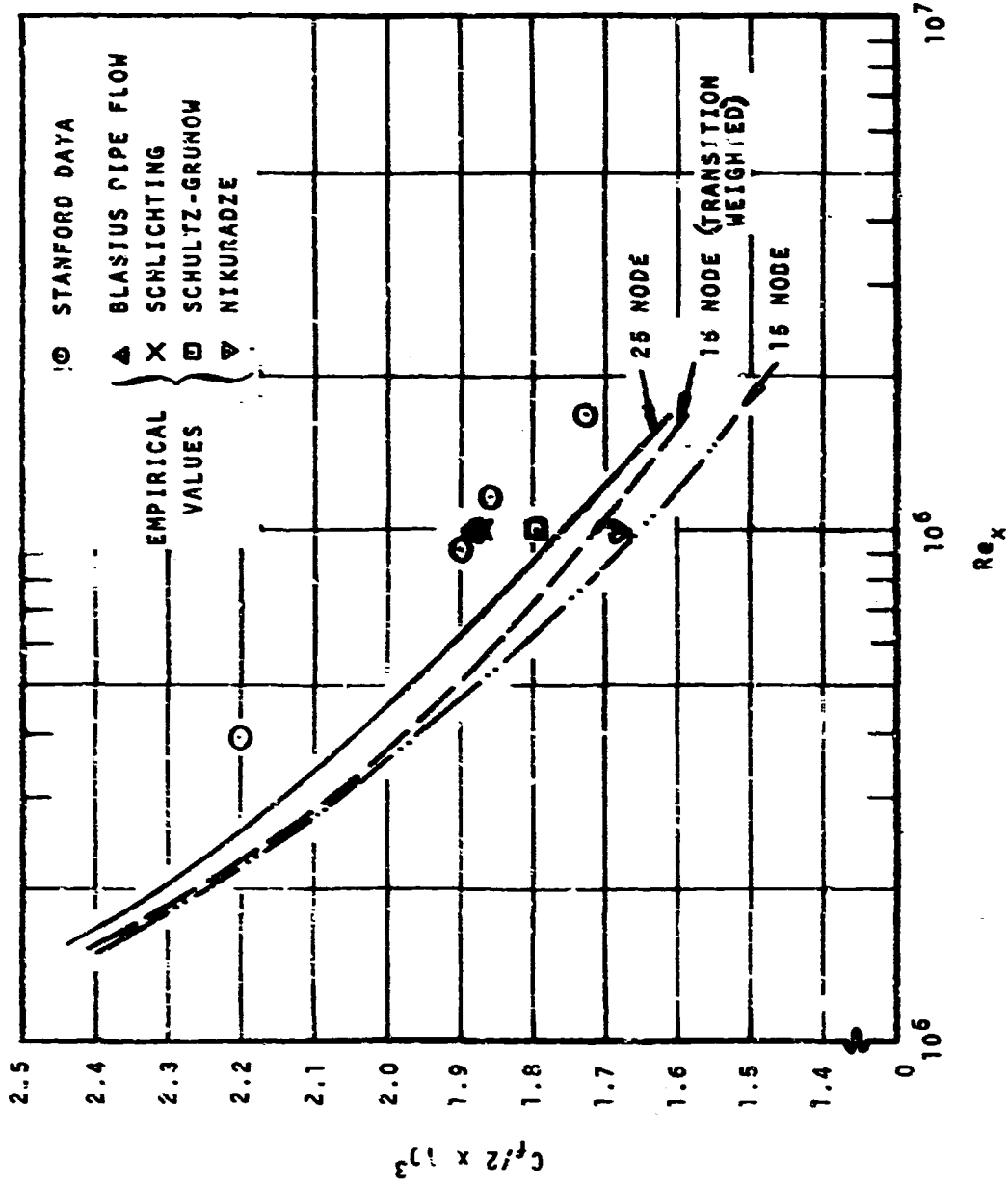


Figure 105. Comparison of Predicted Skin Friction Coefficient for Zero Blowing Stanford Case to Data and Empirical Values

the Coles $M = 3.7$ case. Alternate values of both k_m and y_a^+ were tried for this case, with the result shown in Figures 106 and 107. The small improvement in $C_f/2$ prediction for both the y_a^+ and k_m modifications was made, at the particular station selected, with a corresponding small improvement in profile. These improvements are, of course, intimately related to the nodal distribution through the transition region, therefore it is possible that the results may change at much larger axial distances. It was demonstrated in Section III.3.6 that small changes in the wake law eddy viscosity constant also result in small but detectable profile changes for unblown flows. Based on this evidence, it appears that basic profile shapes and features are unlikely to be changed with modest changes in the model constants. "Fine tuning" of the turbulent model to match drag or heat transfer data, for example, may be accomplished with small adjustments in these constants. Changes should be based on more comparison information than presented here, however. For flows at low Reynolds number or with high heat transfer rates, larger changes in these constants may be in order. The results presented here will be useful in estimating the results of such changes.

For flows with strong blowing, the effects of constant changes are altered somewhat. The wall law constants, y_a^+ and k_m , have the greatest influence in the transition region of the profile, which is much nearer the wall with strong blowing. Thus, there is virtually no change in the outer profile shape for different wall law constants, as shown in Figure 108. Significant differences near the wall do affect the drag coefficient, however, as seen in Figure 109. Manipulation of the y_a^+ type constant is essentially the technique used by both Cebeci and Bushnell and Beckwith to account for blowing in their models, therefore this path does appear to be a strong possibility if blown flow model changes are indeed desired. The question of whether such model changes are in order is addressed in the next subsection.

c. Desirability of Turbulent Model Changes for Blown Flows

A considerable body of data and numerous theories now exist for turbulent boundary layers with injection. The discussion, evaluation, and re-evaluation, of this data has been a favorite topic in the recent fluid mechanics literature. Of particular interest for purposes of the present discussion is the drag coefficient correction due to blowing at any given point on a flat plate. Figure 110, taken from reference 89, presents a number of theoretical solutions to this problem for incompressible flows, along with a few points from Simpson's data. The current Aerotherm theory essentially

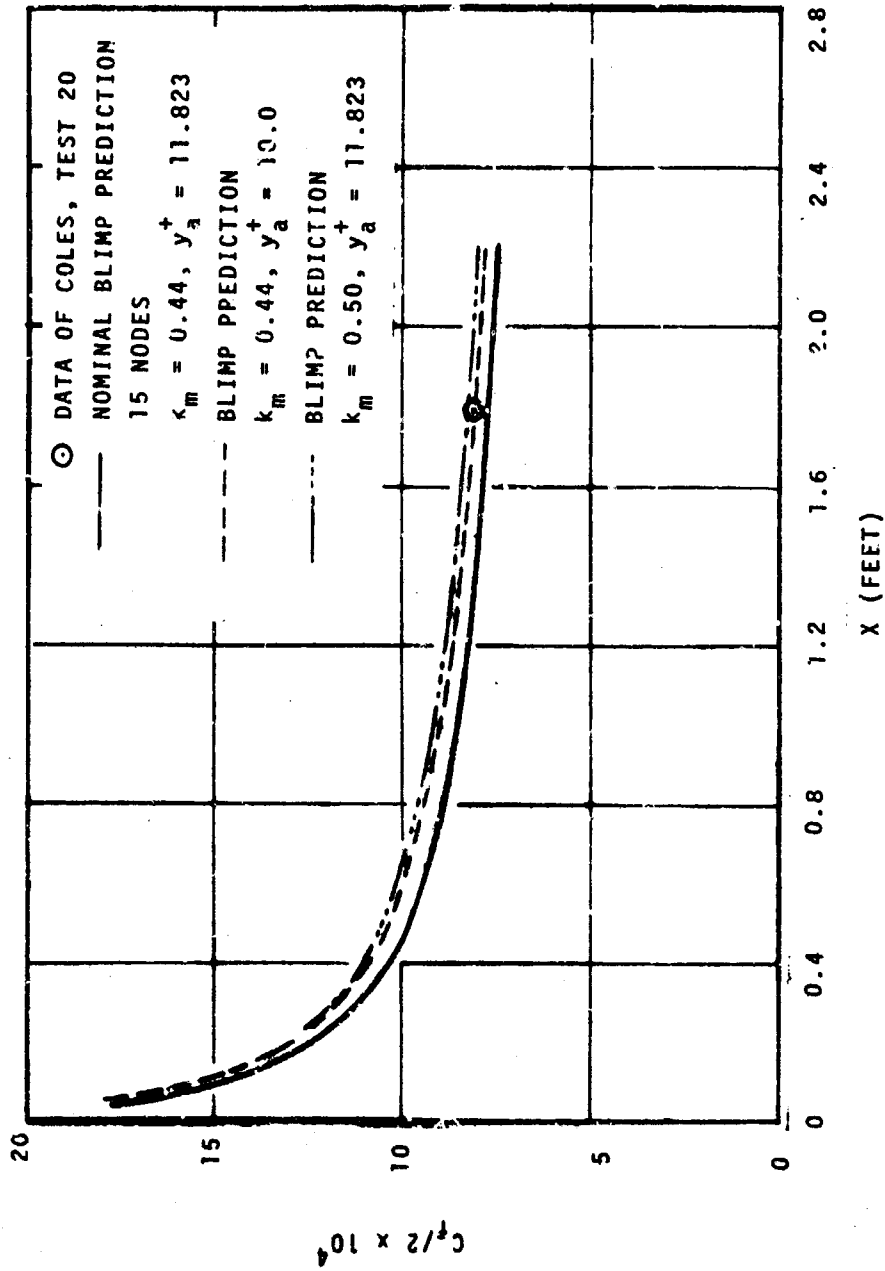


Figure 106. Effect of Wall Law Changes on Drag Coefficient in Unblown Flat Plate Flow

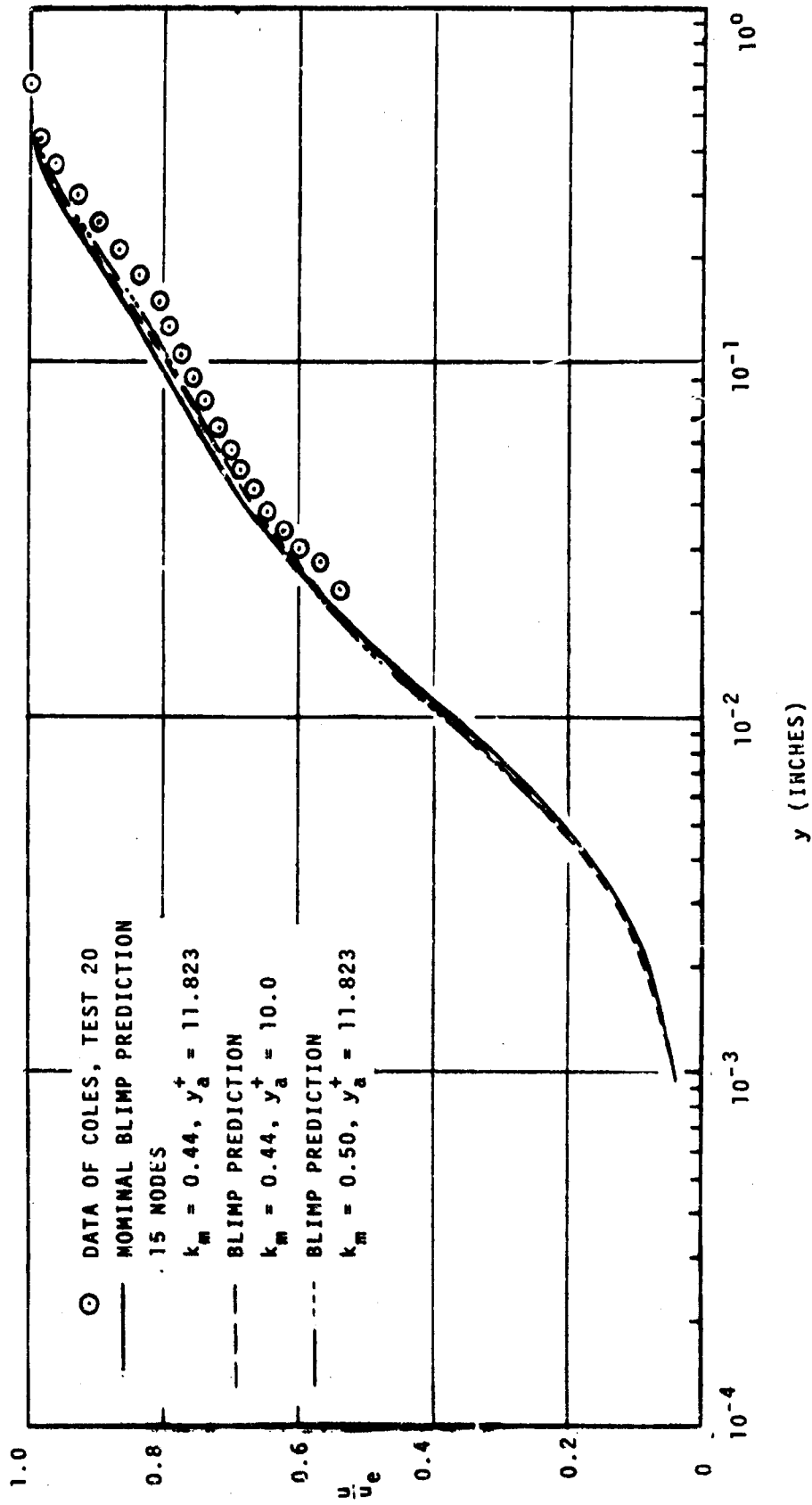


Figure 107. Effect of Wall Law Changes on Velocity Profile in Unblown Flat Plate Flow

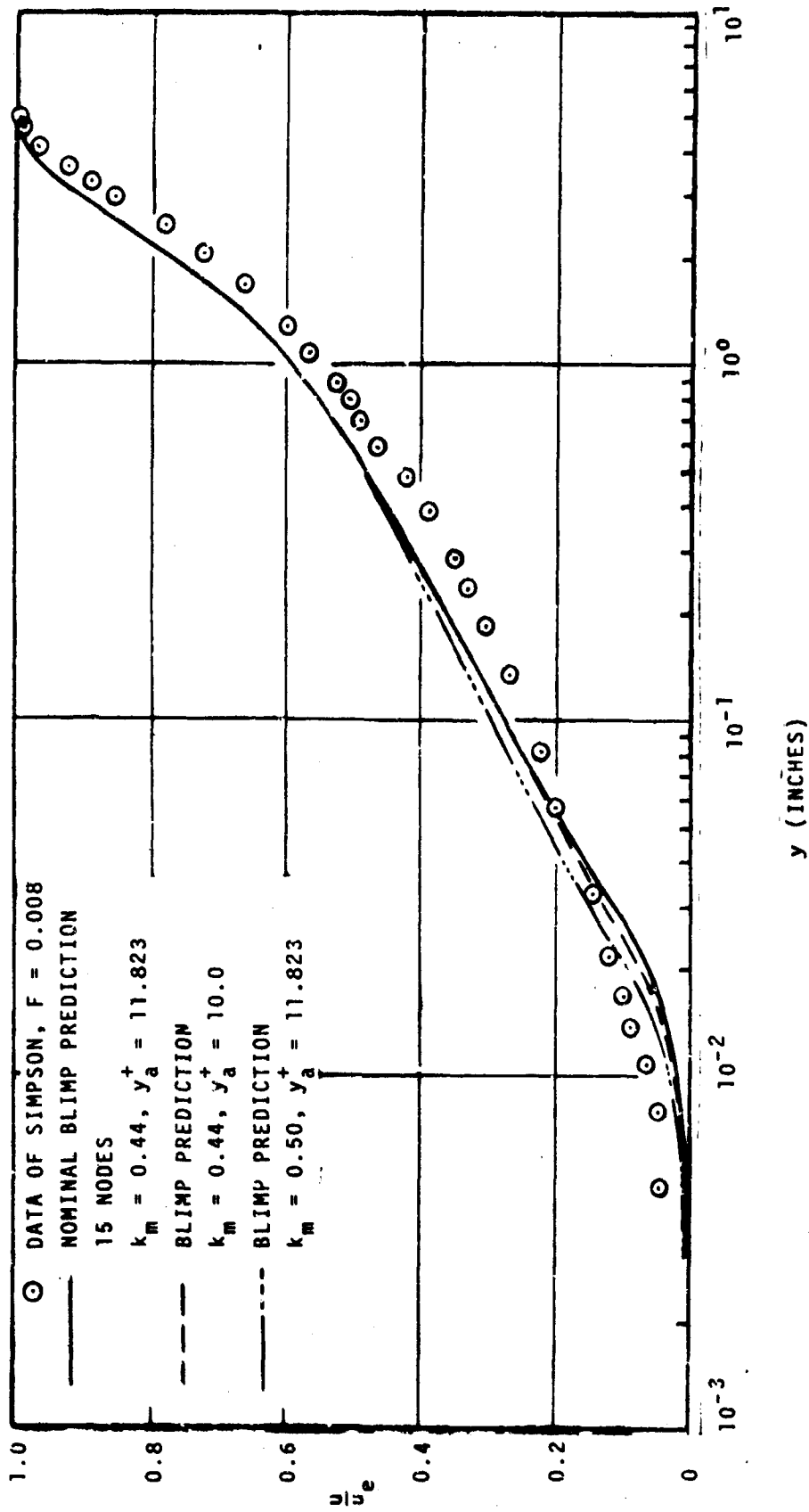


Figure 108. Effect of Wall Law Changes on Velocity Profile in Flat Plate Flow With Blowing

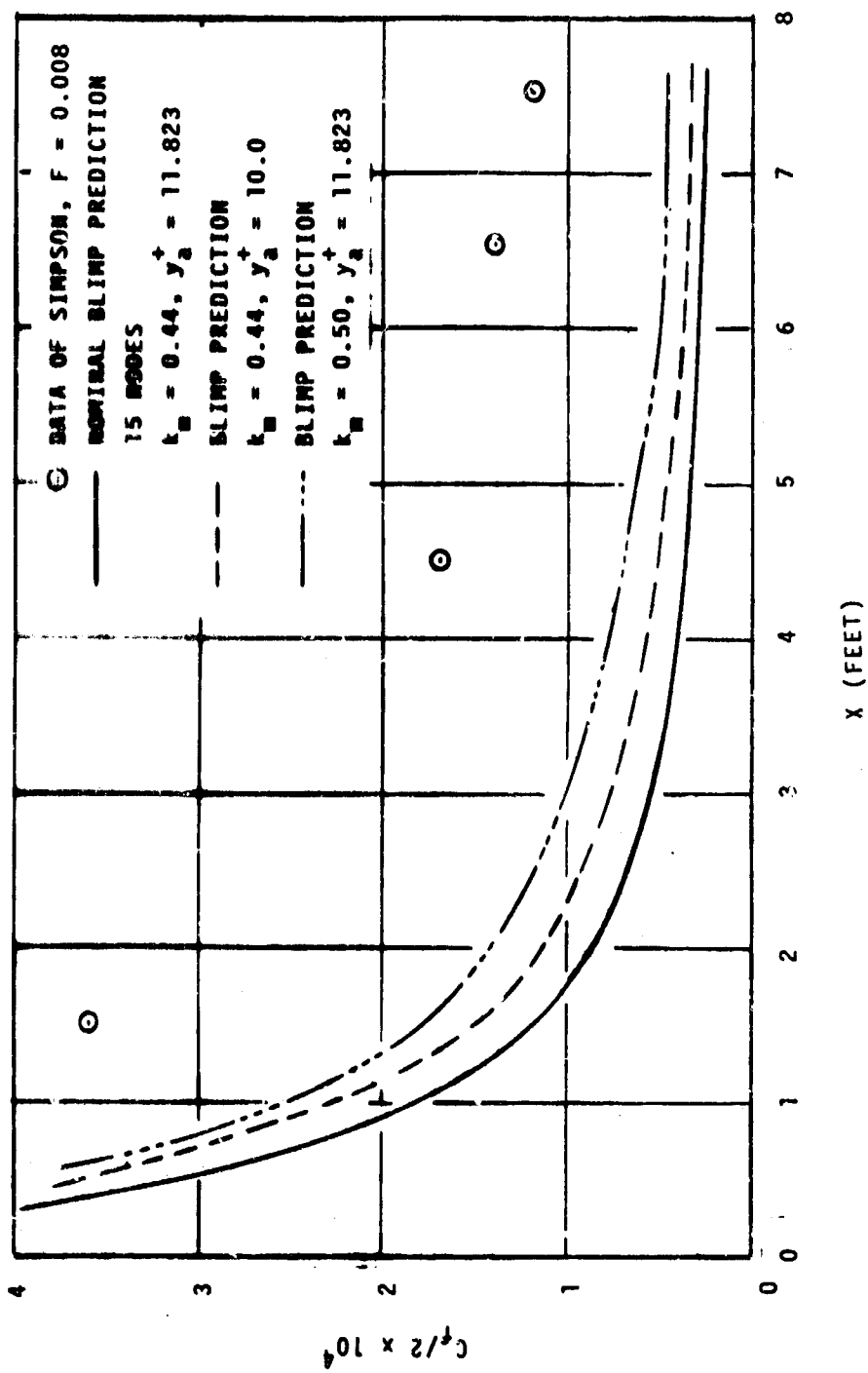


Figure 109. Effect of Wall Law Changes on Drag Coefficient in Flat Plate Flow With Blowing

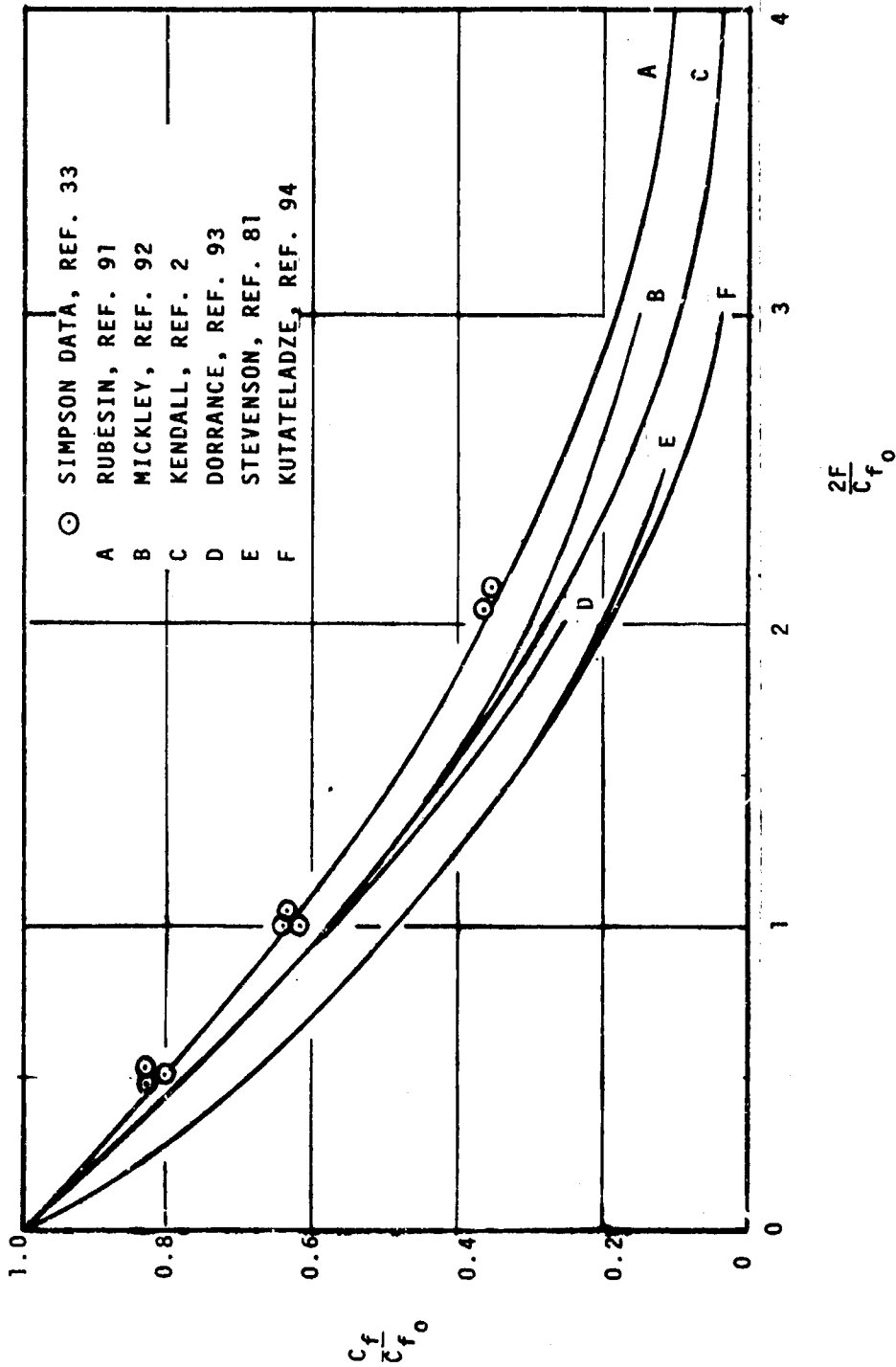


Figure 110. Comparison of Various Theories With Simpson Data, Taken From Reference 89

duplicates the reference 2 curve. It is clear that Simpson's data shows less C_f correction than any of the theories presented. Figure 111, taken from reference 87, illustrates the point that Simpson's data show less C_f correction than that found by other experimentalists. Thus, while the Stanford heat and mass transfer apparatus has been very carefully constructed and operated by competent researchers, there is not universal agreement that the drag data obtained with this apparatus are correct. This merely is a result of the fact that with present measuring techniques, the calculation of drag by either momentum integral or wall profile techniques in blown flows is not sufficiently precise to draw any accurate quantitative conclusions.

It has been shown in Section III.3 that strong blowing is not encountered in typical heatshield or nosetip flight calculations. It is therefore concluded that changes in the Aerotherm wall law model are not warranted until more conclusive experimental data in the strong blowing region are available.

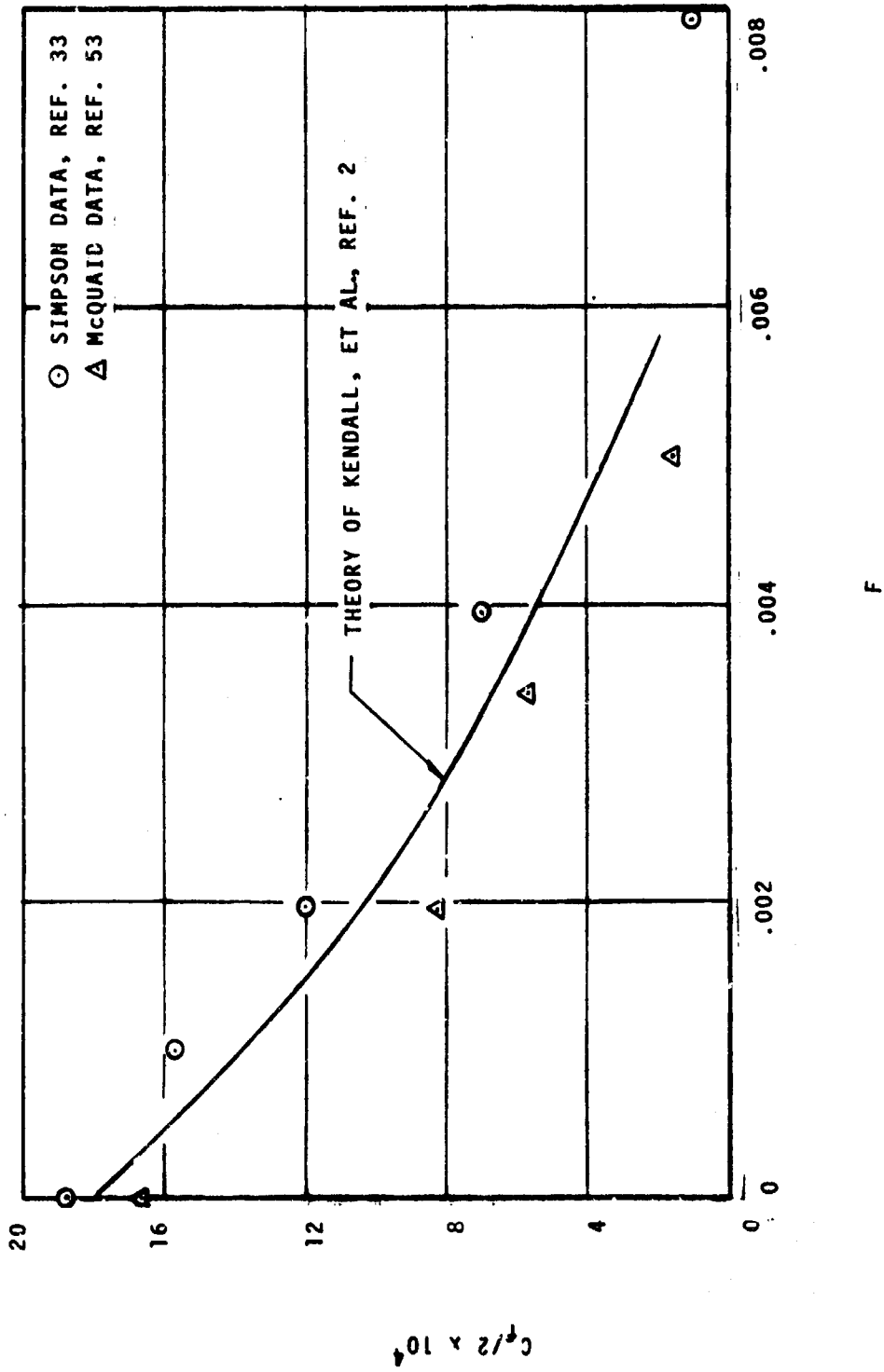


Figure 111. Comparison of Blowing Correction From Several Investigators, Taken From Reference 87

SECTION V
CONCLUSIONS AND RECOMMENDATIONS

Results of this research program are summarized briefly and conclusions are drawn in Section V.1. Recommendations for further work are included in Section V.2.

1. CONCLUSIONS

The research and development program described in this report has uncovered useful information about the state of the art in turbulent boundary layer experimentation and turbulence modeling. It has also answered many questions about the use of BLIMP as a prediction tool. In the literature survey portion of this contract, it became evident that no one set of experimental data is completely suitable for turbulent model studies, i.e., completely error free. There is significant disagreement between various data sets for even very straightforward experiments, such as flat plate subsonic flow. Experimental problems and potential errors are compounded for the more difficult cases, such as flows with blowing.

Comparisons of three leading methods of modeling turbulence in boundary layers showed that the methods were very similar in unblown flows, but contained potentially important differences for flows with blowing. The one-dimensional solution technique which was used to compare these models appears to be useful for further development of turbulent models and possibly for screening new experimental data.

The comparisons of predictions and data presented in this report are valuable in establishing the degree of confidence which should be placed in BLIMP predictions. In general, it can be concluded that the eddy viscosity-type model for turbulence is satisfactory for the type of flows considered here. BLIMP does a good job of predicting velocity and temperature profiles for a wide variety of flows and boundary conditions. Some improvements in profile shape are possible, however, particularly for higher Mach number flows. Of particular interest in the data profile shape is an inflection point in velocity and Mach number profiles which occurs at supersonic and hypersonic speeds. Some changes in the turbulent model, possibly including a variable turbulent Prandtl number, may be necessary to model this particular profile feature.

Drag coefficient predictions for many of the no-blowing cases considered in this report were slightly low. This was found to be a function of the number of nodes used and/or their spacing through the boundary layer. It can be concluded that the use of 15 nodes is very near the lower limit for accurate turbulent boundary layer predictions, and that strong consideration should be given to up-dimensioning the code to 25 nodes.

For boundary layer flows with blowing, profiles were again good. Drag coefficients were typically below the reported values for both the Simpson and the Jeromin data. With the Simpson data, there is considerable disagreement in the literature as to whether the reported drag coefficients are correct. For this reason, the rather poor agreement with the BLIMP predictions could only be termed "consistent but inconclusive." Since strong blowing is not typically encountered in heatshield ablation problems, it is concluded that a change in the turbulent model to fit the Simpson or Jeromin drag data is not justified without further study.

The very large number of computer runs necessary for the preparation of accurate predictions has resulted in new information on the use of the BLIMP code. A technique for starting a problem with a known profile at the first station was developed, and the "data start" runs emphasized some interesting features of the downstream solution. The general conclusion to be made from the data start runs is that wall region profiles (and the associated wall shear) approach the zero start predictions very rapidly, with the outer profile taking somewhat longer. This result then provides some information as to the accuracy inherent in the usual technique of starting a solution far upstream of the region of interest, with the expectation that starting profile errors will die out quickly.

The comparisons included in this report include demonstrations of the sensitivity of the predicted profiles to different numerical values of the turbulent model constants. It is concluded that, for unblown boundary layers, small (<30%) changes in these constants will not have any important effects on profile shapes. On the other hand, for flows with blowing, changes in the constants can have large effects on the profiles very near the wall, and therefore affect drag, heat transfer, etc. Thus, changes in the model constants as a function of blowing rate offers a straightforward method of altering wall parameters with this turbulent model. It may also be concluded that the model would be sensitive to other changes such as the substitution of τ_w for τ in equation 6.

2. RECOMMENDATIONS

Many areas for further investigation have become apparent during this study. Perhaps the foremost of these is the need for a straightforward continuation of the kind of work reported here, i.e., documentation of the validity of the code through comparison with experimental data. Fine tuning of the turbulent model for unblown flows should be carried out in order to make BLIMP the accurate and sophisticated prediction tool which it is intended to be. Initial studies should concentrate on drag data, then be extended to heat transfer. Much of the data screening and model development work could be carried out most efficiently with a one-dimensional code such as the WALAW program described in this report.

Once this fine tuning phase is completed, attention should be given to other types of flows not covered in the present study. Among the many flow regimes which merit attention are flows with large heat transfer, low Reynolds numbers (near transition), chemically reacting flows, and flows in adverse pressure gradient. All these conditions exist at the surface of a reentry vehicle, where the code is used to predict the resulting boundary layer. The need for verification is obvious.

The question of drag prediction in flows with blowing should also be resolved, perhaps through comparison with wall heat transfer rather than drag data. As a minimum, comparisons with some of the other cases shown in Table II should be carried out.

Finally, the need for additional experimental data in all types of flows is apparent. The hypersonic boundary layer area is of most interest for reentry vehicle purposes. Research programs aimed at the development of new instrumentation for use in blown or ablating boundary layer flows are particularly needed in order to eliminate the uncertainties that were brought out in this report.

APPENDIX

GENERAL DISCUSSION OF COMPUTER CODE SETUP AND OPTIONS

This appendix contains information on the use of the BLIMP code for the type of problems encountered with the selected data sets. It also presents details on the new entropy layer option.

1. SELECTION OF NODAL (η) DISTRIBUTION

The BLIMP solution procedure operates in the $(\xi, \bar{\eta})$ coordinate system, where these quantities are defined as

$$\xi = \int_0^s \rho_1 u_1 \mu_1 r_0^{2k} ds \quad (40)$$

$$\bar{\eta} = \frac{u_1}{\alpha_{11} \sqrt{2\xi}} \int_0^y \rho r^k dy \quad (41)$$

A $(\xi, \bar{\eta})$ grid system is assumed to be superimposed on the boundary layer region, where $\bar{\eta}$ is measured normal to the wall and ξ is measured parallel to it (see Figure 112). The boundary layer is divided into $N-1$ strips connecting N nodal points at each ξ station. These nodal points are designated by $\bar{\eta}_i$ where $i = 1$ at the wall and N at the edge of the velocity boundary layer. The nodal system expands and contracts with the boundary layer flow, since $\bar{\eta}_1$ is defined to be located at the wall, and $\bar{\eta}_N$ is defined to be the outer edge of the boundary layer. While the ξ numerical values are calculated automatically by the program from the axial station dimension (s), the $\bar{\eta}_i$ numerical values which it uses are supplied directly as input. This subsection provides some insight into the selection of $\bar{\eta}_i$ values for proper program operation.

a. Number of Nodes Required

Since BLIMP solves a linear matrix of order proportional to N (the number of $\bar{\eta}$ nodes), the time required to obtain a solution can be expected to be roughly proportional to N squared*. Consequently, it is desirable

* An average of the matrix inversion ($\sim N^3$) and other operations which are proportional to N and N^2 .

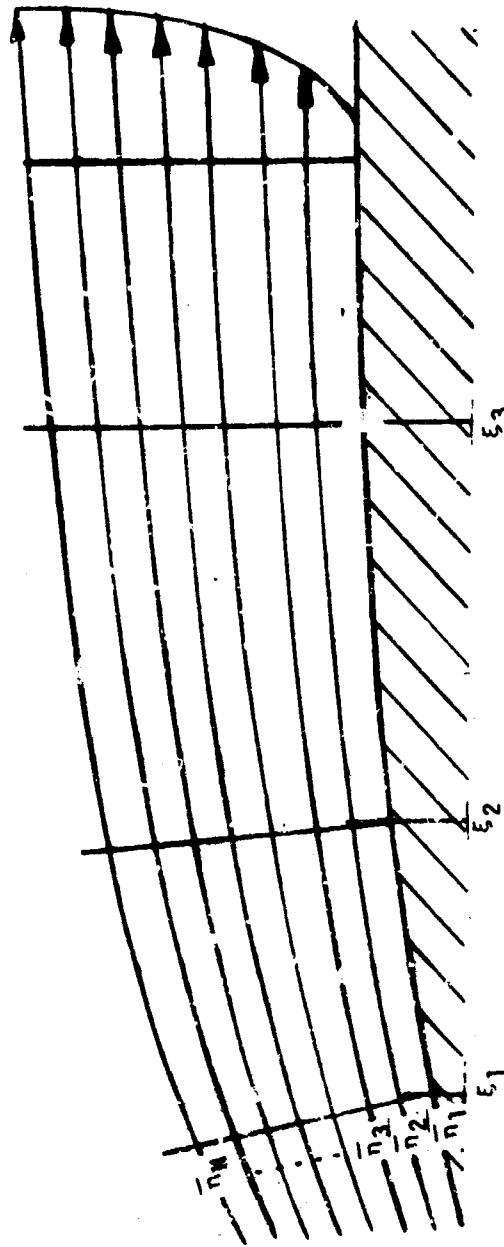


Figure 112. $\bar{\eta}$ - ξ Coordinate System

to determine the minimum number of nodes (and spacing of those nodes) which is consistent with an accurate and stable calculation of the boundary layer. No attempt was made to evaluate the minimum number aspect of this question; however on a number of different runs of Coles, Stanford and others, two BLIMP runs were made which were identical with the exception of the number of nodes, 15 being used on one and 25 on the other.

The results of one of the runs which are representative of all those made are as follows. First, for runs of Coles' test #20 with the same 8 axial stations, the number of iterations to a solution at each station was the same for either 15 or 25 nodes. The time required per iteration averaged 0.47 seconds for the 15-node run compared to 1.46 seconds for the 25-node run, a ratio of 0.31. The ratio of squares is 0.36; that is, a 25-node iteration took slightly longer than estimated by the N-squared proportionality. The differences in skin friction coefficient, C_f , and momentum thickness, θ , were consistently about 2.5 percent; the 15-node run having the lower values. Other comparison runs indicated similar differences (0 to 5 percent in C_f and θ) with the 15 node model giving consistently lower values.

Figure 113 shows the two velocity ratio profiles on a linear-log scale with the 25-node run as a solid line and the 15 node as circles. This evidence together with that above is judged sufficient to conclude that the 15-node model represents a worthwhile saving in computer time while maintaining satisfactory accuracy. Consequently, this model was used extensively for making the final BLIMP predictions. Due to the smaller number of nodes available, however, careful judgement had to be exercised in the choice of the nodal distribution.

b. Distribution of Nodes

Figure 114 depicts a typical turbulent velocity profile and also the variation of the first derivative of velocity through the boundary layer. The velocity gradient typically decreases three to four orders of magnitude between the wall value and the value at $u/u_e = 0.9$. Thus, the a priori selection of a nodal spacing to "curvefit" these variations with ten or fifteen discrete values is a difficult problem.

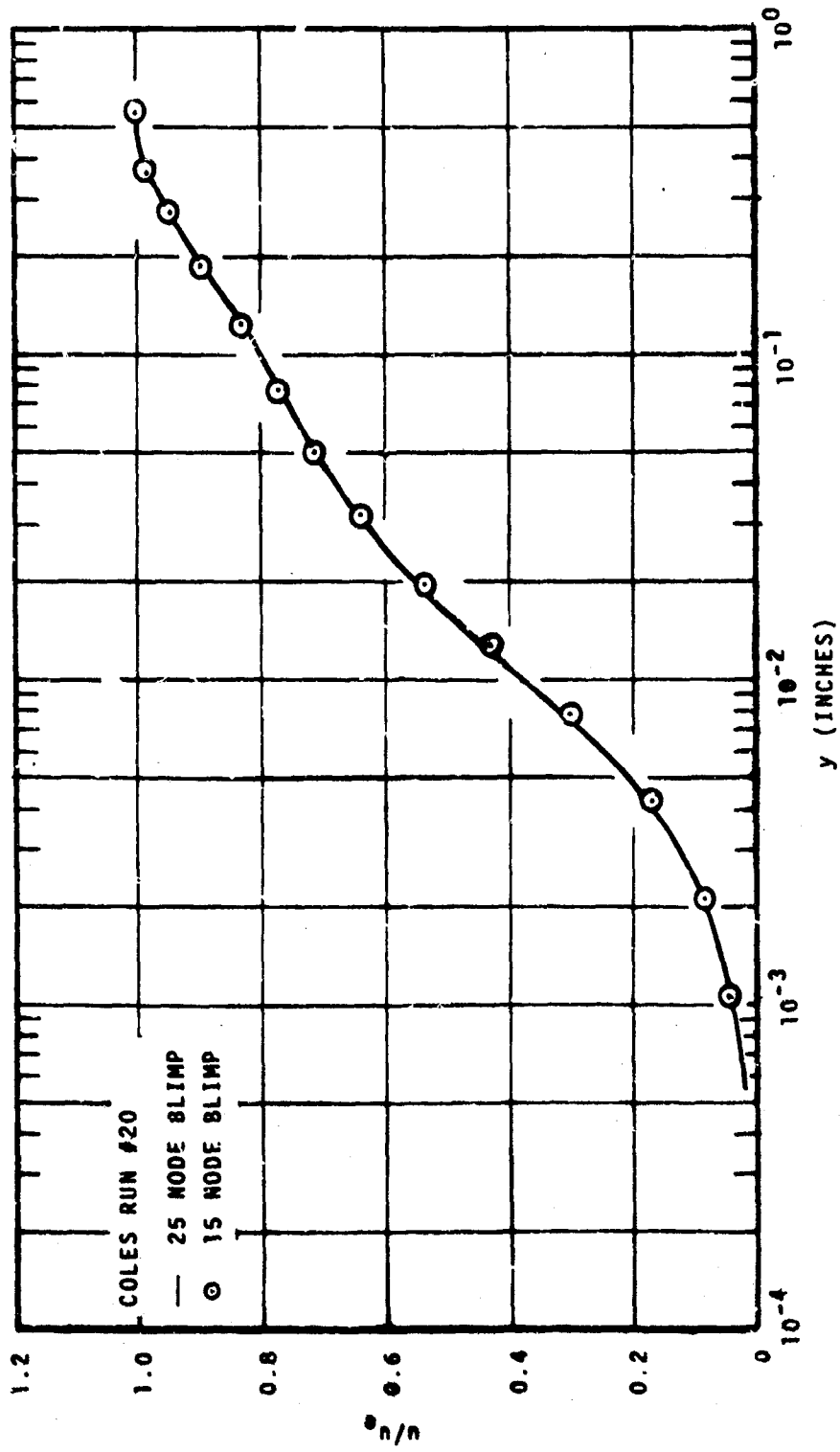


Figure 113. Comparison of BLIMP Velocity Profile Predictions for Different Numbers of Nodes

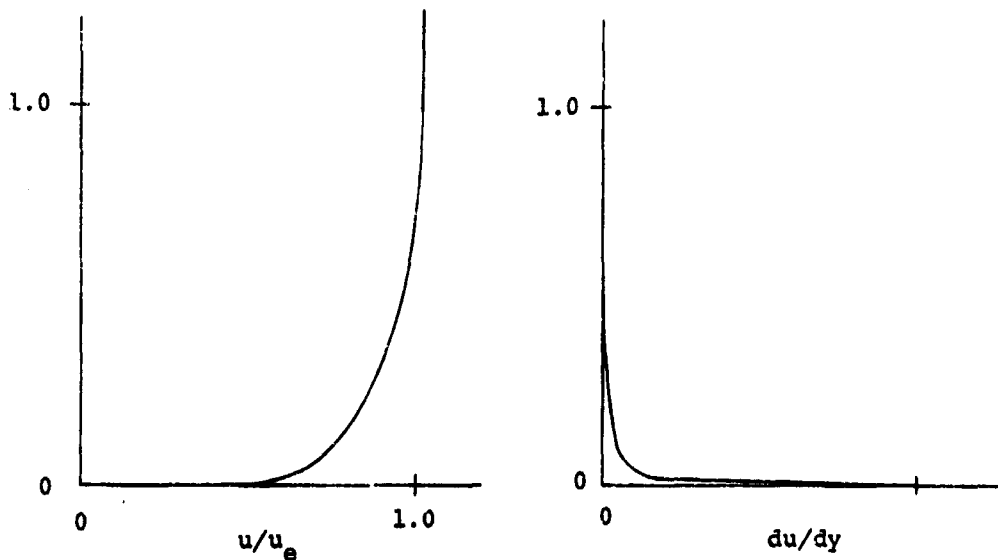


Figure 114. Typical Velocity and Velocity Gradient Profiles in a Turbulent Boundary Layer

The BLIMP manual (reference 90) suggests that the nodal spacing should be such that each successive value of $\bar{\eta}$ not exceed the previous value by much more than a factor of 2. This guideline has proven to be generally valid but should be evaluated relative to each particular type of profile. As profiles become distorted, as in the case of blowing, it may be necessary to warp the distribution as well to be certain that regions of high gradients are represented adequately. For curvefitting purposes, it is undesirable to have a change of greater than 0.1 in the velocity ratio between any adjacent nodes. If experimental data are available, a quick study of reported velocity profiles will enable the user to select a satisfactory distribution. In the event data are unavailable, a short computer run limited to a few stations can confirm the adequacy of the selected distribution or indicate necessary changes.

Perhaps the most important part of the distribution is that nearest the wall. Since BLIMP calculates C_f from the wall velocity gradient, and since the gradient at the wall is taken as the first derivative of the first spline fit quadratic evaluated at $y = 0$ (see reference 1), it is essential that the first several nodal points be located within the laminar sublayer. As a rule of thumb, at least the first two points away from the wall should have velocity ratios less than 0.1. This together with the general spacing guideline above should result in satisfactory prediction of the various wall parameters.

Another less obvious region of concern is the outer edge of the boundary layer. The properties of the quadratic and cubic spline-fits (the outer two points are joined by a cubic) are such that injudicious nodal spacing near the outer edge can cause an oscillatory overshoot of the edge value of 1.000 as shown in Figure 115. In this example the second to last node has been

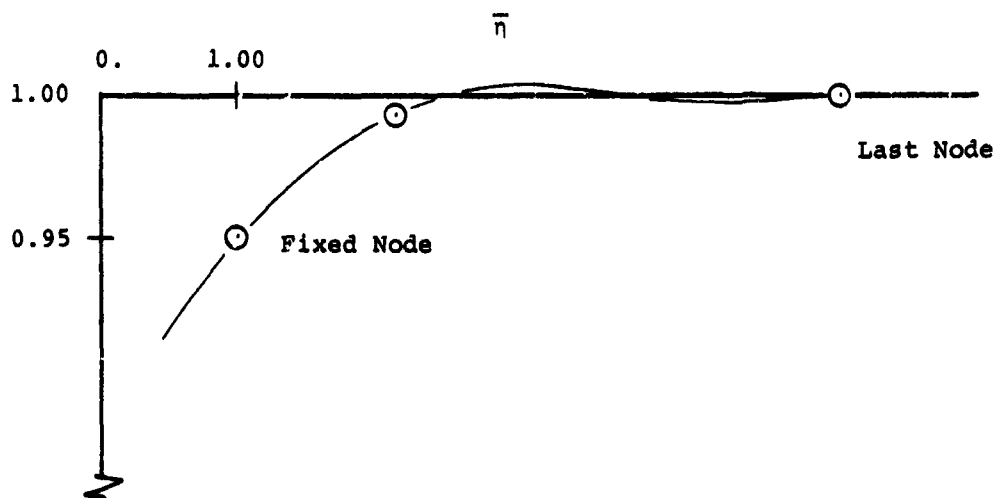


Figure 115. Overshoot of the Spline Fit Procedure

chosen as the fixed node (generally defined as $u/u_e = 0.95$ and $\bar{\eta} = 1.000$). The next to last node may have been chosen too close to the fixed node and/or the last node too far from the fixed node. Since the cubic is constrained to $u/u_e = 1.00$ and $\partial(u/u_e)/\partial\bar{\eta} = 0.00$ at the final point (in the absence of an entropy gradient), it is possible to generate an overshoot. Such an occurrence is especially troublesome since integral properties are computed by an exact integration of the quadratic and cubic curve segments. If the differences in $\bar{\eta}$ are large, even small excursions in u/u_e may lead to large errors in the various thickness integrals. Avoidance of this problem is again possible by observing simple guidelines.

First, if a data profile is available, the spacing of the final nodes can be approximated well enough. For subsonic flow, $\bar{\eta}$ and y are directly proportional. Supersonic flow requires somewhat smaller $\bar{\eta}$ spacing due to the (generally) decreasing density. Flows with blowing tend to approach the edge condition with higher gradients (du/dy) and thus require smaller spacing compared to unblown flows. If a profile is not available, a trial run may be necessary using the generalized approach described below. Special attention should be given to the values of FP (F PRIME = u/u_e) and to FPP (F DOUBLE PRIME = $\partial(u/u_e)/\partial\bar{\eta}$) at the last few points, particularly those points between the fixed point and the final point. If any of the points has a velocity ratio very near or exceeding 1.00 and/or if there is an inflection or change of sign in the derivative, an overshoot may have occurred. It is always helpful to plot these two values over the final few points on a linear scale to be sure.

During the course of this investigation the following choices for the \bar{n} distribution were made and were found to provide satisfactory results. The selection of which node should be the fixed \bar{n} node, the \bar{n} value for that node and the velocity ratio at that node is arbitrary. Choosing the value of \bar{n} as 1.00 makes for ease in ratioing to other values and is traditionally accepted, as is the choice of 0.95 for the velocity ratio (turbulent flow only). Both have been used exclusively for final BLIMP runs presented in this report. The number of the fixed node has been chosen as the 13th out of 15 total nodes. In some earlier runs, the 12th was fixed; however, this increases the possibility and the amplitude of overshoot due to a poor choice of spacing and additionally, places more nodes than necessary in a region of the profile that does not require as much detail. The next to last node should be chosen so as to result in a velocity ratio of 0.980 ± 0.005 . This will minimize the possibility of overshoot. Once again, an available profile is the best guide. The values in Table XI which were used for this contract may be used as a starting point if profiles are not available.

TABLE XI
TYPICAL \bar{n} DISTRIBUTIONS IN THE OUTER WAKE REGION

Type of Flow	14th \bar{n} Point		15th \bar{n} Point	
	Range of Values	Mean Value	Range of Values	Mean Value
Subsonic, no blowing	1.3	1.3	1.8	1.8
Subsonic, blowing	1.2 + 1.3	1.25	1.5 + 1.7	1.6
Supersonic, no blowing	1.3 + 1.5	1.4	1.8 + 2.7	2.1
Supersonic, blowing	1.15 + 1.2	1.2	1.67 + 1.75	1.7
Hypersonic	1.5 + 1.7	1.6	2.5 + 3.0	2.7

One final point should be considered. As the solution procedure progresses axially in the flow direction, the \bar{n} grid system is "stretched" in order to remain fixed to the outer edge of the growing boundary layer. Since the laminar sublayer does not grow as rapidly as the turbulent outer flow, the grid points nearest the wall may eventually be stretched out of the laminar region altogether, thereby giving inaccurate wall gradient information. It is necessary therefore to check the results at all important stations to be certain that the \bar{n} distribution is sufficient, especially at the wall. Restarting the program at some intermediate body station is a possibility for very long running lengths.

2. THE "DATA START" PROCEDURE

In the classical boundary layer problem, the initial and boundary conditions are such that a known profile (or profiles) is provided at an upstream station, and sufficient edge and wall conditions are provided along the flow direction. Profiles are then found at body stations of interest based on the boundary conditions and upstream profiles. In typical AFWL applications of the BLIMP code, however, upstream profile information is not available, and the program has been written to start the solution based on a similar solution profile at the first station (usually close to $X = 0$). When started in this manner sufficiently far upstream of the region of interest, the errors resulting from the approximate profile die out and accurate solutions are obtained at downstream locations. For most of the data sets chosen, edge and wall information were available in sufficient detail and accuracy to enable starting BLIMP in the conventional manner, that is, with a similar solution profile at an axial station slightly greater than zero (chosen here as 0.01 feet). In the supersonic and hypersonic tunnel flows where the test surface forms one side of the nozzle, conditions through the acceleration section are often not defined. Such was the case with Jeromin, Lee, et al., and to some degree with Brott, et al. An alternate procedure to enable comparisons to be made is to start BLIMP in the more classical manner, i.e., at the first reported data profile station with the measured velocity and temperature (enthalpy) profiles. The correct implementation of this starting procedure requires some detailed consideration, however

The BLIMP code instructions as described in reference 90 do indicate that the program can be started with an "input" profile as the solution at the first station. This starting option was intended primarily for restarting purposes, wherein an actual BLIMP solution is used as input to the code for further calculations. As an actual solution, this input profile satisfies the spline fit

quadratic and cubic relations between nodes which are inherent in the integral matrix formulation. Thus, to use this starting option successfully with actual experimental profiles at the first station, the spline fit requirement must also be satisfied. For the "data start" cases presented in this report, another computer program* was used which accepted the measured velocity and temperature profiles in physical coordinates, converted them to the $\bar{\eta}$ coordinate system, performed a least squares spline-type curve fit for 15 preselected $\bar{\eta}$ nodal values, and printed out the standard BLIMP "restart" information. This restart information was then provided to BLIMP as the first station profile. All data start runs reported herein include this technique and in all cases convergence was achieved at the second station in a normal manner, that is, in from 3 to 8 iterations with an average of only four iterations.

A few comments regarding the preparation of data and the resulting performance of the data start procedure are in order at this point to establish the degree of accuracy which has been attained in the use of this technique. Since none of the profiles of present interest are sufficiently defined near the wall, it is necessary to generate additional points for input to the least squares curve fit program. Figure 116 shows a typical case: the data of Jeromin run 2.5-1.2 (Mach 2.5, $F = 0.0012$). Only the portion of the profile near the wall is shown; the circles represent the reported data and the dashed line represents the value of $d(u/u_e)/dy$ at the wall based on the reported value of C_f . The solid curve represents an "eyeball" curve fit from which additional points were chosen. The necessity of this is apparent considering that at least two values of $\bar{\eta}$ not including $\bar{\eta} = 0.0$ should be chosen with $u/u_e < 0.1$ and about 3 more chosen in the remaining interval up to the first reported data point away from the wall. Any other regions which may not contain a sufficient number of data points may be "filled in" in a similar manner. The resulting supplemented experimental data constitute the required input profile. The temperature profile is obtained in the same manner except in Jeromin's cases, wherein temperature was defined by the velocity profile.

It is also of interest to examine the solution at nearby stations once BLIMP accepts the data start profile and proceeds on downstream. Figure 117 shows the progression in profile shape for the Jeromin case mentioned above. The solid curve with circles indicates the input velocity profile. The subsequent change in the solution for each nodal point is shown by the various symbols noted in the legend (including the station location). These solutions

* This program was on hand at Aerotherm and was not developed under this contract.

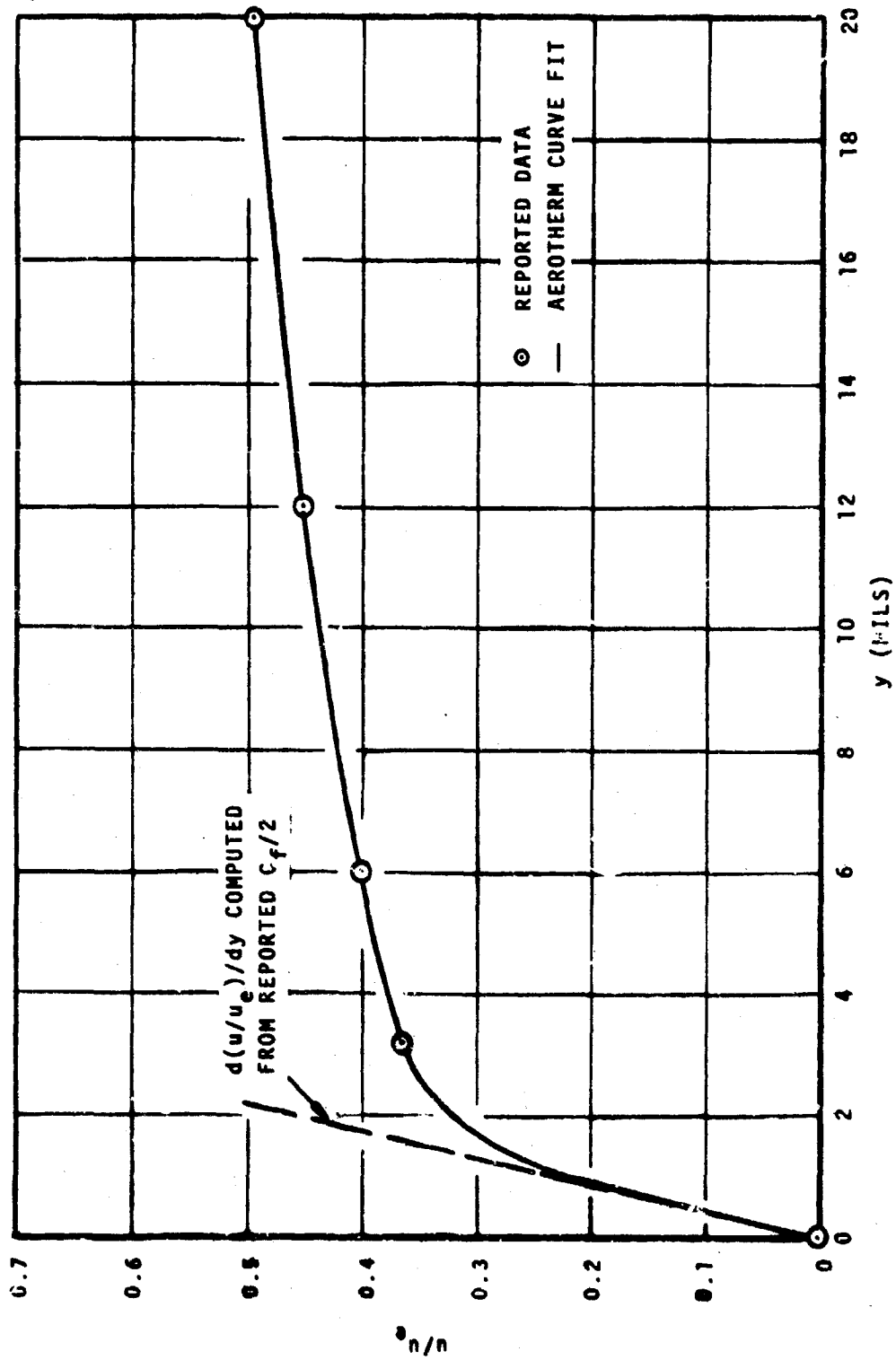


Figure 116. Definition of Near Wall Velocity Profile for Data Start Input

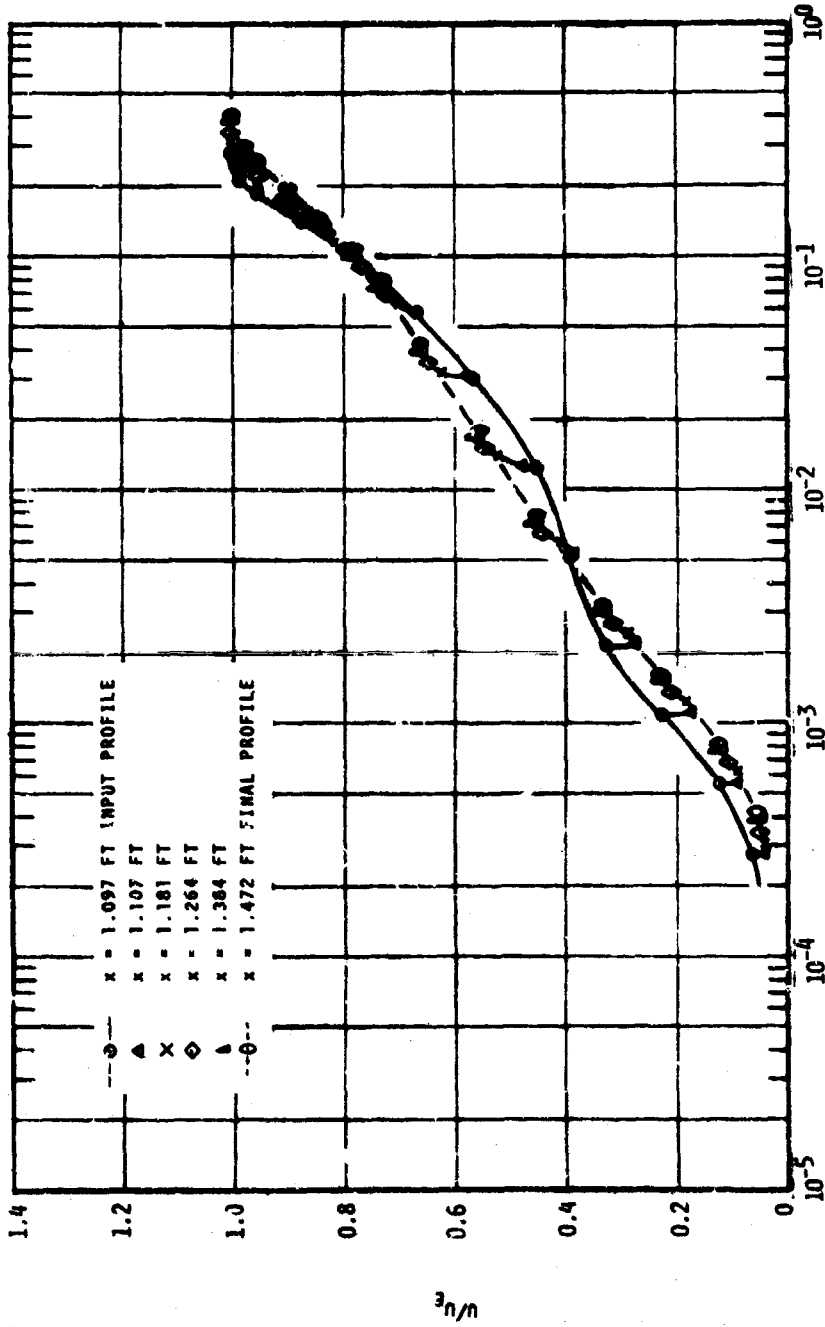


FIGURE 117. RESPONSE OF VELOCITY PROFILE FOLLOWING A DATA START: EXAMPLE, JEROTIN 2.5-1.2

are also connected by lines indicating the loci of the nodal point solutions. The nodal points of the final calculated profile are connected by the dashed curve. From comparisons made on other cases, this dashed curve would be quite similar to the profile shape BLIMP would predict based on a zero start.

At the second axial station (triangle symbols), there is little if any change over the bulk of the profile; however, near the wall major adjustments have occurred. This is due to a difference between the input C_f ($d(u/u_\infty)/dy$ at the wall) and the value BLIMP would predict given the same free stream and wall conditions. This adjustment takes place over very small axial distances. It appears to be identical to adjustments which are made in response to steps in wall conditions such as temperature and blowing rate. Although the magnitude of the adjustment is large, it is limited to a very thin layer near the wall. It therefore has a negligible effect upon thickness integrals which change in a smooth and continuous manner (see Section IV). As the solution continues on downstream, an adjustment is made to the outer portion of the law of the wall region while the overall "normal" growth of the boundary layer is reflected by a steady thickening out in the wake region. By the final dashed profile shown, the adjustments to the shape appear to be complete, and ordinary boundary layer growth accounts for any shifting of the points. A number of examples of the manifestations of this behavior are apparent in the graphical presentations in Section IV. In general, "recovery" from the data start profile is (1) essentially immediate for wall properties such as C_f , (2) for all practical purposes, unaffected by the starting values of the various integral parameters and (3) slow for the overall profile, taking on the order of 10 boundary layer thicknesses. This latter "recovering" simply implies that, given the existing conditions at the first reported profile station, BLIMP would not have predicted that profile, the difference in shape being similar to that between the solid and dashed profiles in Figure 117.

3. HOMOGENEOUS FLOW CONSIDERATIONS

All of the cases considered in this turbulent model study involved only air as a working fluid, both as the main stream gas and as the transpirant. Also, the temperature range under consideration was low enough that no chemical reactions would take place. Thus, it is possible to realize some economies in the operation of the BLIMP program in this limited thermochemical regime. The program was modified to operate in a homogeneous flow mode by accepting a single species in the thermochemical data deck. This species is treated as an element (named "cold air"); it is given its own fictitious atomic number and the usual set of thermochemical curvefit constants. Accurate transport

properties can also be realized in this mode of operation by reading in correct diffusion factor data under Group 12 of the program input.

4. ENTROPY LAYER OPTION

A new feature of the BLIMP code is the entropy layer option, which offers a direct coupling of entropy gradients in the inviscid flow with the boundary layer edge conditions. Inviscid flow entropy can be determined directly as a function of ϕ , the dimensional stream function. Further this functional relation can, for the case of a typical reentry vehicle, be determined from the shock shape. The entropy is established from the shock angle, and the stream function from the simple integration of a uniform freestream flow.

If the boundary layer "swallows" a sufficient flow mass to result in sizeable entropy variations within the swallowed mass, it is necessary to account for this phenomena adequately. An iterative mass balancing procedure is used to establish the correct edge entropy. Given an initial estimate of the edge condition, a solution is generated. The edge stream function from this solution demands a certain edge entropy, which is then compared with the edge entropy calculated from the edge pressure and enthalpy. These two entropies may be different, in which case the estimate of edge conditions is altered and a new solution is obtained. This iteration procedure is an integral part of the existing solution iteration procedure, and therefore does not generally add to the number of iterations required or the program run time.

The fact that the BLIMP code is written in terms of normalized dependent variables adds some confusion to the entropy layer solution. It is well known that the existence of an entropy gradient at the edge of the boundary layer also requires a velocity gradient, i.e.,

$$u \frac{\partial u}{\partial y} = \tau \frac{\partial s}{\partial y} \quad (42)$$

Since velocity varies in the inviscid flow at the edge of the boundary layer, the definition of a u_e value to be used in forming the dimensionless velocity ratio u/u_e is difficult. The problem was solved by using a reference velocity, u_r , defined by an isentropic expansion from stagnation conditions. The formulation of the equations as carried out in reference 1 remains valid with the new stipulation that

$$\frac{f'}{\alpha_H} = \frac{u}{u_r} \quad (43)$$

The pressure gradient parameter β enters the nondimensional formulation of the momentum equation in the same way, since the Bernoulli equation holds for the isentropic expansion

$$-\frac{1}{\rho} \frac{\partial P}{\partial x} = u_r \frac{\partial u_r}{\partial x} \quad (44)$$

and we will define

$$\beta \equiv 2 \frac{\partial \ln u_r}{\partial \ln \xi} \quad (45)$$

The pressure gradient term in the momentum equation remains essentially unaffected as

$$\beta \left(\frac{\rho_r}{\rho} - f'^2 \right)$$

In the BLIMP solution procedure, the value of $u_e/u_r = f'_N/\alpha_H$ is a variable at each station for entropy layer flows. It is determined from straightforward energy relationships for the reference and actual inviscid expansions around the body. As with the isentropic edge condition, the selection of the solution domain (i.e., the selection of the maximum value of $\bar{\eta}$) is arbitrary. Conventional techniques for interpreting the results in this solution domain must be re-examined, however. For example, at any given body station, two individual computer runs with different choices for the numerical value of $\bar{\eta}_N$ would result in two different edge velocity values. Different values of u_e/u_r would also occur. Both solutions are correct, however, since a velocity gradient should exist in an entropy layer region. This velocity gradient will project one edge state to the other and the choice of the $\bar{\eta}_N$ value merely determines how far into the inviscid region the boundary layer solution will extend.

One other interesting feature of the entropy layer operation of the program is the definition of the coordinate stretching parameter, α_{11} . Formerly, coordinate stretching was accomplished by constraining some arbitrary point near the boundary layer edge, $\bar{\eta}_C$, to have a specified velocity ratio, C , near

(but something less than) the edge value (reference 1). With an edge velocity gradient, this constraint has been modified to deal with the straight line extrapolation of the edge velocity, rather than the ratio itself, as shown in Figure 118. The selection of kappa and CBAP input values (Group 4, Card 3 reference 90) is not changed.

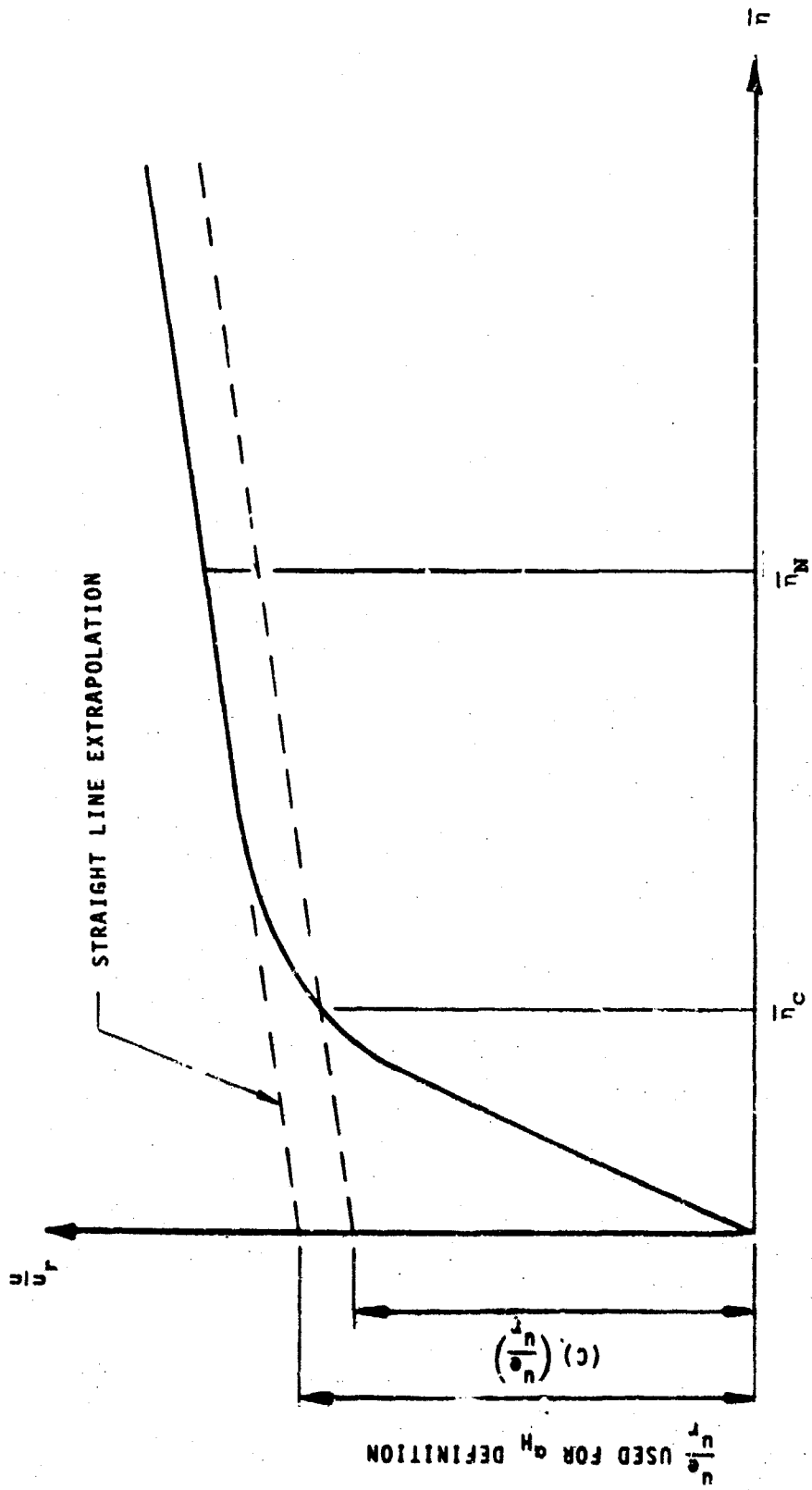


Figure 118. α_H Constraint With Entropy Layer Flow

REFERENCES

1. Anderson, L. W. and Kendall, R. M.; A Nonsimilar Solution for Multicomponent Reacting Laminar and Turbulent Boundary Layer Flows Including Transverse Curvature, Air Force Weapons Laboratory, Kirtland Air Force Base, New Mexico, Report AFWL-TR-69-106, March 1970.
2. Kendall, R. M., Rubesin, M. W., Dahm, T. J., and Mendenhall, M. R.; Mass, Momentum, and Heat Transfer Within a Turbulent Boundary Layer with Foreign Gas Mass Transfer at the Surface, Part I - Constant Fluid Properties, Vidya Division, Itek Corporation, Final Report No. 111, 1964.
3. Adcock, J. B., Peterson, J. B., and McRee, D. I.; Experimental Investigations of a Turbulent Boundary Layer at Mach 6, High Reynolds Numbers, and Zero Heat Transfer, NASA TN D-2907, July 1965.
4. Allen, J. M.; Experimental Preston Tube and Law of the Wall Study of Turbulent Skin Friction on Axisymmetric Bodies at Supersonic Speeds, NASA TN D-5660, February 1970.
5. Brinich, P. F. and Neumann, H. E.; "Some Effects of Acceleration on the Turbulent Boundary Layer," AIAA Journal, Volume 8, No. 5, May 1970, pp. 987-989.
6. Drott, D. L., Yanta, W. J., Voisinet, R. L. and Lee, R. E.; An Experimental Investigation of the Compressible Turbulent Boundary Layer with a Favorable Pressure Gradient, Naval Ordnance Laboratory, White Oak, Maryland, NOLTR 69-143, August 25, 1969.
7. Cary, A. M.; "Turbulent Boundary Layer Heat Transfer and Transition Measurements for Cold Wall Conditions at Mach 6," AIAA Journal, Volume 6, No. 5, May 1968, pp. 958-959.
8. Coles, D. E.; Measurements in the Boundary Layer on a Smooth Flat Plate in Supersonic Flow. III. Measurements in a Flat Plate Boundary Layer at the Jet Propulsion Laboratory, Jet Propulsion Laboratory, California Institute of Technology, Pasadena, California, Report No. 20-71, June 1953.
9. Escudier, M. P.; The Turbulent Incompressible Hydrodynamic Boundary Layer, Ph.D. Dissertation, Imperial College of Science and Technology, University of London, London, England, October 1957.
10. Fischer, M. C., Maddalon, D. V., Weinstein, L. M., and Wagner, R. D.; Boundary Layer Surveys on a Nozzle Wall at M=20 Including Hot Wire Fluctuation Measurements, AIAA Paper No. 70-746, June 1970.
11. Graber, B. C., Weber, H. E., and Softley, E. J.; Comparison of Laminar and Turbulent Cone Boundary Layer Flow With and Without Pressure Gradient, General Electric Company, Missile and Space Division, Philadelphia, Pennsylvania, Report R67SD49, November 1967.
12. Hill, F. K.; "Turbulent Boundary Layer Measurements at Mach Numbers from 8 to 10," The Physics of Fluids, Vol. 2, No. 6, November-December, 1959, pp. 668-690.

13. Hopkins, R. A. and Nerem, R. M.: "An Experimental Investigation of Heat Transfer from a Highly Cooled Turbulent Boundary Layer," AIAA Journal, Vol. 6, No. 10, Oct. 1968, pp. 1912-1918.
14. Jones, R. A. and Feller, W. V.; Preliminary Surveys of the Wall Boundary Layer in a Mach 6 Axisymmetric Tunnel, NASA TN D-5620, February, 1970.
15. Julien, H. L., Kays, W. M., and Moffat, R. J.; The Turbulent Boundary Layer on a Porous Plate, Experimental Study of the Effects of a Favorable Pressure Gradient, Department of Mechanical Engineering, Stanford University, Report HMT-4, April 1969.
16. Kearney, D. W., Kays, W. M., Moffat, R. J., and Lloyd, R. J.; The Effect of Free-Stream Turbulence on Heat Transfer to a Strongly Accelerated Turbulent Boundary Layer, Department of Mechanical Engineering, Stanford University, Report HMT-9, February 1970.
17. Lee, R. E., Yanta, W. A., and Leonas, A. C.; Velocity Profile, Skin Friction Balance, and Heat Transfer Measurements of the Turbulent Boundary Layer at Mach 5 and Zero Pressure Gradient, Naval Ordnance Laboratory, White Oak, Maryland, NOLTR 69-106, June 1969.
18. Unpublished test data received from John E. Lewis, TRW Systems, Redondo Beach, Calif. Data groups 61-77, 134-157, and 200-244 of Project No. VA0094, SAMSO-TRW Turbulent Boundary Layer Study completed August 26, 1970.
19. Lloyd, R. J., Moffat, R. J., and Kays, W. M.; The Turbulent Boundary Layer on a Porous Plate, An Experimental Study of the Fluid Dynamics with Strong Favorable Pressure Gradients and Blowing, Department of Mechanical Engineering, Stanford University, Report HMT-13, May 1970.
20. Lobb, R. K., Winkler, E. M., and Persh, J.: NOL Hypersonic Tunnel No. 4 Results, Part VII, Experimental Investigation of Turbulent Boundary Layers in Hypersonic Flow, U.S. Naval Ordnance Laboratory, White Oak, Maryland, NAVORD Report 3880, March 1955.
21. Matthews, R. K. and Trimmer, L. J.; Nozzle Turbulent Boundary Layer Measurements in the VKF 50 Inch Hypersonic Tunnels, Arnold Engineering and Development Corp., Tullahoma, Tenn., AEDC-TR-69-118, June 1969.
22. Metting, F. W., Chapman, D. R., Nyholm, J. R., and Thomas, A. G.; Turbulent Skin Friction at High Mach Numbers and Reynolds Numbers in Air and Helium, NASA TR-R-82, 1961.
23. Meier, H. U. and Rotta, J. C.; Experimental and Theoretical Investigations of Temperature Distributions in Supersonic Boundary Layers, AIAA Paper No. 70-744, June 1970.
24. Michel, R., Quemard, C. and Elena, M.; "Velocity Distributions in a Turbulent Boundary Layer in Uniform or Accelerated Compressible Flow," translation from la Recherche Aerospaciale, No. 128, January-February, 1969, pp. 33-47, NASA TT-F-12,538, August 1969.
25. Moffat, R. J. and Kays, W. M.; The Turbulent Boundary Layer on a Porous Plate, Experimental Heat Transfer with Uniform Blowing and Suction, Department of Mechanical Engineering, Stanford University, Report HMT-1, August 1967.
26. Moore, D. R. and Harkness, J.; "Experimental Investigation of the Compressible Turbulent Boundary Layer at Very High Reynolds Numbers," AIAA Journal, Vol. 3, No. 4, April 1965, pp. 631-638.

27. Nagamatsu, H. T., Wisler, J. C., and Sheer, R. E.; Hypersonic Laminar and Turbulent Skin Friction and Heat Transfer on a Slender Cone, Ballistic Systems Division, Air Force Systems Command, Norton Air Force Base, California, BSD-TR 67-85, March 1967.
28. Neal, L.; A Study of the Pressure, Heat Transfer, and Skin Friction on Sharp and Blunt Flat Plates at Mach 6.8, NASA TN D-3312, April 1966.
29. Noonan, B. J. and Rand, J. L.; High Temperature Turbulent Heat Transfer Measurements, U. S. Naval Ordnance Laboratory, White Oak, Maryland, NOLTR 63-276, January 1964.
30. Perry, J. H. and East, R. A.; "Experimental Measurements of Cold Wall Turbulent Hypersonic Boundary Layers, In Hypersonic Boundary Layers and Flow Fields," Agard Conference Proceedings, No. 30, May 1968.
31. Samuels, R. D., Peterson, J. B., and Adcock, J. B.; Experimental Investigation of the Turbulent Boundary Layer at a Mach Number of 6 with Heat Transfer at High Reynolds Numbers, NASA TN D-3358, March 1967.
32. Scaggs, Norman E.; Boundary Layer Profile Measurements in Hypersonic Nozzles, Aerospace Research Laboratories, Wright Patterson AFB, Ohio, APL-66-0141, July 1966.
33. Simpson, R. L., Kays, W. M., and Moffat, R. J.; The Turbulent Boundary Layer on a Porous Plate-An Experimental Study of the Fluid Dynamics with Injection and Suction, Stanford University, Department of Mechanical Engineering, Report No. HMT-2, December 1967.
34. Thielkahr, W. H., Kays, W. M., and Moffat, R. J.; The Turbulent Boundary Layer, Experimental Heat Transfer with Blowing, Suction, and Favorable Pressure Gradient, Department of Mechanical Engineering, Stanford University, Report HMT-5, April 1969.
35. Wallace, J. E.; "Hypersonic Turbulent Boundary Layer Studies at Cold Wall Conditions," Proceedings of the 1967 Heat Transfer and Fluid Mechanics Institute, Stanford University Press, Stanford, California June 1967.
36. Wallace, J. E., Hypersonic Turbulent Boundary Layer Measurements Using an Electron Beam, Cornell Aeronautical Laboratory, Inc., Buffalo, New York, Report No. AN-2112-Y-1, August 1968.
37. Whitten, D. G., Kays, W. M., and Moffat, R. J.; The Turbulent Boundary Layer on a Porous Plate, Experimental Heat Transfer with Variable Suction, Blowing, and Surface Temperature, Department of Mechanical Engineering, Stanford University, Report HMT-3, December 1967.
38. Wieghardt, K. and Tillman, W.; U and M 5617 (1944), translated as On The Turbulent Friction Layer for Rising Pressure, NACA TM 1314, 1951.
39. Wilson, D. M.; Measurements of Hypersonic Turbulent Heat Transfer on a Highly Cooled Cone, U. S. Naval Ordnance Laboratory, White Oak, Maryland, NOLTR 67-24, July 1967.
40. Winkler, E. M. and Cha, M. H.; Investigation of Flat Plate Hypersonic Turbulent Boundary Layers with Heat Transfer at a Mach Number of 5.2, U. S. Naval Ordnance Laboratory, White Oak, Maryland, NAVORD Report 6631, Sept. 1959.
41. Alsaji, S. J., The Transpired Turbulent Boundary Layer with Heat Transfer, Ph.D. Dissertation, Mechanical Engineering Department, University of Utah, Salt Lake City, Utah, June 1968.

42. Baker, E.: Influence of Mass Transfer on Surface Friction at a Porous Surface, Ph.D. Dissertation, Imperial College of Science and Technology, University of London, London, England, January 1967.
43. Bartle, E. R. and Leadon, B.M.: "The Effectiveness as a Universal Measure of Mass Transfer Cooling for a Turbulent Boundary Layer," Proceedings of the 1962 Heat Transfer and Fluid Mechanics Institute, Stanford University Press, Stanford, Calif., July 1967, pp. 27-41.
44. Danberg, J.E.: Measurement of the Characteristics of the Compressible Turbulent Boundary Layer with Air Injection, U. S. Naval Ordnance Laboratory, White Oak, Maryland, NAVORD Report 6683, Sept. 1959.
45. Danberg, J. E.: Characteristics of the Turbulent Boundary Layer with Heat and Mass Transfer at $M = 6.7$, Naval Ordnance Laboratory, White Oak, Maryland, NOLTR 64-99, October 1964.
46. Dershin, H., Leonard, C. A. and Gallaher, W. H.: "Direct Measurement of Skin Friction on a Porous Flat Plate with Mass Injection," AIAA Journal, Vol. 5, No. 11, Nov. 1967, pp. 1934-1939.
47. Fernandez, F. L. and Zukoski, E. E.: "Experiments in Supersonic Turbulent Flow with Large Distributed Surface Injection," AIAA Journal, Vol. 7, No. 9, Sept. 1969, pp. 1759-1767.
48. Jeromin, L. O. F.: An Experimental Investigation of the Compressible Turbulent Boundary Layer with Air Injection, ARC R/M 3526, Nov. 1966.
49. Jones, J. W.: A Turbulent Boundary Layer with Mass Addition, Combustion, and Pressure Gradients, Ph.D. Dissertation, University of Utah, Salt Lake City, Utah, June 1970.
50. Kent, R. Martellucci, A. and George, F.: Static Force and Induced Pressure Measurements on a Slender Porous Cone with Gas Injection. (U), Aeromechanics and Materials Laboratory Operation, Re-Entry Systems Dept., General Electric Company, Philadelphia, Pennsylvania, Aerodynamics Lab. Data Memo, ALDM 69-75, February 1969.
51. Kuigain, N.G.: "Transport Processes in a Combustible Turbulent Boundary Layer," Journal of Fluid Mechanics, 12, Part 3, March 1962, pp. 417-437.
52. Martellucci, A.: Static Force, Surface Pressure, and Profile Measurements on a Porous Cone with Gas Injection - Data Presentation - General Electric, Reentry and Environmental Systems Division, Valley Forge, Pa., Document No. 70SD462, GMSO TR-70-152, January 1970.
53. McQuaid, J.: Experiments on Incompressible Turbulent Boundary Layers with Distributed Injection, ARC R/M-3549, Jan. 1967.
54. Muzzy, R. J.: "Surface Mass Addition into a Turbulent Boundary Layer," AIAA Journal, Vol. 5, No. 5, May 1967, pp. 1029-1033.
55. Pappas, C. C. and Okuno, A. F.: "Measurements of Skin Friction of the Compressible Turbulent Boundary Layer on a Cone with Foreign Gas Injection," Journal of the Aerospace Sciences, Vol. 27, No. 5, May 1960, pp. 321-333.
56. Pappas, C. C. and Okuno, A. F.: Measurement of Heat Transfer and Recovery Factor of a Compressible Turbulent Boundary Layer on a Sharp Cone with Foreign Gas Injection, NASA TR D-2210, April 1964.

57. Peterson, J. B., McRee, D. I., Adcock, J. B., and Braslow, A. L.; Further Investigation of Air Injection Through Slots and Porous Surfaces On Flat Plate Turbulent Skin Friction at Mach 3, NASA TN D-3311, March, 1966.
58. Romanenko, P. N. and Kharchenko, V. N.; "The Effect of Transverse Mass Flow on Heat Transfer and Friction Drag in a Turbulent Flow of Compressible Gas Along an Arbitrarily Shaped Surface," Int. J. of Heat and Mass Transfer, Vol. 6, No. 8, August 1963, pp. 727-738.
59. Smith, T. H.; Hot Film Characteristics in a Turbulent Boundary Layer with Foreign Gas Injection, Ph.D. Dissertation, Mechanical Engineering Department, University of Utah, Salt Lake City, Utah, June 1969.
60. Squire, L. C.; Further Experimental Investigations of Compressible Turbulent Boundary Layers with Air Injection, ARC R/M 3627, August 1968.
61. Wimberly, C. R., McGinnis, F. K., and Bertin, J. J.; "Transpiration and Film Cooling Effects for a Slender Cone in Hypersonic Flow.," AIAA Journal, Vol. 8, No. 6, June 1970.
62. Winkler, E. M., Madden, M. T., Humphrey, R. L., and Koenig, J. A.; Supersonic Ablation Studies with Teflon, Naval Ordnance Laboratory, NOLTR 69-125, Oct. 1969.
63. Wooldridge, C. E., and Muzzy, R. J.; "Boundary Layer Turbulence Measurements with Mass Addition and Combustion," AIAA Journal, Vol. 4, No. 11, Nov. 1966, pp. 2009-2016.
64. Kline, S. J., Morkovin, M. V., Sovran, G., and Cockrell, D. J., editors; Proceedings-Computation of Turbulent Boundary Layers, 1968 AFOSR-IFP-Stanford Conference, Stanford University, Department of Mechanical Engineering, 1969.
65. Mickley, H. S. and Davis, R. S.; Momentum Transfer for Flow Over a Flat Plate with Blowing, NACA TN 4017, November, 1957.
66. Kendall, R. M.; Interaction of Mass and Momentum Transfer in the Turbulent Boundary Layer, Ph.D. Dissertation, Massachusetts Institute of Technology, Cambridge, Massachusetts, 1959.
67. Hahn, J. S. and Lutz, R. G.; Experimental Investigation of Turbulent Boundary Layers With Pressure Gradient and Heat Transfer at Mach 4, Arnold Engineering and Development Center, Tullahoma, Tennessee, AEDC-TR-71-3, January, 1971.
68. Cebeci, T.; Calculation of Compressible Turbulent Boundary Layers with Heat and Mass Transfer, AIAA Paper No. 70-741, June, 1970.
69. Bushnell, D. M. and Beckwith, I.E.; Calculation of Nonequilibrium Hypersonic Turbulent Boundary Layers and Comparisons with Experimental Data, AIAA Paper No. 69-684, June 1969.
70. Patankar, S. V. and Spalding, D. B., Heat and Mass Transfer in Boundary Layers, Morgan-Grampian, London, 1967.
71. Martellucci, A., Rie, H., and Sontowski, J. F.; Evaluation of Several Eddy Viscosity Models Through Comparison with Measurements in Hypersonic Flows, AIAA Paper No. 69-688, June, 1969.
72. Powell, T. E. and Strong, A. B.; "Calculation of the Two-Dimensional Turbulent Boundary Layer with Mass Addition and Heat Transfer," in

- Proceedings of the 1970 Heat Transfer and Fluid Mechanics Institute, T. Sarpkaya, editor, Stanford University Press, Stanford, California, 1970.
73. Reyhner, T.; "Finite Difference Solution of the Compressible Turbulent Boundary Layer Equations," in Proceedings, Computation of Turbulent Boundary Layers - 1968 AFOSR-IFP-Stanford Conference, S. J. Kline, et al., editors, Stanford University, Department of Mechanical Engineering, 1969.
 74. Herring, H. J. and Mellor, G. L.; A Computer Program to Calculate Incompressible Laminar and Turbulent Boundary Layer Development, NASA CR-1564, March 1970.
 75. Van Driest, E. R.; "On Turbulent Flow Near a Wall., Journal of the Aerospace Sciences, Vol. 23, No. 11, November 1956.
 76. Klebanoff, P. S.; Characteristics of Turbulence in a Boundary Layer with Zero Pressure Gradient, NACA TN 3178, July 1954.
 77. Cebeci, T., Smith, A. M. O., and Mosinskis, G.; "Calculation of Compressible Adiabatic Turbulent Boundary Layers," AIAA Journal, Vol. 8, No. 11, November 1970.
 78. Cebeci, T.; A Model for Eddy Conductivity and Turbulent Prandtl Number, "McDonnell-Douglas Corporation, Long Beach, California, Report No. MDC-J0747/01, May 1970.
 79. Cebeci, T. and Mosinskis, G. J.; Prediction of Turbulent Boundary Layers with Mass Addition, Including Highly Accelerating Flows, ASME Paper No. 70-HT/SP-19, 1970.
 80. Personal Communication with Dr. Dennis Bushnell, NASA Langley Research Center, November 1970.
 81. Stevenson, T. N.; A Law of the Wall for Turbulent Boundary Layers with Suction or Injection, The College of Aeronautics, Cranfield, England, Report Aero No. 166, July 1963.
 82. Bartlett, Eugene P., and Grose, Ronald D.; The Multicomponent Laminar Boundary Layer Over Graphite Sphere Cones, Solutions for Quasisteady Ablation and Application to Transient Reentry Trajectories, Aerotherm Corporation, Mt. View, Calif., Final Report No. 68-35, 29 May 1968.
 83. Simpson, R. L., Whitten, D. G., and Moffat, R. J.; "An Experimental Study of the Turbulent Prandtl Number of Air with Injection and Suction," International Journal of Heat and Mass Transfer, Volume 13, 1970, pp. 125-143.
 84. Meier, H. U. and Rotta, J. C.; Experimental and Theoretical Investigations of Temperature Distributions in Supersonic Boundary Layers, AIAA Paper No. 70-744, June 1970.
 85. Johnson, D. S.; "Velocity and Temperature Fluctuation Measurements in a Turbulent Boundary Layer Downstream of a Step-wise Discontinuity in Wall Temperature," Journal of Applied Mechanics, Volume 26, 1959, pp. 326-336.
 86. Goldman, I. B. and Marchello, J. M.; "Turbulent Schmidt Numbers," International Journal of Heat and Mass Transfer, Volume 12, 1969, pp. 797-802.
 87. Squire, L. C.; "The Constant Property Turbulent Boundary Layer with Injection; A Reanalysis of Some Experimental Results," International Journal of Heat and Mass Transfer, Volume 13, No. 5, May 1970, pp. 939-947.

88. Squire, L. C.; Further Experimental Investigations of Compressible Turbulent Boundary Layers with Air Injection, Aeronautical Research Council, R and M No. 3627, August 1968.
89. Simpson, R. L., Moffat, R. J., and Kays, W. M.; "The Turbulent Boundary Layer on a Porous Plate: Experimental Skin Friction with Variable Injection and Suction," International Journal of Heat and Mass Transfer, Volume 12, No. 7, July 1969, pp. 771-789.
90. Anderson, L. W., Bartlett, E. P., and Kendall, R. M.; Users' Manual, Boundary Layer Integral Matrix Procedure, Air Force Weapons Laboratory, Kirtland Air Force Base, New Mexico, AFWL-TR-69-114, Volume I, March 1970.
91. Rubesin, M. W.; An Analytical Estimation of the Effect of Transpiration Cooling on the Heat Transfer and Skin Friction Characteristics of a Compressible Turbulent Boundary Layer, NACA Report No. TN 3341, 1954.
92. Mickley, H., Ross, R. C., Squyers, A. L., and Stewart, W. E.; Heat, Mass, and Momentum Transfer for Flow Over a Flat Plate With Blowing or Suction, NACA TN 3208, 1954.
93. Dorrance, W. H. and Dore, F. J.; "The Effect of Mass Transfer on the Compressible Turbulent Boundary Layer Skin Friction and Heat Transfer," Journal of the Aerospace Sciences, Vol. 21, 1954, p. 404.
94. Kutateladze, S. S. and Leont'ev, A. I., Turbulent Boundary Layers in Compressible Gases, Academic Press, New York, 1964.